Orbital-order phase transition and non-adiabatic quantum-classical dynamics in strongly coupled electron-phonon systems

Dissertation
zur Erlangung des mathematisch-naturwissenschaftlichen Doktorgrades
“Doctor rerum naturalium”
der Georg-August-Universität Göttingen

im Promotionsstudiengang Physik
der Georg-August University School of Science (GAUSS)

vorgelegt von

Michael ten Brink

aus München

Göttingen, 2022

Betreuungsausschuss

Prof. Dr. Peter E. Blöchl
Institut für Theoretische Physik
Technische Universität Clausthal

Prof. Dr. Christian Jooß
Institut für Materialphysik
Georg-August-Universität Göttingen

Prof. Dr. Stefan Kehrein
Institut für Theoretische Physik
Georg-August-Universität Göttingen

Mitglieder der Prüfungskommission

Referent: Prof. Dr. Peter E. Blöchl
Institut für Theoretische Physik
Technische Universität Clausthal

Korreferent: Prof. Dr. Fabian Heidrich-Meisner
Institut für Theoretische Physik
Georg-August-Universität Göttingen

Weitere Mitglieder der Prüfungskommission

Prof. Dr. Christian Jooß
Institut für Materialphysik
Georg-August-Universität Göttingen

apl. Prof. Dr. Michael Seibt
IV. Physikalisches Institut
Georg-August-Universität Göttingen

Prof. Dr. Stefan Mathias
I. Physikalisches Institut
Georg-August-Universität Göttingen

Prof. Dr. Matthias Krüger
Institut für Theoretische Physik
Georg-August-Universität Göttingen

Tag der mündlichen Prüfung: 25.11.2022

List of publications

Parts of this thesis were published in peer-reviewed journals:

- M. ten Brink, S. Gräber, M. Hopjan, D. Jansen, J. Stolpp, F. Heidrich-Meisner, and P. E. Blöchl. "Real-time non-adiabatic dynamics in the one-dimensional Holstein model: Trajectory-based vs exact methods", *J. Chem. Phys.* **156**, 234109 (2022)
  doi: 10.1063/5.0092063

- B. Kressdorf, T. Meyer, M. ten Brink, C. Seick, S. Melles, N. Ottinger, T. Titze, H. Meer, A. Weisser, J. Hoffmann, S. Mathias, H. Ulrichs, D. Steil, M. Seibt, P. E. Blöchl, and C. Jooss. "Orbital-order phase transition in $Pr_{1-x}Ca_xMnO_3$ probed by photovoltaics", *Phys. Rev. B* **103**, 235122 (2021)
  doi: 10.1103/PhysRevB.103.235122

Additionally, the author contributed to another publication while working on the thesis:

- B. Kressdorf, T. Meyer, A. Belenchuk, O. Shapoval, M. ten Brink, S. Melles, U. Ross, J. Hoffmann, V. Moshnyaga, M. Seibt, P. Blöchl, and C. Jooss. "Room-Temperature Hot-Polaron Photovoltaics in the Charge-Ordered State of a Layered Perovskite Oxide Heterojunction", *Phys. Rev. Applied* **14**, 054006 (2020)
  doi: 10.1103/PhysRevApplied.14.054006

Contents

1 Introduction

Few innovations have changed our everyday life as much as the introduction of semiconductor technology in the last century. As the most prominent example, the silicon transistor led to the birth of modern electronics and is an integral part of most modern computers and general electronic devices, see Ref. [1]. In addition, semiconductor solar cells, in most cases composed of doped silicon or gallium arsenide, provide nowadays a reliable source of renewable energy and an alternative to burning fossil fuels for meeting the growing energy consumption in our society, see Ref. [2]. Lastly, the direct conversion of electric energy into light emission in certain semiconductors gave rise to the development of light-emitting diodes, which have replaced traditional incandescent or fluorescent sources of illumination in many applications, see Ref. [3].

With their production efficiency rising and costs sinking over time, see, e.g., Ref. [4], the continued use of simple semiconductors such as silicon in the upcoming decades seems very likely. Nonetheless, there is an ongoing scientific search for new materials that could potentially overcome some of the remaining problems of our current silicon-based technology.

One such problem is the Shockley-Queisser efficiency limit of conventional single-junction solar cells, see Ref. [5], which estimates how much of the incoming solar radiation energy can be converted into electrical energy. Its largest limiting contributions are spectral losses: Solar radiation with an energy below the semiconductor's band gap will not be absorbed (a transmission loss), while high energy solar radiation excites electrons far into the conduction band. These "hot" charge carriers loose their energy by fast scattering processes with the nuclear lattice until they reach the bottom of the conduction band. This excess energy thus heats up the material without contributing to the output voltage (thermalization loss). The theoretical efficiency limit from the spectral losses alone is reduced to about 44 % for the band gap of silicon and reduces upon considering further losses in a detailed-balance model to about 30 % for silicon, see Ref. [5].

Increasing solar cell efficiency has been subject to many decades of research, see, e.g., Refs. [6, 7]. One possibility are multi-junction solar cells, which combine several semiconductors of varying band gaps to reduce the spectral losses. An exciting alternative are hot carrier solar cells, see the overview in Ref. [8]. They try to reduce the thermalization losses by extracting the excited state charge-carrier energy before they relax to the bottom of the band gap and loose their excess energy to heat. Such a mechanism was recently proposed for the material class of manganites, in particular $Pr_{1-x}Ca_xMnO_3$ (PCMO), see Refs. [9–11], which forms the basis for many investigations in this thesis.

Manganites show a very strong coupling between the manganese valence electrons and the surrounding lattice distortion modes, also denoted as phonons. The local distortion modes adjust to the electrons and reduce their energy,

leading to a trapping effect. This was first described for polar materials, in which a charged electron causes lattice distortions that follow the electronic movement and change its effective mass, which led to the name polaron for such an electronic quasi-particle, see Refs. [12, 13]. We also refer to Ref. [14] for a recent review of different types of polarons. In manganites, local polarons form various types of complex cooperative ordered structures, depending on the electron-doping of the material, see Refs. [15, 16]. When used as a solar cell, the strong cooperative electron-phonon coupling in the material is assumed to stabilize the excited electrons in a hot polaron state, with measurements predicting a large enough lifetime to allow energy extraction, see Refs. [9, 10]. The hot polaron is formed by fast adjustment of the nuclear lattice to the photo-excited electron, leading to a metastable electron-nuclear configuration. Radiative recombination from such a metastable state might be dipole forbidden and radiationless decay through an energy crossing prevented by the presence of the surrounding cooperative distortions, possibly leading to the long lifetimes, see Ref. [9]. These measurements indicate that a photovoltaic effect sets in only below the long-range ordering temperatures of the polaronic distortions, which was confirmed in the layered Ruddlesden-Popper variant $Pr_{0.5}Ca_{1.5}MnO_4$ in Ref. [11].

Also besides the possibilities of long-living hot charge carriers, many interesting properties arise from the strong coupling of the electronic and lattice degrees of freedom in manganites. For example, for certain dopings in PCMO, a colossal magnetoresistance effect appears, in which the resistivity of the material drops by several orders of magnitude upon applying a magnetic field, see Refs. [17, 18]. The same effect can also be induced by photoexcitation, see Refs. [19–21], external or chemical pressure, see Ref. [22], or electron irradiation, see Ref. [23].

Understanding the role of the strong electron-phonon interactions present in manganites might thus give access to new and yet unexplored physics. Motivated by the measurements of a photovoltaic effect in PCMO, one goal of this thesis is to get a theoretical estimate of the melting temperature of electronic orbital order (concomitant with polaronic order) at certain dopings in the material, and compare the results, for example, to the onset temperatures of the measured photovoltaic effect, see Ref. [24]. For this, we start in chapter 2 with the description of the various interacting degrees of freedom in PCMO and the current understanding of the complicated phase diagram of the material. In chapter 3, we present a theoretical tight-binding model of the material that has been shown to capture many of the relevant ordering principles in manganites, see Refs. [25–27], and whose parameters have been carefully adjusted to first-principles calculations in Ref. [28]. In chapter 4, this model is applied to clarify the ground-state ordered structures at low doping in PCMO. We then perform finite-temperature simulations that heat up the model system and investigate the effect on the cooperative polaronic distortions. This is done by using a molecular dynamics approach for the classical nuclei and an (almost) adiabatic approximation for the fast electronic degrees of freedom. The adiabatic approximation forces the electrons to stay in their instantaneous ground state while following the nuclear motion. As outlined in the published

article, Ref. [24], the resulting melting temperature of the order shows a good agreement with new experimental measurements. Together, they suggest a reevaluation of the low-doped finite-temperature region of the phase diagram. These results are interpreted as a correlation between the onset of a photovoltaic effect and the spontaneous orbital-order transition temperature, supporting the conjecture from previous measurements in Refs. [9–11].

These findings encourage a direct simulation of a photoexcitation in both the long-range ordered and disordered phases to better understand the influence of this order on the relaxation processes. Such simulations, however, cannot be done using the adiabatic approximation for the electrons. Two widely used algorithms to extend quantum-classical electron-phonon dynamics to non-adiabatic regimes are the Ehrenfest dynamics and the fewest-switches surface hopping (FSSH) methods, see Refs. [29–31]. In the former, the nuclei evolve under a potential given by the trace of the mixed quantum-classical Hamiltonian over the electronic subsystem, which one might consider as a mean-field ansatz in the electron-phonon coupling. In the latter, the nuclear potential is determined at any instance of time from a single instantaneous electronic eigenstate, with the possibility of stochastic hops between these eigenstates. Previous studies combining photoexcitation and -relaxation in the manganite tight-binding model with Ehrenfest dynamics yielded promising results, see Refs. [32, 33].

In this thesis, we opt for a more fundamental investigation of both quantum-classical methods and their ability to accurately reproduce electron-phonon coupled dynamics. For this, we review in detail the concepts of adiabatic electronic states and energy surfaces in the Born-Huang framework, see Ref. [34], and describe the relevance of non-adiabatic effects in the description of coupled electron-phonon dynamics in chapter 5. The general theory is build on a complete quantum mechanical treatment of the whole system, but we analyze as well how to retain a non-adiabatic description while approximating the nuclei as classical particles. Both Ehrenfest dynamics and FSSH are introduced in that chapter, together with a variant of exact diagonalization (ED) in the Born-Huang basis in a small model system. We will use the Holstein model, see Ref. [35], as example system during our assessment of the non-adiabatic effects. This is a prototypical model for studying electron-phonon coupling, as it includes (in its simplest form) only non-interacting electrons, uncoupled nuclear harmonic oscillators, and a bi-linear local electron-phonon coupling. Despite its simplicity, it has been successfully used to analyze absorption spectra in PCMO, see Ref. [36].

Important for the application of Ehrenfest dynamics or FSSH to the tight-binding model is a correct description of the general transport behavior of excited electrons and the energy transfer between the electronic and nuclear subsystems. Unbiased benchmark studies comparing these methods to numerically exact and fully quantum mechanical results in extended condensed matter systems are scarce, see Ref. [37], mostly due to the lack of exact comparison data. One recent advancement of a reciprocal space formulation of FSSH has been compared to Ehrenfest dynamics and a numerically exact hierarchical equations of motion (HEOM) method (see Ref. [38]) in Holstein and Peierls model systems with up to 10 sites in Ref. [39]. A coupled extension

of Ehrenfest dynamics, the multiconfigurational Ehrenfest (MCE) method, see Refs. [40, 41], has been benchmarked against the HEOM method and a second coupled trajectory method (the multiple Davydov D2 ansatz, see Ref. [42]) in a similar model with up to 16 sites, see Ref. [43]. In addition, a benchmark study between Ehrenfest dynamics, FSSH and MCE was carried out in large chromophores in Ref. [44]. In the field of cavity quantum electrodynamics, both Ehrenfest dynamics and FSSH have been compared to numerically exact methods in Ref. [45]. All these investigations were carried out in the last few years and older benchmark studies are in most cases limited to small few-state problems, see, e.g., Refs. [46, 47]. Of these above benchmark studies only the reciprocal space FSSH study in Ref. [39], provides a comparison of both quantum-classical methods in a condensed-matter like system that has some similarity with the manganite model. The study finds that the agreement with the exact data is better in FSSH than in Ehrenfest dynamics in the single studied observable of the transient electronic populations of the lowest reciprocal-space state.

Further investigations are definitely needed to assess the performance of the quantum-classical methods in view of their potential application to the manganite tight-binding model. We presented such an extended benchmark study, carried out in a collaborative project, in Ref. [37]. The single-electron results of that study, together with a few additional results, are presented and discussed in detail in chapter 6. This study includes Ehrenfest dynamics, FSSH, MCE and the numerically exact methods exact diagonalization and density matrix renormalization group (DMRG) with local basis optimization (LBO) (see Refs. [48–53]) in the extended one-dimensional Holstein model with up to 51 sites. We start with small systems that can still be analyzed easily in the Born-Huang framework and use the same formalism to evaluate the methods' performance in the larger systems. Various single-electron initial states are analyzed. These include a "bare local" electron state, corresponding to a local charge carrier injected into an empty Holstein chain, which was also denoted as "Franck-Condon" initial state in another tensor network state method study, see Ref. [54], and a "dressed local" initial state, in which the nuclei are already adjusted locally to the inserted electron. One might describe the following non-equilibrium dynamics as the development or stabilization of a trapped polaron, and we discuss which of the studied methods can reproduce the qualitative behavior predicted by the exact reference methods. For smaller systems, initial states restricted to adiabatic eigenstates are studied as well.

While we do not apply the quantum-classical methods to the manganite tight-binding model in this thesis, we believe that the evaluation of the methods' performance (and of the various tested improvements of the FSSH method) provides a starting point for such future non-adiabatic simulations. In particular, the FSSH method seems to be a promising candidate to study the correlation of the photovoltaic effect and the orbital-order phase transition in PCMO.

The thesis concludes with a summary and an outlook in chapter 7.

2 Manganites

2.1 Perovskite structure

Owing to the early work published by Jonker and van Santen, see Ref. [55], the material class of "manganites" is somewhat different from the usual chemical notation associated with all manganese oxides crystallizing in a perovskite structure. This structure, which has its name from the original perovskite material of calcium titanite, is depicted in its undistorted form in Fig. 2.1. For oxides, such as manganites, it has the chemical formula ABO_3.

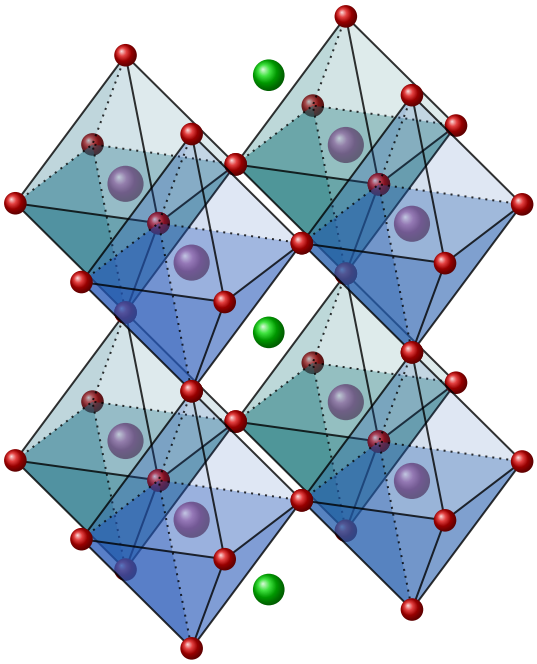

Figure 2.1: Sketch of the (undistorted) perovskite structure for ABO_3 with cubic symmetry. The (purple) B-type cations are at the center of six (red) oxygen atoms forming the corners of an octahedron. Neighboring octahedra are corner-, i.e., oxygen-sharing. Between the octahedra lie (green) A-type cations. For manganites, the B-type cations are manganese atoms, while the A-type cations are, in most cases, trivalent rare earth or divalent alkaline earth metals. Figure reproduced from Ref. [56].

The B-type cations, which in the following are always manganese ions, are positioned at the centers of the oxygen octahedra. We will see that most of the relevant physical interactions take place on these manganese sites. With the oxygen atoms being formally in the state O^{2-}, the valence on the manganese atoms is determined by the A-type cations. There are three to four d-electrons on the manganese sites, depending on the amount of divalent

($A^{2+}Mn^{4+}O_3^{2-}$) and trivalent ($A^{3+}Mn^{3+}O_3^{2-}$) A-type cations. In this thesis, we will only consider the specific material class of praseodymium-calcium manganite $Pr_{1-x}Ca_xMnO_3$, or as shorthand PCMO, with the divalent calcium and trivalent praseodymium A-type cations. The parameter x is the hole-doping on the manganese sites, allowing for any mixture between pure $PrMnO_3$ ($x = 0$) and pure $CaMnO_3$ ($x = 1$). The partially filled d-shell of the manganese sites leads to the formation of various complicated ordered structures in the entire doping range of $0 \leq x \leq 1$, see Sec. 2.4.

The actual atomic structure of PCMO deviates from the ideal cubic one presented in Fig. 2.1 and has the orthorhombic Pbnm-space group, see Refs. [57, 58]. This is both due to stretching modes of the manganese-oxygen bond distances (investigated in more detail in Sec. 2.2.2) and due to a buckled tilting of the oxygen octahedra. The tilting is influenced by the effective radii of the A-type cations, which are too small to completely fill the space between the octahedra, as can be quantified by a Goldschmidt tolerance factor $t = d_{A-O}/(\sqrt{2}d_{Mn-O})$ that is smaller than one, see Refs. [59, 60]. Here, d_{A-O} and d_{Mn-O} are the bond distances between oxygen and the A-type cation, and oxygen and manganese, respectively. With the radii of praseodymium and calcium being slightly different, the tilting angle of the octahedra varies in the doping range from a stronger buckling for $PrMnO_3$ to a nearly cubic symmetry for $CaMnO_3$, see Ref. [57]. The tilt-pattern is known as a $GdFeO_3$-type distortion, and is also observed in the similar, and more commonly studied, material of $LaMnO_3$, see Refs. [61–63]. The unit cell of the Pbnm-space group consists of four octahedra, with its lattice vectors being, in a pseudo-cubic approximation, close to $\mathbf{a} \approx (\mathbf{x} - \mathbf{y})$, $\mathbf{b} \approx (\mathbf{x} + \mathbf{y})$ and $\mathbf{c} \approx 2\mathbf{z}$. Here, $\mathbf{x}$, $\mathbf{y}$ and $\mathbf{z}$ are the vectors connecting manganese atoms in neighboring octahedra, see also Refs. [63, 64] for a graphical depiction of the Pbnm unit cell, and Fig. 2.6 for a sketch of the Pbnm lattice vectors in the cubic lattice. For low hole-dopings (with strong buckling and significant influence of the Mn-O stretching "Jahn-Teller" modes (see Sec. 2.2.2)), the lengths of the lattice vectors split according to $b > a > c/\sqrt{2}$ at low temperatures, see Ref. [57]. The system becomes more orthorhombic and the manganese-oxygen-manganese bond angles deviate from the ideal cubic 180° angle, see Ref. [60]. We will now investigate the physics of a single octahedron, composed of the central manganese atom and the surrounding six oxygen atoms, in more detail.

2.2 Single octahedron interactions

2.2.1 Crystal field splitting and electronic configuration

The central building block of manganites are the octahedra shown in the sketch in Fig. 2.1. With the manganese atom being formally in the 4+ or 3+ valence state, there are between three and four d-electrons on every manganese atom. While the d-levels are degenerate for an isolated atom, this is not the case in the presence of the surrounding atomic structure. For an undistorted octahedral structural environment (cubic symmetry), the five real d-orbitals

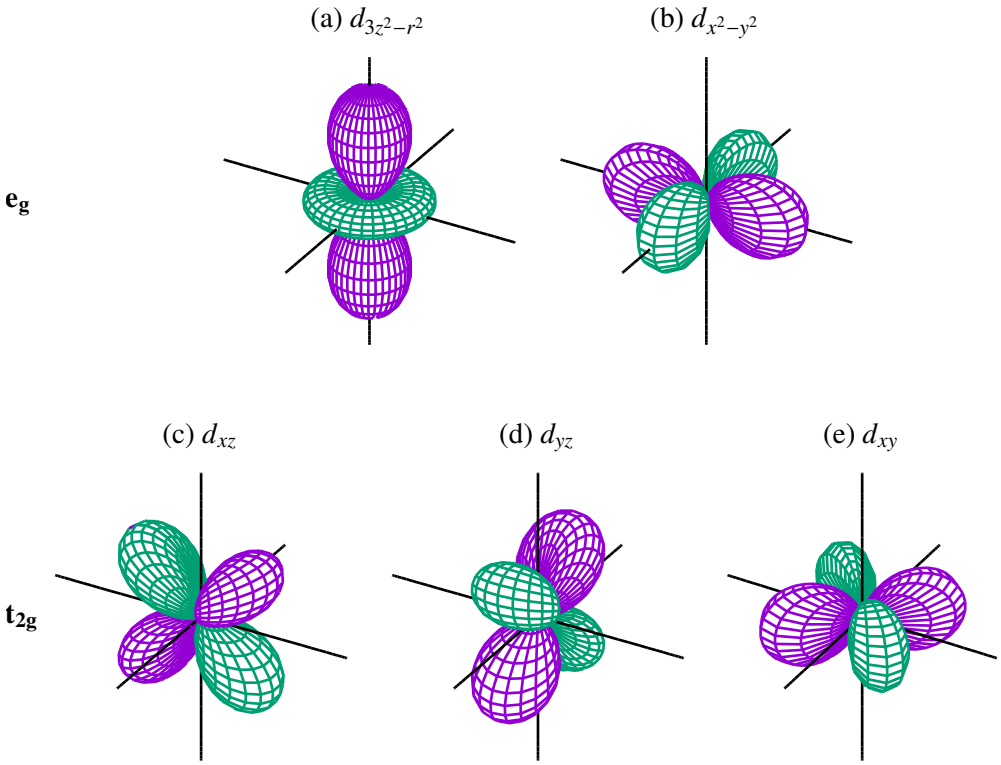

Figure 2.2: The five real d-orbitals on the manganese atom, separated into the two symmetry groups of e_g (a), (b) and t_{2g} (c)-(e), with the octahedral crystal field indicated by black lines pointing toward the neighboring oxygen atoms.

are split into two symmetry-groups. The e_g orbitals, composed of the $d_{3z^2-r^2}$ and the $d_{x^2-y^2}$ state, which both have lobes pointing toward the oxygen neighbors, see Figs. 2.2(a),(b), and the t_{2g} orbitals, composed of the d_{xz}, d_{yz} and d_{xy} states, which have their lobes pointing in between the Mn-O bonds, see Figs. 2.2(c)-(e). We note that the orbitals have no preferred direction in the cubic case, and linear combinations of the e_g orbitals lead to rotated versions of these two, e.g., $|3x^2 - r^2\rangle = -\cos(60°)\,|3z^2 - r^2\rangle + \sin(60°)\,|x^2 - y^2\rangle$, restoring the cubic symmetry.

Using standard ligand field theory, one can determine the energetic separation of the two groups of orbitals due to the surrounding crystal field from their electro-static interaction with the oxygen-p (O-p) orbitals, see, e.g., Ref. [65]. Estimates of the resulting expression suggest that the e_g energy levels are in the order of a few meV higher than the t_{2g} levels, which is much smaller than the measured energy splitting, see Ref. [27]. Instead, the majority of the splitting is caused by a hybridization of the manganese-d (Mn-d) with the O-p orbitals, see Ref. [28]. The e_g states form σ-bonds with the O-p states, resulting in bonding and antibonding contributions. The bonding states are mostly of oxygen character and always filled; they are typically attributed solely to the oxygen atoms and referred to as O-p. In contrast, the antibonding

states, which still have significant O-p contribution (see the densities of states in Ref. [28]), are attributed to the manganese atoms and formally denoted as the new Mn-e_g states. The antibond significantly raises their energy (in the order of eV) compared to the t_{2g} levels. While this is different from the crystal field normally considered in ligand field theory, we still refer to this energy splitting as crystal field splitting. The t_{2g} states can form π-bonds with the O-p states, which are, however, much weaker compared to the σ-bonds of the e_g states. The different energy levels can split further if the local symmetry is reduced, e.g., to a tetragonal case ($z < x = y$), but the orbitals will in the following still be referred to, in a pseudo-cubic fashion, as e_g and t_{2g} orbitals. In particular, the Jahn-Teller effect (see Sec. 2.2.2) leads to a considerable distortion of the cubic symmetry and a large separation of the two e_g energy levels.

For Mn^{4+}, as present in $CaMnO_3$, the three t_{2g} orbitals, Figs. 2.2(c)-(e) are occupied. They are all spin-aligned due to Hund's rule, and have a total spin of $S = \frac{3}{2}\hbar$. Since they are always occupied, any further minor splitting of these orbitals due to distortions of the ideal oxygen octahedron is not relevant for understanding ground state properties. A sketch of the density of states of the Mn-d states of $CaMnO_3$ is shown in Fig. 2.3(a), which indicates the Hund's splitting of the majority and minority spin directions, and the crystal field splitting between t_{2g} and e_g states.

The picture changes once we move to Mn^{3+}, as present in $PrMnO_3$. The additional fourth Mn-d electron occupies one of the e_g electrons in the same spin direction as the t_{2g} electrons (for an isolated octahedron), which means that the Coulomb interaction outweighs the crystal field splitting, leading to a high-spin configuration, see Refs. [25–27]. The degenerate but only partially occupied e_g states of the majority spin direction are highly susceptible to further lattice distortions that could lift this degeneracy. The main source of such distortions is the Jahn-Teller effect, outlined in the next section, which leads to a distortion of the oxygen octahedron in line with the occupied e_g orbital and thus breaks the cubic symmetry. One such example is shown in the schematic density of states of $PrMnO_3$ in Fig. 2.3(b).

2.2.2 The Jahn-Teller effect

Jahn and Teller investigated in their fundamental work, see Ref. [66], the stability of partially occupied, symmetry-induced orbital-degenerate electronic states in molecules, just like the high-spin configuration in a single octahedral Mn^{3+} manganite. Based on group symmetry arguments, they showed that the symmetric nuclear configuration leading to the orbital degeneracy will not be stable for a non-linear molecule, in that a nuclear distortion exists which lifts the degeneracy linearly around the degeneracy seam. For our manganite system, the nuclear distortions lifting the e_g orbital degeneracy can already be estimated from the shape of the orbitals shown in Figs. 2.2(a) and 2.2(b). We mentioned that the energy increment of these states in the crystal field splitting is caused by their antibond with the O-p states. If the Mn-O bond distance is now increased in the direction of their orbital lobes, then this antibond will be weakened, thus reducing their energy. While the $d_{3z^2-r^2}$ orbital is mainly

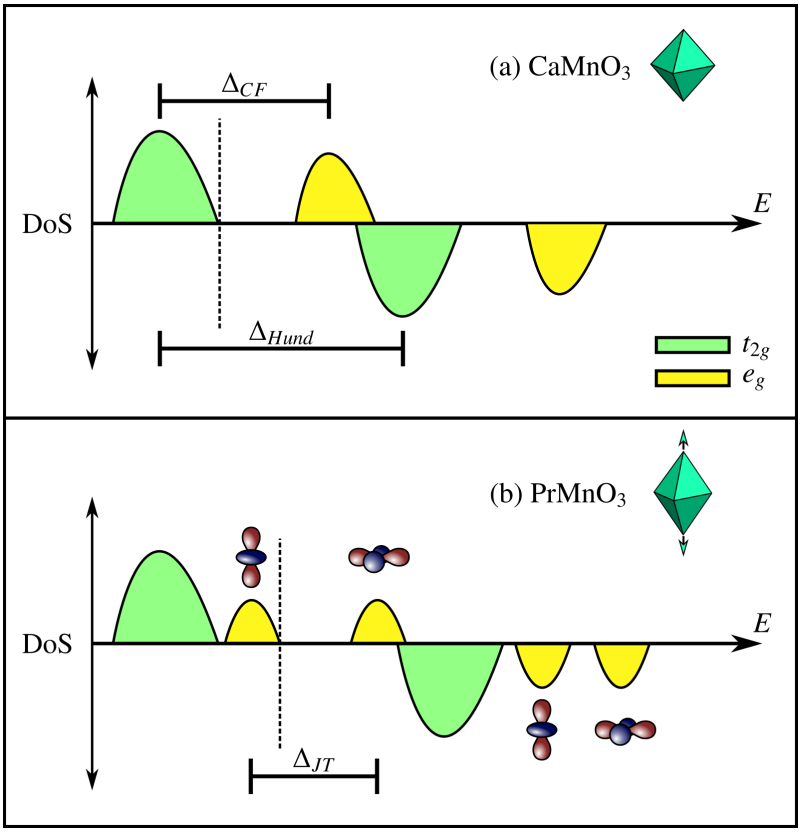

Figure 2.3: Schematic illustration of the densities of states (DoS) for the Mn-d states of (a) $CaMnO_3$ and (b) $PrMnO_3$, with the majority and minority spin direction shown with positive and negative values, respectively. The Fermi-energy is indicated with a dashed vertical line. In $CaMnO_3$, the crystal field splitting Δ_{CF} between t_{2g} and e_g states, and the Hund's splitting Δ_{Hund} between majority and minority spin directions are included. For $PrMnO_3$, an example of a Jahn-Teller distortion of the oxygen octahedron with the Jahn-Teller splitting Δ_{JT} of the corresponding e_g states is shown (the occupied and unoccupied orbitals are further separated due to their Coulomb interaction, which has to be considered for estimating these splitting energies). For a realistic density of states of the materials obtained from a hybrid density-functional calculation we refer to Ref. [28].

oriented in the z-direction, the $d_{x^2-y^2}$ orbital is mainly oriented in the x-y-plane. The distortion mode splitting these two orbitals linearly (in first order) is the so-called Q_3 mode, see Refs. [67, 68], which is one of the *Jahn-Teller* modes in an octahedral environment. It is defined as

$$Q_3 = \frac{1}{\sqrt{6}} \left(2\Delta_z - \Delta_x - \Delta_y\right), \tag{2.1}$$

where Δ_i are the deviations of the O-Mn-O bond distances from their equilibrium value in the direction i (in cubic notation). For positive Q_3, the oxygen octahedron is elongated in the z-direction and compressed in the x-y-plane, which reduces the energy of the $d_{3z^2-r^2}$ orbital, while the $d_{x^2-y^2}$ orbital increases in energy by the same amount (in first order). For negative Q_3, this

energy splitting happens in the opposite direction. The case of positive Q_3 was also indicated in the schematic density of states of $PrMnO_3$, see Fig. 2.3(b).

As mentioned previously, the two e_g orbitals form a two-dimensional manifold of electronic states and linear combinations of the two orbitals lead to rotated versions of them in other cubic directions. The distortion modes lifting the orbital degeneracy build a similar two-dimensional space, with a second Jahn-Teller mode Q_2 being responsible for splitting the degeneracy of the linear combinations $\frac{1}{\sqrt{2}}(|3z^2 - r^2\rangle \pm |x^2 - y^2\rangle)$ (see Refs. [67, 68]):

$$Q_2 = \frac{1}{\sqrt{2}} \left(\Delta_x - \Delta_y\right) . \tag{2.2}$$

One can form continuous distortions combining both modes: $Q(\theta) = \cos(\theta)Q_3 + \sin(\theta)Q_2$. For example, $Q(\frac{2\pi}{3})$ corresponds to a Q_3 mode rotated onto the x-axis. A detailed energy expression for this electron-phonon coupling is given when introducing the tight-binding model, see Sec. 3.2.3, but we will already discuss the qualitative nature of the electron-phonon coupling here.

If one starts at $\theta = 0$ in the (classical) Q_3-distorted octahedron (with $|Q| > 0$), the $d_{3z^2-r^2}$ orbital will have the lowest energy and is occupied for an isolated octahedron. By continuously increasing the Jahn-Teller angle θ from 0 to 2π (always with $|Q| > 0$), the *adiabatic* lowest energy e_g orbital will change as well according to the formula $|\theta/2\rangle = \cos(\theta/2)\,|d_{3z^2-r^2}\rangle - \sin(\theta/2)\,|d_{x^2-y^2}\rangle$ (note the half angle in this expression). Adiabatic electronic states will be introduced rigorously in Ch. 5, and we note here only that they refer to electronic eigenstates obtained for fixed nuclear positions. These lowest-energy orbitals are drawn in Fig. 2.4 in steps of 30° of the Jahn-Teller angle θ. The corresponding Jahn-Teller distortion is indicated with red arrows for the positive and negative pure Q_2 and Q_3 modes.

For these Mn^{3+} sites, the occupied electronic orbital is always concomitant with the Jahn-Teller distortion at not too high temperatures. This stabilized electron-nuclear local configuration is also denoted as a Jahn-Teller polaron, see, e.g., Ref. [14]. Some authors differentiate between a static and dynamic Jahn-Teller effect, see, e.g., Ref. [69]. In the dynamic Jahn-Teller effect, the Jahn-Teller angle θ can adjust freely, but always together with the electronic orbital mixing angle $|\theta/2\rangle$, so that the e_g electron stays in the instantaneous lowest-energy orbital. In a static Jahn-Teller effect, the Jahn-Teller angle θ (and mixing angle $|\theta/2\rangle$) is fixed by a long-range ordering of the lattice distortions and electronic orbitals. This can also be seen as a cooperative Jahn-Teller distortion, see Sec. 2.3 for more details on inter-octahedral interactions. Depending on whether the local distortions are part of a long-range or short-range order, one might refer to the arrangement as a polaron crystal or polaron liquid, respectively.

After completing one loop from $\theta = 0$ to $\theta = 2\pi$, the Jahn-Teller distortion returns to a pure Q_3 mode. This is not the case for the occupied e_g orbital, which changes sign during this loop, as is evident from Fig. 2.4 and indicated there with a dotted line, and from the expression given above, which contained only half the Jahn-Teller angle $\theta/2$ as the mixing angle.

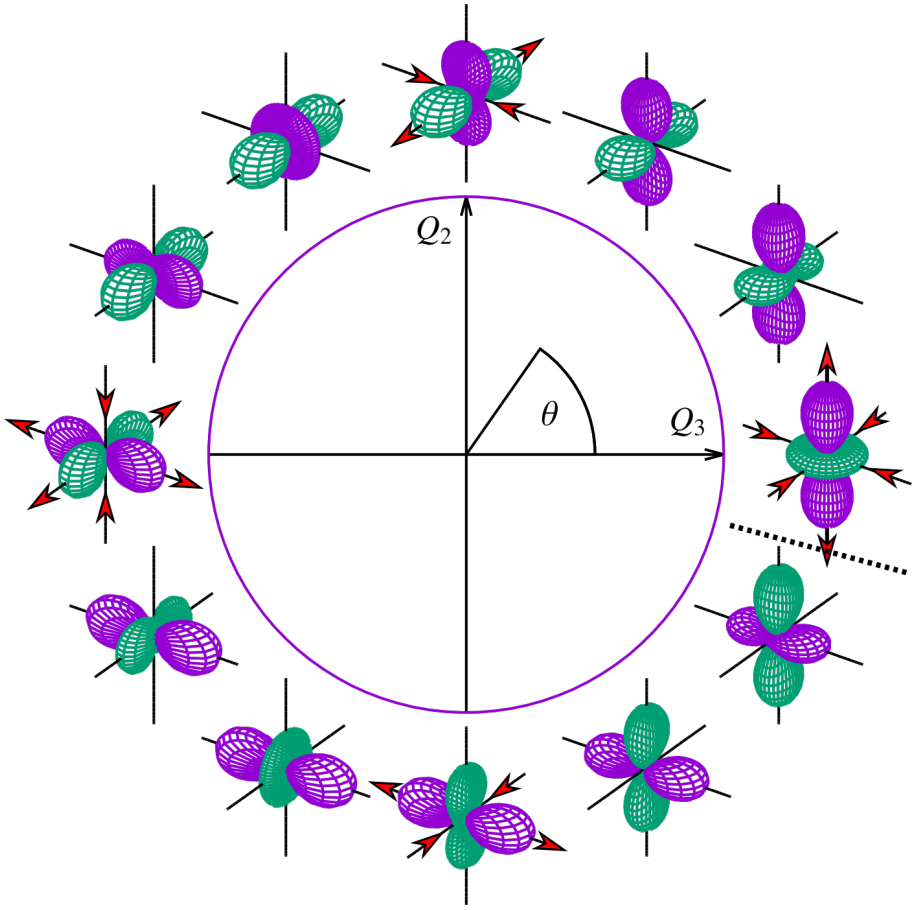

Figure 2.4: The e_g orbitals with the lowest energy in an isolated octahedron with a Jahn-Teller distortion of $Q(\theta) = \cos(\theta)Q_3 + \sin(\theta)Q_2 \neq 0$ are shown in steps of 30° in the Jahn-Teller angle θ. The Jahn-Teller distortions of the oxygen octahedron for a pure Q_3 or Q_2 mode (in both positive and negative directions) are shown with red arrows.

The excited electronic state (the e_g orbital with the highest energy for a certain nuclear configuration), is the state $|(\theta + \pi)/2\rangle$, which is always the orbital drawn on the opposite site of the circle in Fig. 2.4. Except for the symmetric (cubic) nuclear configuration at $Q = 0$, the energies of these two orbitals will always be split. For more details, we refer to the energy expression introduced in Sec. 3.2.3. The sign-change of the electronic wave function upon completing an (adiabatically slow) loop around the symmetric configuration is one realization of the geometric phase effect, also called Berry phase, see Refs. [70–74]. In the following, we refer to Mn-sites in which the lower adiabatic e_g orbital has a larger occupation than the higher adiabatic orbital as "orbital-polarized". At low temperatures any site with a significant Jahn-Teller distortion is typically orbital-polarized.

Other nuclear modes that remove the 90°-angles between the different Mn-O bonds, or simply shift the whole surrounding oxygen lattice, will not be considered here, although they exist, see Ref. [67]. However, one additional relevant phonon mode remains: the breathing mode, Q_1, see Refs. [67, 68], which is an

isotropic expansion of the oxygen octahedron:

$$Q_1 = \frac{1}{\sqrt{3}} \left(\Delta_x + \Delta_y + \Delta_z \right) . \tag{2.3}$$

With the e_g state being an antibond, a larger breathing distortion will reduce the energy of the occupied state, but it is independent of the orbital mixing angle.

2.3 Inter-octahedral interactions

The ground-state configuration of an isolated octahedron seems to be relatively straightforward: For Mn^{4+}, the spins of the t_{2g} electrons are aligned and there is no Jahn-Teller distortion. For Mn^{3+}, the e_g electron is spin-aligned with the t_{2g} electrons and its orbital mixing angle is coupled to the Jahn-Teller angle θ of the nuclear modes Q_2 and Q_3, see also the densities of states in Fig. 2.3. The situation becomes much more complicated once we turn to a full perovskite configuration with many corner-sharing octahedra, see Fig. 2.1, as the different degrees of freedom have competing tendencies for their ordering.

Let us start with the magnetic interactions. The electronic configuration of the manganese atoms leads to the development of a magnetic moment (from the three t_{2g} electrons and potentially the one e_g electron). Since the manganese atoms are separated by oxygen atoms in the perovskite structure, a direct magnetic exchange interaction between the manganese sites is suppressed and instead indirect interactions via the oxygen atom dominate the magnetic ordering.

The first description of a magnetic interaction of two cations through a non-magnetic anion was given with the superexchange mechanism, see Ref. [75] in which the general formulation of a previous work, Ref. [76], was evaluated for practical purposes. In this original formulation, the superexchange effect is derived with perturbation theory of an ionic bond picture, in which one of the O-p electrons (along the bond direction) is virtually excited to one of the neighboring manganese sites and subject to an onsite interaction, while the second O-p electron has a direct exchange interaction with the other neighboring manganese site. In the case of two Mn^{4+} ions connected by an oxygen bridge (as in $CaMnO_3$), there is no large overlap between the occupied Mn-t_{2g} and the O-p orbitals, which allows a ferromagnetic (FM) interaction for both the onsite coupling of the first electron, and the direct exchange of the second electron. Since the two O-p electrons have opposite spin, this leads in total to an antiferromagnetic (AFM) interaction between the t_{2g} spins of the neighboring Mn^{4+} sites.

A similar result was obtained with various theoretical explanations, all leading to this same antiferromagnetic Mn^{4+}-Mn^{4+} interaction, see Ref. [77]. These include the successful theory of semicovalent exchange of Goodenough and Loeb, see Refs. [16, 78], in which each of the two relevant O-p electrons form a partial (one-electron) bond with empty manganese orbitals on the two opposite sites of the oxygen atom. With each of these bonding electron states being ferromagnetically coupled to the t_{2g} electrons, one once again arrives at the

AFM interaction. As mentioned above, what we refer to as O-p orbitals are in fact the bonding states of the hybridized O-p and Mn-d orbitals, and the semicovalent exchange extends this approach by recognizing that the two different spin directions of the relevant O-p orbital will form directional bonds with the Mn-neighbor that is spin-aligned with them. The sign of the superexchange interaction can change if the Mn-O-Mn bond deviates strongly from 180°, as demonstrated in Ref. [77], and can become ferromagnetic for a 90° bond. The superexchange is thus influenced by the tilting distortion mentioned previously, see Sec. 2.1.

In $PrMnO_3$, at least along one axis on each Mn^{3+} ion, some of the relevant manganese orbitals will already be occupied (e.g., the $d_{3x^2-r^2}$ orbital for the x-direction). Due to the strong overlap of this orbital with the O-p state, an AFM interaction between the two is preferred by the Pauli principle, see, e.g., Ref. [79], and instead of semicovalent, this bond was denoted as ionic in Ref. [16]. In a situation where the oxygen atom can form one semicovalent (FM) bond in one direction, and an ionic (AFM) bond in the other direction, the total Mn-Mn interaction becomes ferromagnetic (the two O-p electrons still have opposite signs). With this idea Goodenough could reproduce the spin-ordering in the material $LaMnO_3$ (which is a manganite in the similar Mn^{3+} configuration as $PrMnO_3$), see Ref. [16]. $LaMnO_3$ shows an antiferromagnetic ordering along one axis, where two semicovalent bonds could be formed, and a ferromagnetic ordering in the perpendicular plane, where a staggered orbital configuration of the e_g orbitals leads to alternating mixed semicovalent-ionic Mn-O-Mn bonds of a ferromagnetic type. The same orbital and spin order is also present in $PrMnO_3$ and shown in Fig. 2.6. This type of ferromagnetic superexchange comes along with an asymmetry of the Mn-O-Mn bond in that the oxygen atom moves closer to the direction of the semicovalent bond. We can already understand this mechanism from the Jahn-Teller distortion induced by the occupied e_g orbitals and in fact the experimental anisotropic magnetic ordering can also be understood from these polaronic interactions without referring to the concepts of semicovalent exchange, see Ref. [25].

The e_g electrons of Mn^{3+} sites can in principle hop to neighboring manganese sites, as they have a large overlap with the bridging oxygen atoms. This is suppressed in the previously discussed Mn^{3+}-Mn^{3+} bonds, due to Coulomb interactions between the e_g electrons, and additionally Jahn-Teller (if a different orbital is occupied) or Hund's interaction (if a different spin direction is occupied). The situation changes in mixed valence compounds with Mn^{3+}-Mn^{4+} bonds. Here, the e_g electron can delocalize between the sites and favors both a ferromagnetic spin alignment, as well as a similar Jahn-Teller distortion to minimize the respective interaction energies. This is known as the double-exchange mechanism, see Ref. [80]. The spin- and Jahn-Teller-aligned configurations on two neighboring sites reduce the energy of the e_g electron delocalized between both sites, and the combined structure is also referred to as Zener-polaron, see Refs. [14, 80]. In contrast to the ferromagnetic superexchange, the double-exchange leads to a strong conductance and can result in metallic ground-state phases in manganites, but by itself it cannot explain the complex phase diagram of many manganites, see Refs. [25, 27]. The e_g electron hopping underlying

the double exchange is influenced by Jahn-Teller and tilting deformations of the lattice, see Refs. [63, 78], as well as the relative spin orientation of the t_{2g} electrons on neighboring sites, see Ref. [81].

Besides the t_{2g} and e_g interactions, we also have to consider the cooperative Jahn-Teller distortions themselves. Since the octahedra share the oxygen-atom corners, it seems intuitive that if one octahedron expands, e.g., in the z-direction, that the $\pm z$-neighbors compress in the same direction, thus making similar Jahn-Teller modes in neighboring octahedra unlikely and leading to an alternating Jahn-Teller distortion pattern as already induced by the ferromagnetic superexchange mechanism. Kanamori introduced in Ref. [68] the notion of an orbital spin $(\cos(\theta), \sin(\theta))$, a pseudo spin, describing the Jahn-Teller distortion in the Q_3-Q_2 plane (see Fig. 2.4). The alternating Jahn-Teller distortions then correspond to an antiferro-Jahn-Teller ordering (which will be accompanied by an antiferro-orbital (AFO) ordering, referring to the e_g electrons whose mixing angle adjusts according to the Jahn-Teller angle).

In the real material, the AFO ordering is not necessarily enforced by the cooperative distortions, as there are two alternatives: First, the bonds are not straight but tilted, as discussed in Sec. 2.1, with a Mn-O-Mn bond angle smaller than 180°. Upon the expansion in z-direction this tilting bond angle could reduce further to allow two neighboring octahedra to have the same Jahn-Teller mode. We mention, however, that these modes are not perfectly aligned in the real tilted material, as the local coordinate system for the phonon modes build from the position of the six oxygen neighbors will be different for different sites. Second, the Mn-Mn distance could increase, even on a global scale, in a certain direction, to accommodate for larger distortions in that elongated direction. The lattice constants in fact vary strongly in the low-temperature phase diagram for different doping x, allowing for such global trends, and also the tilting angle depends slightly on the doping, see Ref. [58]. However, both of these distortions lead to strain in the material and the induced stress will counteract these options to some degree. Since the double exchange favors a ferro-orbital (FO) alignment, at least of close-by Mn-sites, it competes with the AFO tendency of the cooperative Jahn-Teller distortions, which can lead to intricate orbital-ordered ground-state phases in the mixed valence regime, as we will see in the next section.

The onsite Coulomb interaction can influence the e_g-electron hopping similarly as the Jahn-Teller distortions in preventing double occupations of Mn-e_g orbitals. This is also outlined in Refs. [27, 82], which show that models including a strong Jahn-Teller interaction can predict most of the ordering principles of manganites even without considering the Coulomb interaction.

2.4 The phase diagram of $Pr_{1-x}Ca_xMnO_3$

The first systematic analysis of a manganite phase diagram was carried out by Wollan and Koehler (see Ref. [15]) with neutron diffraction experiments on $La_{1-x}Ca_xMnO_3$. Depending on the hole doping in the system they found a variety of complex magnetic ground state phases, including both FM and AFM

spin patterns, often with a directional dependence. The magnetic structures were named after the classification presented in that study. The most important patterns are (see also Ref. [28]): (a) A-type AFM, with FM spin alignment in the x-y-plane and AFM alignment in the z-direction, (b) B-type FM, with FM spin alignment in all directions, (c) C-type AFM, with FM spin alignment in the z-direction and AFM alignment in the x-y-plane, (d) G-type AFM, with an AFM spin alignment in all directions, and (e) CE-type AFM, with ferromagnetic zig-zag chains in the x-y-plane and AFM coupling to other chains. All these spin patterns appear also in $Pr_{1-x}Ca_xMnO_3$ and are sketched later in Fig. 2.6, where the experimental phases at very low temperature are outlined (in the following denoted as zero-temperature phases).

For $Pr_{1-x}Ca_xMnO_3$, detailed neutron diffraction, X-ray diffraction, magnetic susceptibility and electrical resistivity measurements were carried out, see Refs. [57, 58, 83], and interpreted in terms of the superexchange and double exchange mechanisms to predict the magnetic and orbital ordering in the entire doping range. The obtained phases are close to the ones of $La_{1-x}Ca_xMnO_3$ and could in many cases be well explained with the superexchange theory of Goodenough, Ref. [16]. In contrast to $La_{1-x}Ca_xMnO_3$, the material stays insulating (or semiconducting, see Ref. [58]) in the whole composition range at zero temperature, which is attributed to the stronger buckling (tilting) and thus reduced electron hopping bandwidth (see, e.g., Ref. [25]). The coarse distribution of these phases is indicated in Fig. 2.5 for the doping range $0 \leq x \leq 1$ and temperatures up to 1000 K.

The detailed zero-temperature phases will be described in the next section, but we can already see that antiferromagnetic and ferromagnetic insulating phases with orbital ordering are formed in the low doping region (close to $PrMnO_3$), while for higher doping an additional charge ordering is observed in a variety of antiferromagnetic insulating phases. Close to $CaMnO_3$, the orbital and charge order vanishes, but the AFM-insulating character remains. The influence of an increased temperature, which melts first the magnetic and then the orbital and charge order, is analyzed in detail in Sec. 2.4.2. Here, the striped region at small doping x is of special importance, as the established literature-phase diagram predicts a melting of the orbital order only at very high temperatures (up to 900 K for $PrMnO_3$). As presented in Ref. [24], we argue that the spontaneous orbital order vanishes already at much lower values below the striped region, which is described in detail in Ch. 4.

2.4.1 Zero-temperature phases

Many experimental investigations of the phases at low temperatures (denoted here as zero-temperature phases) followed the initial investigations of Refs. [57, 58, 83], see Refs. [17, 18, 20–22, 84–98], but the underlying ordering principles in many doping regions are still not unambiguously agreed upon. In some doping ranges, however, especially $x = 0$, $x = 0.5$, $x \approx 0.75$ and $x = 1$, the magnetic and orbital order has been verified in many experiments (although not completely unanimously). In addition, all experiments agree in that around $x = 0.25$ a ferromagnetic insulating phase develops, although the nature of

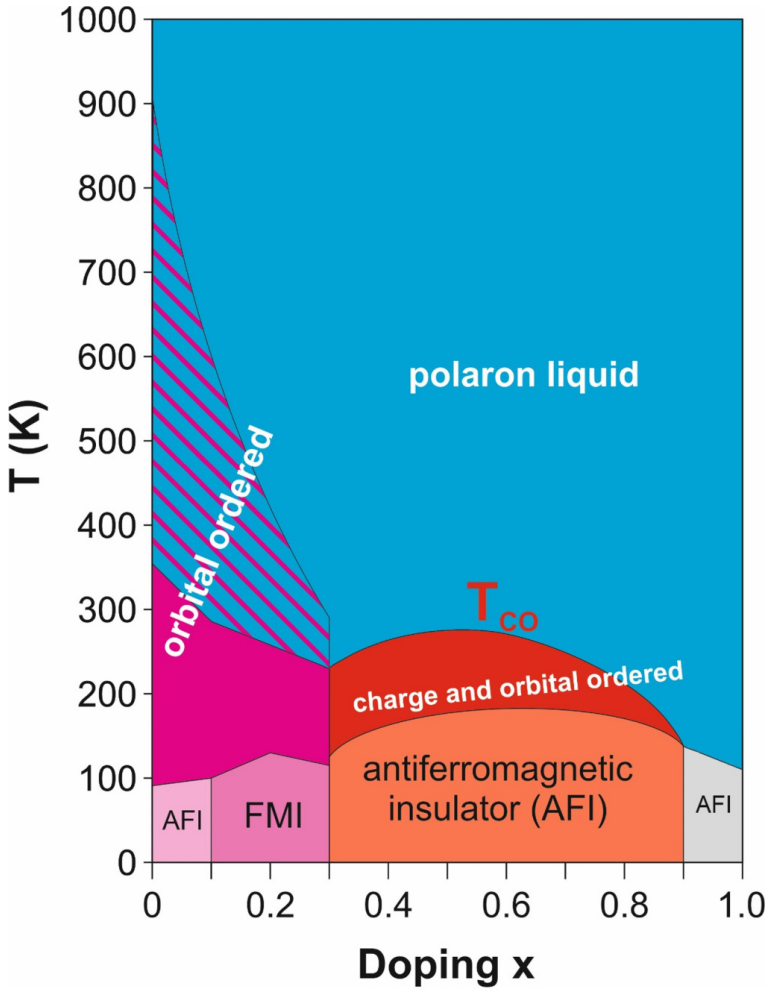

Figure 2.5: Sketch of the relevant ordered phases of $Pr_{1-x}Ca_xMnO_3$, including antiferromagnetic and ferromagnetic insulators (AFI and FMI), combined in some doping ranges with orbital and charge order, according to the results from Refs. [57, 58, 83]. At high temperatures a polaron liquid phase with short- but without long-range orbital order develops. The phase transition at even higher temperatures to a pseudo-cubic phase without short-range order is not shown here. The zero-temperature phases are discussed in detail in Sec. 2.4.1 and the finite-temperature phase transitions in Sec. 2.4.2. Adapted figure with permission from Ref. [24]. Copyright (2022) by the American Physical Society.

the orbital order (and potentially charge order) is still under debate. These phases are sketched in Fig. 2.6. We will now discuss the current experimental understanding of the zero-temperature phases in the whole doping range.

At $x = 0$ (pure $PrMnO_3$), the material is orthorhombic with $c/\sqrt{2} \lesssim a < b$, see Ref. [58], and has an A-type AFM spin order, i.e., FM coupling in the x-y-plane and AFM coupling between planes (see Fig. 2.6). The magnetic order is accompanied by an alternating in-plane $d_{3x^2-r^2} - d_{3y^2-r^2}$ orbital order, exactly like predicted from Goodenough's theory of superexchange (or semicovalent exchange) for the similar material $LaMnO_3$, see Ref. [16]. The orbital order has been further verified by theoretical *ab initio* calculations, see Refs. [28, 100]. As pointed out in Ref. [28], a weak admixture of a $d_{3z^2-r^2}$ orbital is found, which shifts the Jahn-Teller angle from the pure $d_{3x^2-r^2}$ and $d_{3y^2-r^2}$ modes ($\theta = 120°$ and $\theta = 240°$, see Fig. 2.4) to values around $\theta = 110°/\theta = 250°$.

The orthorhombic distortions decrease with the hole doping until they are nearly gone at $x = 0.25$, which is also accompanied by a transition to a completely ferromagnetic (B-type) phase, see Ref. [58] and Fig. 2.6. For the transition region, especially around $x = 0.1$, two alternative descriptions and interpretations of the experimental data exist: First, a spin-canted phase very similar to pure A-type $PrMnO_3$, but with an FM moment building up in-plane, eventually leading to the ferromagnetic phase at higher doping, see Refs. [58, 101]. Second, in light of more recent experiments, nanoscale phase separation between the A-type AFM and B-type FM phases, see Refs. [84, 85], which could explain experiments showing a photoinduced ferromagnetism. As the proposal of a phase separation is able to explain more of the observed measurements, it might be regarded as "more physical", see Ref. [86], but this matter is still open to new research.

At $x = 0.25$, various experiments confirmed a completely ferromagnetic phase, see Refs. [58, 87]. Double-exchange based theories (see Ref. [102]) would predict such an FM phase to be metallic, as the spin-alignment in the double-exchange picture is caused by delocalized e_g electrons. However, as mentioned above, all zero-temperature phases are insulating in $Pr_{1-x}Ca_xMnO_3$. An alternative was already presented above with the ferromagnetic superexchange mechanism (see Sec. 2.3), which can be stabilized with a long-range orbital order, see Ref. [16]. Two types of orbital order with accompanying charge order have been proposed based on simple model calculations: A layered orbital order with Mn^{4+} sites appearing only every second layer in z-direction (see Ref. [82]), and the appearance of "orbital polarons", see Ref. [103], which are Mn^{4+} sites surrounded by six Mn^{3+} sites. These orbital polarons are regularly placed on every second site in all three directions in two interlaced sublattices, forming a body-centered cubic charge order, see Ref. [103]. Such charge-ordered phases fit well to the ferromagnetic superexchange, as the Mn-O-Mn bond between the Mn^{4+} and Mn^{3+} sites fulfills the mixed ionic-semicovalent character needed for the ferromagnetic alignment (see Ref. [16]), and the regular placement of Mn^{4+} sites thus allows the development of FM bonds in all directions, which is prohibited in pure $PrMnO_3$. We note that an FM coupling between the two sublattices in the orbital-polaron structure is less clear, although supported by Hartree-Fock calculations, see Ref. [103].

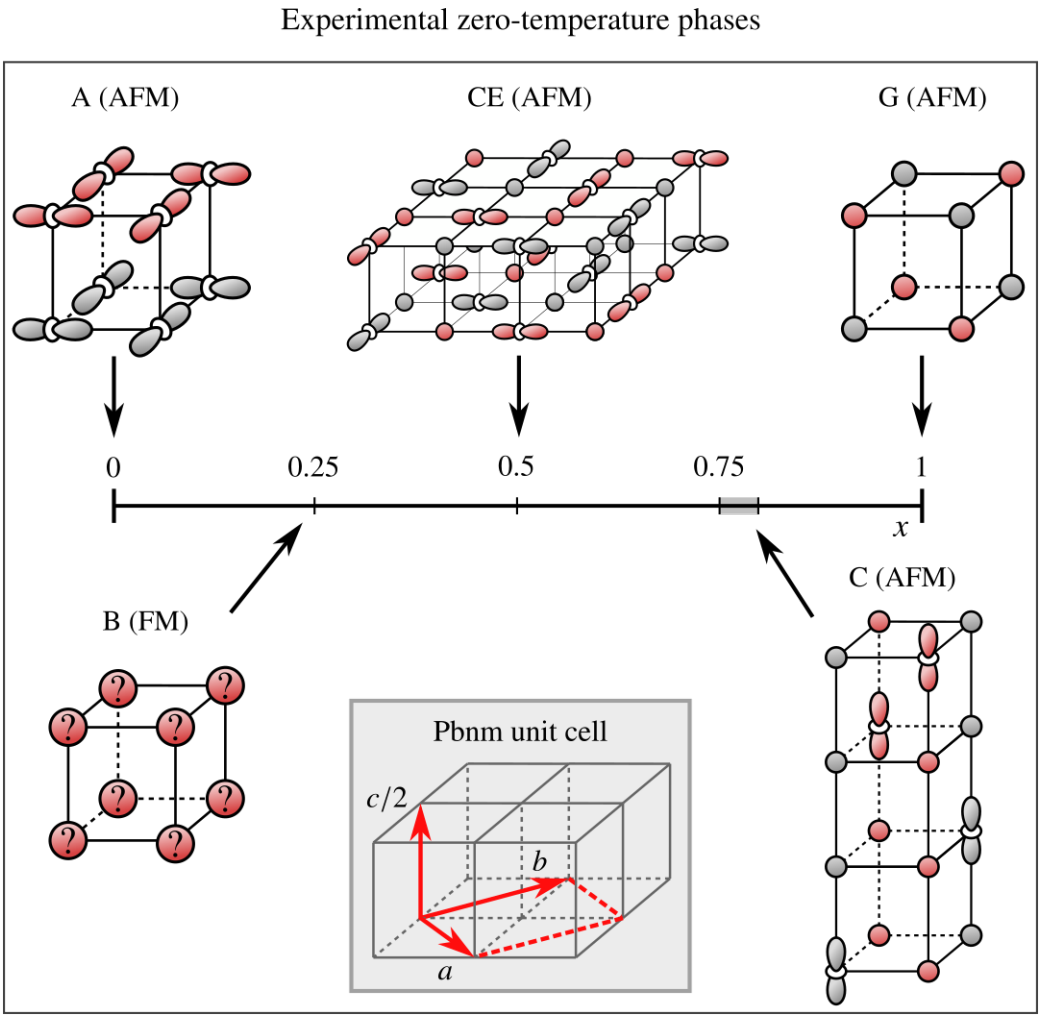

Figure 2.6: Sketches of the spin and orbital order of the experimental zero-temperature phases at $x = 0$, $x = 0.25$, $x = 0.5$, $x \approx 0.75$ and $x = 1$. The gray and red colors refer to spin-up and -down direction, respectively, and visualize the A-, B-, CE-, C- and G-type spin orders. Mn-sites without a strong orbital-polarization are shown as small colored circles, while $d_{3i^2-r^2}$-polarized Mn-sites are indicated by sketches of the orbitals pointing in the corresponding i-direction, with the color of the elongated lobes indicating the spin-direction of the e_g electron. For $x = 0.25$, a ferromagnetic spin order has been confirmed, see Refs. [58, 87], but the underlying orbital order is still under debate (see the discussion in the text), which is indicated by question marks in the colored circles. The style of the orbital-sketches is inspired by Ref. [99]. We also included a sketch of the Pbnm lattice vectors in the cubic structure.

From diffraction peaks of neutron scattering experiments, see Ref. [87], the former variant of charge order could be ruled out, while the orbital polaron peaks could not be clearly distinguished from Bragg peaks of twinned crystal structures, and this orbital and charge ordered phase remains possible. Alternatively to such an intrinsic ferromagnetic-insulating (FM-I) phase, a phase separation between an FM-metallic (FM-M) phase (with double exchange) and an AFM-insulating (AFM-I) phase could be a possible explanation, which, however, was dismissed as well by the same experimental study, see Ref. [87]. Instead, in that study and supported by previous resonant X-ray studies, see Ref. [88], a $PrMnO_3$-like orbital order was suggested, with a stronger $d_{3z^2-r^2}$-admixture. It is not clear why a pure $PrMnO_3$-like orbital order should lead to an insulating FM phase, and in fact the theoretical results from Ref. [87] indicate that the proposed FM phase is not insulating. As suggested in Ref. [88], the additional Mn^{4+} ions could be disordered throughout the system, which would allow a ferromagnetic superexchange in their environment. Overall, we consider the type of orbital or charge order as not fully determined at this doping and the respective region in the phase-diagram (see Fig. 2.5) could just as well belong to the charge and orbital ordered region, with the orbital polarons of Ref. [103] still remaining one possibility.

At higher hole dopings, the material was observed to be charge ordered over a wide doping range, $0.3 < x < 0.75$, see Refs. [58, 89, 95, 96, 98, 104], with the orbital structures strongly influenced by the half-doped system $x = 0.5$, accompanied by a (pseudo)tetragonal lattice distortion $c/\sqrt{2} < a \approx b$. At $x = 0.5$, a CE-type AFM magnetic structure emerges, see Ref. [58], consisting of FM zigzag chains in the x-y-plane that are antiferromagnetically stacked in the z-direction, which was already suggested on experimental (Ref. [15]) and theoretical (Ref. [16]) grounds for $La_{0.5}Ca_{0.5}MnO_3$. As the name suggests, the magnetic structure is composed of alternating unit cells of x-y-plane C-type and E-type structures (see Refs. [27, 28] for sketches of the E-type AFM order). Along the zigzag chains (formal) Mn^{3+} and Mn^{4+} ions alternate, forming a checkerbord-like charge order, although density-functional calculations indicate a smaller charge difference of $0.26 - 0.5\,e$ between the two sites, which might be even smaller in the real material, see Ref. [28]. The Mn^{3+} sites are at the center of the trimer segments constituting the zigzag chains, and their orbital polarization alternates between the elongated $d_{3x^2-r^2}$ and $d_{3y^2-r^2}$ orbitals, see Fig. 2.6. From a pure superexchange interaction model, other structures are possible as well, and only with the additional condition to minimize the elastic strain in the system, this CE-type structure could be rationalized on a qualitative level, see Ref. [16]. More successful are models including two-band e_g electrons with a strong Jahn-Teller coupling, in which it could be shown that the zigzag structure leads to a band-insulating behavior, see Refs. [25, 105].

Introducing additional e_g electrons at $x < 0.5$ (electron doped CE), a spin-canted variant of the CE-ordering was proposed according to early neutron diffraction experiments, see Ref. [58], where the previously collinear spins of the CE structure all gain a uniform small ferromagnetic moment. The existence of charge order has been questioned for $x = 0.4$ and alternative dimerized phases based on the two-site Zener polaron have been proposed,

see Refs. [90, 91, 106]. Resonant X-ray diffraction studies confirmed the lack of indications for charge disproportion, see Ref. [92], but re-assured the formation of a CE-like trimerized orbital order, albeit without the strong charge order implied by the formal Mn^{3+} and Mn^{4+} oxidation states. The trimer CE-type structure can be converted into a dimer structure by a small symmetry breaking while keeping the same magnetic order, which might lead to the different experimental explanations. Even closer to the FM-I phase, in the region $0.3 < x < 0.4$, different experiments proposed a phase separation of FM and AFM phases, see Refs. [21, 58, 97], or still a spin-canted AFM phase, see Refs. [89, 93]. Transmission electron microscopy studies indicated an ordering of additional Mn^{3+} ions in a half-doping like structure, see Ref. [94]. All experiments agree in that at least some kind of orbital order or charge order exists at low temperatures in the $0.3 < x < 0.5$ doping region, which leads to an insulating state (as this is the case both for the half-doped perfect CE-structure and the FM-I phase at quarter doping). Upon applying a strong magnetic field, a ferromagnetic metallic (orbital/charge disordered) phase develops with its resistivity decreased by several orders of magnitude, see Refs. [17, 18], which is known as the colossal magnetoresistance (CMR) effect. The CMR can also be induced by a photoexcitation, as first presented for $x = 0.3$ in Ref. [19], and confirmed, e.g., in Refs. [20, 21], although the character of the photo-induced FM-M phase might be different from the field-induced FM-M phase, see Ref. [21] (and references therein). The charge order of the ground state can also be removed with external or chemical pressure, inducing a metal-insulator transition accompanied with CMR, see Ref. [22], or by electron irradiation, see Ref. [23].

Hole dopings of $x > 0.5$ are generally much less investigated in the literature. In the early neutron diffraction experiments, see Ref. [58], it was suggested that close to half doping ($x = 0.6$) the CE-type structure remains with an additional small inter-plane ferromagnetic coupling, while at higher hole doping ($x = 0.7$) a new kind of spiral spin structure of non-collinear spins emerges. From the similar compound $La_{1-x}Ca_xMnO_3$, which has received more attention in the literature, especially at high hole dopings, an alternative explanation is the development of charge and orbital ordered striped phases, similar to the CE-structure, but with a smaller wave vector to account for the lower number of e_g electrons, see Refs. [107–110], which was also supported by theoretical considerations, see Ref. [105]. Here, the phase at $x = 2/3$ has received special attention, where for two (formal) Mn^{4+} sites there is only one Mn^{3+} site. Two types of zigzag-striped structures were suggested at this doping: First, a bi-stripe phase, in which the Mn^{3+} sites are separated by only a single Mn^{4+} site in a 90° angle, as in the CE-structure, while the three remaining Mn^{4+} sites separate these bi-stripes, see Ref. [108]. Second, a "Wigner"-crystal phase, in which Mn^{4+}-Mn^{3+}-Mn^{4+} trimers develop as in the CE-structure, but without overlap in their Mn^{4+} sites, see Ref. [109]. In the direction of the elongated Mn^{3+} sites a double-exchange induced ferromagnetism develops in both proposed structures, while the coupling between these clusters is antiferromagnetic or frustrated, see Ref. [109], and might be non-collinear, see Ref. [110]. As mentioned in Ref. [26], these two structures might be very close in energy and

it is not clear which one develops in $Pr_{1/3}Ca_{2/3}MnO_3$.

Interestingly, these striped phases do not continue to much higher dopings, as a transition to a (pseudo)tetragonal lattice with $c/\sqrt{2} > a \approx b$ is observed at $x > 0.75$, see Ref. [58]. The resulting magnetic structure was interpreted as C-type, which occurs at these dopings also in other manganite compounds, see Ref. [99]. The orbital order in the C-type magnetic structure is again composed of (formal) Mn^{4+}-Mn^{3+}-Mn^{4+} trimers, now oriented in the z-direction. These trimers are assumed to appear with a periodicity of four sites in the z-direction, with an additional Mn^{4+} site between them, see Ref. [58] and the sketch in Fig. 2.6. Originally it was proposed that in the x-y-plane the trimers avoid each other, see Ref. [58], however, as known from theoretical considerations around the half doped phase, the antiferromagnetic superexchange coupling favors a charge stacking, see Refs. [25], and an in-plane stacked variant of the C-type trimer structure cannot be ruled out. For the $x = 0.75$ phase itself, besides the C-type structure proposed in Ref. [58], also an x-y-plane zigzag structure has been proposed, similar to the $x = 2/3$ phase, but with a smaller wave vector, see Ref. [111].

Close to pure $CaMnO_3$, the antiferromagnetic superexchange between Mn^{4+} sites dominates the magnetic ordering, leading to a G-type antiferromagnet at $x = 1$, see Refs. [16, 58]. Both the missing Jahn-Teller distortions and the higher tolerance factor of the Ca ions lead to a nearly cubic lattice symmetry, see Refs. [57, 58]. In electron-doped $CaMnO_3$, phase separation between the C-type $x = 0.75$ doping and the G-type $x = 1$ doping might occur, see Ref. [58]. For the similar La-doped $CaMnO_3$, nanoscale phase separation was assumed between small double-exchange enhanced ferromagnetic clusters caused by the additional e_g electrons, and the AFM matrix of $CaMnO_3$ for very small electron dopings, see Refs. [112–114]; where only at $x \lesssim 0.94$ the C-type AFM phase starts to enter the phase competition, see Refs. [113, 114].

Overall, it is surprising how many uncertainties still exist in the ground-state (zero-temperature) phase diagram, despite more than 35 years of continued research since the original investigation of Jirak *et al.* in 1985 (Ref. [58]). With diverging experimental interpretations of the different phases, theoretical investigations of the phase diagram might provide additional insight. Many of the confirmed ground state phases, e.g., around $x = 0$, $x = 0.5$ and $x = 1$, and partially $x = 0.25$ and $x = 0.75$, can be reproduced by qualitative arguments, as presented before, for example by the theory of semicovalent exchange, see Ref. [16]. For a quantitative analysis, in particular one that is able to differentiate between several experimentally proposed and energetically similar structures, more involved models are needed, as described in detail in Refs. [25–27]. One such model, with parameters determined from *ab initio* calculations, will be used in this thesis, as introduced in Ch. 3. Before that, let us consider the finite-temperature phase transitions presented in the sketch in Fig. 2.5.

2.4.2 Finite-temperature phase transitions

Many of the experimental studies presented above did not only describe the ground-state phases, but also the melting of their order with increasing tem-

perature, with the observed behavior during the phase transition often being substantial in their interpretation of the ground-state experimental data. The agreement of the studies is much closer for the melting of the magnetic structure than for the exact ordering mechanisms of the ground-state phases, and up to today given mostly by the neutron diffraction studies by Jirak *et al.*, see Ref. [58, 83] (and for pure $CaMnO_3$ by Wollan and Koehler, see Ref. [15]). The Curie- and Néel-temperatures range between $\approx 90\,K$ and $170\,K$, with the highest values in the charge- and orbital-ordered region $0.4 < x < 0.8$, and the lowest values close to $PrMnO_3$. The transition temperatures are indicated in Fig. 2.5 and summarized in Ref. [24].

Of more relevance for this thesis are the transition temperatures for the charge and orbital order, in particular, of the latter in the low-doped region of the phase diagram. Even without a long-range orbital order, the strong electron-phonon coupling will lead to local Jahn-Teller distortions, possibly accompanied by short-range order. We thus refer to this high-temperature phase as a polaron liquid. At even higher temperatures also the local Jahn-Teller distortions melt, which is not included in the phase diagram sketch in Fig. 2.5.

Measuring the charge and orbital order is more difficult compared to the magnetic transitions, which in our opinion is also partially responsible for the remaining uncertainties in the ground-state phase diagram. One approach to infer the charge or orbital order is a structural refinement of electron, X-ray, or neutron diffraction experiments. Thereby one can obtain information about the average Jahn-Teller distortions, as outlined in detail in Ref. [115], and thus indirectly about the order in the system. This approach is especially helpful in the orbital and charge ordered phases $0.3 < x < 0.875$, where the appearance of superlattice reflections in the diffraction experiments allows to investigate the emergence of Pbnm-symmetry breaking ordering below a certain temperature, see Refs. [90, 106]. Various such experiments confirmed charge- and orbital-order melting temperatures T_{CO} in the $0.3 \leq x \leq 0.5$ doping region in the range between 200 K and 250 K, see Refs. [58, 83, 93, 116], supported by resistivity measurements, see Ref. [89]. Similar values are reported for the charge and orbital ordered region $0.5 < x < 0.875$, see Refs. [58, 117]. Below T_{CO}, the formation of two-phase ordered-disordered regions was suggested, see Refs. [91, 106]. The transition temperatures are again indicated in Fig. 2.5 and summarized in Ref. [24].

The same procedure is not as trivial around $x = 0$, where the orbital order (see Fig. 2.6) produces no new superlattice reflections compared to the higher-temperature tilting-induced Pbnm lattice. However, similar experiments can measure variations in the average lattice constants to observe structural changes: Pollert *et al.* (Ref. [57]) described two structural phase transitions at $x = 0$, both deduced from changes in the lattice parameters. First, an orthorhombic-to-orthorhombic $O' \rightarrow O$ transition between 815-945 K, with the critical temperature estimated at ~945 K. This transition was attributed to the melting of the cooperative Jahn-Teller order (together with the supporting orbital order) and a simultaneous adjustment of the tilt-pattern. This temperature is indicated by the upper end of the striped region in Fig. 2.5, and extends almost linearly down to $x = 0.25$, following the established representation of the phase dia-

gram presented in Ref. [58]. Second, a transition to a nearly cubic symmetry $O \rightarrow C$, completed above 1060 K, at which the tilting-induced $GdFeO_3$-type distortions of the lattice parameters vanish (at least on average), which is not included in Fig. 2.5. The structural changes of the first, $O' \rightarrow O$ transition were also observed in the neutron diffraction experiments of Ref. [118], although at a higher temperature of 1050 K. They attributed it to the Jahn-Teller/orbital order melting as well. The second transition to a quasicubic system at even higher temperatures was expected, but not measured in that reference. A drop in the resistivity and thermoelectric power around 1000 K was also interpreted as the orbital order transition temperature in Ref. [119], with order-disorder fluctuations continuing down to a temperature T^* at about 750 K. It is unclear whether this lower temperature matches the beginning of the $O' \rightarrow O$ transition observed in Ref. [57]. While the existence of a structural phase transition at these high temperatures, possibly combined with a metal-insulator transition, is undisputed, these measurements give only indirect information about the underlying orbital order.

A convincing experimental technique to directly observe the orbital order in the system is the resonant X-ray scattering. Here, polarized X-rays are tuned to the Mn-K edge to probe the Mn-1s to -4p transition. The presence of orbital order will split the energy levels of the 4p orbitals, either by direct or indirect Coulomb interaction, or by the coupling of the Mn-4p orbitals with the Jahn-Teller distorted oxygen octahedra, see Refs. [88, 120], giving access to the relative occupations of, for example, the $d_{3x^2-r^2}$ and $d_{3y^2-r^2}$ orbitals. Mn-L edge transitions for probing orbital or magnetic order are possible as well, see Ref. [121]. The transition temperatures for the charge and orbital order T_{CO}, indicated in Fig. 2.5, have been confirmed in the resonant X-ray scattering experiments at $x = 0.4$ and $x = 0.5$, see Ref. [88].

For the quarter-doped phase, $x = 0.25$, the temperature dependence of the $PrMnO_3$-like orbital order peak shows an interesting behavior, see Ref. [88]: A sharp drop is observed around room temperature, just as indicated as the transition temperature in Fig. 2.5, but the peak vanishes only at very high temperatures around 850 K. Resonant X-ray scattering of $LaMnO_3$ (similar to $PrMnO_3$, $x = 0$) for the same kind of orbital order shows a similar two-step feature, see Ref. [120], although here the intensity after the first drop (at 200-250 K) is still at about 60 % of the low-temperature value. The peak vanishes completely around 800 K, which is attributed to the orbital order transition, while the first drop is associated with the magnetic transition at 140 K. It seems inconsistent that in one case the lower transition temperature is attributed to the orbital-order transition (at $x = 0.25$) and in the other case the higher transition temperature (at $x = 0$). As mentioned already in Ref. [57], the cooperative Jahn-Teller distortions in the low-doping region (with its alternating short and long Mn-O bonds in the x-y-plane, see, e.g., the visualization in Ref. [64] and Fig. 2.6) might couple to the $GdFeO_3$-type tilting distortion. It was outlined in Ref. [24] that the onset of spontaneous orbital order might thus be hidden in an induced order by the tilt-pattern.

The investigation of the orbital-order transition temperature at the dopings $x = 0$ and $x = 0.1$ is one of the focus points of this thesis and presented

in Ch. 4. The results of these theoretical investigations support experimental evidence, such as the onset of a photovoltaic effect and anomalies in X-ray diffraction, magnetization, electron transport and optical properties, indicating that the spontaneous orbital-order phase transition actually takes place already around room temperature, and thus much lower than previously believed. This has been indicated in Fig. 2.5 by the lower end of the striped orbital-ordered region at low dopings. These results have been published in Ref. [24]. A discussion of the nature of the induced order at higher temperatures and a possible reevaluation of the phase diagram is given in Ref. [24] and in Ch. 4.

3 Tight-binding description for ground-state and finite-temperature calculations

In the last chapter, we presented the various interactions and ordering principles arising from the partially filled manganese d-shell, including the crystal field splitting caused by the surrounding octahedral structure, onsite Coulomb and Hund's interactions among Mn-e_g and -t_{2g} electrons, and the important overlap of their orbitals with the oxygen-p states, leading to the Jahn-Teller splitting of the e_g energy levels (caused by octahedral distortion modes), and to the (mostly) antiferromagnetic Mn-O-Mn superexchange through the intermediate oxygen atom. In addition, we presented the current experimental understanding of the resulting rich phase diagram, which included ferro- and antiferromagnetic spin-alignments, often of a non-isotropic type, and similar "ferro-" and "antiferrorbital" order of the occupied Mn-e_g orbitals, in some cases accompanied by an additional charge order.

Many theoretical models have been proposed in the past to explain the emergence of the different ordering principles and phases, with one of the more successful ones being the previously presented theory of semicovalent exchange (see Ref. [16]). At least on a qualitative level it could explain some of the ordered phases and magnetic structures, in particular the $x = 0$ and $x = 1$ pure $PrMnO_3$ and $CaMnO_3$ cases, and with additional assumptions also the half-doped CE-magnetic structure.

Various alternative models have been proposed for a quantitative description of the ordered phases, and a pure double-exchange model, see Refs. [80, 102], was being of high popularity in the early times of manganite studies, see Ref. [25]. This model, in its simplest form, includes only a single Mn-e_g orbital per site, with the t_{2g} spins coupled in a large Hunds-coupling assumption to only modify the e_g-electron hopping term, and the explicit influence of the oxygen atoms being completely discarded. Already for the magnetic transitions, double exchange model predictions did not coincide well with experimental results, as summarized in Ref. [25]; one core problem remaining that in this model a ferromagnetic interaction is always associated with an e_g-electron delocalization that leads to a larger conductance.

It is clear that any model hoping to describe the true orbital order of the system needs to include at least the two e_g orbitals per manganese site, which was subsequently adopted by most recent theories of manganites, see the overview in Ref. [25]. In addition, it was postulated that the combination of electron-phonon interaction (between Mn-e_g electrons and the oxygen ligands) in the form of Jahn-Teller interactions, the e_g to t_{2g} Hund's coupling and the inter-site hopping of the e_g electrons are the dominant effects necessary to understand

the physics of manganites in the low-doped region, see Refs. [25, 122]. This is also supported by modern benchmarks of such a model with density-functional calculations in the local spin-density approximation, see Ref. [62]. Combining these energy terms with an onsite Coulomb interaction and the antiferromagnetic superexchange (which is necessary to understand, for example, the G-type magnetic order in $CaMnO_3$ without e_g electrons), one arrives at an intricate model of manganites that is able to reproduce basically all the magnetic, charge and orbital orders at the various doping regions of manganites, and is reviewed in detail in Refs. [25–27].

As described in Sec. 2.4.1, in various doping regions of the zero-temperature phase diagram, the existing experimental results could not yet conclusively agree upon the ground state's spin, charge and orbital order, with several ordered structures, spin-canted regions, or phase coexistence being proposed. Without a consistent determination of the model's parameters, a quantitative assessment of the energies of the various structures is impossible, as is a calculation of the orbital-order melting temperature, discussed in Sec. 2.4.2. Such a consistent parameter determination was provided for this manganite model in Ref. [28] on the basis of hybrid density-functional calculations.

In that approach, the electrons in the manganite model were described by a Slater determinant composed of one-particle wave functions, see Ref. [28], similar as in a Hartree-Fock approximation, see, e.g., Ref. [123], or as the effective one-particle Kohn-Sham system in density-functional theory, see Refs. [124, 125]. Among other things, see Sec. 3.2.5 and Ref. [28] for details, the parameters of the model have been determined by comparing the density of states of the density-functional calculations (constructed from its effective Kohn-Sham system with the hybrid correction) with the one-particle energies of a single-site version of the manganite model. The resulting model can hence be called a parametrized density-functional model, or a parametrized Hartree-Fock model.

This manganite model, in the form presented in Ref. [28], is used in this thesis for the investigation of $Pr_{1-x}Ca_xMnO_3$ and will be outlined in detail in the following. It will be denoted as the tight-binding model for manganites in this thesis, due to the tight-binding description of the Mn-e_g electrons. Small variations which were later introduced in Refs. [32, 126] are presented in Sec. 3.2.6.

3.1 General description of the tight-binding model for manganites

The tight-binding model described in Refs. [25–28] is not a full electronic structure method, like a density-functional calculation, but is instead focused on the most important degrees of freedom, which are included on different levels of theory: (a) The Mn-e_g electrons are described as a quantum mechanical wave function $|\Psi\rangle$, in a tight-binding basis of the two e_g orbitals $d_{x^2-y^2}$ and $d_{3z^2-r^2}$, indexed by $\alpha \in \{a, b\}$, on every manganese site, each with both spin-up and -down $\sigma \in \{\uparrow, \downarrow\}$ component. Their full basis hence includes four spin-orbitals

per Mn-site R: $|\chi_{\sigma,\alpha,R}\rangle$. Following Ref. [28], the wave function is described by a single Slater determinant composed of the one-particle wave functions $\{|\psi_n\rangle\}$:

$$|\psi_n\rangle = \sum_{\sigma,\alpha,R} |\chi_{\sigma,\alpha,R}\rangle\, \psi_{\sigma,\alpha,R,n}. \tag{3.1}$$

(b) The three spin-aligned t_{2g} electrons are replaced by a single classical spin $\vec{S}_R$ of length $\frac{3\hbar}{2}$, localized on each manganese site R. (c) The octahedral distortions are included by considering the classical nuclear positions of the oxygen atoms $\vec{O}$.

Instead of allowing free three-dimensional displacements of the oxygen positions $\vec{O}$ from their equilibrium positions, they are restricted in this model to a movement along the straight (180°-angle) Mn-O-Mn line, without considering the octahedral tilting of the Mn-O-Mn bond angle and with the Mn-sites placed on a regular grid (we note, however, that the model parameters were obtained from the full tilted structure in Ref. [28], see also Sec. 3.2.5, and one might consider the influence of the tilting on the parameters to be included on an average level). Hence, each oxygen atom position can be quantified by its one-dimensional displacement $O_{i,R}$ from its equilibrium position at half the distance between the manganese sites R and its neighbor R_{+i}. $R_{\pm i}$ refers to the manganese neighbor of site R in the positive or negative $i \in \{x, y, z\}$ direction. The difference of these oxygen displacements in positive and negative orientation along a cubic axis $\Delta_{i,R} = O_{i,R} - O_{i,R_{-i}}$ are then the deviations of the O-Mn-O bond distances around site R from their equilibrium value. These are the bond distances that were used for describing the Jahn-Teller $Q_{2,R}$, $Q_{3,R}$ and breathing $Q_{1,R}$ modes introduced in Sec. 2.2.2.

As mentioned in Refs. [25, 27], depending on whether the octahedral modes $Q_{a,R}$, $a \in \{1, 2, 3\}$ or the oxygen displacements $O_{i,R}$ are used as the fundamental degrees of freedom, one can switch between an individual and a cooperative treatment of the distortion modes. We will follow the cooperative treatment here, as also done in Refs. [127, 128], by considering variations of the underlying oxygen displacements $O_{i,R}$, which influence the octahedral modes around both neighboring manganese sites.

Besides the obvious Hartree-Fock approximation for the electrons, the classical and straight-line approximations for the oxygen atom positions, the regular placement of the manganese atoms and the classical spin approximation for the t_{2g} electrons, several further approximations are necessary to reach the tight-binding model for manganites. These include: The A-type cations are assumed to always be in the formal oxidation states Ca^{2+} and Pr^{3+}; any effect of these ions despite the electron doping of the remaining system is ignored. In a similar manner, the oxygen atoms are, for the purpose of the actual calculations, assumed to be in the formal oxidation state O^{2-}, leaving on average exactly $(4 - x)$ Mn-d electrons per site and discarding the possibility of oxygen vacancies. While the Mn-e_g-O-p hybridization and the resulting crystal field splitting was implicitly taken into account by separating the e_g and t_{2g} manganese d-states, the oxygen-p electrons do not appear explicitly in the model,

although we keep in mind that the Mn-e_g states actually refer to the Mn-e_g-O-p antibonding orbitals, see Sec. 2.2.1.

Further approximations for determining an effective Mn-Mn e_g-electron hopping, for the form of the Jahn-Teller interaction potential, and for the antiferromagnetic superexchange interaction are described when the respective energy terms are introduced in Secs. 3.2.1, 3.2.3 and 3.2.4.

3.2 The energy functional

Similar to the energy functional of density-functional theory, see Refs. [124, 125], we now present the energy functional of the tight-binding model for manganites. In the spirit of the later introduced Car-Parrinello framework, see Ref. [129], it will be denoted as the potential energy functional of the model $E_{pot}(\psi, S, O)$, depending on the one-particle Mn-e_g wave functions $|\psi_n\rangle$, see Eq. (3.1), the t_{2g} spins S, and the oxygen displacements O. The six fundamental terms of the model, already mentioned above, are:

$$E_{pot} = E_e + E_{e-e} + E_{e-ph} + E_{ph} + E_{e-S} + E_{AFM}, \tag{3.2}$$

including the e_g-electron hopping E_e, the onsite e_g electron-electron Hartree-Fock interaction E_{e-e}, the Jahn-Teller and breathing interactions of the oxygen atoms (the classical phonons) with the e_g electrons E_{e-ph}, the restoring forces on these phonons E_{ph}, the Hund's interaction between e_g electrons and t_{2g} spins E_{e-S} and the t_{2g} spin antiferromagnetic superexchange interaction E_{AFM}. All these terms have been presented and discussed in detail in Refs. [25–28, 56, 126], and this section follows the same scheme.

To get some flexibility in describing excited one-particle states, a one-particle occupation number f_n is introduced in the following expressions, see Ref. [28], which in the single-Slater determinant description is either one or zero for the occupied or unoccupied states. For describing the onsite interactions, the definition of the local one-center reduced density matrix will be useful, see Ref. [28]:

$$\rho_{\sigma,\alpha,\sigma',\beta,R} = \sum_n f_n \psi_{\sigma,\alpha,R,n} \psi^*_{\sigma',\beta,R,n}, \tag{3.3}$$

where $\alpha, \beta \in \{a, b\}$ (and later also $\gamma, \delta \in \{a, b\}$) are the orbital indices (referring to $d_{x^2-y^2}$ and $d_{3z^2-r^2}$), while $\sigma, \sigma' \in \{\uparrow, \downarrow\}$ are the spin indices. The local spin-orbital densities are given by $n_{\sigma,\alpha,R} = \rho_{\sigma,\alpha,\sigma,\alpha,R}$, and the local electron density by $n_R = \sum_{\sigma,\alpha} n_{\sigma,\alpha,R}$.

We note that from the potential energy functional, Eq. (3.2), one can directly derive the effective Hartree-Fock Hamiltonian for the electronic one-particle states, which in the basis of the e_g spin-orbitals becomes:

$$\hat{H}_{HF} = \sum_{\sigma,\alpha,R} \sum_{\sigma',\beta,R'} |\chi_{\sigma,\alpha,R}\rangle \frac{\partial E_{pot}(\psi, S, O)}{\partial \tilde{\rho}_{\sigma,\alpha,\sigma',\beta,R,R'}} \langle \chi_{\sigma',\beta,R'}|, \tag{3.4}$$

with the reduced density matrix $\tilde{\rho}_{\sigma,\alpha,\sigma',\beta,R,R'} = \sum_n f_n \psi_{\sigma,\alpha,R,n} \psi^*_{\sigma',\beta,R',n}$. This Hartree-Fock Hamiltonian will then still depend on the classical spins S and nuclei O, but also on the local one-center reduced density matrices of the e_g electrons $\rho_{\sigma,\alpha,\sigma',\beta,R}$, as typical in a Hartee-Fock description. All the following terms can also be represented in such a Hartree-Fock Hamiltonian form, as done, e.g., in Ref. [56]. For a non-Hartree-Fock version of the total Hamiltonian we refer to Refs. [25–27].

3.2.1 Electron hopping

With the direct overlap of e_g states on different sites being negligible, any hopping of e_g electrons between manganese sites is mediated by the intermediate oxygen atoms. The relevant oxygen-p states are downfolded to allow for an effective Mn-Mn hopping description, see Refs. [25, 27]. These effective hopping terms are obtained from the orbital overlaps of the Mn-e_g and O-p states, according to the Slater-Koster tables, see Ref. [130]. The resulting kinetic energy term for the electrons describes an orbital- and direction dependent hopping:

$$E_e = \sum_{R,R',\sigma,\alpha,\beta} \sum_n f_n \psi^*_{\sigma,\alpha,R,n} T_{\alpha,\beta,R,R'} \psi_{\sigma,\beta,R',n}, \tag{3.5}$$

where $T_{\alpha,\beta,R,R'}$ is non-zero only for R and R' being nearest neighbors, and then taking different forms depending on the bond direction $i \in \{x, y, z\}$ between R and R'. Apart from the bond-direction, the hopping matrices $\boldsymbol{T}_{R,R'}$ are assumed to be independent of the site indices, and can be described by direction dependent matrices $\boldsymbol{T}^i$. In the basis of the two e_g orbitals $d_{x^2-y^2}$ and $d_{3z^2-r^2}$ they become:

$$\boldsymbol{T}^x = -t_h \begin{pmatrix} 3/4 & -\sqrt{3}/4 \\ -\sqrt{3}/4 & 3/4 \end{pmatrix} \tag{3.6}$$

$$\boldsymbol{T}^y = -t_h \begin{pmatrix} 3/4 & \sqrt{3}/4 \\ \sqrt{3}/4 & 3/4 \end{pmatrix} \tag{3.7}$$

$$\boldsymbol{T}^z = -t_h \begin{pmatrix} 0 & 0 \\ 0 & 1 \end{pmatrix}. \tag{3.8}$$

From the downfolding, two additional energy terms emerge, which can be regarded as onsite-hopping terms for $R = R'$ (see Ref. [28]): The first being proportional to the local electron density: $3t_h \sum_R n_R$, with $n_R = \sum_{n,\sigma,\alpha} f_n |\psi_{\sigma,\alpha,R,n}|^2$, which adds an energy per Mn-site of $3t_h(1 - x)$ and is included in the model of this thesis. The second term is a constant energy contribution of $-6t_h$ per Mn-site, which is neglected in this thesis.

The single remaining parameter describing the e_g-electron hopping is t_h. Since the hopping is oxygen mediated, the hopping amplitude should depend on the local distortion modes and on the local octahedral tilting angle. These variations are ignored in choosing such a uniform hopping description. Density-functional calculations of $LaMnO_3$ show a good agreement with a tight-binding

model using such a uniform hopping description, see Ref. [62], although next-nearest neighbor hopping was included in that model.

3.2.2 Electron-electron interaction

Here, we consider the onsite Coulomb interaction between e_g electrons only, as the effective interaction between the t_{2g} and e_g states is only included on the level of a Hund's coupling, see Sec. 3.2.4. For more details on the various Mn-d shell Coulomb interactions, we refer to Ref. [27]. Inter-site Coulomb interactions are strongly screened, see Ref. [27], and neglected here as well.

On a Hartree-Fock level, and using the local one-center reduced density matrices (Eq. (3.3)), the e_g-e_g Coulomb interaction terms can in general be written as:

$$E_{e-e} = \frac{1}{2}\sum_{R}\sum_{\alpha,\beta,\gamma,\delta}\sum_{\sigma,\sigma'} W_{\alpha,\beta,\gamma,\delta}\left[\rho_{\sigma,\gamma,\sigma,\alpha,R}\rho_{\sigma',\delta,\sigma',\beta,R} - \rho_{\sigma',\delta,\sigma,\alpha,R}\rho_{\sigma,\gamma,\sigma',\beta,R}\right], \tag{3.9}$$

where the square brackets include the Hartree and exchange terms of the reduced density matrix, and the prefactor W describes the various orbital scattering terms. These onsite electron-electron interaction terms for the e_g and t_{2g} orbitals in a cubic symmetry have been presented by Kanamori, see Ref. [131], and the interaction parameters are termed Kanamori parameters. They include an intra- and inter-orbital Coulomb interaction U and U', as well as an inter-orbital exchange term J and pair-hopping term J', where $J = J'$ see Refs. [27, 131]. When applied to the e_g orbitals only, we have $U = U' + J + J'$, see Ref. [27], leaving only two independent parameters. They can be best visualized by presenting $W_{(\alpha,\beta),(\gamma,\delta)}$ as a matrix in the orbital tupels (a,a), (a,b), (b,a) and (b,b):

$$\boldsymbol{W} = \begin{pmatrix} U & 0 & 0 & J' \\ 0 & U' & J & 0 \\ 0 & J & U' & 0 \\ J' & 0 & 0 & U \end{pmatrix} = \begin{pmatrix} U & 0 & 0 & J \\ 0 & U-2J & J & 0 \\ 0 & J & U-2J & 0 \\ J & 0 & 0 & U \end{pmatrix}, \tag{3.10}$$

which can be decomposed into three components: $W_{\alpha,\beta,\gamma,\delta} = (U-2J)\delta_{\alpha,\gamma}\delta_{\beta,\delta} + J\delta_{\alpha,\delta}\delta_{\beta,\gamma} + J\delta_{\alpha,\beta}\delta_{\gamma,\delta}$. Inserting this W into the Hartree-Fock interaction energy, Eq. (3.9), one obtains the following energy contributions on every site :

$$\begin{aligned} E_{e-e,R} = \frac{1}{2}\sum_{\alpha,\sigma}\Bigg[& U\left(n_{\sigma,\alpha}n_{\bar{\sigma},\alpha} - |\rho_{\sigma,\alpha,\bar{\sigma},\alpha}|^2\right) + (U-3J)\left(n_{\sigma,\alpha}n_{\sigma,\bar{\alpha}} - |\rho_{\sigma,\alpha,\sigma,\bar{\alpha}}|^2\right) \\ & + (U-2J)\left(n_{\sigma,\alpha}n_{\bar{\sigma},\bar{\alpha}} - |\rho_{\sigma,\alpha,\bar{\sigma},\bar{\alpha}}|^2\right) + J\Big(\rho_{\sigma,\bar{\alpha},\sigma,\alpha}\rho_{\bar{\sigma},\alpha,\bar{\sigma},\bar{\alpha}} \\ & + \rho_{\sigma,\bar{\alpha},\sigma,\alpha}\rho_{\bar{\sigma},\bar{\alpha},\bar{\sigma},\alpha} - \rho_{\bar{\sigma},\alpha,\sigma,\alpha}\rho_{\sigma,\bar{\alpha},\bar{\sigma},\bar{\alpha}} - \rho_{\bar{\sigma},\bar{\alpha},\sigma,\alpha}\rho_{\sigma,\bar{\alpha},\bar{\sigma},\alpha}\Big)\Bigg], \end{aligned} \tag{3.11}$$

where the site-index R is omitted in the local one-center reduced density matrices and the local electron densities for clarity. Here, the indices $\bar{\sigma}$ and $\bar{\alpha}$ refer to the opposite spin/orbital as σ and α.

Considering for a moment only the spin-orbit density-density interaction terms ($n_{\sigma,\alpha}n_{\sigma',\beta}$) in Eq. (3.11), which all have a corresponding exchange contribution ($|\rho_{\sigma,\alpha,\sigma',\beta}|^2$), we can identify three major interaction contributions: The intra-orbital interaction (with different spin), proportional to U, the inter-orbital interaction with the same spin, proportional to $(U - 3J)$, and the inter-orbital interaction with different spin, proportional to $(U - 2J)$. Hence, the onsite Coulomb energy has the largest contribution for electrons with different spin, and would in case of a double-occupation instead prefer a spin-aligned occupation of both e_g orbitals (which is just another manifestation of Hund's rule). With Jahn-Teller interactions shifting the e_g energy levels, the occupations in the full model might differ from this pure electron-electron interaction picture. Kugel and Khomsky showed that one can actually describe orbital ordering relying mainly on the Coulomb interaction, see Ref. [132], although modern investigations attribute more importance to the Jahn-Teller effect (see, e.g., Ref. [28]).

Another collection of the energy terms presented in Eq. (3.11) was shown in Ref. [28]:

$$E_{e-e} = \frac{U - 3J}{2} \sum_R \left\{ (\mathrm{Tr}_R[\boldsymbol{\rho}_R])^2 - \mathrm{Tr}_R\left[\boldsymbol{\rho}_R^2\right] \right\} + E_{OR}, \tag{3.12}$$

separating the Coulomb interaction into a Hartree- and self-interaction correction term (where the trace $\mathrm{Tr}_R[\cdot]$ is taken over the onsite spin- and orbital degrees of freedom on site R), and another contribution E_{OR}, which is only relevant for sites without full spin-polarization. Since the inter-spin interaction is the largest contribution of the Coulomb terms (see Eq. (3.11)), the first term in Eq. (3.12), proportional to $(U - 3J)$, can be regarded as the dominant Coulomb interaction between different orbitals. As pointed out in Ref. [28], this effective Coulomb interaction strength is much lower compared to the bare intra-orbital interaction term U.

3.2.3 Phonon modes and the electron-phonon interaction

We already mentioned that the oxygen ligands are described by the classical nuclear oxygen displacements $O_{i,R}$ along the Mn-Mn straight bond line between the Mn-sites R and R_{+i} (where $R_{\pm i}$ is the Mn-neighbor-site in the $\pm i$ cubic direction). With only the straight-cubic distortions allowed in the model, the possible distortion modes around every manganese site are exactly the two Jahn-Teller active phonon modes $Q_{2,R}$ and $Q_{3,R}$ and the breathing mode $Q_{1,R}$, which were defined in Sec. 2.2.2 and depend on the O-Mn-O bond distances $\Delta_{i,R} = O_{i,R} - O_{i,R_{-i}}$. The tight-binding model assumes a quadratic restoring

force on these phonon modes:

$$E_{ph} = \frac{1}{2} \sum_R \left[k_{JT} \left(Q_{2,R}^2 + Q_{3,R}^2 \right) + k_{br} Q_{1,R}^2 \right] . \tag{3.13}$$

In addition, these modes couple to the Mn-e_g electronic orbitals. The breathing mode, which is an isotropic expansion, couples to the onsite electron density n_i. In contrast, the Jahn-Teller modes split the e_g-orbital energy levels, with the Q_3 mode separating the $d_{3z^2-r^2}$- and $d_{x^2-y^2}$-orbital energies, and the Q_2 mode separating the positive and negative linear combination of these orbitals. The whole electron-phonon interaction can then be written as:

$$E_{e-ph} = g_{JT} \sum_R \sum_\sigma \sum_{\alpha,\beta} \rho_{\sigma,\alpha,\sigma,\beta,R} M^Q_{\beta,\alpha}(Q_{2,R}, Q_{3,R}) - g_{br} \sum_R n_R Q_{1,R}, \tag{3.14}$$

with

$$\boldsymbol{M}^Q (Q_2, Q_3) = \left[\boldsymbol{\sigma}_P^z \cdot Q_3 + \boldsymbol{\sigma}_P^x \cdot Q_2 \right] = \begin{pmatrix} Q_3 & Q_2 \\ Q_2 & -Q_3 \end{pmatrix}, \tag{3.15}$$

where $\boldsymbol{\sigma}_P^{x/z}$ are the x/z Pauli matrices (again in the two-orbital basis $\alpha \in \{a, b\}$, corresponding to $\{d_{x^2-y^2}, d_{3z^2-r^2}\}$).

Let us omit the spin degree of freedom for a moment and consider a singly occupied isolated octahedron with a general e_g-electronic state described by the linear combination $|\theta/2\rangle = \cos(\theta/2)\,|d_{3z^2-r^2}\rangle - \sin(\theta/2)\,|d_{x^2-y^2}\rangle$. Inserting the corresponding wave function into Eq. (3.14) and considering only the Jahn-Teller term on that single site, one arrives at: $E_{e-ph,JT} = -g_{JT}\,[\cos(\theta)Q_3 + \sin(\theta)Q_2]$. Minimizing the local Jahn-Teller coordinates for such an electronic state yields $(Q_2, Q_3) = g_{JT}/k_{JT}(\cos(\theta), \sin(\theta))$. Hence, the classical minimum of the Jahn-Teller distortions can change continuously, but with constant absolute value $\sqrt{Q_2^2 + Q_3^2} = g_{JT}/k_{JT}$, depending on the mixing angle of the occupied electronic state, see also Ref. [68]. The Jahn-Teller angle is twice as large as the orbital mixing angle, leading to a sign change of the wave function after one loop in the Jahn-Teller angle, which was already discussed in Sec. 2.2.2.

One can obtain the one-particle electronic eigenenergies of such an isolated octahedron for any given (classical and fixed) Jahn-Teller distortion (Q_2, Q_3) by diagonalizing the 2×2 matrix of Eq. (3.15) plus the diagonal restoring forces of Eq. 3.13 (this corresponds to determining the adiabatic electronic energies of the one-particle isolated octahedron, as mentioned in Sec. 2.2.2; more details on adiabatic states and energies also outside of a classical approximation for the nuclei are given in Ch. 5). This diagonalization leads to $E_\pm(Q_2, Q_3) = \pm g_{JT}|Q_{JT}| + \frac{k_{JT}}{2}|Q_{JT}|^2$, where $|Q_{JT}| = \sqrt{Q_2^2 + Q_3^2}$ does not depend on the Jahn-Teller angle and the whole energy expression is thus isotropic in orbital space. These energy surfaces are depicted in Fig. 3.1. Without Jahn-Teller distortion, the two orbital energies are degenerate, while any type of distortion

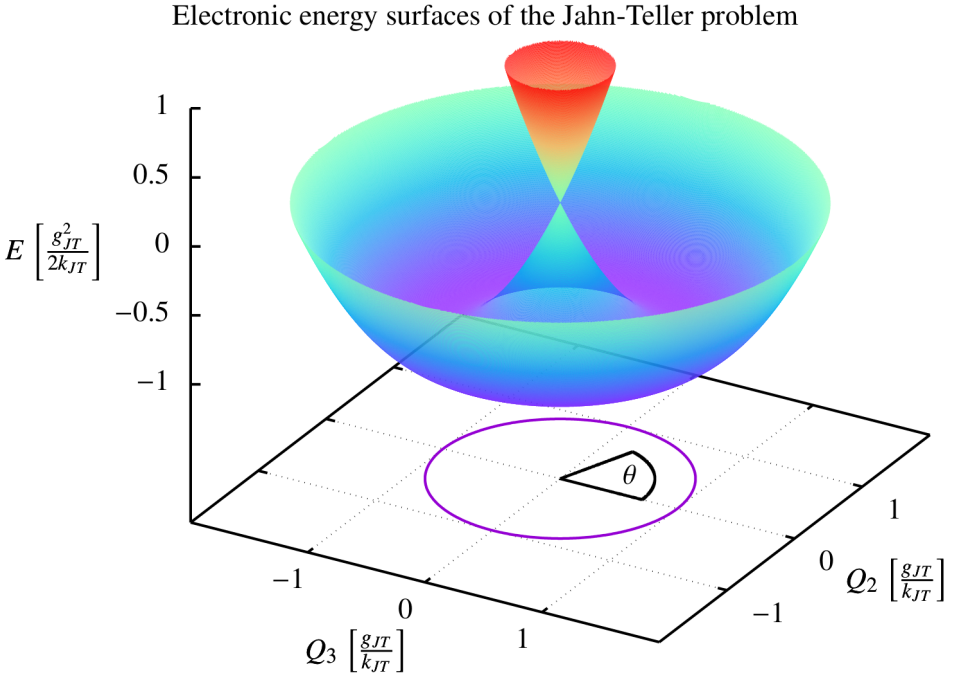

Figure 3.1: Electronic energy surfaces $E_{\pm}(Q_2, Q_3) = \pm g_{JT}|Q_{JT}| + \frac{k_{JT}}{2}|Q_{JT}|^2$ of the one-electron single-site Jahn-Teller problem in the space of the fixed Jahn-Teller distortions Q_2 and Q_3. The Jahn-Teller and restoring force constants have been chosen as a dimensionless $g_{JT} = k_{JT} = 2$ in this figure. The lower surface has its minimal values at the circle $|Q_{JT}| = g_{JT}/k_{JT}$, also indicated on the x-y-plane, together with the Jahn-Teller angle θ. Real-valued sketches of the corresponding adiabatic lower energy states are shown in Fig. 2.4. The lower and upper energy surface become degenerate at $|Q_{JT}| = 0$.

will lift the degeneracy in a double-conical form. For any Jahn-Teller angle θ, the lower and upper electronic eigenstate are proportional to the $|\theta/2\rangle$ and $|(\theta + \pi)/2\rangle$ state, as mentioned previously (see also Fig. 2.4 for sketches of the lower e_g state for some Jahn-Teller angles). Any octahedron occupied by a pure one-electron state will undergo a Jahn-Teller distortion matching the electronic state at zero temperature. For mixed-electron states this is not true in general: A site half occupied by each one electron in the $|d_{3z^2-r^2}\rangle$ orbital and another one in the $|d_{x^2-y^2}\rangle$ orbital will not undergo a Jahn-Teller distortion. One can describe such sites as not-orbital-polarized and they can occur in some phases in the complete model.

Electronic energy surfaces of the type presented here (see Fig. 3.1) are called conical intersections and have received much attention in literature, see the overview of various aspects in Ref. [133]. In particular, they allow for a radiationless decay of excited electronic states by undergoing a structural deformation, see also Ref. [134]. We note that the restoring force energy terms presented in Eq. (3.13) can be understood as a lowest order approximation. As discussed in Ref. [68], higher order terms can lift the isotropy of the Jahn-Teller distortions, and will in general lead to local minima in the lower energy surface of Fig. 3.1 at Jahn-Teller angles $\theta = 0, \pm 2\pi/3$, corresponding to the prolate

Jahn-Teller distortions (see Fig. 2.4) in the three cubic directions.

3.2.4 t_{2g} spins, Hund's coupling and antiferromagnetic superexchange

One of the larger approximations in the model is the description of the t_{2g} electrons as a classical spin of length $\frac{3\hbar}{2}$. While assessing the important interactions in manganites, see Ch. 2, we mentioned that the t_{2g} orbitals are always occupied in one spin-direction, independent of the doping, and that their hybridization with the oxygen-p states is much weaker compared to the e_g orbitals. Their rather large combined total spin justifies the classical approximation for the spins, as has been stated and tested in Ref. [26], see also the references therein. Ultimately, a quantum mechanical description of the t_{2g} electrons, or their spin, complicates the model significantly and would limit finding solutions mostly to one-dimensional applications, see Ref. [26], which are then, however, not able to accommodate the necessary 3D-ordered structures. Testing the classical spin approximation against more intricate descriptions in small model systems might be an interesting challenge in a future study, but is not done in this thesis.

The localized t_{2g} spins are nonetheless important for the correct description of the magnetic phases of $Pr_{1-x}Ca_xMnO_3$, as they are strongly coupled to the e_g electrons with a Hund's coupling (see Ref. [28]):

$$E_{e-S} = -J_H \sum_R \sum_\alpha \sum_{\sigma,\sigma'} \rho_{\sigma,\alpha,\sigma',\alpha} M^S_{\sigma',\sigma}(\vec{S}_R), \tag{3.16}$$

with $\vec{S}_R = (S_{x,R}, S_{y,R}, S_{z,R})$ and

$$\boldsymbol{M}^S\left(\vec{S}\right) = \left(\frac{3\hbar}{2}\right)\left[\sum_i \boldsymbol{\sigma}^i_P \cdot S_i\right] = \begin{pmatrix} S_z & S_x - iS_y \\ S_x + iS_y & -S_z \end{pmatrix}. \tag{3.17}$$

The $\boldsymbol{\sigma}^i_P$ denote again the $i \in \{x, y, z\}$ Pauli matrices and $\vec{S}$ is a general three-dimensional spin vector.

In addition, we outlined the importance of the superexchange interaction (or similarly semicovalent exchange) in Sec. 2.3. As this interaction can be understood by virtual hopping processes of the oxygen-p electrons to the manganese neighbors, and then the local interaction with the occupied Mn-d states, it is clear that the t_{2g} spins will be subject to some effective exchange interaction, even though a direct t_{2g} to oxygen-p hopping is suppressed. We pointed out that for a straight Mn-O-Mn bond, the Mn^{4+}-Mn^{4+} superexchange interaction is always of the antiferromagnetic type, and thus the tight-binding model includes an antiferromagnetic nearest neighbor spin-spin interaction between the t_{2g} electrons:

$$E_{AFM} = J_{AF} \sum_R \sum_{i\in\{x,y,z\}} \left(\frac{3\hbar}{2}\right)^{-2} \vec{S}_R \vec{S}_{R_{+i}}. \tag{3.18}$$

Just as discussed for the e_g-electron hopping, see Sec. 3.2.1, the AFM superexchange interaction should depend on the local tilting angle and octahedral distortions modifying the Mn-O-Mn bonds. As before, a uniform description is chosen here instead, with global Hund's coupling and AFM superexchange parameters J_H and J_{AF}.

3.2.5 Model parameters

We described in the introduction to this chapter that we will use a parameter set for the model that was determined in Ref. [28] on the basis of density-functional calculations. In this determination it was first noted that the Jahn-Teller and breathing electron-phonon coupling parameters g_{JT} and g_{br} should not be independent. This was concluded by considering the situation of a pure elongation of an octahedron in one direction, e.g., along the z-axis. The e_g orbital with a δ-symmetry along that axis, here the $d_{x^2-y^2}$ orbital, should have its orbital energy level unchanged, since it is mostly unaffected by the Mn-O bond distance in the z-direction. The same holds also for the other two pure elongated distortions, which can all be constructed by demanding the relation between Jahn-Teller and breathing distortion of $\sqrt{2}Q_1 = |Q_{JT}|$. The orbital energies of the δ-symmetry orbitals for these three distortions are unchanged under the condition $g_{JT}|Q_{JT}| = g_{br}Q_1$. Combined, these two equations lead to the relation $g_{br} = \sqrt{2}g_{JT}$. Similarly, a relation of the restoring force constants k_{br} and k_{JT} was deduced by demanding that an isolated singly-occupied octahedron with its electron in the $d_{3z^2-r^2}$ orbital will undergo a pure axial Jahn-Teller distortion, which leads to $k_{br} = 2k_{JT}$. This is one of the two assumptions that was discarded in later applications of the tight-binding model, as described in Sec. 3.2.6.

With the two breathing parameters fixed, all other onsite terms, U, J, J_H, g_{JT}, and k_{JT}, were fitted to the density of states of $CaMnO_3$ and $PrMnO_3$ and to the obtained Jahn-Teller distortion of $PrMnO_3$ from the density-functional calculations, by considering a single-site (onsite) version of the tight-binding model, see Ref. [28] for details. Most importantly, this onsite model assumed perfect spin and orbital polarization when applied to the $x = 0$ ($PrMnO_3$) case, which might deviate from the true degree of spin and orbital polarization of $PrMnO_3$ in the corresponding density-functional calculation. We nonetheless stick to these onsite parameters determined in Ref. [28]. The hopping term was averaged over all oxygen bridges, dopings and magnetic structures investigated in Ref. [28], and site-dependent variations of the hopping term are not considered in this thesis. Finally, the antiferromagnetic superexchange J_{AF} was determined by considering the energy difference per site of a ferromagnetic and an antiferromagnetic configuration of the t_{2g} spins in pure $CaMnO_3$. This is the only parameter which needed an adjustment in the fitting process of Ref. [28]: The value obtained from the density-functional calculations, $J_{AF} = 3.326\,\text{meV}$ is much too low to correctly predict the various magnetic orders observed in the material, in particular the CE-type phase at half doping. Instead it was suggested to use an increased value of $J_{AF} = 14\,\text{meV}$, which we will also use in this thesis. It was mentioned in Ref. [28] that a similar stabilization of

the CE-type phase can be reached if the e_g hopping term is reduced slightly around this doping, and that the hopping amplitudes in fact varied strongly depending on whether a ferromagnetic or CE-type spin structure was assumed. The necessity to increase J_{AF} might thus come from the assumption of uniform hopping taken in the tight-binding model.

The final parameters used in this thesis are listed in Table 3.1. They correspond exactly to the parameters presented in Ref. [28], with the adjustment of k_{br} already included (see Sec. 3.2.6 for details).

t	0.585 eV
U	2.514 eV
J	0.692 eV
g_{JT}	2.113 eV/Å
g_{br}	2.988 eV/Å
k_{JT}	5.173 eV/Å^2
k_{br}	9.04 eV/Å^2
J_{Hund}	0.653 eV
J_{AF}	0.014 eV

Table 3.1: The tight-binding model parameters used in this thesis. With the exception of k_{br} (see Sec. 3.2.6), they correspond to the parameters obtained in Ref. [28] by comparing to hybrid density-functional calculations.

3.2.6 Alterations of the tight-binding model

Two alterations of the tight-binding model have been proposed following the parameter determination of Ref. [28], both of which were introduced in Ref. [126] and used in later applications of the tight-binding model for real-time dynamics after an optical excitation, see Refs. [32, 33]. The first concerns the breathing restoring force k_{br}, which in Ref. [28] was determined from the assumption that the occupation of the $d_{3z^2-r^2}$ orbital in an isolated octahedron should lead to a purely axial Jahn-Teller distortion (see also Sec. 3.2.5). An alternative, also followed in this thesis, is to adjust k_{br} in order to reproduce the ratio of Jahn-Teller to breating distortion $|Q_{JT}|/Q_1$ found in the $PrMnO_3$ density-functional calculation, see Ref. [126], leading to $k_{br} \approx 9.04$, slightly lower than the value used in Ref. [28] ($k_{br} = 10.346$).

The second, more substantial, change to the model includes the introduction of an additional degree of freedom: the average Mn-Mn distance, i.e., the cubic lattice constants T_i, $i \in \{x, y, z\}$. Until now, the Mn-Mn distance was fixed and the local Jahn-Teller and breathing distortions solely determined by the difference of the one-dimensional oxygen displacements along the various axes $\Delta_{i,R} = O_{i,R} - O_{i,R_{-i}}$. When using periodic boundary conditions (which will always be done here), the cooperative description of the oxygen positions leads to a sum rule within every row $\Omega^i_{j,k}$ of the three-dimensional crystal (where i denotes the orientation of the row and j and k the position in the perpendicular two-dimensional grid): $\sum_{R\in\Omega^i_{j,k}} \Delta_{i,R} = 0$, $\forall i, j, k$. This sum rule carries over to

the Jahn-Teller and breathing modes, which cannot have a uniform contribution on the various sites. In addition, global compression and expansions of the lattice parameters are forbidden, while experimental results show a strong variation of the c/a ratio (in the Pbnm unit cell) in the various doping regions, see Ref. [58] and Sec. 2.4.1.

While variations in the b/a ratio of the Pbnm orthorhombic unit cell are seen as well, see Ref. [58], these cannot be captured in the simplified cubic lattice structure of the tight-binding model. Hence, while the lattice constants are introduced as a new degree of freedom, we constrain the in-plane constants to be equal at all times $T_x = T_y$. Thus, a uniform Q_2-type distortion is still prohibited, while a uniform Q_3 distortion (modifying the c/a ratio), or a global breathing term (global expansion/compression) is allowed. The oxygen displacement $O_{i,R}$ is still taken as the deviation of the oxygen atom from the center position between both manganese neighbors, but these center positions move as the (global) Mn-Mn distance changes with the lattice constants T_i. The O-Mn-O bond distances relevant for determining the Jahn-Teller and breathing distortions can then be expressed as: $\Delta_{i,R} = O_{i,R} - O_{i,R-i} + T_i - \bar{d}$, where $\bar{d}$ is the equilibrium value of the lattice constants, which will be their actual value for the system without e_g electrons, at $x = 1$ ($CaMnO_3$). We mention that with the constraint $T_x = T_y$, we have effectively introduced only two new (scalar) degrees of freedom, which can be defined according to the Q_1 and Q_3 modes (see Sec. 2.2.2): $T_{Q_3} = \frac{2}{\sqrt{6}}(T_z - T_x)$ and $T_{Q_1} = \frac{1}{\sqrt{3}}\left(T_x + T_y + T_z\right)$. The T_{Q_1} mode couples only to the total number of electrons in the system and it can be minimized independently in a ground-state search to a fixed value of $T_{Q_1} = \frac{g_{br}}{k_{br}}(1-x) + \sqrt{3}\bar{d}$, where x is the hole doping, and thus $(1-x)$ the average number of e_g electrons per Mn-site.

While the equilibrium value of the lattice constants $\bar{d}$ has no influence on the rest of the system in the tight-binding model whatsoever, it is necessary to be determined if one wants to extract actual values for the lattice constants to compare to other simulations or experiments. Two possibilities are conceivable here: One could adjust $\bar{d}$ to the average Mn-Mn distances, which directly relate to the experimental lattice constants, yielding a value of $\bar{d}_{Mn-Mn} = 3.748$ Å for $CaMnO_3$, see Ref. [58]. Alternatively, one could adjust $\bar{d}$ to twice the Mn-O bond distances, which changes the meaning of the lattice constants to the average O-Mn-O bond distance. Obtained from density-functional calculations for $CaMnO_3$, see Ref. [28], this gives a value of $\bar{d}_{O-Mn-O} = 3.846$ Å. It is clear that the latter value is larger than the former, because the octahedra are tilted in the Pbnm space group, with the Mn-O-Mn bond angles varying between 149° and 160°, see Ref. [58]. Taking the Mn-Mn definition d_{Mn-Mn} and by setting $x = 0$ in the expression for the T_{Q_1} mode, we can get a direct theoretical estimate for the average cubic lattice constants of $PrMnO_3$, which gives $\bar{T} = \frac{1}{\sqrt{3}}T_{Q_1} = 3.939$ Å, which is very close to the experimental average cubic lattice constant of $\frac{1}{3}\left(a/\sqrt{2} + b/\sqrt{2} + c/2\right) = 3.933$ Å, see Ref. [135].

3.3 Ground-state search

With all terms and parameters of the potential energy functional of the tight binding model (Eq. (3.2)) clarified, one can now try to find its ground-state (zero-temperature) configurations. We mention that if one would seek a quantum mechanical description for the nuclei, then one would have to add their kinetic energy term as well, but this is not necessary to find their classical minimum (at which their kinetic energy is zero). With analytic solutions to the full tight-binding model being not available, one straightforward numerical approach is the use of Monte Carlo simulations. Originally used for a numerical evaluation of an integral by a random sampling of the integration points, they have been successfully applied to partition functions and observable averages in classical and quantum systems, see Ref. [136], and Refs. [137, 138] and references therein for more details. Monte Carlo approaches have been applied with some success to the manganite tight-binding model, however, mostly in limiting cases where either the Coulomb interaction was turned off (reducing the model to a one-electron problem and avoiding the so-called sign-problem of quantum Monte Carlo simulations), or without electron-phonon interactions in a mostly Coulombic system with small system sizes, see Ref. [26] for an overview of these results. This will not be the path followed in this thesis, where we instead turn to (real-time) dynamical procedures of finding the ground state. This is done in the spirit of the Car-Parrinello approach, introduced by Car and Parrinello in their seminal work in Ref. [129].

3.3.1 Minimization constraints

We seek to find a minimum of the potential energy $E_{pot}(\psi, S, O, T)$ (now including the lattice constants T), by varying the underlying degrees of freedom $|\psi_n\rangle$, $\vec{S}_R$, $O_{i,R}$ and T_i under a set of constraints. In a general many-particle description for the e_g electron states, one would search for the many-particle ground state $|\Psi_0(O, S)\rangle$ and for the nuclear and spin configuration O_0 and S_0 that produce the lowest many-particle eigenenergy $E_0(O_0, S_0)$ (a mixed quantum-classical minimization). In the Hartree-Fock approach, the ground-state wave function is fixed to a single-Slater determinant composed of the (N) one-particle wave functions $|\psi_n\rangle$, defined in Eq. (3.1). In a minimization procedure directly modifying these one-particle wave functions, we thus have to enforce the constraint of orthonormality between these wave functions. Another constraint for freely optimized spins is to fix their lengths at $\frac{3\hbar}{2}$. The constraints of keeping the oxygen displacements along the Mn-Mn straight bond lines, and for keeping the x-y-plane dynamical lattice constants equal ($T_x = T_y$) do not have to be added, because we can remove the unnecessary degrees of freedom completely. In the formalism of Lagrange multipliers, the orthonormality constraint for the one-particle wave functions and the length constraint for the spins can be written as:

$$\mathcal{L}_{constr} = \sum_{n,m} \Lambda_{m,n} \left(\langle \psi_n | \psi_m \rangle - \delta_{n,m} \right) + \sum_R \lambda_R \left(|\vec{S}_R| - \left(\frac{3\hbar}{2} \right) \right) . \tag{3.19}$$

3.3.2 Car-Parrinello approach

The Car-Parrinello approach outlined in Ref. [129] was proposed as a unified perspective on molecular dynamics and density-functional theory (or general *ab initio* electronic structure methods), and hence directly aimed at mixed quantum-classical systems as our tight-binding model. As outlined in Ref. [129], it can be used both for determining ground-state properties and to perform *ab initio* finite-temperature molecular dynamics, and in fact both applications will be used in this thesis to determine the zero-temperature phases and finite-temperature phase transitions in the tight-binding model.

For finding ground states, the method can also be described as a dynamical simulated annealing method, see Ref. [129]. The fundamental idea is to describe both quantum and classical degrees of freedom on a similar level, by introducing physical or fictitious kinetic energy terms for all degrees of freedom in the system, and then dynamically evolving all of them simultaneously according to Euler-Lagrange equations under some constraints.

This is done by defining a fictitious Lagrangian composed of the kinetic energy terms $\mathcal{L}_{kin}$, the potential energy expression to be minimized $\mathcal{L}_{pot}$, and the added constraints $\mathcal{L}_{constr}$:

$$\mathcal{L} = \mathcal{L}_{kin} - \mathcal{L}_{pot} - \mathcal{L}_{constr}. \tag{3.20}$$

For our tight-binding model, the potential energy expression is given in Eq. (3.2) ($\mathcal{L}_{pot} = E_{pot}$), and the constraints were already outlined in Eq. (3.19). The new kinetic energy expression includes not only the kinetic energy of the nuclei, but also the fictitious terms for the one-particle wave functions and the t_{2g} spins. With the lattice constants added as new degrees of freedom, a kinetic energy term is included for them as well:

$$\mathcal{L}_{kin} = \sum_{\sigma,\alpha,R,n} f_n M_\psi |\dot{\psi}_{\sigma,\alpha,R,n}|^2 + \frac{1}{2}\sum_{i,R} M_O \dot{O}_{i,R}^2 + \frac{1}{2}\sum_{R} M_S \dot{\vec{S}}_R^{\,2} + \frac{1}{2}\sum_{i\in\{x,z\}} M_T \dot{T}_i^2. \tag{3.21}$$

For a ground-state search all masses (M_Ψ, M_O, M_S and M_T) can be set to arbitrary values, as all these kinetic energy terms should vanish once the minimal energy configuration is reached. Writing down the Euler-Lagrange equation for the various degrees of freedom, one arrives at:

$$f_n M_\psi \ddot{\psi}_{\sigma,\alpha,R,n} = -\frac{\partial E_{pot}}{\partial \psi^*_{\sigma,\alpha,R,n}} - \sum_m \Lambda_{m,n}\psi_{\sigma,\alpha,R,m}, \tag{3.22}$$

$$M_O \ddot{O}_{i,R} = -\frac{\partial E_{pot}}{\partial O_{i,R}}, \tag{3.23}$$

$$M_S \ddot{\vec{S}}_{i,R} = -\frac{\partial E_{pot}}{\partial \vec{S}_{i,R}} - \lambda_R \frac{\vec{S}_{i,R}}{|\vec{S}_R|}, \tag{3.24}$$

$$M_T \ddot{T}_i = -\frac{\partial E_{pot}}{\partial T_i}. \tag{3.25}$$

The derivatives of the potential energy function with respect to quantities not directly appearing in the various terms presented in Sec. 3.2 are obtained via the chain rule from the derived quantities, e.g., $\frac{\partial E_{pot}}{\partial O_{i,R}} = \sum_{a,R'} \frac{\partial E_{pot}}{\partial Q_{a,R'}} \frac{\partial Q_{a,R'}}{\partial O_{i,R}}$. The force acting on the wave functions can also be expressed in terms of the Hartree-Fock Hamiltonian $\hat{H}_{HF}$ (see Eq. (3.4)) using $\frac{\partial E_{pot}}{\partial \psi^*_{\sigma,\alpha,R,n}} = f_n \langle \chi_{\sigma,\alpha,R} | \hat{H}_{HF} | \psi_n \rangle$.

It is evident that all equations of motion (3.22)-(3.25) are now of a (coupled) Newtonian form, and they can be solved, for example, with a Verlet algorithm, see Ref. [139]. The constraints for the one-particle wave functions and the spins need to be enforced during this integration. Thereby one obtains fictitious, coupled, and energy conserving dynamics of the various degrees of freedom. For the ground-state search in the form of a dynamical simulated annealing, the fictitious kinetic energy needs to be damped over time. This can be done in the form of friction terms for each degree of freedom X: $-M_X \dot{X} \alpha_X$, added to the right-hand-side of the Euler-Lagrange equations (3.22)-(3.25). The friction parameters α_X can be tuned for each degree of freedom to control the speed of annealing.

For the Verlet integration, both the first and second derivative of the degrees of freedom are expanded symmetrically up to second order around the current time step t. One time step $t \rightarrow t + \Delta t$, with the added friction term, but without constraints, for a degree of freedom X can then be written as (see, e.g., Ref. [140]):

$$X(t + \Delta t) = X(t) \frac{2}{1 + a_X} - X(t - \Delta t) \frac{1 - a_X}{1 + a_X} + F_X(t) \frac{\Delta t^2}{M_X} \frac{1}{1 + a_X}, \qquad (3.26)$$

where F_X is the force acting on the degree of freedom X (determined from the corresponding derivative of the potential energy), and $a_X := \frac{\alpha_X \Delta t}{2}$.

The additional terms for the constraints are added afterward in each time step, and the Lagrange parameters are determined such that after this correction the degrees of freedom fulfill the constraint exactly at the beginning of the next time step. This procedure was first suggested in Ref. [141]. For the wave functions, this leads to a quadratic matrix equation that can be solved iteratively, see, e.g., Refs. [141–143]. For additional details on Verlet integration of Car-Parrinello dynamics with constraints, we refer to Ref. [144].

With an appropriately chosen damping of the various kinetic energy terms, the system ends up in a local minimum of the potential energy functional. At this point all kinetic energy terms in Eq. (3.21) vanish and the resulting potential energy is independent of the chosen mass and friction parameters. As with all annealing methods, it is possible that the system relaxes toward a local minimum (a metastable state), instead of the global energy minimum. While the convergence to the global minimum can be improved by using a smaller damping and thus giving the various degrees of freedom enough kinetic energy to overcome local minima, one cannot rule out the possibility of obtaining a metastable state.

This is especially true in our tight-binding model, in which the different competing structures have completely different spin and orbital order. Even within a pure phase of long-range order, several domains separated by domain

walls can emerge if the system size is chosen large enough. A detailed analysis of the obtained short- to intermediate-range order, combined with starting simulations from various initial states, is thus necessary to reliably identify the true ground states of the model. More details on these optimization strategies are given in Sec. 3.3.3, as well as in Ref. [126]. We found that the convergence behavior of the model is barely influenced by the exact choice of the fictitious masses or friction parameters, as long as the latter are chosen small enough and not in an overdamped regime. One option for the masses is to adjust them to have similar natural frequencies for all degrees of freedom, and then to take the friction terms in the slightly underdamped regime (estimated from the critical damping of a harmonic oscillator of $a = \omega_0 \Delta t$, see Ref. [140], where ω_0 is the oscillator frequency), see also Ref. [126] for such an example parameter set.

3.3.3 Numerical details

Simulation setups for the ground-state search

One first important decision is the system size to be simulated (with periodic boundary conditions). While some of the proposed literature ground-state structures (see Fig. 2.6) fit into a $2 \times 2 \times 2$ unit cell (e.g., $PrMnO_3$ at $x = 0$, given here in cubic lattice dimensions of sites $N_x \times N_y \times N_z$), others (e.g., the CE-type structure at $x = 0.5$) need a larger $4 \times 4 \times 2$ cubic unit cell. Even larger system sizes are needed for testing the Wigner or bi-stripe ground states that were proposed at dopings close to $x = 2/3$ for $La_{1-x}Ca_xMnO_3$, or for simulating a phase separation. Increasing the system size thus has the advantage that one does not easily rule out more complicated ordered structures, which could not fit into smaller unit cells. Conversely, it becomes increasingly difficult to confirm the ground state in unbiased simulations in larger systems.

The gold standard for unbiased simulations is to start from a completely random setup of one-particle wave functions, spins and nuclei (and possibly lattice constants, although in practice we initialized them at $T_x = T_z$), and independently of the initial state to obtain the same lowest energy structure. The random setup includes selecting the spins in random directions and initializing the one-particle wave functions with random values with a subsequent orthonormalization, while for the nuclei both starting at their equilibrium values and with random uniform distortions in the range of ± 0.1 Å are used as strategies. The unbiased confirmation of the same ground state was in many cases possible in a $2 \times 2 \times 2$ system, which, however, excludes many ordered structures. In larger systems, different ordered sub-domains, smaller defects (like flipped spins) or frustrated configurations can emerge. In most cases these metastable states have the same short-range order as the true ground-state configuration. In regions of competing phases, however, several types of short-range order can be found in sometimes intertwined arrangements. To determine the true ground state as predicted from the tight-binding model, it can then be necessary to construct the long-range ordered structures of all found variants and compare their energies.

We find that in most cases once the spin configuration has been determined,

the convergence for the remaining charge and orbital order is much improved. Hence, it proves valuable to start a set of calculations from various different initial spin configurations. The spins are still allowed to adjust dynamically during the simulation, but there are some simulations starting close to a ferromagnetic or to different types of antiferromagnetic arrangements. We are aware that this introduces some bias into the ground-state search, as a very complicated spin pattern might have been overlooked. Such a slightly biased search is carried out for the A-, B-, C-, CE-, E- and G-type spin structures in a $4 \times 4 \times 4$ system. With the exception of the E-type AFM spin order, all other spin structures are already included in the current experimental understanding of the phase diagram, see Fig. 2.6. We refer to Refs. [27, 28] for sketches of the remaining E-type AFM order. The unbiased random setup and the slightly biased spin-ordered setup are complemented by testing out various structures proposed in the literature, see the overview in Sec. 2.4.1, where we again allow for a subsequent relaxation after the setup. It is reassuring for the convergence properties of our model that the literature orders did either correspond to the ones obtained by our independent search, or were higher in energy. For the ground-state results presented in this thesis, the lowest energy structures could always be obtained from the random or spin-ordered setups; combined in the cases of the metastable states analyzed later in Sec. 4.1.4 with a construction of long-range ordered variants of the observed short-range order.

We mention that the importance of the spin structure for the model's convergence immediately suggests a (classical) Monte Carlo simulation of the spin subsystem, where the electronic and nuclear subsystems are adjusted to each new spin configuration before performing the next Monte Carlo step. An application to large system sizes requires well adapted Monte Carlo steps, beyond simple spin flips and allowing for non-collinear spins, which is left for future investigations of the tight-binding model.

k-points

The tight-binding simulations presented in this thesis are always carried out with periodic boundary conditions. The system sizes mentioned in the last paragraphs hence rather refer to simulation supercells, rather than true manganite system sizes, and determine the size of the ordered structures of spins and phonons that can be described. Taking the spin and phonon configuration as a periodically repeating background potential for the electronic wave functions, one can apply Bloch's theorem and take the electron wave vector $\vec{k}$ as a valid quantum number to quantify the one-particle states as $\psi_{n,k}$ (where k is the index corresponding to the wave vector $\vec{k}$). These states now each carry a $\vec{k}$-dependent Bloch phase $e^{i\vec{k}\vec{R}}$, where $\vec{R}$ defines the three-dimensional position vector of the sites R. With a suitable redefinition of the wave functions incorporating the Bloch phase projected on the first supercell, see, e.g., Ref. [56], the Bloch phase enters only in the form of an additional phase $e^{i\vec{k}\vec{t}}$ in the hopping terms across the supercell boundaries, where $\vec{t}$ defines the supercell lattice constants in the three cubic directions. We can now take a discrete set of k-points in the first Brillouin zone to allow for additional freedom in the

inter-supercell-phase of the wave functions. In our cubic crystal, the number of k-points N_i^k in any direction i determines how many times larger the effective electron-supercell is compared to the simulation supercell for the spins and phonons, and thus this number should be chosen larger if the simulation supercell is small in the particular direction. The potential energy is still given for the simulation supercell, and one can incorporate the different k-points by dividing the occupation number $f_{n,k}$ (now depending on k) by the total number of k-points $N^k = \sum_i N_i^k$ in all above equations, as well as adding a sum over the k-points in the respective terms in the Lagrangian.

Increasing the number of k-points is computationally much less demanding than increasing the supercell size: the number of spin and phonon degrees of freedom stays constant, which reduces the problem of metastable structures found during the optimization. In addition, the costly orthonormalization of the one-particle wave functions does only have to be carried out within the same k-point. The computational cost of this step, similar to a normal Gram-Schmidt orthogonalization, scales with the second power of the number of vectors to be orthonormalized (here the number of considered occupied and empty one-particle wave functions), and with the first power of the dimension of the one-particle basis, which, for a fixed doping and neglecting empty states, gives a total scaling with the third power of the system size. In contrast, the computational cost scales only linearly with the number of k-points.

Differently from the problem of metastable states mentioned previously, the convergence with respect to the number of used k-points can be controlled easily, although it will depend on the doping and structures of the ground-state phases. An exemplary k-point convergence study for various fixed t_{2g} spin backgrounds at eight different hole dopings x is shown in Fig. 3.2. It shows the convergence of the ground-state energy for different k-grids $\boldsymbol{N^k} = N_i^k \times N_i^k \times N_i^k$ for the different spin structures, with the energy difference to the largest tested k-grid ($N_i^k = 6$) indicated on the y-axis. To ensure that all simulations actually refer to the energy of the same ordered structure, the oxygen positions and lattice constants have been fixed to the ones from the $N_i^k = 6$ calculation. After convergence for the fixed nuclear structure, the oxygen positions and lattice constants were set unrestrained and convergence continued. However, the ground-state energy did not change on scales visibly in Fig. 3.2 during this second convergence step, indicating that the $N_i^k = 6$ ground-state structure is at least metastable also for all other tested number of k-points. Using a single k-point can lead to larger variations and these values are omitted here (in the simulations of this thesis we will never use $N_i^k = 1$). For all larger k-grids, the energy deviations are in the range of a few meV, and below 1 meV for $N_i^k \geq 4$ for the tested spin structures and dopings. In most cases we rely on a k-grid of at least $\boldsymbol{N^k} = 4 \times 4 \times 4$ for an average $4 \times 4 \times 4$ system (and correspondingly larger or smaller if the system's dimensions change), but for costly finite-temperature simulations a smaller k-grid of $\boldsymbol{N^k} = 2 \times 2 \times 2$ will be used (although confirmed at least partially with larger k-grid simulations). The results from Fig. 3.2 indicate that the convergence might be better in the low-doped region investigated in this thesis.

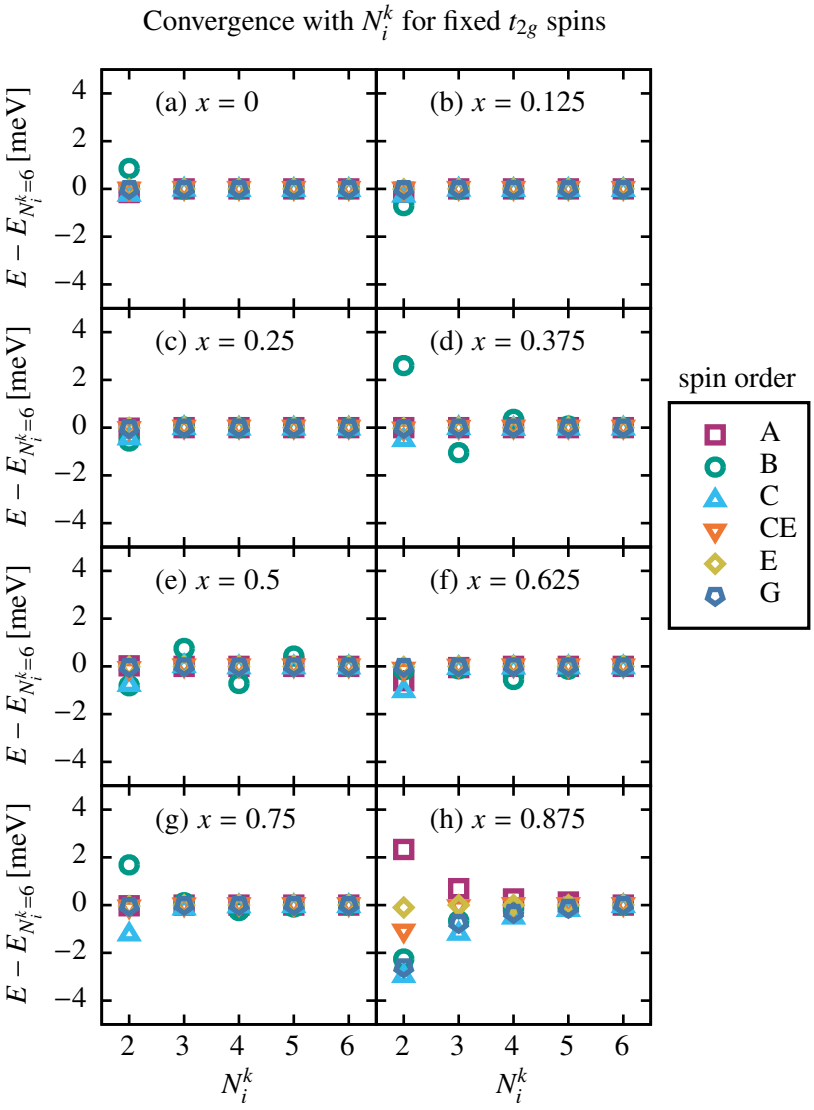

Figure 3.2: Convergence of the tight-binding ground-state energy with the number N_i^k of k-points per direction i, i.e., for a k-grid of $\boldsymbol{N^k} = N_i^k \times N_i^k \times N_i^k$ points, for fixed spin structures of A-, B-, C-, CE-, E- and G-type (see Fig. 2.6 for visualizations of most of these spin orders and, e.g., Ref. [28] for a sketch of the remaining E-type AFM order). The ground-state energy of the $N_i^k = 6$ system has been determined first. Afterward, simulations starting with the different N_i^k are started with the oxygen positions and lattice constants fixed to the configuration of the predetermined $\boldsymbol{N^k} = 6 \times 6 \times 6$ system, in order to analyze the effect of the k-grid on the energy convergence only and to not have the possibility of encountering metastable states affect the results. The difference on the resulting ground-state energies $E(N_i^k)$ from the $(N_i^k = 6)$-simulation are shown.

3.4 Finite-temperature calculations

3.4.1 Car-Parrinello molecular dynamics

We mentioned in Sec. 3.3.2 that the Car-Parrinello method was introduced not just for describing a dynamical simulated annealing for a ground-state search, but also for describing *ab initio* (finite-temperature) molecular dynamics, see Ref. [129]. In going beyond the minimization procedure outlined in Sec. 3.3.2, the Car-Parrinello ansatz transitions from a numerical optimization technique to an actual approximation for the combined quantum-classical dynamics: The Car-Parrinello molecular dynamics (CP-MD).

Let us give a short remark on notation: Molecular dynamics (MD) refers in general to the numerical solution for the time-evolution of a set of classical degrees of freedom, which are typically atoms/phonons, under Newtonian forces, see Ref. [137]. If these forces are obtained from pre-determined (parametrized) potentials, then the method is also called classical molecular dynamics, see Ref. [144]. If instead the forces are determined from on-the-fly electronic structure methods, such as the popular density-functional or Hartree-Fock calculations, then the method is called *ab initio* molecular dynamics, see Ref. [144], which, however, still describes the nuclei as classical particles. Examples for *ab initio* molecular dynamics are Car-Parrinello, Born-Oppenheimer, or Ehrenfest molecular dynamics, see Ref. [144].

In order to use the Car-Parrinello approach for a molecular dynamics simulation, its equations of motion need to capture the real-time dynamics of the nuclear degrees of freedom. This is done by setting the atomic mass M_O in the nuclear equation of motion (3.23) to its physical value (and similarly the lattice-constant mass (M_T, see Eq. (3.25)) if one seeks a dynamical description of the lattice expansions/contractions), and by omitting the friction terms. The electronic and spin masses (M_Ψ and M_S, see Eqs. (3.22) and (3.24)) are still fictitious and should be chosen such that there is little energy transfer between these degrees of freedom (in the remainder of this section collectively termed the electrons) with the "physical" nuclear subsystem, see also Ref. [144]. After preparing the electrons in their ground state for the initial nuclear configuration, they can approximately adiabatically follow the nuclear dynamics. Since the nuclear forces are obtained on-the-fly from the time-evolved electronic degrees of freedom, this is an example for *ab initio* molecular dynamics (see the previous remark on notation). While CP-MD is not restricted to an adiabatic electron description, it is in most cases used in this way and can be understood as an approximation to the true Born-Oppenheimer molecular dynamics (BO-MD), see Ref. [144].

In BO-MD, the electrons in each nuclear propagation time step are set exactly to their instantaneous ground state at that nuclear configuration, building a position-dependent potential energy surface, called Born-Oppenheimer surface, for the nuclei. This completely separates the electronic and nuclear time scales according to the Born-Oppenheimer (BO) approximation. We note that the BO approximation is independent of the classical approximation for the nuclei, and is defined and analyzed in a more general context in Ch. 5. BO-

MD simulations require to obtain the electronic ground state at every nuclear configuration encountered along the trajectory, which can be costly for large systems. In contrast, the electrons in CP-MD are included dynamically in the time-evolution, and the costly BO ground-state search at every nuclear time step can be avoided. The introduction of CP-MD led to a breakthrough of *ab initio* molecular dynamics, with many applications in solid-state theory and quantum chemistry, see Ref. [144], and this method will also be used to investigate the orbital-order phase transition in low-doped $Pr_{1-x}Ca_xMnO_3$, see Sec. 4.2. For such a description, the molecular dynamics needs to be applied to a canonical ensemble at finite temperature.

3.4.2 Finite atom temperature: The Nosé-Hoover thermostat

Several approaches exist that extend molecular dynamics to describe a constant temperature ensemble, see Ref. [137]. One of the most common forms is the introduction of a Nosé-Hoover thermostat, see Refs. [145, 146], which is also used in this thesis. The fundamental idea is to introduce an additional degree of freedom, acting like a constant temperature heat bath, which couples to the nuclei and constantly shuffles energy into and out of the system. In the original formulation, see Ref. [145], which involves a re-scaling of time, an extended system containing both the real system and the heat bath is defined, whose microcanonical distribution function equals the canonical distribution function of the real system. Under the assumption of an ergodic movement of a nuclear trajectory in this extended system, one can thus recover the canonical ensemble of the real system. Here, we follow the reformulation proposed by Hoover, see Ref. [146], which avoids a re-scaling of time and results in simpler equations, while leading to the same canonical ensemble for the real system (and is still relying on ergodicity of the trajectory movement). We also refer to the excellent review [147]. Hoover's reformulation introduces a time-dependent friction value for the nuclear degrees of freedom, which is itself given by a differential equation depending on the difference of the current nuclear kinetic energy from the finite-temperature expectation value:

$$M_O \ddot{O}_{i,R} = -\frac{\partial E_{pot}}{\partial O_{i,R}} - M_O O_{i,R} \dot{\zeta}, \ \forall i, R \tag{3.27}$$

$$M_{TS} \ddot{\zeta} = \left(\sum_{i,R} M_O \dot{O}_{i,R}^2 - g k_B T \right). \tag{3.28}$$

Here, g is the number of free nuclear degrees of freedom, k_B is the Boltzmann constant and T is the temperature of the thermostat. M_{TS} is an effective mass for the single thermostat variable $\dot{\zeta}$. The variable $\dot{\zeta}$ acts as a global friction parameter for the nuclei and can take positive and negative values. It oscillates with a thermostat oscillation period of $T_{TS} = 2\pi\sqrt{M_{TS}/2gk_BT}$. The variable ζ, whose derivative is used as the friction variable in the above equations, can be integrated with a normal Verlet algorithm together with all other degrees of freedom in the Car-Parrinello propagation algorithm, see Sec. 3.3.2.

After the setup of the initial positions and momenta, a Nosé-Hoover thermostat calculation is completely deterministic. It is known that the standard Nosé-Hoover thermostat is rather stiff and does not fulfill ergodicity for very small systems, such as the important case of an isolated harmonic oscillator, see Ref. [146]. An extension was proposed in the form of Nosé-Hoover chains, in which the thermostat variable is thermostatted itself, which can be done recursively, see Ref. [148]. For the large systems studied in the tight-binding model, we will stay with the original single-variable Nosé-Hoover thermostat defined by the above equations.

Applying the atom thermostat to a CP-MD simulation can lead to a coupled system of hot nuclei and "cold" electrons (where their effective temperature refers to their fictitious kinetic energy terms). In particular, when the electronic energy gaps become small, or the system even metallic, the assumption of a negligible energy flow between the electronic and nuclear subsystem might not hold. In such cases (and also in general to ensure that the electrons stay close to their ground state) several variants have been proposed to keep the electronic subsystem at a low effective temperature, such as using a second independent thermostat for the electronic degrees of freedom, or to directly switch to BO-MD, see Ref. [144] for an overview. In this thesis, we will ensure the cooling of the electronic and spin subsystems by applying a constant small friction to them, similar as in the optimization procedure, see Sec. 3.3.2. It needs to be ensured that the finite-temperature results do not depend on the choice of this friction parameter (within reasonable bounds).

Ensemble averages of an observable A are calculated under the ergodic hypothesis as the mean value of the sampled values A_S taken during the thermostat calculation: $\langle A \rangle = \frac{1}{N_S} \sum_s A_s$ (where N_S is the number of sampling points). Estimating the standard deviation of the ensemble average $\sigma_{\langle A \rangle}$ is non-trivial, as subsequent sampling points are likely to be correlated. Here, we resort to a blocking method, see Refs. [149, 150], where the sampling points are grouped into a number of N_B blocks B_i, each including L sampling points, and the mean value over each block $\langle A \rangle_{B_i}$ is treated as a new effective sampling point. The block-estimate for the standard deviation of the total mean is then given via $\sigma_L^2 = \frac{1}{N_B(N_B-1)} \sum_{i=1}^{N_B} \left(\langle A \rangle_{B_i} - \langle A \rangle \right)^2$. For sufficiently large blocks, the mean values of the different blocks should become uncorrelated and the block-estimate independent of further increments of the block size L. The block-estimate for such large L should then approach the true standard deviation of the ensemble averaged value. However, if the blocks sizes become comparable to the sampling size, the block-estimate σ_L itself will have a large error. Reaching a plateau in σ_L upon increasing L and before the errors are too large is thus an indication of a sufficient simulation time and the plateau-value a good estimate for the standard deviation of the ensemble average, see Refs. [149, 150] for details.

We observe in general that this blocking approach converges in most cases for temperatures away from the phase transition that will be investigated later in Sec. 4.2. One such example is given for a CP-MD run at 600 K, away from any phase transition, in Fig. 3.3(a). The figure shows block-estimates for the standard deviation of the ensemble average of the order parameter divided

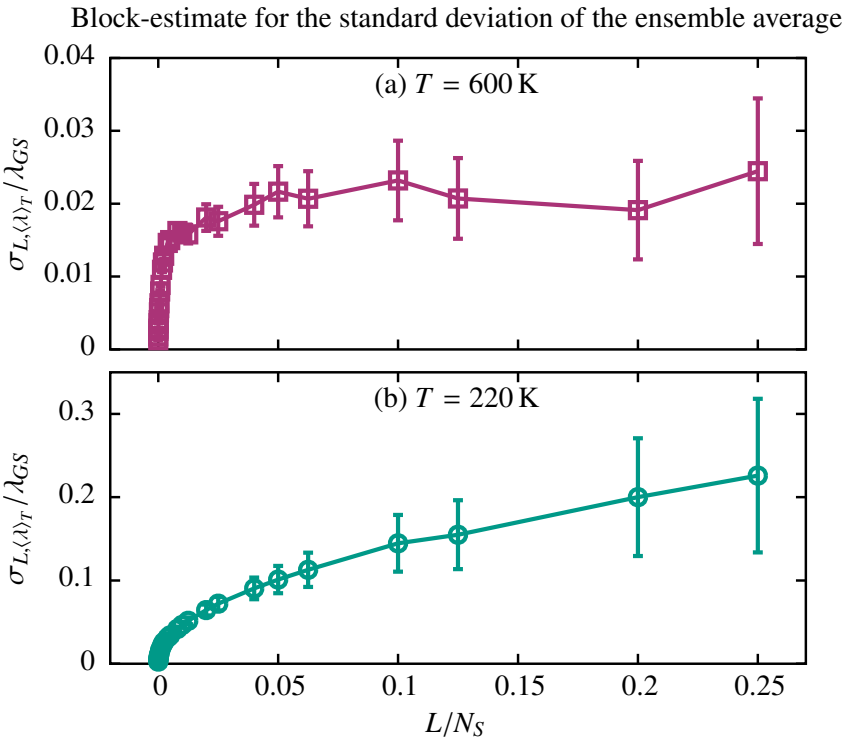

Figure 3.3: Error estimate of the ensemble average of the order parameter (Eq. (4.6)) divided by the ground-state value of that order parameter, obtained by the blocking method for a CP-MD run at (a) 600 K and (b) 220 K. These runs are selected from the heating thermostat calculations presented later in Fig. 4.6. They use a $4 \times 4 \times 4$ simulation cell with $N_i^k = 2$ k-points in every direction at doping $x = \frac{6}{64}$. Starting from the ground state at that doping (see Sec. 4.2) the system is equilibrated at the target temperature for 2.42 ps and thermal averaging is done for 12.1 ps with sampling points obtained every 100 time steps of each $\Delta t = 2.42$ as. See Table 4.2 for the thermostat parameters and the results section 4.2 for further discussions on the simulation procedure and the selected order parameter. The connecting lines are guides for the eye.

by the order parameter of the ground-state phase. This is done for any integer division of the number of sampling points up to $L = N_S/4$. The order parameter corresponds to the in-plane checkerboard Jahn-Teller correlation function and is defined in Eq. (4.6), discussed in more detail when presenting the results of the tight-binding model in Ch. 4. Increasing the block sizes beyond $L = 0.05 \cdot N_S$ changes the error estimate only within the growing uncertainty of the estimate itself. This is considered a well converged error estimate.

We note that when cooling the system to low temperatures, it can end up for a long time in a metastable state. In this case, the finite simulation time might be too short to even capture that the error estimate is not converged. One should thus not over-interpret these values. The situation becomes worse close to the phase transition, for which one example is shown in Fig. 3.3(b). Here, the error estimate still grows with the block size, indicating that longer total simulation times are needed for an accurate error estimate (and an accurate

thermal averaging). In this case it is advised to take the maximum error estimate obtained for any block-division and consider this as a lower bound to the error of the ensemble average, see Refs. [149, 150]. We will always follow this procedure to take the maximum error estimate when presenting the results in Ch. 4.

Both BO-MD and approximately CP-MD rely on the adiabatic approximation for the fast degrees of freedom, which for the tight-binding model are the e_g electrons and the t_{2g} spins. We note that one could still obtain the exact mixed quantum-classical ensemble averages if one uses the thermostatted CP-MD (or BO-MD) as an importance sampling for the true ensemble and corrects in the calculation of observables for the adiabatic path taken, see, e.g., Ref. [151]. For the electrons this requires the calculation of the excited electronic eigenstates at every sampled nuclear configuration, which can be obtained, for example, from linear-response time-dependent Hartree-Fock or density-function theory, see, e.g., the overviews in Refs. [152, 153]. When a quantum mechanical treatment of the spins is too costly, one could apply a thermostat to the classical spin system as well, which can be done by using extensions of the Nosé-Hoover thermostat, see Refs. [147, 154, 155]. Neither of these extensions or corrections is used in this thesis, in which we concentrate on the breakdown of the long-range orbital-order (which is strongly coupled to the long-range Jahn-Teller order of the oxygen atoms). An independent melting of the spin-order at lower temperatures, as expected from the experimental phase diagram, see Fig. 2.5, thus cannot be described with this approach. Since we cannot exclude that the adiabatic approximation for the fast degrees of freedom influences the melting temperature of the orbital-order as well, further complementary studies are needed in the future.

For non-equilibrium setups definitely including excited electronic states, such as the relaxation after a photoexcitation, one has to question the validity of the adiabatic approximation. Methods of including excited electronic states in a dynamical simulation with classical nuclei (quantum-classical trajectory-based methods) are described in detail in Ch. 5, and benchmarked in an electron-phonon coupled system (the Holstein model) in Ch. 6. Combining these methods with the CP-MD approach in the manganite tight-binding model is an intriguing future prospect, but beyond the scope of this thesis. We note that a combination of one of the quantum-classical trajectory methods, the Ehrenfest dynamics method, has been applied to the manganite tight-binding model without a thermostat in Refs. [32, 33]. However, it is known that Ehrenfest dynamics combined with a nuclear thermostat cannot correctly reproduce the mixed quantum-classical canonical ensemble (in general), see, e.g., Ref. [151], and we stay for now with the well-established adiabatic molecular dynamics approaches described above.

4 Ground states and orbital-order phase transition in low-doped $Pr_{1-x}Ca_xMnO_3$, obtained with the manganite tight-binding model

The tight-binding model presented in the last chapter, with the parameter determination based on density-functional calculations, presents an important step toward independent theoretical predictions about the various phases emerging in the $Pr_{1-x}Ca_xMnO_3$ phase diagram. With a fixed parameter set, see Table 3.1, and without further adjustments to the individual doping regions, it is able to correctly recover most of the ordering principles of the experimentally known phases and can provide new insight in regions of diverging experimental explanations, see Refs. [56, 126].

A systematic study of the ground-state predictions of the model was started by Sangeeta Rajpurohit during her doctoral studies, and later joined by myself with an independent code implementation. Ground-state results for selected phases have been presented already in the Master's thesis of the author of this thesis, although without the alterations of the model presented in Sec. 3.2.6, see Ref. [56]. An elaborate evaluation of the complete ground-state phase diagram, including various metastable states between the pure phases, was presented in the PhD thesis of S. Rajpurohit in Ref. [126]. A joint publication combining the analysis of all ground-state results might follow in the future. We will not repeat the results for the whole ground-state phase diagram in this thesis, for which we refer to Ref. [126], but instead focus completely on the low doped region $0 \leq x \leq 0.25$, which we analyze in more detail. This is necessary to understand the starting points for the finite-temperature orbital-order phase transitions investigated at $x = 0$ and $x = 0.1$, which is at the heart of this chapter.

Let us nonetheless shortly summarize, we refer to Ref. [126] for details, that the model reproduces all magnetic phases presented in the experimental phase diagram, see Fig. 2.6. This includes the A-type (AFM) phase at zero doping and the B-type (FM) phase at quarter doping (which are both outlined in more detail in the following), the striped CE-type (AFM) phase at half doping, the C-type (AFM) phase at three-quarter doping (which, according to the model, is energetically slightly preferred over the in-plane zig-zag spin structures that have also been suggested, see Sec. 2.4.1), and (trivially) the G-type (AFM) phase at $x = 1$. In addition, the Wigner-crystal phase at $x = 2/3$ is predicted at slightly lower energies than the bi-stripe phase (by a few meV per site), and obtained as an additional pure phase.

All other obtained and tested structures are energetically higher than the predicted phase separated mixtures between these pure phases, and might

be designated as metastable states. If the energy difference is small, we can expect to encounter these structures regularly beyond absolute zero temperature. Furthermore, a phase separation of differently doped phases will lead to a long-range Coulomb interaction (in the real material, but not included in the model). Hence, for metastable states very close in energy to the phase separation, we cannot definitely conclude on the ground-state structure of the material.

Besides the spin structures, the model predicts orbital and charge ordering in the $x \geq 0.5$ phases in line with experimental measurements, see Ref. [126]. At $x = 0.25$, where the experimental results for the orbital or charge order are not yet conclusive (see Sec. 2.4.1), the model proposes a new kind of ordering, not excluded by previous experimental results, also discussed in the following in Sec. 4.1.3. For $x = 0$, the in-plane orbital order is reproduced, but the Jahn-Teller angles differ from the experimental and *ab initio*-results (discussed in Sec. 4.1.2). This leads to qualitative deviations of the lattice constant ratio c/a in the low-doped region from experimental results, while this ratio accurately matches the experimental values for all dopings $x > 0.25$, see Ref. [126]. In summary, the existing results with the tight-binding model have shown its capability of describing the various ground-state phases. The largest observed deviations from confirmed experimental structures are at $x = 0$ in the c/a-ratio (and correspondingly in the Jahn-Teller angles), which is also shown in the following.

4.1 Zero-temperature phases $0 \leq x \leq 0.25$

Let us now investigate in more detail the doping region $0 \leq x \leq 0.25$. This is the electron-rich side of the phase diagram with one e_g electron per site for pure $PrMnO_3$ at $x = 0$, and on average 0.75 e_g electrons per site at quarter doping.

4.1.1 Overview

We start with an overview of the energy-over-doping diagram of the low lying structures. At $x = 0$, an A-type spin structure has the lowest energy, see Sec. 4.1.2, while at $x = 0.25$, a B-type ferromagnet emerges, see Sec. 4.1.3. All other tested and obtained spin structures are higher in energy (see Sec. 3.3.3 for details on the optimization procedures) and we did not observe any canted spin structure, or small-scale phase separation, being close in energy. Fig. 4.1 shows the energy per site for various dopings for fixed B-type and A-type spin structures, obtained in a $4 \times 4 \times 4$ lattice with $\boldsymbol{N^k} = 6 \times 6 \times 6$. In between of these pure phases, we could not find any structure with an energy lower than the phase-separation energy of $E(x) = (E_B x + E_A(0.25 - x))/0.25$, where E_A and E_B are the energies per site of the $x = 0$ and $x = 0.25$ phase. Ignoring interface energies and long-range Coulomb interactions, the phase-separation energy is the theoretical energy of a two-phase mixture of (large) clusters composed of the two pure phases. This phase-separation energy is included as black line in Fig. 4.1, with the extended line toward the next pure (CE-type) phase at $x = 0.5$

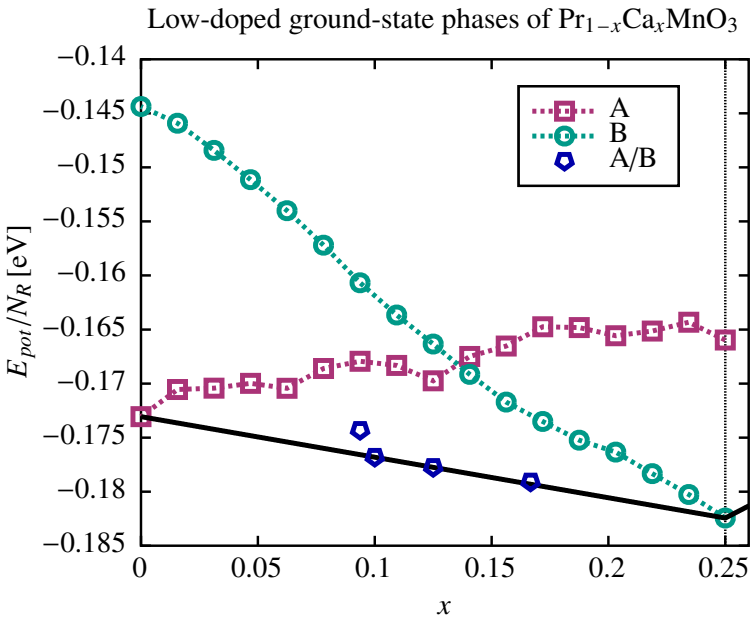

Figure 4.1: Energy per manganese site over doping x, for fixed t_{2g} spins of A-type (magenta squares) and B-type (green circles), as well as low-lying A/B-type mixed phases (blue pentagons) analyzed in more detail in Sec. 4.1.4. A thick black line connects the pure phases at $x = 0$ and $x = 0.25$, with an extension to the $x = 0.5$ pure CE-type phase indicated at $x > 0.25$.

with an energy per site of $E_{CE} = -0.15446\,\text{eV}$ indicated (but not analyzed in more detail here). Several metastable structures could be realized that are very close in energy to the phase separation, which is analyzed in more detail in Sec. 4.1.4. We will see that these metastable phases are actually mixtures of the A-type and B-type spin order of the neighboring pure phases, although their orbital order is adjusted to reduce the interface energies.

4.1.2 $x = 0$

For pure $PrMnO_3$ ($x = 0$), the model reproduces the A-type spin order of the experimental results (see Fig. 2.6). It shows a checkerboard-like x-y-plane orbital order as well. Density-functional calculations of this phase predict alternating Jahn-Teller angles of $\theta = \pm 110°$, close to pure alternating $d_{3x^2-r^2}$ and $d_{3y^2-r^2}$ orbitals that would emerge at $\theta = \pm 120°$ (depicted in Fig. 2.4), see Ref. [28]. The Jahn-Teller angles in the tight-binding results are reduced to $\theta = \pm 69.2°$, which leads to orbitals closer to the form of alternating $d_{x^2-z^2}$ and $d_{y^2-z^2}$ orbital shapes, as shown in a sketch in Fig. 4.2(a).

From the pure Q_2 distortions at $\theta = \pm 90°$, the density-functional angles thus indicate a constant negative Q_3 mode on every site, which, besides octahedral tilting, leads to a decreased $c/a < 1$ lattice constant ratio, in agreement with the experimental results, see Refs. [58, 135]. The tight-binding angles lead to a constant positive Q_3 mode on every site, which results in an increased $c/a > 1$ ratio (with $c = 0.27864\,\text{Å} + \bar{d}$ and $a = 0.14693\,\text{Å} + \bar{d}$, see Sec. 3.2.6 for details

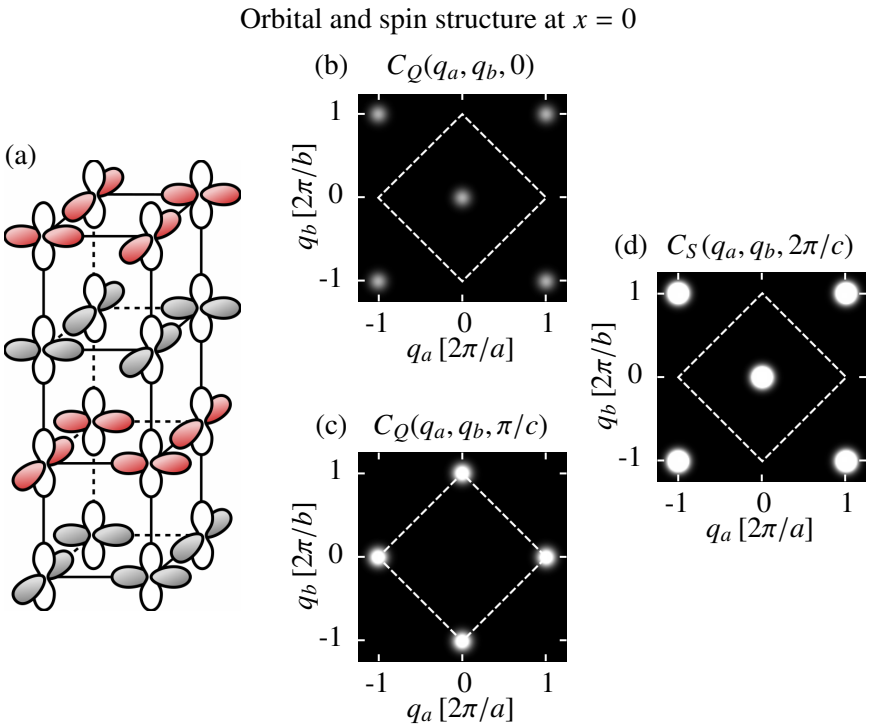

Figure 4.2: (a) Sketch of the orbital and spin order obtained for $PrMnO_3$ ($x = 0$). Similar to Fig. 2.6, we indicate the t_{2g} spin-orientation by the red/gray-shade of one of the orbitals' isosurfaces, with the e_g spins being aligned with the t_{2g} spins in all cases. The orbitals show a checkerboard-like x-y-plane order and an A-type spin order. (b)-(d) Planar cuts of the correlation functions of the Jahn-Teller and spin order (see Eqs. (4.2) and (4.1)) at different values of q_c, for an $\boldsymbol{N} = 4 \times 4 \times 4$ simulation cell with $\boldsymbol{N^k} = 6 \times 6 \times 6$. Non-zero values are obtained at discrete points due to the finite system sizes and Gauss-broadened at these positions. With the prefactors defined in Eqs. (4.1)-(4.4), they are all plotted on a constant (but arbitrary) color-scale. The white dashed line shows the size of the reciprocal unit cell.

on the value of $\bar{d}$), deviating from the experimental results. As mentioned previously, the low-doped region $x < 0.25$ is the only part of the ground-state phase diagram which shows this discrepancy in the obtained lattice constants. The tendency of superexchange coupled models to produce such reduced Jahn-Teller angles at $x = 0$ has been pointed out already in early studies by Kugel and Khomskii, see Ref. [132], and one possible suggested solution is the inclusion of anharmonic terms in the Jahn-Teller energy expression. It was mentioned before (see Sec. 3.2.3) that higher order restoring forces lead to local minima in the lower energy surface of the Jahn-Teller problem at angles $\theta = 0, \pm 2\pi/3$, which stabilizes the prolate over the oblate orbital types. We note that the Q_2-part of the Jahn-Teller angle ($\pm \sin(\theta)$), responsible for the in-plane checkerboard orbital order, agrees excellently with the density-functional theory results. As we are mainly interested in this in-plane orbital order when considering finite-temperature phase transitions, we do not include any further

correction terms into the model.

In general, the z-direction orbital order is very weak. The structure shown in Fig. 4.2(a) has the lowest energy of the possible z-direction orderings (in the tested $4\times4\times4$ simulation supercell), and alternates every second plane. A pure C-type orbital order (where the same orbital order repeats without shift between planes) is only less than 0.4 meV per site higher in energy, and we consider the different z-type orderings as nearly degenerate. It was pointed out in Ref. [127] that a small z-direction hopping between the $d_{x^2-y^2}$ orbitals stabilizes the C-type orbital order. This term is zero in the ideal cubic setup when considering σ-bonds only (see Sec. 3.2.1), but incorporating the octahedral tilting of the real material would lead to a small non-zero value in that hopping term.

A good measure for the various types of order can be given in terms of correlation functions in reciprocal space. We define these correlation functions for the spin, Jahn-Teller, orbital, and charge order as dimensionless quantities in the following ways:

$$C_S(\vec{q}) = \frac{1}{N_R^2}\left(\frac{3\hbar}{2}\right)^{-2} \sum_{j\in\{x,y,z\}} \left|\sum_R e^{-i\vec{q}\vec{R}} S_{j,R}\right|^2, \tag{4.1}$$

$$C_Q(\vec{q}) = \frac{1}{N_R^2}\frac{k_{JT}^2}{g_{JT}^2} \sum_{j\in\{2,3\}} \left|\sum_R e^{-i\vec{q}\vec{R}} Q_{j,R}\right|^2, \tag{4.2}$$

$$C_O(\vec{q}) = \frac{1}{N_R^2} \sum_{j\in\{x,z\}} \left|\sum_R e^{-i\vec{q}\vec{R}} \langle\hat{\sigma}_{j,R}^O\rangle\right|^2, \tag{4.3}$$

$$C_C(\vec{q}) = \frac{10}{N_R^2}\left|\sum_R e^{-i\vec{q}\vec{R}} (n_R - (1-x))\right|^2, \tag{4.4}$$

where we introduced the expressions $\hat{\sigma}_{j,R}^O = \sum_{\alpha,\beta,\sigma} |\chi_{\sigma,\alpha,R}\rangle \left(\boldsymbol{\sigma}_P^j\right)_{\alpha,\beta} \langle\chi_{\sigma,\beta,R}|$ for the orbital correlation function, with $\boldsymbol{\sigma}_P^j$ referring to the $j \in \{x, y, z\}$ Pauli matrices. The x and z components of this term couple directly to the Q_2 and Q_3 Jahn-Teller distortions, see Sec. 3.2.3, while the y component does not couple to the Jahn-Teller distortions and is ignored in the correlation function in Eq. (4.3).

The correlation functions will always be given in terms of the Pbnm-space group with the lattice constants a, b, and c, see Fig. 2.6 for a sketch of the orientation of the Pbnm lattice vectors in the cubic manganite tight-binding structure. The relevant non-zero a-b-plane correlation functions (corresponding to in-plane rotated x-y planes), are shown in Figs. 4.2(b)-(d). Due to the finite system sizes, the correlation functions are non-zero only at discrete values, at which they are Gauss-broadened for visibility in these figures. The intensities of the diffraction spots indicate the value of the correlation function at the corresponding wave vectors and the white dashed line shows the size of the reciprocal unit cell.

Figs 4.2(b) and (c) show the Jahn-Teller correlation function at $q_c = 0$ and

$q_c = \pi/c$. At $q_c = 0$, we see a smaller diffraction spot at $q_a = q_b = 0$, which represents the constant uniform positive Q_3 mode on every site. Larger diffraction spots are visible in the $q_c = \pi/c$ plane at $(q_a, q_b) = (\frac{2\pi}{a}, 0)$ (or equivalently in our lattice at $(q_a, q_b) = (0, \frac{2\pi}{b})$). This diffraction spot corresponds to the checkerboard-in-plane Jahn-Teller order (caused by the alternating Q_2 modes). With the near-degeneracy of the out-of-plane Jahn-Teller orders, we consider its q_c position as not well determined, and we refer to $(\frac{2\pi}{a}, 0, q_c)$ as the general checkerboard-order diffraction peak. The orbital correlation function (Eq. (4.3)) shows diffraction spots at the same spots as the Jahn-Teller order (not shown), with even the relative magnitude of the spots corresponding exactly to the Jahn-Teller order values. This reflects that in this ground-state the cooperative Jahn-Teller order matches the orbital order of the e_g electrons. Combined they could be described as a polaronic order, and the structure as a polaronic crystal. The spin correlation function is shown in 4.2(d), which has a non-zero value only at the A-type diffraction spot at $(q_a, q_b, q_c) = (0, 0, \frac{2\pi}{c})$. There is no charge order in the system, i.e., $C_C(\vec{q}) = 0,\ \forall \vec{q}$.

$PrMnO_3$ is one of the systems investigated with density-functional calculations in Ref. [28] that have been used to determine the parameters of the tight-binding model. In the used on-site model that was fitted to the densities of states, a perfect spin and orbital polarization of the e_g electrons was assumed for $PrMnO_3$. It is clear that this will not be the case in the real material or in the tight-binding results, as the electrons will delocalize to some extend to the neighboring sites to reduce their kinetic energy. The spin and orbital polarization n_S and n_O can be obtained from the expectation values of the Pauli matrices in the space of the spin- or orbital degrees of freedom: $n_S = \sqrt{\sum_{j\in\{x,y,z\}} \langle \hat{\sigma}^S_{j,R} \rangle^2}$ and $n_O = \sqrt{\sum_{j\in\{x,z\}} \langle \hat{\sigma}^O_{j,R} \rangle^2}$, where the spin expression is defined analogous to the orbital expression given above as $\hat{\sigma}^S_{j,R} = \sum_{\alpha,\sigma,\sigma'} |\chi_{\sigma,\alpha,R}\rangle \left(\boldsymbol{\sigma}^j_P\right)_{\sigma,\sigma'} \langle \chi_{\sigma',\alpha,R}|$. In the tight-binding model we obtain a spin polarization on every site of $n_S = 0.94$, which is very close to a full spin polarization, fitting to the large Hund's coupling present in the system. This also explains why the z-direction orbital order (where the spin changes between planes) is nearly irrelevant for the system's energy. In contrast, the orbital polarization is $n_O = 0.742$, which shows a non-negligible mixing of an e_g electron occupying the adiabatic lowest orbital of a certain site toward its (mostly in-plane) neighbors having a different Jahn-Teller angle. It might prove worthwhile to confirm the orbital polarization in density-functional calculations (which will, however, strongly depend on the studied doping and spin order) and potentially include it in a future adjusted parameter determination model. This is, however, not done in this thesis.

Lastly, from the final ground-state structure we can obtain the (Hartree-Fock) energy levels also of the unoccupied one-particle wave functions according to $\epsilon_n = \langle \psi_n | \hat{H}_{HF}(\Psi_{GS}) | \psi_n \rangle$, where $\hat{H}_{HF}(\Psi_{GS})$ is the Hartree-Fock Hamiltonian (see Eq. (3.4)) for the ground-state Slater-determinant wave function, and $|\psi_n\rangle$ are the one-particle eigenstates of this Hamiltonian. We note, however, that the energy levels of the unoccupied one-particle wave functions do not correspond to true excitation energies (one could obtain improved excitation energies,

for example, by using linear-response theory, see Refs. [152, 153], which is not done in this thesis). Here, we only use the difference between the highest-occupied and lowest-unoccupied one-particle eigenstate Δ_{E_g}, which also depends on the chosen k-point density, as the Hartree-Fock estimate of the electronic band gap. We obtain a value of $\Delta_{E_g} \approx 0.967\,\text{eV}$, which is close to the density-functional calculation band gap of 1.05 eV (see Ref. [28]).

In total, the tight-binding model reproduces both the A-type spin order and the in-plane checkerboard orbital order known to appear in undoped $PrMnO_3$ as the lowest-energy results. The lattice constant c/a-ratio is, however, not reproduced and shows a positive rather than a negative Q_3 admixture on every site.

4.1.3 $x = 0.25$

Next, we consider the opposite end of the investigated doping regime: the ferromagnetic (B-type) structure at $x = 0.25$. We outlined in detail in Sec. 2.4.1 that the type of orbital or potentially charge order is still under debate for this phase, with suggestions ranging from a phase separation between ferromagnetic metallic and antiferromagnetic insulating phases, over $PrMnO_3$-like orbital order with potentially disordered Mn^{4+} ions, to charge and orbital ordered intrinsically ferromagnetic insulating phases, see Refs. [58, 82, 87, 88, 103].

Our tight-binding model clearly shows (see also Ref. [56]) the development of an intrinsically ferromagnetic insulating phase (with $\Delta_{E_g} = 0.310\,\text{eV}$), where the metallic double-exchange is suppressed by an orbital ordering of the Mn^{3+} ions. In our results, this orbital order is accompanied by a charge ordering of the Mn^{4+} sites in a pattern indicated as sketch in Fig. 4.3(a). The formal Mn^{4+} "hole" sites in the sketch are without any orbital polarization and have no Jahn-Teller distortion, but the charge disproportion between the sites is smaller than their formal oxidation state, with the e_g electron density of the electron-rich and electron-poor sites being 0.882 e and 0.353 e, respectively. The electrons on the electron-rich sites (formal Mn^{3+} sites) occupy oblate shaped orbitals in the three cubic planes, corresponding to Jahn-Teller angles of $60° - \Delta\theta$, $180° - \Delta\theta$ and $300° - \Delta\theta$, where $\Delta\theta = 13.348°$ denotes the shift from the $d_{z^2-x^2}$, $d_{x^2-y^2}$ and $d_{y^2-z^2}$ orbitals (see Fig. 2.4). We observe an orbital polarization of $n_O = 0.602$ on these sites (and $n_O = 0$ on the hole sites). These oblate orbitals all have one opposite pair of lobes pointing toward the hole site (the white colored lobes in the sketch in Fig. 4.3(a), which are slightly smaller than the red lobes due to the Jahn-Teller angle shift), while the other pair of lobes points to the neighboring oblate orbitals oriented perpendicular to the oxygen bond. Hence, the electrons occupying all three types of orbitals extend to some degree into the hole sites, leading to the orbital-unpolarized state. Interpreted in the theory of semicovalent exchange (see Ref. [16]), the hole sites allow for a semicovalent bond in all three cubic directions, which gives rise to a ferromagnetic superexchange coupling between all sites, without leading to a large conductivity as one would obtain in an orbital-disordered double-exchange dominated structure. We note that this type of orbital order could in principle also occur without any charge order if a larger part of the

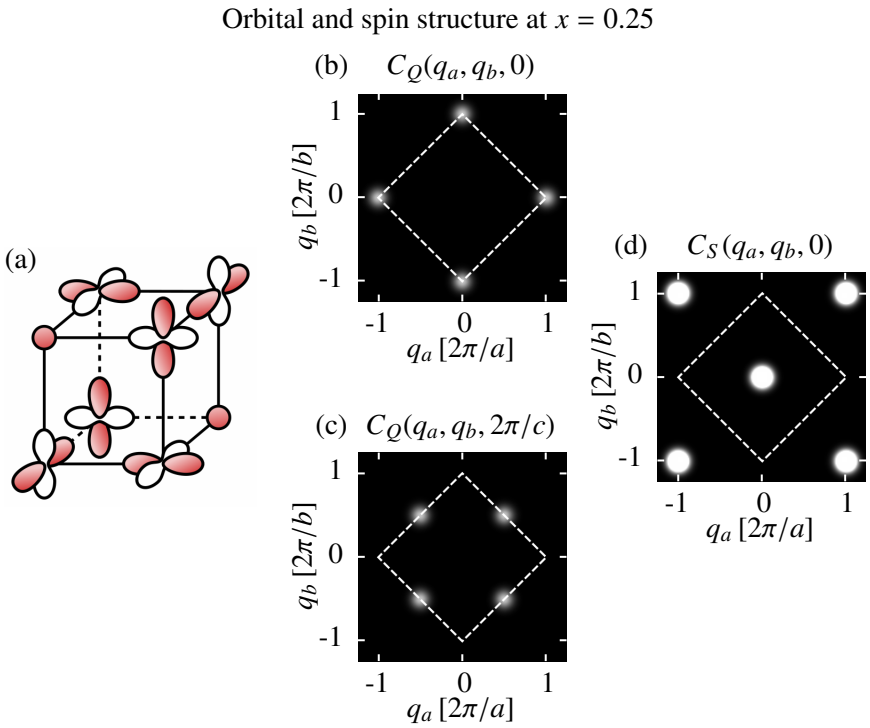

Figure 4.3: (a) Sketch of the orbital and spin order obtained at $x = 0.25$. The orbital shapes and spin directions are indicated in the same way as in Figs. 2.6 and 4.2. The system is ferromagnetic and shows the development of orbital-unpolarized sites (drawn as small circles). (b)-(d) Planar cuts of the correlation functions of the Jahn-Teller and spin order (see Eqs. (4.2) and (4.1)) at different values of q_c, for an $\boldsymbol{N} = 4 \times 4 \times 4$ simulation cell with $\boldsymbol{N^k} = 6 \times 6 \times 6$. We use the same Gaussian-broadening as before (see Fig. 4.2), and the white dashed line shows the size of the reciprocal unit cell.

e_g electrons localized to the Mn^{3+} sites would delocalize into the hole sites. In contrast to the previously suggested orbital-polarons composed of prolate orbital types (see Ref. [103]), this structure has the advantage that all sites are interconnected in a single superstructure, without the development of two separate sublattices. The orbital or charge order diffraction peaks are, however, the same as for the orbital-polarons presented in Ref. [103], and we adopt the name orbital-polaron for the hole sites encased by six Mn^{3+} sites.

The system is invariant under cubic rotations and we obtain equal lattice constants in all directions $c/a = 1$, which fits to the experimental results showing a minimum in the octahedral distortions around this doping (see Ref. [58]). Disordered variants of the orbital-polarons are only slightly higher in energy (in the order of a few meV). With the orthorhomic constraint of $L_x = L_y$ we observe that the metastable states typically have an intact x-y-plane orbital and charge order, while the order in the z-direction is weaker, see also Ref. [126] for a sketch of such a metastable state.

The described order (in the symmetric lowest-energy structure) leads to equal diffraction peaks in the orbital, charge and Jahn-Teller correlation functions

at $(q_a, q_b, q_c) = (\frac{2\pi}{a}, 0, 0)$, $(\frac{\pi}{a}, \frac{\pi}{b}, \frac{2\pi}{c})$, and $(\frac{\pi}{a}, \frac{-\pi}{b}, \frac{2\pi}{c})$, with all peaks having the same intensity, see Figs. 4.3(b),(c) for the example of the Jahn-Teller correlation function. The first diffraction peak in the $q_c = 0$ plane corresponds to the same checkerboard-type pattern also present at $x = 0$, although here with a different value of q_c. In the metastable variants of both phases, this peak remains, and the diffraction spots are extended to all values of q_c. The ferromagnetic order leads to a single diffraction spot in the spin correlation function at $(q_a, q_b, q_c) = (0, 0, 0)$, see Fig. 4.3(d).

4.1.4 $0 < x < 0.25$

Let us now turn to the intermediate region between the A-type AFM phase at $x = 0$ and the B-type FM phase at $x = 0.25$. As presented in Sec. 4.1.1, we could not find any structure lower in energy than the phase separation line. Without interface or long-range Coulomb interactions we can thus expect a mixture of the two phases presented above. A direct simulation of this phase separated structure with negligible interface energy is beyond the reach of the tight-binding model.

We could, however, find several low-lying states that are composed of mixtures of A-type and B-type phases. We observe two types of x-y-plane checkerboard-type orbital order in these metastable states, which is the type of order that is shared between both pure phases analyzed above. First (type-(I) order), the alternating oblate $d_{x^2-z^2}/d_{y^2-z^2}$ orbitals already found at $x = 0$ (see Fig. 4.2(a)), and second (type-(II) order) alternating $d_{x^2-y^2}$ orbitals with orbital-unpolarized formal Mn^{4+} sites. The type-(II) order is thus accompanied by charge order and has a formal hole doping of 0.5. The magnetic order in the x-y-plane within each type of orbital order is ferromagnetic, while between both orders it is antiferromagnetic. In the z-direction, the magnetic order is antiferromagnetic between sheets of type-(I) order, and ferromagnetic between the two types of orbital order. We find very low energies for structures in which the different types of order fill complete x-y-planes. The approximately half-doped planes (type-(II) order) are then encased by two $PrMnO_3$-like type-(I) order planes and build a three-layer ferromagnetic cluster in the otherwise A-type antiferromagnetic matrix. Such a structure is visualized in Fig. 4.4(a).

The doping determines the ratio of the two types of order. We could only stabilize these metastable states as long as the ferromagnetic clusters are non-overlapping, which leads to a maximum doping of $x = 1/6$. At higher dopings we could not find metastable states being this close to the phase separation energy. The exact placement of the ferromagnetic clusters in the A-type matrix has only very little effect on the total energy, which is evident from a few examples listed in Table 4.1, where the magnetic alignment of the subsequent layers is shown by spin-arrows ↑ and ↓. We note that while the short-range order sketched in Fig. 4.4(a) could be obtained with the usual ground-state search optimization procedures (see Sec. 3.3.3), the low-energy structures outlined in Table 4.1 were obtained by testing various spin and orbital configurations using manual inputs.

The two different tested spin patterns for the $x = 0.1$ doping have nearly the

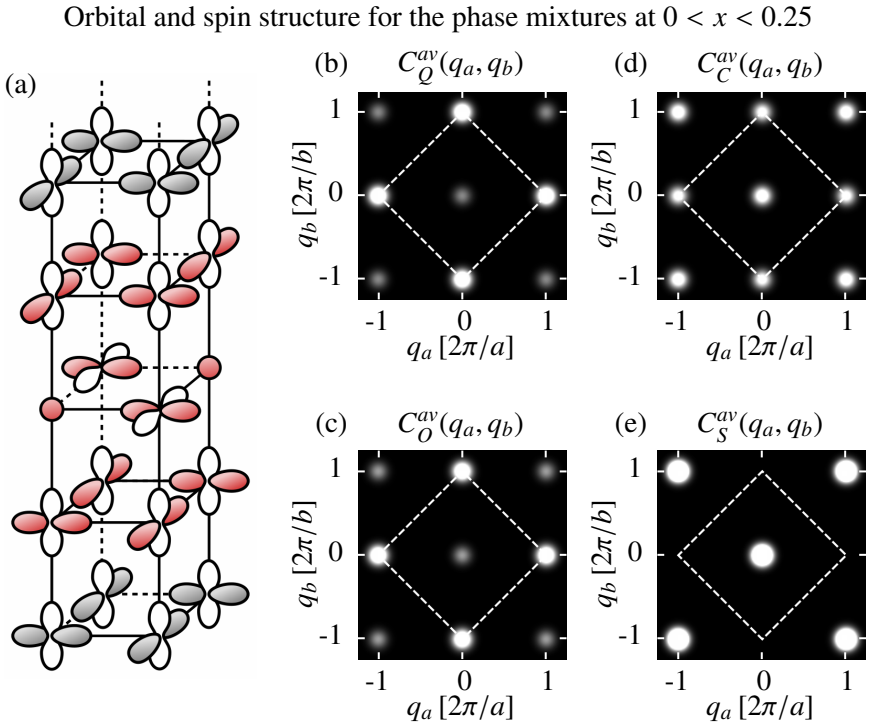

Figure 4.4: (a) Sketch of the type of orbital and spin order obtained in the metastable states presented in Table 4.1. The orbital shapes and spin directions are indicated in the same way as in Figs. 2.6 and 4.2. (b)-(e) c-averaged correlation functions of the Jahn-Teller, orbital, charge, and spin order (see Eq. (4.5)), for the $\boldsymbol{N} = 4\times4\times8$ simulation cell with $\boldsymbol{N^k} = 4\times4\times2$ at $x = 0.125$, with the c-direction spin pattern presented in the third row in Table 4.1. We use the same Gaussian-broadening as before (see Fig. 4.2), and the white dashed line shows the size of the reciprocal unit cell.

same energy, with the first pattern being antiferromagnetic, while the second pattern has a weak residual ferromagnetic moment averaged over the simulation cell (and the same applies to the two patterns analyzed for $x = 0.125$). This shows again that the ordering in the z-direction is much weaker than the in-plane checkerboard orbital order inherent to all observed structures. We note that experimental interpretations of a spin-canted phase in this region (see Refs. [58, 101]) could be caused by such an averaging over antiferromagnetic and weakly ferromagnetic patterns, but our results are more in line with a nanoscale phase separation of A-type and B-type phases, as proposed by newer experimental studies, see Refs. [84–86] and as a more general ordering principle by theoretical considerations in Ref. [26]. The energies of all presented spin patterns presented in Table 4.1 are very close to the phase separation energy of the pure $x = 0$ and $x = 0.25$ phases at the corresponding doping (differing by less than 1 meV), see also Fig. 4.1. From the tight-binding results presented here, we can thus expect to encounter all variants already at temperatures significantly lower than the orbital-order transition temperatures indicated in Fig. 2.5. The lower obtained energies at each doping account for three of the blue pentagons included in the energy-over-doping graph at $x = 0.1$, $x = 0.125$

doping x	simulation cell	spin configuration	E_{pot}/N_R [eV]
0.1	$\boldsymbol{N} = 2\times2\times10$ $\boldsymbol{N^k} = 8\times8\times2$	↑↓↓↓↑↓↑↑↑↓	-0.1768
0.1	$\boldsymbol{N} = 2\times2\times10$ $\boldsymbol{N^k} = 8\times8\times2$	↑↓↓↓↑↓↑↓↓↓	-0.1767
0.125	$\boldsymbol{N} = 4\times4\times8$ $\boldsymbol{N^k} = 4\times4\times2$	↑↑↑↓↓↓↑↓	-0.1776
0.125	$\boldsymbol{N} = 2\times2\times8$ $\boldsymbol{N^k} = 8\times8\times2$	↑↓↓↓↑↓↓↓	-0.1778
$\frac{1}{6}$	$\boldsymbol{N} = 2\times2\times6$ $\boldsymbol{N^k} = 8\times8\times3$	↑↑↑↓↓↓	-0.1791

Table 4.1: Exemplary low-lying (metastable) A/B-mixed structures obtained at dopings $x = 0.1$, $x = 0.125$ and $x = 1/6$. The simulation cells and k-grids are given, as well as the used spin-configuration. These spins refer to the t_{2g} (and aligned e_g) spin orientation in subsequent planes in the z-direction, see also the sketch in Fig. 4.4(a) for an example of a ↓↑↑↑↓-pattern. The energy per site is given in the last column. The energetically lower structure at each doping is also included in the energy-over-doping graph in Fig. 4.1.

and $x = \frac{1}{6}$, see Fig. 4.1.

With the order in the z-direction having such little effect on the total energy, it is useful to concentrate on the in-plane ordering only. For this we introduce the z-direction (or in Pbnm notation c-direction) averaged correlation functions:

$$C_A^{av}(q_a, q_b) = \sum_{q_c} C_A(q_a, q_b, q_c),\ A \in \{S, Q, O, C\}, \tag{4.5}$$

where the C_A, $A \in \{S, Q, O, C\}$ were defined in Eqs. (4.1)-(4.4). The c-averaged correlation functions are qualitatively the same for all spin patterns and dopings presented in Table 4.1, with the example correlation functions of the antiferromagnetic pattern at $x = 0.125$ (third row in Table 4.1) shown in Figs. 4.4(b)-(e). The Jahn-Teller, charge, and orbital correlation functions are all very similar, although the charge correlation function has a larger contribution at the $(q_a, q_b) = (0, 0)$ peak, which comes from the out-of-plane charge order. The checkerboard-peak at $(q_a, q_b) = (\frac{2\pi}{a}, 0)$ is present in all three types of order, and weakest in the charge correlation function (relatively to the total weight), where only the type-(II) order planes contribute. The spin correlation function has a peak at $(q_a, q_b) = (0, 0)$, with the contributing q_c components of the wave vector determined from the exact spin pattern.

Depending on the hole-doping (and the chosen simulation cell), the two types of orbital order might not fill complete x-y-planes. In this case, they form clusters in the mixed layers, with an in-plane antiferromagnetic coupling between both types of order. The energy of such an example is included in the energy-over-doping Fig. 4.1 at $x = \frac{6}{64}$ obtained in a $4\times4\times4$ simulation cell (with $\boldsymbol{N^k} = 4\times4\times4$). Its energy of $E_{pot}/N_R = -0.1743\,\text{eV}$ is about

2 meV above the phase separation line. When analyzing the finite-temperature phase transition close to $x = 0.1$ we will start most simulations from this state, and a sketch of the x-y-plane orbital order of such a structure is shown there, see Fig. 4.5. The increased size in the x-y-direction allows for a melting of the long-range checkerboard-like orbital order (in contrast to the $2 \times 2 \times 10$ simulation cells presented in Table 4.1), while still being small enough to obtain a sufficient thermal averaging time in the simulation.

4.2 Orbital-order phase transition at $x = 0$ and $x = 0.1$

Let us now turn to the orbital-order phase transition at dopings $x = 0$ and $x = 0.1$. As outlined in Sec. 2.4.2, the established experimental understanding (see Refs. [57, 58, 118–120]) is a transition at very high temperatures: 945 K-1050 K for $x = 0$ and >675 K for $x = 0.1$ (see Ref. [58] for the estimate of the latter). This was also indicated in Fig. 2.5 as the upper end of the striped region at low doping. The direct measurement of the orbital order by resonant X-ray scattering for the similar material $LaMnO_3$ indicated a two-step decrease of the orbital order peak: Once around 200-250 K and the second drop to zero at the high temperature (800 K) structural transition of that material, see Ref. [120]. The same behavior was observed at $x = 0.25$ for $Pr_{1-x}Ca_xMnO_3$ in Ref. [88], although here the high-temperature tail had a reduced weight, compared to the $LaMnO_3$ measurements. We mention that the thermoelectric power measurements presented in Ref. [119] for $PrMnO_3$ also show a peak shortly below 400 K. Already from these literature results, a detailed study of the orbital order between 200 K and 400 K seems to be worthwhile.

Based on a series of new experimental measurements presented in Ref. [24], we conjectured that the spontaneous orbital-order phase transition might happen already at these lower temperatures, similar to the higher doping regions. The theoretical simulations carried out by the author of this thesis, which are presented in this chapter and partially in Ref. [24], support this evidence. Much of the discussion presented here and at the end of this section follows the argumentation of the published article, Ref. [24]. Before we continue with the theoretical simulations, let us summarize the experimental evidence shown in that article.

Of special importance is the observed onset temperature for a photovoltaic effect (as quantified by the open-circuit voltage) in $Pr_{1-x}Ca_xMnO_3$ (PCMO). Previous measurements for PCMO-$SrTi_{1-y}Nb_yO_3$ (STNO, $y = 0.002$) heterojunctions, see Refs. [9, 10], revealed that the photovoltaic effect in the visible-to-infrared excitation range only sets in below the respective ordering temperatures of the charge and orbital order ($x = 0.34$) or magnetic order ($x = 0.95$). A connection of the Mn-d-O-p intraband photo-excitation lifetime to the surrounding long-range order was given in Ref. [9], based on a simple two-octahedron "Jahn-Teller dimer" model. Here, the dipole-allowed intraband excitation creates an electronic state in the excited Born-Oppenheimer surfaces. Without the cooperative lattice effects created by the long-range

order, a quick radiationless relaxation through conical intersections into the electronic ground-state is possible. This is qualitatively similar to the Jahn-Teller "monomer" (single site Jahn-Teller problem), whose energy surfaces are depicted in Fig. 3.1: Without surrounding lattice effects, an excited electron-nuclear wave function can relax toward the ground state by going through the symmetric nuclear configuration. Cooperative lattice effects prevent this relaxation through the symmetric configuration. A similar effect is observed in the more realistic Jahn-Teller dimer model (see Ref. [9]), where the position of the conical intersection shifts away from the minimum of the excited energy surface, trapping the electron-nuclear system in a metastable state. This excited electron-phonon configuration is also called a hot-polaron state, see Ref. [9], and can have a long lifetime in the range of nanoseconds, allowing for the extraction of the photo-excitation energy and the stabilization of a photovoltaic effect. The correlation of long-range orbital and charge order (always combined with the corresponding Jahn-Teller order) with the development of a photovoltaic effect has been further confirmed in the effectively two-dimensional Ruddlesden-Popper variant $Pr_{0.5}Ca_{1.5}MnO_4$, where the transition and onset temperatures could be raised above room-temperature to 320 K, see Ref. [11].

The new measurements presented in the published article (Ref. [24]) show the onset of a photovoltaic effect in $x = 0.1$ doped $Pr_{1-x}Ca_xMnO_3$ thin films around 220 K. This is much below the believed orbital order transition, and higher than the magnetic transitions happening at 70 K and 80-130 K (see Refs. [58, 83–86])). In addition, anomalies were reported in the $x = 0.1$ thin films at 200-250 K. These anomalies appear (a) in the temperature dependence of the optical band gap and the in-plane resistivity (with the latter linked to the polaron hopping mobility), (b) in the transient optical response in a pump-probe transmission experiment, which shows an increased hot-polaron lifetime below around that temperature, and are visible (c) by the onset of a magnetoresistance effect below 260 K that was linked to an orbital order transition at slightly lower temperatures. We refer to Ref. [24] for a detailed discussion of these experiments.

Furthermore, temperature dependent changes of the lattice parameters in bulk PCMO measured by X-ray diffraction were reported in Ref. [24]. They showed a change in slope of thermal expansion at the temperatures 350 K and 300 K for $x = 0$ and $x = 0.1$, interpreted as a continuous phase transition. The higher temperatures observed in these bulk samples compared to the thin films were attributed to misfit strain and growth-induced defects in the latter, see Ref. [24]. Since our manganite tight-binding model is a bulk description of PCMO, we will mainly compare to these higher transition temperatures. The anomalies in various physical parameters fit to the drop in the orbital order peak observed at similar temperatures in the resonant X-ray diffraction studies of $LaMnO_3$ and $Pr_{0.75}Ca_{0.25}MnO_3$, see Refs. [88, 120].

Although this orbital order peak does not vanish to zero at these temperatures, the drop seems to have broad repercussions in the different analyzed physical quantities, and only in the lower temperature region a photovoltaic effect could be observed. We mentioned in Sec. 2.4.2 that the high-temperature transition is

expected to involve a coupled change of both the tilt-pattern and the cooperative Jahn-Teller distortions, see also Ref. [57]. A tilt-transition is observed in $CaMnO_3$ as well, even without Jahn-Teller distortions, see Ref. [156]. This led to the following proposal, presented in Ref. [24]: the high-temperature transition is mainly a tilt-transition, which induces a weaker cooperative Jahn-Teller (and orbital) order below $\sim 945\,\mathrm{K}$. Below 350/300 K ($x = 0/x = 0.1$), a stronger orbital order occurs spontaneously due to Mn-e_g electronic and electron-phonon interactions.

At this point, an independent confirmation by theoretical simulations using the manganite tight-binding model can provide further insight. All ground-state ordered phases in this model (see Sec. 4.1) are obtained solely from the interactions presented in Sec. 3.2, without an external tilt-pattern supporting the alternating $PrMnO_3$-like orbital order. Thus, in this section (and the published article, Ref. [24]), we investigate the melting of orbital order by direct simulation with Car-Parrinello molecular dynamics (see Sec. 3.4.1) applied to the manganite tight-binding model, for the dopings $x = 0.1$ and $x = 0$.

With most of the experimental results presented in Ref. [24] carried out for a doping of $x = 0.1$, we will concentrate on this composition as well. The results are presented first in Sec. 4.2.1. Afterward we turn to pure $PrMnO_3$ in Sec. 4.2.2, which has the advantage that less uncertainty exists about its ground state. Lastly, we discuss with a simplified model the connection of the spontaneous and induced order, and provide an updated phase-diagram incorporating the new results, both of which have been presented in Ref. [24].

4.2.1 $x = 0.1$

The $N = 4 \times 4 \times 4$, $N^k = 2 \times 2 \times 2$ system

The ground-state structure at $x = 0.1$ is not as clear as for the pure $PrMnO_3$ phase at $x = 0$, see Sec. 4.1.4. The energies of the A/B-type mixtures sketched in Fig. 4.4(a) are almost degenerate with the phase separation energy between the neighboring pure phases. Since we are limited in system size in the practical simulations, we will study such an A/B-mixture for the phase transitions. A good candidate would be the layer-filling variants presented in Table 4.1 for $x = 0.1$. A 2×2 simulation cell in the x-y-plane is, however, too small to capture the breakdown of long-range in-plane order, while a full $4 \times 4 \times 10$ simulation cell leads to very long simulation times. We thus carry out the main simulations in a $4 \times 4 \times 4$ simulation cell, and confirm the transition temperature in larger systems with less statistical averaging. We choose a doping of $x = \frac{6}{64} = 0.09375$, close to the experimental doping of $x = 0.1$, which in an ionic picture leads to six hole-sites. In the $4 \times 4 \times 4$ simulation cell, the two types of orbital order are not completely layer-filling, as already mentioned in Sec. 4.1.4, and instead form clusters in the partially filled layers, which is indicated in a sketch in Fig. 4.5. In this sketch, the in-plane Pbnm lattice vectors $\boldsymbol{a}$ and $\boldsymbol{b}$ are indicated for a cubic lattice.

The relevant type of order is the x-y-plane alternating orbital or Jahn-Teller order (which are strongly coupled and give the same transition temperatures in

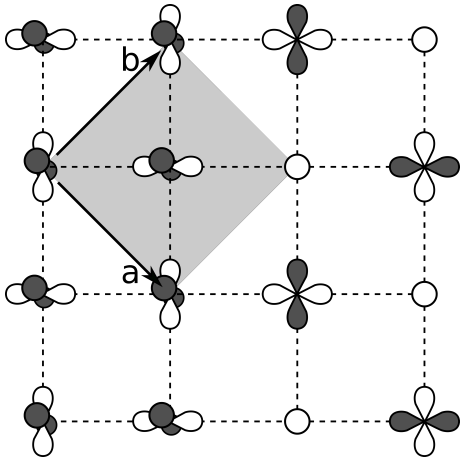

Figure 4.5: Sketch of the coexisting types of x-y-plane orbital order in the $0 < x < 0.25$ A/B-mixed phases, when the order is not layer-filling as in Fig. 4.4(a). The left site shows the type-(I), $PrMnO_3$-like alternating $d_{x^2-z^2}/d_{y^2-z^2}$ order, and the right site the type-(II) alternating arrangement of $d_{x^2-y^2}$ orbitals and orbital-unpolarized sites. Both lead to an in-plane checkerboard peak of the orbital and Jahn-Teller correlation functions. We also included the $\boldsymbol{a}$ and $\boldsymbol{b}$ vectors of the Pbnm unit cell.

all studied cases). This checkerboard-like pattern is shared by both the type-(I) and type-(II) orders present in the A/B-mixture phases, as is also apparent from the sketch in Fig. 4.5. The order parameter λ of the phase transition is thus set to the $(q_a, q_b) = (\frac{2\pi}{a}, 0)$ peak of the c-averaged Jahn-Teller correlation function (which is equivalent ot the $(0, \frac{2\pi}{b})$ peak in our lattice):

$$\lambda = C_Q^{av}\left(\frac{2\pi}{a}, 0\right). \tag{4.6}$$

We note that this order parameter cannot become negative and does not change when the in-plane order shifts by one site in the x- or y-direction. This is similar to the mean squared magnetization sometimes used to study finite-size phase transitions in magnetic materials, see Ref. [157]. The transition probability between different shifted types of in-plane order is non-zero in a finite system for any non-zero temperature. Therefore, one would have to be careful when using, for example, the staggered orbital-pseudomagnetization $(\sum_+ \sum_j \langle \hat{\sigma}^O_{j,R}\rangle - \sum_- \sum_j \langle \hat{\sigma}^O_{j,R}\rangle$, where the sums $\sum_\pm$ are over two different checkerboard-like in-plane sublattices) as order parameter, or equivalently the staggered Jahn-Teller distortions. For such an order parameter, one has to ensure not to run the molecular dynamics simulation for too long, as the order parameter would eventually average out to zero. No such problem occurs with the order parameter chosen here.

Finite-temperature ensemble averages of this order parameter are carried out using Car-Parrinello molecular dynamics, which was outlined in Sec. 3.4.1. The e_g electrons and t_{2g} spins are kept close to their adiabatic ground state by applying a constant small friction on their subsystem, and choosing a small mass for their fictitious dynamics. The Nosé-Hoover thermostat is applied to

m_ψ	m_S	α_ψ	α_S	M_O	T_{TS}	Δ_t
$1.0\,m_e \cdot a_o^2$	$1.0\,m_e \cdot \left(\frac{a_o}{3/2\hbar}\right)^2$	$0.41\,\frac{1}{\text{fs}}$	$0.41\,\frac{1}{\text{fs}}$	15.999 u	100 fs	2.42 as

Table 4.2: Parameters used for the finite-temperature thermostat calculations: fictitious masses m and constant friction α for the e_g electrons and spins m_ψ, m_S, α_ψ and α_S, as well as oxygen nuclear masses M_O, thermostat oscillation period $T_{TS} = 2\pi\sqrt{M_{TS}/2gk_BT}$ (see Sec. 3.4.2), and the time step Δt. m_e is the electron mass, a_o the Bohr radius, and u the atomic mass unit.

the nuclear degrees of freedom, which use the real oxygen atom masses. We do not allow a dynamic movement of the lattice constants during the thermostat calculation and instead keep them fixed at their ground-state values. The chosen parameters for the electron and spin masses and friction, as well as nuclear masses, thermostat oscillation period and the time step are given in Table 4.2, see also Ref. [24].

For each target temperature T, the nuclei start at the (local) minima of the potential energy surface obtained in the ground-state search, and their momenta are initialized by a random Gauss distribution to reproduce an average kinetic energy of $0.5k_BT$ per degree of freedom (some non-zero momenta are necessary to start the thermostat simulation). Several runs are started with different random initial velocity distributions to ensure that the results do not depend on this initialization. Afterward, each run is equilibrated for 2.42 ps with the thermostat at the target temperature, which corresponds to about 24 thermostat oscillation periods. For obtaining the ensemble average $\langle\lambda\rangle_T$ of the order parameter at a certain temperature T, the calculations continue for further 12.1 ps and sampling points are obtained every 100 time steps. Since the nuclei started at the ground-state configuration, this will be denoted as the "heating" of the system, and the values for temperatures up to 800 K are shown in Fig. 4.6 for six simulation runs for every temperature.

Here and in the following, the included error-bars show the maximum block-estimate for any integer division of the number of sampling points up to a block size of one-fourth of the total number of sampling points, see Sec. 3.4.2 for details. In the temperature region of the phase transition this should only be taken as a lower bound to the true standard deviation of the ensemble average, as pointed out in Sec. 3.4.2. We use a k-grid of $\boldsymbol{N^k} = 2 \times 2 \times 2$, but the transition is confirmed with a larger k-grid, see Fig. 4.10.

We observe a large drop of the order parameter between 200 K and 400 K, after which the order parameter remains at a low (but non-zero) value. The sharpest decent occurs around 270 K. To confirm this transition in the order parameter we performed additional "cooling" simulations, which start from the final configurations of the six heating runs at 400 K. We then set the target temperature to new values between 20 K and 400 K. These temperatures are typically reached in the order of one thermostat cycle, which corresponds to an ultra-fast cooling of up to $\sim 4\,\frac{\text{K}}{\text{fs}}$. For a direct cooling from 400 K to temperatures below 200 K not all simulations runs were able to recover the high order of the ground state in the simulation time available, although

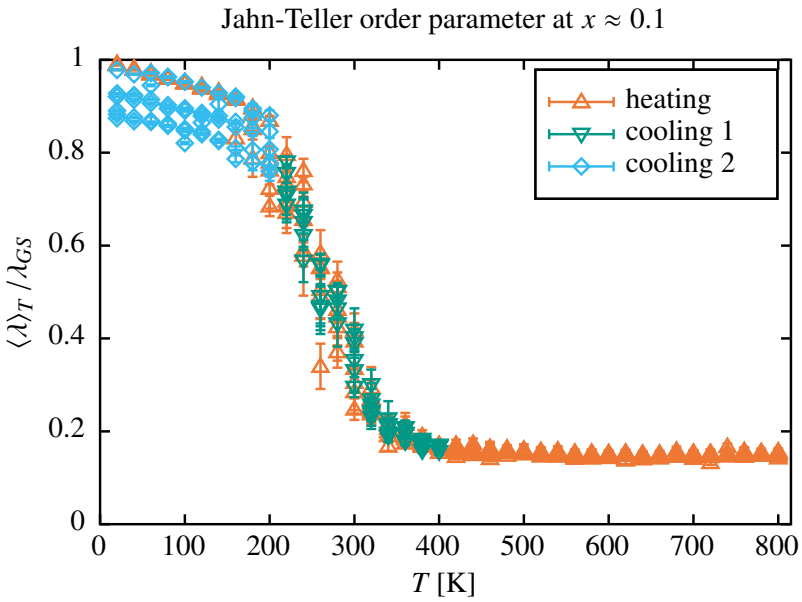

Figure 4.6: Jahn-Teller order parameter (Eq. (4.6)) obtained in a $4 \times 4 \times 4$ simulation cell with $N_i^k = 2$ k-points in every direction at doping $x = \frac{6}{64}$. The order parameter at every temperature is divided by the value at $T = 0$ (the ground state). We show 6 different heating runs for temperatures up to 800 K, which start from the ground state configuration and are obtained from thermostat calculations with 12.1 ps of thermal averaging after 2.42 ps of equilibration. In addition, we show six cooling runs starting from the final configurations of the 400 K heating runs, down until 220 K (cooling 1), and further cooling runs that start from the 200 K final configurations of the first cooling runs down until 20 K (cooling 2). These cooling runs are obtained with 9.68 ps of equilibration and 19.36 ps of thermal averaging. The used thermostat parameters are listed in Table 4.2. All error bars represent the maximum block-estimate of the thermal averages' standard deviations (see Sec. 3.4).

we increased these times to 9.68 ps of equilibration and 19.36 ps of thermal averaging. Therefore, we performed a second set of cooling runs starting from the final configuration of the 200 K runs of the first set of cooling simulations. This second cooling procedure recovers high values of the order parameter as $T \to 0$, see Fig. 4.6. One run could nearly completely recover the ground-state orbital order, while most of the simulation runs show some defects slightly decreasing the order in the system. We confirmed the transition in additional calculations starting from such defect structures, leading to the same transition temperatures around 270 K (not shown here). The combined heating-cooling cycle shows no hysteresis in the transition.

To better understand the nature of the transition, let us investigate the complete c-averaged Jahn-Teller correlation functions at three temperatures before, during, and after the transition. They show no large deviations between the simulation runs and one example for each of the temperatures 20 K, 280 K and 400 K is shown in Figs. 4.7(a)-(c). We also included the orbital correlation function at the same temperatures (Figs. 4.7(d)-(f)). They are almost propor-

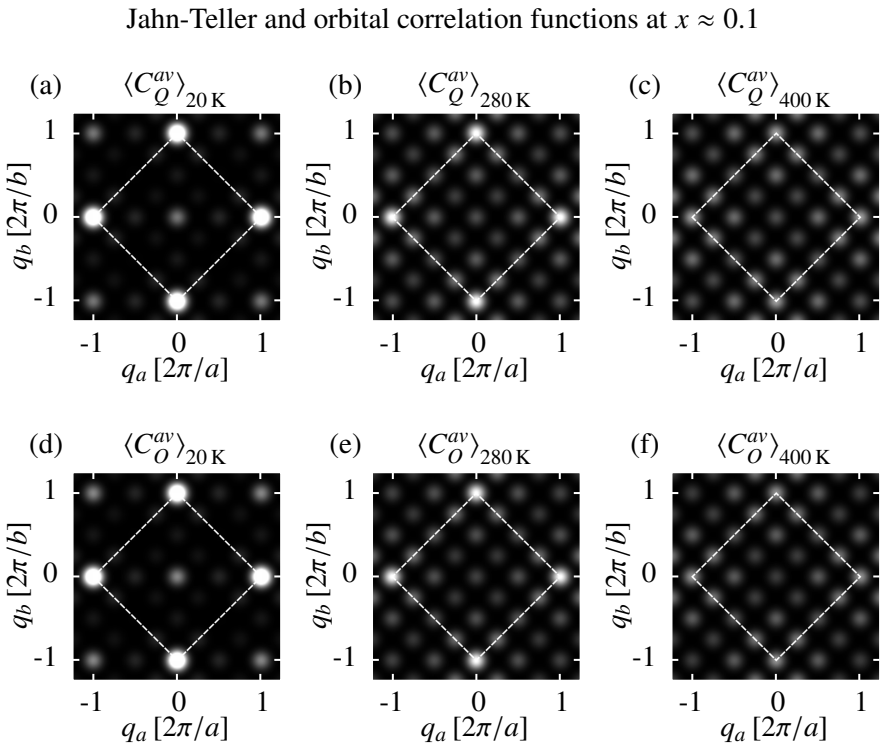

Figure 4.7: (a)-(c) c-averaged Jahn-Teller correlation functions and (d)-(f) orbital correlation functions (see Eqs. (4.2), (4.3) and (4.5)), for an exemplary heating run at temperatures 20 K, 280 K and 400 K, in the $4 \times 4 \times 4$ simulation cell with $N_i^k = 2$ k-points in every direction at doping $x = \frac{6}{64}$. We use the same simulation protocol and thermostat parameters as in Fig. 4.6, and the same Gaussian-broadening as before (see Fig. 4.2). The white dashed lines indicate the size of the reciprocal unit cell.

tional to the Jahn-Teller correlation functions at all temperatures and we will mainly analyze the Jahn-Teller correlation functions in the following.

At 20 K, the main peaks are still the checkerboard order at $(q_a, q_b) = (\frac{2\pi}{a}, 0)$ and a weaker peak at $(q_a, q_b) = (0, 0)$. At higher temperature we observe that all other possible peaks get an increasing weight as well. This is similar to a discrete broadening of the previous checkerboard-peak. Above the transition at $T = 400$ K almost all peaks have the same weight and the correlation function becomes nearly independent of the wave vector, although the sum-rules for the oxygen distortions along rows through the crystal (see Sec. 3.2.6) reduce the weight along the diagonal lines. The peaks show a redistribution of weight, while their total weight is mostly unaffected (and even slightly increased), which corresponds to the breakdown of long-range order, but not of local Jahn-Teller distortions.

It is instructive to analyze this in real-space as well, for which we consider the real-space Jahn-Teller correlation function for the absolute in-plane distances

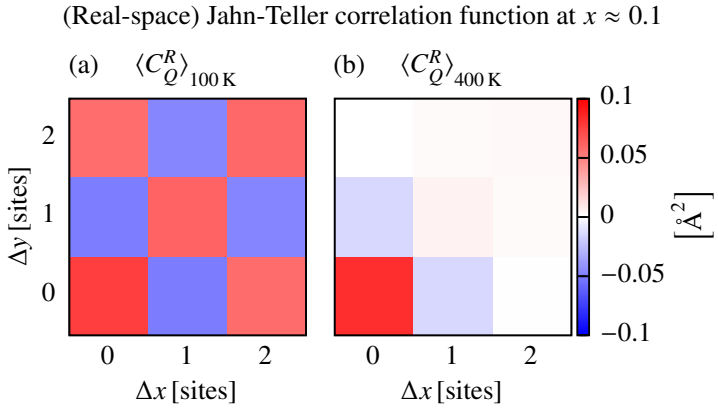

Figure 4.8: Real-space Jahn-Teller correlation function (see Eq. (4.7)) for an exemplary heating run at temperatures (a) 100 K and (b) 400 K, in the $4 \times 4 \times 4$ simulation cell with $N_i^k = 2$ k-points in every direction at doping $x = \frac{6}{64}$. We use the same simulation protocol and thermostat parameters as in Fig. 4.6.

Δ_x and Δ_y:

$$C_{Q_2}^R(\Delta_x, \Delta_y) = \frac{1}{N_R m_{x,y}} \sum_{R,R'} \sum_{j \in \{2,3\}} Q_{j,R} Q_{j,R'} \left[\delta_{\Delta_x, |R_x - R'_x|} \delta_{\Delta_y, |R_y - R'_y|} \delta_{0, |R_z - R'_z|} \right] . \tag{4.7}$$

Here, δ denotes the Kronecker delta and $|R_i - R'_i|$ is the smallest absolute distance in the i-direction between any periodic images of sites R and R'. We also included the multiplicity $m_{x,y}$, which equals the number of relative distances $(R_i - R'_i)$ contributing to the same absolute distance (e.g., $m_{0,1} = 2$, since both $(R_x - R'_x = 1)$ and $(R_x - R'_x = -1)$ contribute). The results for two such real-space correlation functions obtained at 100 K and 400 K are shown in Fig. 4.8.

At 100 K, the correlation function is still similar to the ground-state configuration, and consists mostly of the in-plane Q_2 order, which leads to a checkerboard-like pattern in the real-space correlation function. The additional constant Q_3 mode increases the contribution at the $(\Delta_x, \Delta_y) = (0, 0)$ peak. This peak is proportional to the average squared local Jahn-Teller distortion on every site $\propto \sum_R |Q_R|^2$, and thus an indication of the remaining local Jahn-Teller distortions and (indirectly) the orbital polarization. After the transition, at 400 K, a strong $(0, 0)$ peak remains, but the long-range order vanishes. We still observe a negative Jahn-Teller correlation function for neighboring sites $(\Delta_x, \Delta_y) = (1, 0)$ and $(\Delta_x, \Delta_y) = (0, 1)$, indicative of a short-range checkerboard order, but at larger distances the values are close to zero. This supports the interpretation that only the cooperative Jahn-Teller and orbital order melts down, while local distortions and orbital polarization remain. With the remaining short-range order, this could be denoted as the transition from a polaron crystal into a polaron liquid.

In the CP-MD, we aim at keeping the spins and electrons close to their

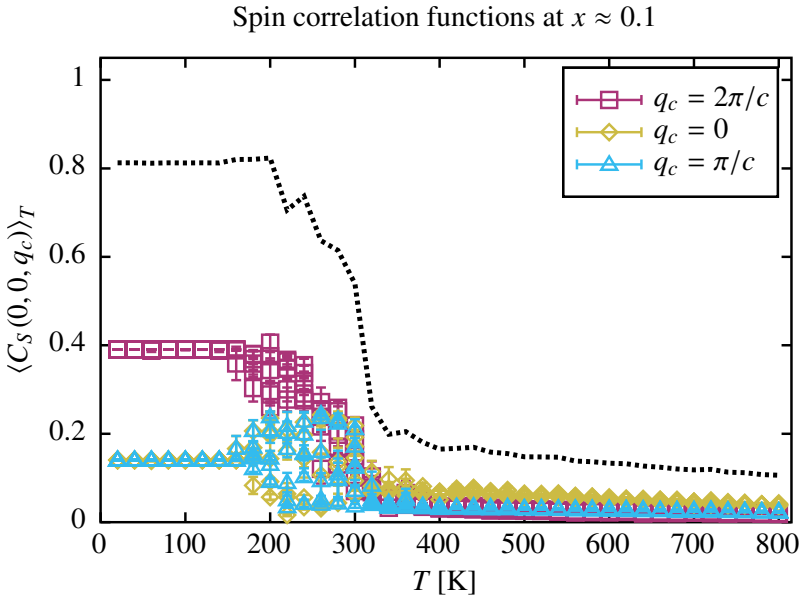

Figure 4.9: Spin correlation functions $\langle C_S(0,0,q_c)\rangle_T$ obtained from thermal averaging during the heating runs in the $4\times4\times4$ simulation cell with $N_i^k = 2$ k-points in every direction at doping $x = \frac{6}{64}$ (see Fig. 4.6 for details of the simulation). We show the peaks at $q_c = 2\pi/c$ (A-type AFM), $q_c = \pi/c$ (which is equal to $q_c = -\pi/c$) and $q_c = 0$ (B-type FM). The sum of all these x-y-plane-ferromagnetic peaks $\sum_{q_c}\langle C_S(0,0,q_c)\rangle_T$ is included as black dashed line. All error bars represent the maximum block-estimate of the thermal averages' standard deviations (see Sec. 3.4).

ground state during the thermostat run. Thus, we cannot hope to capture the independent magnetic phase transitions expected from experimental results (see Refs. [58, 83–86]) at very low temperatures at this doping: below 80-130 K the system changes from paramagnetic to ferromagnetic in a large temperature interval, and below 70 K the system becomes mostly antiferromagnetic, with a mixture of FM and A-type AFM clusters currently being the most likely explanation instead of a canted spin structure, see Sec. 2.4.1 and Ref. [86]. Our ground-state results reproduce the FM/A-type AFM mixture, as presented in Fig. 4.4, although a small in-plane AFM contribution appears for the $\boldsymbol{N} = 4\times4\times4$ simulation cell, because the different types of order are not completely layer-filling, see Sec. 4.1.4. The finite-temperature results are shown in Fig. 4.9, now resolved for the different relevant spin-peaks. These all have the same in-plane wave vector of $(q_a, q_b) = (0,0)$: The B-type FM-peak ($q_c = 0$), and different antiferromagnetic peaks ($q_c = 2\pi/c$ and $q_c = \pm\pi/c$), where the A-type AFM peak ($q_c = 2\pi/c$) has the largest weight. We note that the sum of all spin correlation function peaks is conserved to 1 by definition (Eq. (4.1)), and a reduction of these $(q_a, q_b) = (0,0)$ peaks is always accompanied by shifting weight to all other peaks. We observe no change in the spin order at the experimentally expected transition temperatures. During the orbital-order transition, the total weight of the $(q_a, q_b) = (0,0)$ peaks decays (included as black-dashed line), and the individual peak weights vary strongly between

simulation runs. From the experimental results, we would expect the spins to be disordered at these temperatures, while in the CP-MD simulations, they follow the atomic structure adiabatically and should not be over-interpreted. Their summed weight stays low after the orbital-order phase transition, although we observe a continued slow decay until 800 K.

In total, we cannot reproduce the magnetic phase transition with the used adiabatic CP-MD simulation, and extensions to correctly capture the spin-temperature are necessary for a better description. We cannot exclude that this magnetic phase transition influences the orbital-order transition happening at higher temperatures. Since the spin order supports the orbital order at these dopings, we can speculate that a correct description of the spin transition would lower the orbital-order transition temperature. Further studies are needed in the future to investigate this in more detail.

Numerical confirmations and larger system sizes

In the CP-MD simulation, the spins and e_g electrons are only approximately in their ground states, which is achieved by the large mass difference to the nuclei and by the application of a constant small friction. We need to ensure that the friction is not chosen too large to impede with the atom dynamics. For this, we repeat the heating simulations with both the electron and spin friction reduced to half the values presented in Table 4.2. The results of three such simulation runs in the heating-setup with equilibration and sampling times equal to the previous heating runs are shown in Fig. 4.10(a).

In addition, we confirm the near-adiabatic CP-MD results with a Born-Oppenheimer molecular dynamics simulation (see Sec. 3.4.1), at least for the electronic degrees of freedom. For this, we search for the electronic ground state at each propagation time step and use the ground-state configuration for determining the nuclear forces. This is done in an iterative procedure: We construct the Hartree-Fock Hamiltonian (Eq. (3.4)) for the given nuclear and spin configuration, and with a trial one-center reduced electronic density matrix for the electron-electron interaction. By diagonalizing the quadratic Hamiltonian in the electronic basis, we obtain a new electronic wave function that is used to update the trial one-center reduced density matrix. These steps are repeated until no element of the reduced density matrix changes by more than 10^{-7} between iteration cycles. The spins are still treated with the Car-Parrinello approach, as finding the spin ground state for each nuclear configuration is computationally too expensive. Since no dynamical evolution of the electronic degrees of freedom is carried out in a BO-MD simulation, we use an increased time step of ten times the value presented in Table 4.2. The Car-Parrinello treatment of the spins limits us in further increasing this time step. Unfortunately, the larger time step is more than compensated by the self-consistency routines, so that we only reach shorter total times with this ansatz. Fig. 4.10(a) includes two such BO-MD heating runs with 1.21 ps of equilibration and 6.05 ps of thermal averaging.

As another numerical test, we perform a simulation with a larger k-grid of $\boldsymbol{N^k} = 4 \times 4 \times 4$, with 1.21 ps of equilibration and 3.63 ps of thermal averag-

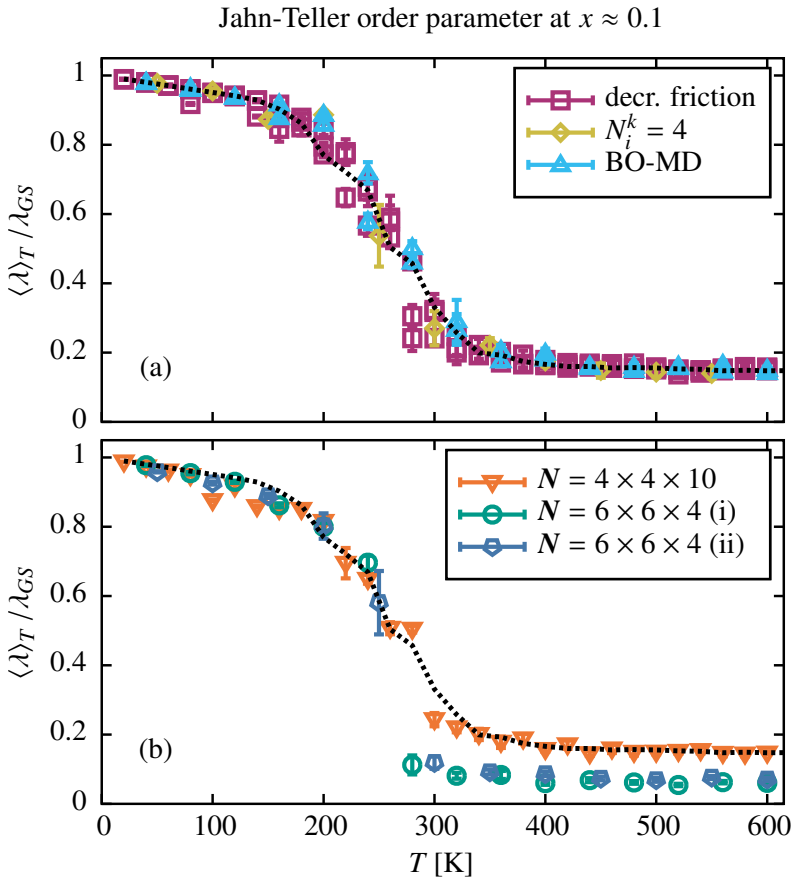

Figure 4.10: Jahn-Teller order parameter (Eq. (4.6)) for various heating thermostat calculations. The order parameters at every temperature is divided by the value at $T = 0$ of the corresponding ground state calculations. Except for the deviations outlined in the following, the simulations use the same parameters and heating protocol as in Fig. 4.6. The average (normalized) order parameter values of these previous heating runs of Fig. 4.6 are included as dotted black line for comparison. (a) Calculations in a $4 \times 4 \times 4$ simulation cell at doping $x = \frac{6}{64}$. Results are shown for: (decr. friction) three simulation runs with decreased friction, which use half the friction values presented in Table 4.2, ($N_i^k = 4$) one simulation with increased k-grid of $N_i^k = 4$ in every direction, and a reduced equilibration time of 1.21 ps and thermal averaging time of 3.63 ps, and (BO-MD) two simulation runs using a Born-Oppenheimer ansatz for the electronic degrees of freedom (see the description in the text), while the atoms and spins still use the parameters of Table 4.2, with 1.21 ps of equilibration and 6.05 ps of thermal averaging. (b) Calculations in increased system sizes of $\boldsymbol{N} = 4 \times 4 \times 10$ at $x = 0.1$ and $\boldsymbol{N} = 6 \times 6 \times 4$ at $x = \frac{14}{144}$, using $N_i^k = 2$ k-points in every direction. The two variants (i) and (ii) of the $6 \times 6 \times 4$ simulation cell correspond to layer-ordered and layer-disordered metastable state variants for starting the thermostat calculations. These three simulations are carried out with 1.21 ps of equilibration and 3.63 ps of thermal averaging. All error bars represent the maximum block-estimate of the thermal averages' standard deviations (see Sec. 3.4).

ing. All three of these simulations, the reduced friction, the BO-MD, and the increased k-grid, confirm the orbital-order phase transition around 270 K. The averages of the heating-runs from Fig. 4.6 are included for comparison as a dashed black line in Fig. 4.10. In the shorter simulations we still observe a rather good convergence of the block-estimate of the mean's standard deviation (similar to Fig. 3.3(a)) away from the transition region, while the error estimate in the transition region should only be regarded as a lower bound and longer simulation times are needed to even estimate the error. We consider these shorter simulation runs mainly as a qualitative confirmation of the transition temperature presented in Fig. 4.6.

All the finite-temperature results presented so far have been carried out in the $4 \times 4 \times 4$ simulation cell at doping $x = \frac{6}{64} = 0.09374$. As outlined while discussing the metastable mixtures at $0 < x < 0.25$ in Sec. 4.1.4, the ground-state configuration found in this simulation cell is about 2 meV higher in energy compared to the phase separation energy line (see also the energy-over-doping diagram, Fig. 4.1). To confirm that this choice has no influence on the order of magnitude of the phase transition temperature, we carried out a shorter qualitative simulation in a $\boldsymbol{N} = 4 \times 4 \times 10$ simulation cell at the exact doping $x = 0.1$. The two types of order are completely layer-filling for this structure and the spin-pattern is given by the first entry of Table 4.1. Its energy is less than 1 meV above the phase separation energy line. We stay with a k-grid of $\boldsymbol{N}^{\boldsymbol{k}} = 2 \times 2 \times 2$. The simulation is again carried out with 1.21 ps of equilibration and 3.63 ps of thermal averaging and presented in Fig. 4.10(b). The decay-behavior of the order parameter is very close to the results obtained in the smaller simulation cell (included as dashed black line in Fig. 4.10(b)). The high-temperature residual values match as well, which is not surprising, as the systems share the same dimensions in the x and y direction.

Of more interest are thus systems which increase these in-plane dimensions. We carried out simulations in a $\boldsymbol{N} = 6 \times 6 \times 4$ simulation cell at doping $x = \frac{14}{144} \approx 0.0972$, starting from two different (metastable) ground states: (i) with all hole-defects accumulated in a single x-y-layer, which we believe is the energetically lowest structure to be found for these system dimensions and doping, with an energy of $E_{pot}/N_R = -0.1747$ eV; about 2 meV above the phase separation line and (ii) from a metastable state with the hole-defects rather disordered throughout the cluster, encased by the $PrMnO_3$-like type-(I) order, with $E_{pot}/N_R = -0.1702$ eV; about 6 meV above the phase separation line. Due to the large system size, both simulations are again carried out with the reduced 1.21 ps equilibration and 3.63 ps thermal averaging time and should be taken as qualitative confirmations of the phase transition. The results are presented in Fig. 4.10(b). In both simulations, we observe a large drop of the order parameter close to 270 K. The higher-temperature tail of the order parameter after the main drop is much reduced compared to all previous calculations, which indicates that it was caused by the small in-plane system size taken before. We cannot exclude that the slightly different doping of the calculations presented in Fig. 4.10(b) compared to the previous results has some influence on the transition behavior or temperature as well.

The curves for this system size ($6 \times 6 \times 4$) have some resemblance with

the typical $(1 - T/T_c)^\beta$ decay of the order parameter when approaching the transition temperature in a continuous phase transition, see, e.g., Ref. [158]. A naive non-linear least squared fit using the Levenberg–Marquardt algorithm (see Refs. [159, 160]) implemented in the software gnuplot (see Ref. [161]) of this function to the data points up until 300 K yields (i) $\beta = 0.141 \pm 0.006$, $T_C = 280.0 \pm 0.2$ K, and (ii) $\beta = 0.21 \pm 0.02$, $T_C = 299.8 \pm 0.6$ K. However, we already mentioned that the sampling time in these larger systems is much reduced and the mean values of each block in the blocking method (see Sec. 3.4 and Refs [149, 150]) are still likely to be correlated, thus underestimating the error given in Fig. 4.10(b).

In addition, even larger systems and more sampling points close to the transition temperature are needed to truly estimate finite-size effects and perform a rigorous finite-size scaling that could provide more information about the type of the phase transition, see, e.g., Refs. [157, 162–164]. Such large systems and long run times will require a significant speed-up of the thermostat calculations in a potential future study. One direct approach would be to increase the fictitious masses of the electrons and spins, together with the integration time-step Δt. Such an adjustment has to be carefully evaluated, as too large fictitious masses will lead to an increased energy transfer between the atoms and the fast degrees of freedoms. Alternatively, one could reduce the complexity of the model, for example by neglecting the electron-electron interaction. We mentioned that models using a strong Jahn-Teller interaction can describe manganites quite accurately also without the electron-electron interaction (see Sec. 2.3 and Refs. [27, 82]), and this could give access to thermostat calculations of larger system sizes.

In this thesis, we settle for the statement that we find strong indications for a Jahn-Teller and accompanied orbital-order phase transition at temperatures much lower than according to the established phase diagram (see Fig. 2.5). Increasing the system size and performing a longer sampling might shift the exact transition temperature away from the current estimate of around 270 K, but is unlikely to move it to the high values of about 675 K according to Ref. [58].

Of more relevance might be an improved description of the spin degrees of freedom, beyond the adiabatic approximation, and of their independent magnetic phase transitions. This is an interesting subject for a future study, but beyond the scope of this thesis. As outlined before, we can speculate that the spin-disordered state is more likely to reduce the orbital-order transition temperature further, but this cannot be verified without additional calculations.

The adiabatic approximation is used for the e_g electrons as well, and we could even confirm that the transition temperature stays unchanged when switching from CP-MD to BO-MD. Non-adiabatic corrections for the electronic degrees of freedom become more relevant when the system becomes metallic. This does not happen in the temperature range of the orbital-order transition presented here, as observed by experimental measurements (see Ref. [24]), but also in our tight-binding model from the one-particle estimate of the band gap, which stays positive during the phase transition. For example, at 280 K, it has an average value of $\Delta_{E_g} \approx 0.131$ eV in the CP-MD runs presented in Fig. 4.6.

However, this value should be taken with much caution, as the dynamic e_g electrons do not necessarily reproduce the ground-state densities during the snapshots and because the estimate relies on the small k-grid only. Non-adiabatic effects are analyzed in much more detail in the chapters 5 and 6. One of the methods presented and benchmarked there and in Ref. [37], the fewest-switches surface hopping (see Ref. [29]), is an intriguing candidate to extend the adiabatic molecular dynamics carried out here to non-adiabatic regimes. While including non-adiabatic effects might already be useful to confirm the transition temperatures in future studies beyond the adiabatic approximation, it is of more importance as soon as one seeks a direct simulation of non-equilibrium setups, such as after a photoexcitation.

4.2.2 $x = 0$

Next, we look at the orbital-order phase transition for pure $PrMnO_3$ at $x = 0$. Here, there is no ambiguity of the ground-state structures as for the mixed phases studied around $x = 0.1$. The general protocol of the simulations is similar to before, and we use the parameters outlined in Table 4.2. The calculations are performed in a $4\times4\times4$ simulation cell with $N_i^k = 2$ k-points in every direction. For both the heating and cooling runs we use an equilibration time of 2.42 ps, followed by 12.1 ps of thermal averaging. We resort again to a two-step cooling procedure, with the first set of runs cooling down from 500 K below the main transition region, and a second set of runs continuing down until 20 K, starting from the 360 K final configurations of the first set of cooling runs. The heating and cooling results for the Jahn-Teller order parameter are shown in Fig. 4.11.

In these simulations, we observe that the two-step cooling procedure recovers the high order of the ground state almost perfectly, with only one of the six simulation runs ending up in a defect state for some low temperatures. In contrast to the results at $x = 0.1$, the transition is much more abrupt around a temperature of 400 K. The transition is again unchanged upon decreasing the frictions to half their values (not shown). The errors estimated from the blocking method (see Sec. 3.4.2) indicate high uncertainties in the transition region, while the convergence in the ordered and disordered regions is very good. We cannot rule out that the type of the transition differs from the $x = 0.1$ phase transition at this point, and larger system results with an increased thermal averaging time in the transition region are needed for a further analysis.

The behavior in the ordered and the disordered temperature regimes is, however, very similar to before. We still observe a short-range ordering and strong local Jahn-Teller distortions at high temperatures, while the long-range Jahn-Teller and orbital order melts. This can be seen from the c-averaged Jahn-Teller correlation functions in Fig. 4.12, shown for three temperatures of an example heating run at (a) $T = 300$ K, (b) $T = 400$ K, and (c) $T = 500$ K. For 300 K, most of the weight is still at the $(\frac{2\pi}{a}, 0)$ peak and to a smaller extend on the $(0, 0)$ peaks, which is caused by the uniform Q_3 mode of the ground state. In addition, we already observe some weight on all other possible diffraction spots. For 500 K, above the transition temperature, the Jahn-Teller correlation function is again mostly independent of the wave vector, with the sum rules

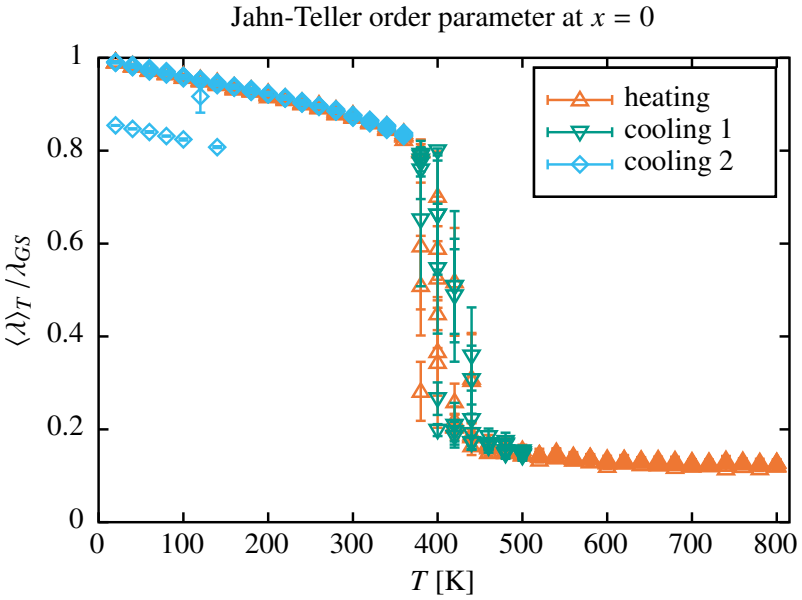

Figure 4.11: Jahn-Teller order parameter (Eq. (4.6)) obtained in a $4 \times 4 \times 4$ simulation cell with $N_i^k = 2$ k-points in every direction at doping $x = 0$. The order parameter at every temperature is divided by the value at $T = 0$ (the ground state). We show 6 different heating runs for temperatures up to 800 K, which start from the ground state configuration, and two sets of six cooling runs, with the first (cooling 1) starting from the 500 K heating simulations, and the second (cooling 2) continuing from the 360 K final configurations of the first set of cooling runs. The results are obtained from thermostat calculations with 12.1 ps of thermal averaging after 2.42 ps of equilibration. The used thermostat parameters are listed in Table 4.2. All error bars represent the maximum block-estimate of the thermal averages' standard deviations (see Sec. 3.4).

of the oxygen displacements still reducing the weight on the diagonals (as discussed before, see Sec. 4.2.1). Due to the larger uncertainties of the thermal averaging at 400 K, we find varying amounts of long-range order in the different simulation runs, and selected an average example in Fig. 4.12(b).

As before, we cannot reproduce the magnetic phase transition with our adiabatic description of the spin degrees of freedom, which is shown with the different spin correlation function peaks $(0, 0, q_c)$ in Fig. 4.13. In contrast to the A/B-mixture obtained at higher doping, presented in Fig. 4.9, we observe a pure A-type antiferromagnetic order at low temperatures. The A-type order vanishes together with the orbital order around 400 K, which does not fit to the experimental results indicating a Néel-temperature of ≈ 91 K, see Refs. [58, 83].

Both, the influence of including a physical temperature for the spin degrees of freedom and a larger system analysis at this doping are interesting prospects for future investigation of this phase transition, but are not available. The results here are again taken as a qualitative assessment of the orbital-order phase transition temperature, trying to estimate whether the orbital order can persist up to the proposed ≥ 900 K (see Refs. [57, 58, 118, 119]) in our tight-binding thermostat calculations, which does not seem to be the case.

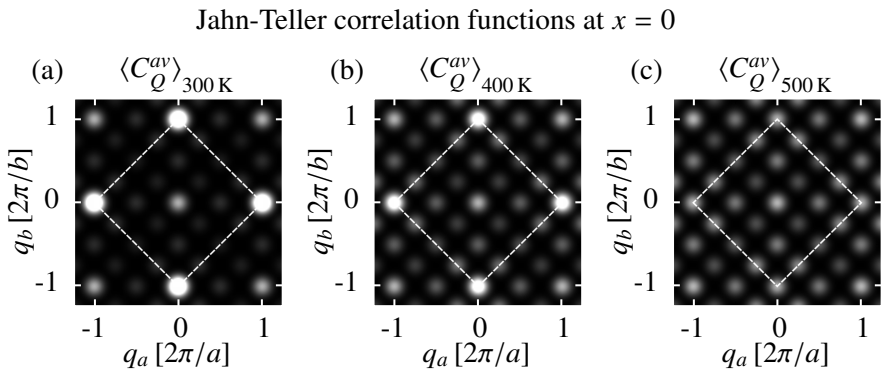

Figure 4.12: c-averaged Jahn-Teller correlation functions (see Eqs. (4.2) and (4.5)), for an exemplary heating run at temperatures (a) 300 K, (b) 400 K, and (c) 500 K, in the $4 \times 4 \times 4$ simulation cell with $N_i^k = 2$ k-points in every direction at doping $x = 0$. We use the same simulation protocol and thermostat parameters as in Fig. 4.11, and the same Gaussian-broadening as before (see Fig. 4.2). The white dashed lines indicate the size of the reciprocal unit cell.

4.2.3 Reevaluation of the phase diagram of $Pr_{1-x}Ca_xMnO_3$

The breakdown of the long-range Jahn-Teller and orbital order at $\sim$ 270 K for $x = 0.1$ and 400 K for $x = 0$ in our thermostat calculations fits well to the measured change in the lattice parameters at 300 K and 350 K with X-ray diffraction experiments in Ref. [24]. The results support the proposed idea that spontaneous orbital order driven by the Mn-e_g electron-electron and Jahn-Teller electron-phonon interactions melts at much lower temperatures than previously believed, see Ref. [24]. The remaining orbital order measured with resonant X-ray diffraction in the similar material $LaMnO_3$ (see Ref. [120]) at higher temperatures might be induced by the tilting in the real system.

The coupling of several types of order parameters in the Landau theory of phase transition has been discussed, for example, in Ref. [165]. In a similar spirit, P. E. Blöchl proposed in Ref. [24] the introduction of a bilinear term in a Landau-type free energy expression for the orbital x and tilting y order parameters: $-\alpha x y$. The orbital-order parameter x could, e.g., be the staggered orbital-pseudomagnetization (see the discussion below Eq. (4.6)), with a coupling to the octahedral tilting y. Introducing this coupling term for two second-order phase transitions and assuming a finite-width transition toward a saturated value for both transitions individually by using a prefactor of $\tanh\left(\frac{T-T_C}{\Delta}\right)$, one can write down a simplified free energy expression:

$$F_T(x,y) = \frac{1}{4}x^4 + \tanh\left(\frac{T-T_x}{\Delta_x}\right)\frac{1}{2}x^2 + \frac{1}{4}y^4 + \tanh\left(\frac{T-T_y}{\Delta_y}\right)\frac{1}{2}y^2 - \alpha x y. \tag{4.8}$$

Without coupling, each order parameter undergoes a second-order like phase transition at the temperatures T_x and T_y with a finite width of Δ_x and Δ_y. Using the values $T_x = 300$ K and $\Delta_x = 50$ K for the orbital order, and $T_y = 700$ K

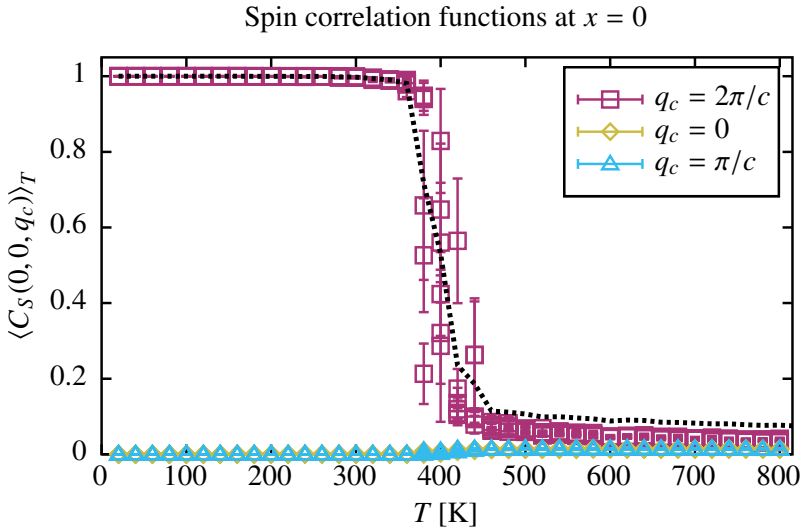

Figure 4.13: Spin correlation functions $\langle C_S(0,0,q_c)\rangle_T$ obtained from thermal averaging during the heating runs in the $4 \times 4 \times 4$ simulation cell with $N_i^k = 2$ k-points in every direction at doping $x = 0$ (see Fig. 4.11 for details on the simulation). We show the peaks at $q_c = 2\pi/c$ (A-type AFM), $q_c = \pi/c$ (which is equal to $q_c = -\pi/c$) and $q_c = 0$ (B-type FM). The sum of all the x-y-plane-ferromagnetic peaks $\sum_{q_c} \langle C_S(0,0,q_c)\rangle_T$ is included as black dashed line. All error bars represent the maximum block-estimate of the thermal averages' standard deviations (see Sec. 3.4).

and $\Delta_y = 100\,\mathrm{K}$ for the tilting, one arrives at temperature-dependent order parameters given by the two dotted lines in Fig. 4.14. The tilting (gray dots) breaks down at 700 K, and independently the orbital order (black dots) at 300 K (both have been scaled to 1 at $T = 0\,\mathrm{K}$).

With a coupling turned on, here $\alpha = 0.9$ (preferring equal order parameter signs), we instead observe the blue-dashed line for the tilting parameter and the solid red line for the orbital order parameter in Fig. 4.14. The orbital order shows two plateaus, the first at high values (higher than without coupling) at low temperatures, with a drop toward a second plateau at the spontaneous orbital-order transition temperature T_x. Only at the tilt-transition at T_y the remaining orbital order vanishes. The parameters of the free energy model have been chosen such that the orbital-order curve resembles that of the resonant X-ray diffraction results of $LaMnO_3$, presented in Ref. [120]. We differentiate between the spontaneous and induced order by the question whether they still persist without the coupling to the tilt pattern.

One cannot easily turn off the tilt pattern and no additional symmetries are broken by the spontaneous orbital order in the presence of the octahedral tilt, hence, one might still refer to the high-temperature tilt transition as the orbital-order transition. Since a weaker tilt-coupling to the orbital order around $x = 0.25$ is present as well, and visible in a second plateau in the resonant X-ray diffraction experiments, see Ref. [88], this would shift the orbital-order transition temperature also in this regime to much higher values. The observed change in the physical parameters at the lower, spontaneous orbital-order transi-

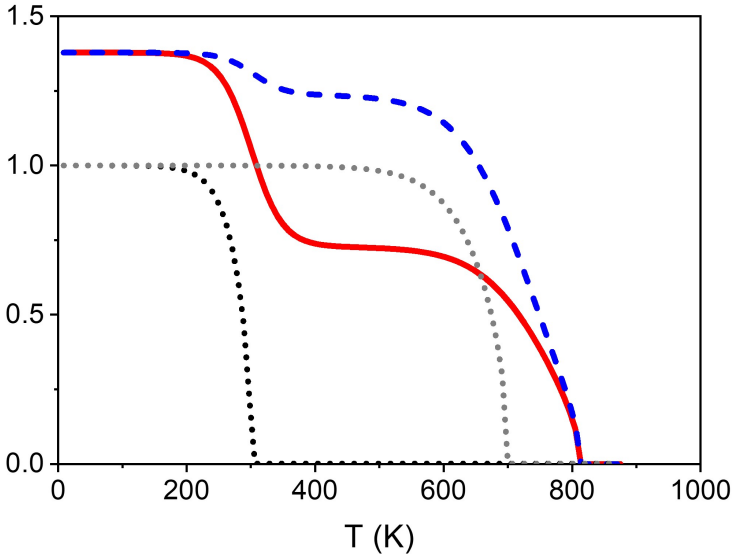

Figure 4.14: Order parameters for a range of temperatures according to the free energy expression of two coupled order parameters, see Eq. (4.8), with the parameters $T_x = 300\,\mathrm{K}$, $\Delta_x = 50\,\mathrm{K}$, $T_y = 700\,\mathrm{K}$ and $\Delta_y = 100\,\mathrm{K}$. The dotted lines show the x (black line) and y (gray line) order parameter for $\alpha = 0$, and the blue-dashed and red-solid lines the same order parameters for $\alpha = 0.9$. All values are scaled to the $T = 0\,\mathrm{K}$ values obtained with $\alpha = 0$. Reprinted figure with permission from Ref. [24]. Copyright (2022) by the American Physical Society.

tion is, however, similar to the orbital- and charge-order transition in the region $0.3 < x < 0.8$. This includes the important onset of a photovoltaic effect only below the spontaneous ordering temperatures.

We thus follow Ref. [24] and locate the transition temperature for the orbital order at the proposed spontaneous transition. In the search for new manganite-like materials with a high onset-temperature for a photovoltaic effect, it might be this spontaneous orbital order one has to look out for, instead of just considering general structural changes of the material. In this sense, a revised phase diagram has been presented in Ref. [24], emphasizing the spontaneous transition at low temperatures, and including the literature results outlined in this chapter and in Sec. 2.4.2. This revised phase diagram is shown in Fig. 4.15, with the theoretical results from this chapter indicated as crossed-out golden squares. In Ref. [24], preliminary results for the $x = 0$ phase transition indicated a transition temperature of about 360 K. We adjusted the values to 400 K according to the well-sampled results presented in Sec. 4.2.2.

The theoretical results presented in this chapter provide a starting point for various possible improvements and further studies. Increasing the system sizes and thermal averaging, especially around the transition temperature, could give further access to the type of transition. We cannot, however, rule out that the neglected octahedral tilt-pattern influences this type in the real material. An explicit treatment of the tilt-pattern is thus another possibility, either as a static background potential, or dynamically in hope to capture the high-temperature

tilt transition. This requires further parameter adjustment to experimental measurements or *ab initio* calculations. Of most interest in our point of view is an improved description of the spin subsystem, beyond the adiabatic approximation. This could allow to capture the magnetic transition at lower temperatures and observe the influence of this transition onto the orbital-order transition. One possibility for such an improved description is the introduction of a generalized thermostat for the spin system, see Refs. [147, 154, 155].

Beyond just the investigation of phase transitions, a direct simulation of the photoexcitation could give further insight into how the spontaneous orbital order is coupled to the onset of the photovoltaic effect. This definitely requires to leave the adiabatic description for the electronic degrees of freedom. A detailed review and benchmark study of two quantum-classical methods that are able to describe the relevant non-adiabatic effects is described in the next two chapters. In particular, the fewest-switches surface hopping might be a potential candidate for non-equilibrium thermal studies with the tight-binding model in the future.

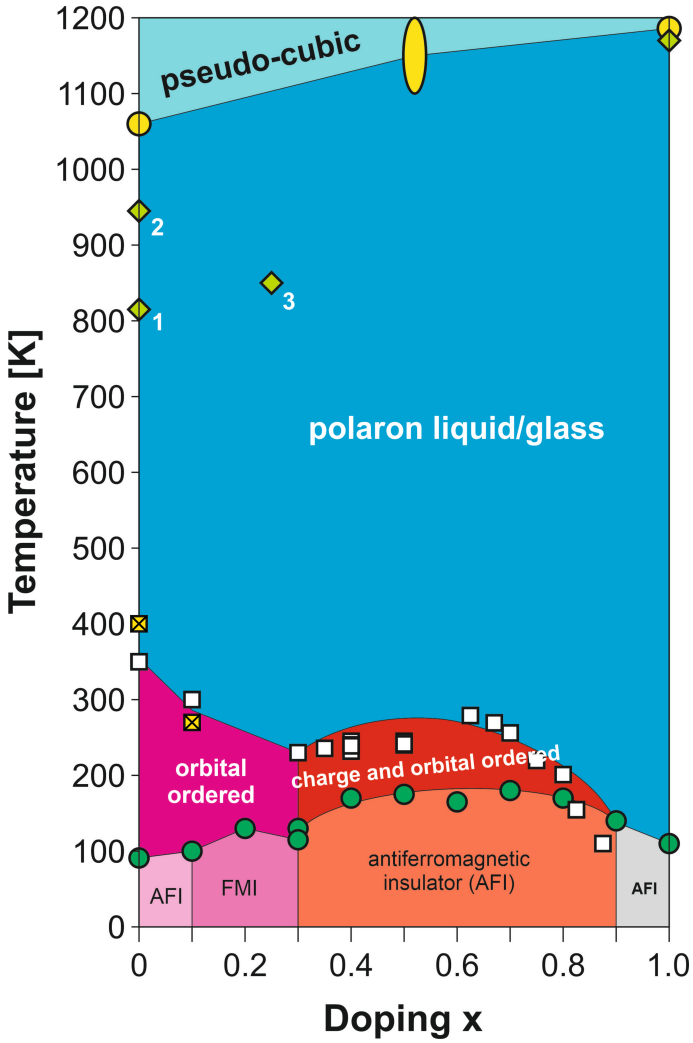

Figure 4.15: Revised phase diagram of bulk $Pr_{1-x}Ca_xMnO_3$ with the spontaneous orbital-order transition indicated at low doping. Results from Refs. [57, 58, 83, 88, 89, 93, 117, 156, 166] are included, see Ref. [24] for a list of the various transition temperatures. In comparison to Fig. 2.5, the high-temperature transition to a pseudo-cubic phase has also been indicated at dopings $x = 0$, $x = 0.52$ and $x = 1$, see Refs [57, 156, 166] (yellow circles/ellipse). The high-temperature tilting/structural transitions according to Refs. [119] (1), [57] (2), [88] (3) and for $CaMnO_3$ (Ref. [156]) are included as green diamonds. Magnetic transitions are shown as green circles. The detailed magnetic arrangements in the low-temperature region of the phase diagram are not resolved, see Ref. [58] for details. The charge- and orbital-order transitions are indicated by white squares, which for $x = 0$ and $x = 0.1$ are set to the new values obtained from the second-order change in the lattice parameters at 350 K and 300 K obtained by X-ray diffraction experiments, see Ref. [24]. The thermostat transition temperatures presented in this thesis in Secs. 4.2.2 and 4.2.1 are included as crossed out golden squares. Adapted figure with permission from Ref. [24]. Copyright (2022) by the American Physical Society. The color of the theoretical results indicators has been changed, and the position at $x = 0$ adjusted to the values obtained in this thesis.

5 Non-adiabatic effects in electron-phonon coupled systems: Exact and quantum-classical descriptions

In the last chapter we observed a correlation between the spontaneous orbital-order phase transition and the onset of the photovoltaic effect (see Ch. 4), which immediately suggests the direct simulation of a photoexcitation and the investigation of the subsequent relaxation process in both the orbital ordered and disordered phases. Such a non-equilibrium simulation requires to lift the restriction of keeping the electrons in their instantaneous adiabatic ground state and instead demands an adequate description of excited-state dynamics. A dynamical evolution starting from these excited states leads in most cases to transitions between different adiabatic electronic states, called "non-adiabatic transitions", and the breakdown of the Born-Oppenheimer approximation implicitly invoked in the previous chapters when separating the electronic and nuclear motion, see Refs. [167, 168]. In this chapter, we will review in detail all these concepts and the challenges associated with describing non-equilibrium dynamics in electron-phonon coupled systems on a more fundamental level.

Previous photoexcitation and -relaxation studies for our manganite tight-binding model exist, see Refs. [32, 33], which use an Ehrenfest dynamics description for the coupled dynamics. We want to understand this method with its underlying approximations and explore alternatives and improvements to this approach for future studies of manganites or general polaronic systems. In particular, we are interested in methods that retain the mixed quantum-classical description of the electron-phonon system, while at the same time being able to accurately capture the strong interactions between both subsystems during non-equilibrium dynamics.

The concepts of adiabatic electronic states and surfaces, as well as non-adiabatic effects, will be introduced in the framework of the Born-Huang expansion, which is an exact representation of the composite electron-nuclear wave-function, see Ref. [34]. In this framework, we will introduce and analyze two trajectory-based mixed quantum-classical methods, the previously mentioned Ehrenfest dynamics and the fewest-switches surface hopping approach, see Refs. [29–31]. In the next chapter, Ch. 6, these methods will be carefully benchmarked and tested in the paradigmatic Holstein model, which is much simpler than the manganite tight-binding model, including only non-interacting electrons, uncoupled harmonic phonon oscillators, and a bi-linear electron-phonon coupling, making it the perfect system to focus on electron-nuclear interactions. The Holstein model will already serve as an example system for understanding the Born-Huang expansion, and is introduced in the

next section. The results of the benchmark study and some parts of the theory and methods introduced in this chapter have been published in the article [37], which forms the basis for this and the next chapter.

5.1 The Holstein model

One of the prototypical electron-phonon composite systems is the Holstein model, introduced in Ref. [35]. It includes a lattice of local harmonic oscillator phonon degrees of freedom, which, in the most simple case, are uncoupled and have the same frequency, i.e. dispersionless Einstein phonons. The phonons are combined with non-interacting electrons that can hop between the lattice sites in a one-orbital tight-binding fashion. The electron density on every site couples to the local harmonic oscillator displacement with a bi-linear term. In this model, which does not include electron-electron or phonon-phonon interaction, the electron-phonon interaction is emphasized. Both short and extended polarons emerge, depending on the parameters of the system. With the local creation and annihilation operators for the phonons $\hat{b}_i^\dagger$ and $\hat{b}_i$, and the spinless electron operators $\hat{c}_i^\dagger$ and $\hat{c}_i$ at site i, we can write the Hamiltonian of the model as:

$$\hat{H} = \sum_{<i,j>} -t_0(\hat{c}_i^\dagger \hat{c}_j + \hat{c}_j^\dagger \hat{c}_i) + \sum_i \left[\hbar\omega_0(\hat{b}_i^\dagger \hat{b}_i + 1/2) - \gamma \hat{n}_i \left(\hat{b}_i^\dagger + \hat{b}_i\right)\right] . \quad (5.1)$$

Here, $\hat{n}_i = \hat{c}_i^\dagger \hat{c}_i$ is the electron density on site i and the sum in the hopping term $\sum_{<i,j>}$ sums over all distinctive pairs of nearest neighbor sites. The three relevant parameters of the Holstein model are included in the Hamiltonian (5.1): the electron hopping matrix element t_0, the phonon frequency ω_0 and the electron-phonon coupling γ. In this thesis, we will only consider the special case of one spatial dimension, for which the model was also originally suggested (see Ref. [35]). This allows us to compare approximate methods to numerically exact results of the density matrix renormalization group (DMRG) (see Refs. [48–50]), which works most efficient in 1D-systems. We will always use open boundary conditions for the Holstein model in this work.

Originally, the model was expressed in terms of real-space position $\hat{x}_i$ and momentum $\hat{p}_i$ operators, see Ref. [35], which is also useful for applying the Born-Huang framework in a later step (see Sec. 5.2.2). We can transform the phonon operators using the typical harmonic oscillator ladder operator definition: $\hat{b}_i = \sqrt{\frac{m\omega_0}{2\hbar}}\left(\hat{x}_i + \frac{i}{m\omega_0}\hat{p}_i\right)$, with the nuclear mass m. For our one-dimensional system the Hamiltonian becomes:

$$\hat{H} = \sum_{i=1}^{L-1} -t_0(\hat{c}_i^\dagger \hat{c}_{i+1} + \hat{c}_{i+1}^\dagger \hat{c}_i) + \sum_{i=1}^{L}\left[\frac{m\omega_0^2}{2}\hat{x}_i^2 + \frac{1}{2m}\hat{p}_i^2 - \sqrt{\frac{2m\omega_0}{\hbar}}\gamma \hat{n}_i \hat{x}_i\right], \quad (5.2)$$

where L is the number of lattice sites.

The Holstein model is strongly simplified in contrast to the manganite tight-

binding model. It lacks cooperative phonon distortions, electron-electron interaction and the spin degree of freedom, and has only a single electronic orbital and nuclear mode per site. Hence, it is clear that we cannot use the model to test all the approximations that have been used in the previous chapters, and instead focus on the nuclei and their coupling to the electrons. Here, we can compare a classical to a quantum description for the nuclei, and various treatments of the electron-phonon interaction in trajectory-based algorithms. We note that the model has been used to analyze absorption spectra in $Pr_{1-x}Ca_xMnO_3$ in Ref. [36]. The model in the single-electron variant (also called polaron problem) serves as an example and testbed for the benchmark calculations performed in the next chapter, Ch. 6, and it is not the aim of this thesis to better understand or explore the model itself, which has been studied extensively, see Refs. [169–175]. As we outlined in Ref. [37], in particular the two-site Holstein model, the Holstein dimer, is a well studied system in literature, see Refs. [176–185]. It is studied in quantum chemistry, where it is a simple model system to describe a reaction path, see Refs. [186, 187], but it corresponds also to the one-mode simplification of the spin-boson model, see Ref. [188]. The two-site system will be helpful to understand the concepts of adiabatic surfaces/states and non-adiabatic effects introduced in this chapter.

With the natural length scale of the harmonic oscillators $\hat{\bar{x}}_i = \hat{x}_i / \sqrt{\frac{\hbar}{m\omega_0}}$ (and correspondingly for the momenta) and by setting $\hbar\omega_0$ as energy unit, we can bring the Hamiltonian into a dimensionless form. In the following, dimensionless variables will always be indicated by a bar over the symbols: $\hat{\bar{H}} = \frac{\hat{H}}{\hbar\omega_0}$, $\bar{t}_0 = \frac{t_0}{\hbar\omega_0}$ and $\bar{\gamma} = \frac{\gamma}{\hbar\omega_0}$. This simplifies the Hamiltonian to the following form:

$$\hat{\bar{H}} = \sum_{i=1}^{L-1} -\bar{t}_0(\hat{c}_i^\dagger \hat{c}_{i+1} + \hat{c}_{i+1}^\dagger \hat{c}_i) + \sum_{i=1}^{L} \left[\frac{1}{2}\hat{\bar{x}}_i^2 + \frac{1}{2}\hat{\bar{p}}_i^2 - \sqrt{2}\bar{\gamma}\hat{n}_i\hat{\bar{x}}_i \right]. \tag{5.3}$$

For the dimer, we switch to a relative $\hat{\bar{q}} = (\hat{\bar{x}}_1 - \hat{\bar{x}}_2)/\sqrt{2}$, and a center-of-mass phonon mode $\hat{\bar{Q}} = (\hat{\bar{x}}_1 + \hat{\bar{x}}_2)/\sqrt{2}$, with $\hat{\bar{p}}_q$ and $\hat{\bar{p}}_Q$ the corresponding momenta, to rewrite the Hamiltonian in Eq. (5.3) as:

$$\begin{aligned} \hat{\bar{H}}_{L=2} = &- \bar{t}_0(\hat{c}_1^\dagger \hat{c}_2 + \hat{c}_2^\dagger \hat{c}_1) + \frac{\hat{\bar{q}}^2}{2} + \frac{\hat{\bar{p}}_q^2}{2} + \frac{\hat{\bar{Q}}^2}{2} + \frac{\hat{\bar{p}}_Q^2}{2} \\ &- \bar{\gamma}\left[\hat{\bar{q}}\left(\hat{n}_1 - \hat{n}_2\right) + \hat{\bar{Q}}\left(\hat{n}_1 + \hat{n}_2\right) \right]. \end{aligned} \tag{5.4}$$

In general, the center-of-mass phonon displacement $\frac{1}{\sqrt{N}}\sum_i \hat{\bar{x}}_i$, which corresponds for the Holstein dimer to the variable $\hat{\bar{Q}}$, couples to the constant total number of electrons $N = \sum_i \langle \hat{n}_i \rangle$ and is a simple harmonic oscillator that is independent from the rest of the system. For the dimer, we are left with an effectively one-phonon-mode Hamiltonian in the relative coordinate $\hat{\bar{q}}$, which couples to the difference of the electronic population on the two sites. For larger systems, one can single out the center-of-mass phonon mode by constructing the real discrete Fourier transform of the local nuclear modes. We

use this approach in this thesis only for the dimer and trimer to simplify the visualization of the Born-Oppenheimer surfaces and reduce the computational effort of the numerically exact methods.

For the Holstein trimer, we introduce the three nuclear coordinates:

$$\hat{\tilde{X}} = \frac{1}{\sqrt{3}} \left(\hat{\tilde{x}}_1 + \hat{\tilde{x}}_2 + \hat{\tilde{x}}_3 \right)$$

$$\hat{\tilde{x}}_s = \frac{2}{\sqrt{6}} \left(\hat{\tilde{x}}_2 - \frac{\hat{\tilde{x}}_1 + \hat{\tilde{x}}_3}{2} \right) \tag{5.5}$$

$$\hat{\tilde{x}}_a = \frac{1}{\sqrt{2}} \left(\hat{\tilde{x}}_3 - \hat{\tilde{x}}_1 \right) . \tag{5.6}$$

As for the dimer, the center-of-mass coordinate $\hat{\tilde{X}}$ does not couple to the rest of the system. The symmetric phonon mode $\hat{\tilde{x}}_s$ interacts with the difference of electron density on the central site to the average density on the edge sites. The antisymmetric phonon mode $\hat{\tilde{x}}_a$ couples to the difference of electron densities on the edge sites.

5.2 Non-adiabatic effects in the framework of the Born-Huang expansion

One of the central challenges of both quantum-chemistry and solid-state physics is the description of electron-nuclear composite systems. This includes molecular systems and their chemical reactions, but also extended lattices with any form of interaction between the electrons and the lattice nuclei. An intuitive understanding and qualitative predictions for the dynamics of these systems can be achieved by implicitly or explicitly invoking a separation of the electronic and nuclear time scales. This separation is often justified with the vastly different masses of the respective particles, which M. Born and R. Oppenheimer utilized in their seminal paper, see Ref. [189], to first solve the electronic eigenvalue problem for fixed nuclear positions, and then finding perturbative solutions for nuclear displacements around these positions, see also Ref. [190]. Nowadays, one understands under the "Born-Oppenheimer approximation", or sometimes called "adiabatic approximation", see Ref. [191], the complete separation of electronic and nuclear time-scales, so that electronic eigenenergies are obtained for fixed nuclear positions and the nuclei evolve under the influence of a single electronic eigenenergy, see Refs. [190, 192]. This approximation is useful in both the short-time (∼ femtosecond) and long-time (∼ picosecond-nanosecond) regime of the microscopic time scale, as one singles out the dynamics of only the electrons or the nuclei, respectively. The adiabatic approximation is implicitly utilized when electronic excitation spectra, or short-time dynamics after an excitation or quench, are calculated for fixed nuclear positions in an electron-nuclear composite system, and also forms the basis of Born-Oppenheimer molecular dynamics simulations where classical atoms move in an effective potential build from the instantaneous electronic ground state, see Ref. [190]

and Sec. 3.4.1. A nearly adiabatic approximation was used in Sec. 4.2 when the nuclei where heated with a thermostat, while the electron and spin system were kept close to their ground state using Car-Parrinello molecular dynamics (see Sec. 3.4.1).

While much of the intuitive pictures of molecular dynamics is driven by the adiabatic approximation, it certainly is not always applicable, as sometimes the instantaneous electronic eigenstates change rapidly with the nuclear coordinate, leading to so-called "non-adiabatic effects", which often dynamically couple different electronic states. This becomes especially relevant when analyzing the dynamics of excited electronic states with a strong coupling to surrounding phonons, see Refs. [31, 167, 168], for example after an optical excitation. Fast relaxation channels through radiationless decay involve intersections, or avoided crossings, between electronic states, at which the adiabatic approximation breaks down, analyzed in various aspects in the excellent book in Ref. [133]. It is thus important to better understand which terms are neglected in the adiabatic approximation and how to go beyond the Born-Oppenheimer picture. In this section we review the Born-Huang formalism, see Ref. [34], which is an exact expansion of the total wave function in adiabatic electronic eigenstates. Its language is strongly inspired by the adiabatic approximation, but it allows to directly identify the correction terms to this approximation and to properly define non-adiabatic effects.

5.2.1 A position-dependent electronic basis

In the Born-Huang formalism, but also in the adiabatic approximation, one often talks about electronic states which depend on the nuclear position. This is not an approximation, but simply a change of the representation of the total state. We denote the vector of nuclear positions as R, which contains all $d \cdot N$ nuclear degrees of freedom of the d-dimensional N nuclei: $R = (R_1, \ldots, R_{dN})$. The nuclear momenta are correspondingly described by $P = (P_1, \ldots, P_{dN})$ and the masses of each mode k by m_k. The electrons are described by a discrete orthonormal basis $\{|\chi_a\rangle\}$, which for now does not depend on the nuclear positions (one could also generalize this to the continuous position basis r). The total wave function describing the composite state is thus $\Psi_a(R) = \langle R, \chi_a|\Psi\rangle$, with the abstract total state $|\Psi\rangle$ and the composite electron-nuclear basis $\langle R, \chi_a| = \langle R| \otimes \langle \chi_a|$.

It is straightforward to transform the electronic basis at each nuclear position into a different orthonormal basis:

$$|\Psi(t)\rangle = \sum_a \int \mathrm{d}R\, |R, \chi_a\rangle\, \Psi_a(R,t) = \sum_b \int \mathrm{d}R'\, |R', \phi_b(R')\rangle\, \Psi'_b(R',t) \quad (5.7)$$

$$:= \sum_b \int \mathrm{d}R'\, |R', \phi_b(R')\rangle \left[\sum_a \int \mathrm{d}R\, \langle R', \phi_b(R')|R, \chi_a\rangle\, \Psi_a(R,t) \right]. \quad (5.8)$$

We only need to require that the overlap $\langle R', \phi_b(R')|R, \chi_a\rangle = \delta(R-R')U_{b,a}(R)$ is

defined by a proper unitary transform $U(R)$ for every position R. Here, $\Psi'_b(R', t)$ is a multi-component nuclear wave function in an R-dependent electronic basis. With the knowledge of the transform $U(R)$ at every nuclear position R, it contains the same information as the previous wave function $\Psi_a(R, t)$.

Let us insert the total state in the form of Eq. (5.8) into the Schrödinger equation $i\hbar\frac{\mathrm{d}}{\mathrm{d}t}|\Psi(t)\rangle = \hat{H}|\Psi(t)\rangle$, where $\hat{H}$ is the total (non-relativistic) electron-nuclear Hamiltonian of the system, which for a typical molecular or solid-state system contains the kinetic energy of electrons and nuclei, and interaction terms between all particles. It is instructive to separate the Hamiltonian into two parts: the kinetic energy of the nuclei $\hat{T}_{nuc} = \sum_k \frac{\hat{P}_k^2}{2m_k}$ and all other terms, which do not depend on the nuclear momentum:

$$\hat{H} = \hat{T}_{nuc}(\hat{P}) + \hat{H}^{BO}(\hat{R}). \tag{5.9}$$

These remaining terms are summarized in a term called the Born-Oppenheimer (BO) Hamiltonian $\hat{H}^{BO}$. Inserting the state of Eq. (5.8) into the Schrödinger equation and multiplying from the left with $\langle R, \phi_a(R)|$, we arrive at an equation for the nuclear wave function $\Psi'_a(R, t)$, see Ref. [191]:

$$i\hbar\frac{\mathrm{d}}{\mathrm{d}t}\Psi'_a(R,t) = \sum_b \left[\sum_k \frac{1}{2m_k}\left(\mathbf{1}\frac{\hbar}{i}\nabla_k + \bar{\bar{\boldsymbol{A}}}_{(k)}(R)\right)^2 + \boldsymbol{V}(R)\right]_{a,b} \Psi'_b(R,t). \tag{5.10}$$

Here, bold-face symbols are matrices in the chosen R-dependent electronic basis, with the identity $(\mathbf{1})_{a,b} = \delta_{a,b}$ and the two quantities:

$$V_{a,b}(R) = \langle R, \phi_a(R)|\hat{H}^{BO}(\hat{R})|R, \phi_b(R)\rangle = \langle \phi_a(R)|\hat{H}^{BO}(R)|\phi_b(R)\rangle\,, \tag{5.11}$$

$$\bar{\bar{A}}_{a,b,(k)}(R) = \langle R, \phi_a(R)|\hat{P}_k|R, \phi_b(R)\rangle = \langle \phi_a(R)|\frac{\hbar}{i}\nabla_k|\phi_b(R)\rangle\,. \tag{5.12}$$

The $V_{a,b}(R)$ are matrix elements of the Born-Oppenheimer Hamiltonian in the electronic basis, the R-dependence enters only parametrically. The $\bar{\bar{A}}_{a,b,(k)}(R)$ capture the influence of the nuclear momentum operator on the R-dependent electronic basis. The double-bar over the quantity A is introduced here for the general position dependent basis $\{|\phi_b(R)\rangle\}$. In most cases this quantity is used for the specific basis of the Born-Oppenheimer states, see Sec. 5.2.2, for which we will omit the bars. The k-components of each matrix element can be summarized into a vector $\vec{\bar{\bar{A}}}_{a,b}(R) = \langle \phi_a(R)|\frac{\hbar}{i}\vec{\nabla}|\phi_b(R)\rangle$, which is called the derivative coupling between the electronic states a and b. The derivative couplings take the form of a vector potential in the nuclear Schrödinger equation (5.10). For a nuclear-position-independent electronic basis $|\chi_a\rangle$, as in Eq. (5.7), this term vanishes and we are left with the typical Schrödinger equation containing the nuclear kinetic energy and matrix elements of all other terms. The R-dependence of the electronic basis, however, provides an additional flexibility, as we can choose a different basis set for each nuclear position. This is used in the Born-Huang expansion explained in the next subsection.

5.2.2 The Born-Huang expansion

The central idea of the Born-Huang formalism (see Ref. [34]) is to use an electronic basis in which the V-matrix defined in Eq. (5.11) becomes diagonal. This is exactly the eigenbasis of the Born-Oppenheimer Hamiltonian, which can be obtained from the (R-dependent) eigenvalue problem:

$$\hat{H}^{BO}(R)\,|\phi_a^{BO}(R)\rangle = E_a^{BO}(R)\,|\phi_a^{BO}(R)\rangle\,, \tag{5.13}$$

to expand the total state as:

$$|\Psi(t)\rangle = \sum_a \int \mathrm{d}R\,|R, \phi_a^{BO}(R)\rangle\,\Psi_a(R,t). \tag{5.14}$$

The states $|\phi_a^{BO}(R)\rangle$ are called Born-Oppenheimer states and form a complete electronic basis for every nuclear position R. Correspondingly, the Born-Oppenheimer energies $E_a^{BO}(R)$ describe electronic energies for every nuclear position and thus form energy surfaces named "Born-Oppenheimer surfaces" in the nuclear configuration space. In the nuclear Schrödinger equation (Eq. (5.10)) they take the form of potential energy surfaces $V_{a,b}(R) = \delta_{a,b}E_a^{BO}(R)$, along which the multi-component nuclear wave function evolves under the influence of the derivative couplings $\vec{A}_{a,b}(R) = \langle\phi_a^{BO}(R)|\frac{\hbar}{i}\vec{\nabla}|\phi_b^{BO}(R)\rangle$ (now for the Born-Oppenheimer states and without the bars) as vector potential:

$$i\hbar\frac{\mathrm{d}}{\mathrm{d}t}\Psi_a(R,t) = \sum_b \left[\sum_k \frac{1}{2m_k}\left(\mathbf{1}\frac{\hbar}{i}\nabla_k + \boldsymbol{A}_{(k)}(R)\right)^2 + \boldsymbol{E}^{BO}(R)\right]_{a,b} \Psi_b(R,t). \tag{5.15}$$

Here, $\boldsymbol{E}^{BO}(R)$ is the diagonal matrix containing the Born-Oppenheimer energies $E_a^{BO}(R)$ as diagonal entries. One might ask what we gained from this change of the electronic basis. In a nuclear-position-independent electronic basis $\{|\chi_a\rangle\}$, different electronic states are coupled via the off-diagonal elements of the V-matrix $V_{a,b}(R) = \langle\chi_a|\hat{H}^{BO}(R)|\chi_b\rangle$ in Eq. (5.10). If one thinks of a typical tight-binding Hamiltonian, this might be a constant electron-hopping matrix element $V_{a,b}(R) = -t_0$, which does not depend on the nuclear position and thus has to be taken into account in the whole nuclear configuration space. In contrast, in the Born-Oppenheimer basis different electronic states are coupled via the derivative couplings $\vec{A}_{a,b}(R)$ (and the derivative thereof). These terms can become highly peaked around certain nuclear configurations, as can be seen from an alternative representation (see Ref. [191]):

$$A_{a,b,(k)}(R) = \frac{\langle\phi_a^{BO}(R)|\left(\frac{\hbar}{i}\nabla_k\hat{H}^{BO}(R)\right)|\phi_b^{BO}(R)\rangle}{E_a^{BO}(R) - E_b^{BO}(R)}, \quad a \neq b. \tag{5.16}$$

From the denominator, one can expect the derivative couplings to become dominant whenever two Born-Oppenheimer surfaces come close in energy. For regions where the derivative couplings are negligible, which is thus often

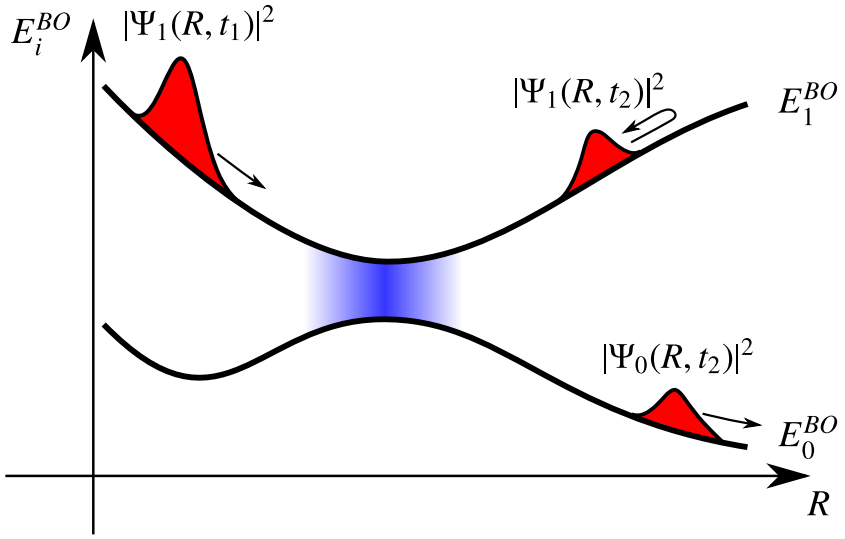

Figure 5.1: A sketch of two Born-Oppenheimer surfaces $E_i^{BO}(R)$ for a nuclear coordinate R. The surfaces are drawn as thick black lines, the derivative couplings between the surfaces as blue area between the surfaces, and an exemplary wave function density $|\Psi_i(R,t)|^2$ at two times t_1 and t_2 as red filled curves on top of the respective surfaces. The wave function is initially (t_1) on the upper surface and splits into two wave packets (t_2) after moving through the non-adiabatic coupling region.

the case for far separated surfaces, the different components of the nuclear wave function will evolve independently in their corresponding *adiabatic* potential energy surfaces, making it easy to develop an intuitive understanding of its time evolution.

In the next section we will introduce the adiabatic, or Born-Oppenheimer, approximation, in which the dynamics on the different energy surfaces are regarded as completely independent from one another. Any effect that cannot be described in such an isolated adiabatic surface picture, and thus going beyond the Born-Oppenheimer approximation, is called a *non-adiabatic effect*, see Ref. [191]. The derivative couplings, which are responsible for breaking this approximation, are also called non-adiabatic couplings (see, e.g., Ref. [191]).

A sketch of a visual representation of the electron-nuclear dynamics in the Born-Huang picture is shown in Fig. 5.1. It includes two Born-Oppenheimer surfaces $E_{i=0,1}^{BO}$ as function of some nuclear coordinate R as thick black lines and the region of significant non-adiabatic coupling as a blue area between the surfaces. Outside of this region, the derivative couplings (and their derivatives) are negligible and the wave function will evolve corresponding to the potential build by the Born-Oppenheimer surfaces, while within this region, the derivative couplings allow for transitions between the surfaces and modify the effective potential acting on the wave function. An example wave function is shown at two times with its density $|\Psi_i(R,t)|^2$ drawn as red filled curves on the respective surfaces $i = 0, 1$. At time t_1 the wave function starts on the upper surface. The shape of the surface forces the wave packet toward the non-adiabatic coupling region, where it partially transitions to the lower surface (a

non-adiabatic transition). After both portions of the wave function leave this region, their dynamics are again dictated by the Born-Oppenheimer surfaces alone. The different shapes of the two surfaces will lead to a spatial separation of both wave packets at later times $t > t_2$.

Often only a few adiabatic surfaces are necessary to describe the whole dynamical evolution accurately, while higher and lower lying states are ignored (for example, the system described by the sketch in Fig. 5.1 might include more Born-Oppenheimer states, which are, however, far separated for all nuclear configurations and thus irrelevant for the dynamics). This feature of the adiabatic basis is also called compactness, see Ref. [74]. We note that one should be careful in discarding states too easily. In particular, only because two energy surfaces are far separated in the nuclear configuration space occupied by the wave function during the whole time evolution, it is not guaranteed that they do not influence each other. This is due to the possibility of surface crossings in the form of conical intersections, at which the derivative couplings diverge and a geometric phase effect emerges, see Refs. [70–72, 74], also called Berry phase, see Ref. [73].

An obvious question is whether there is an alternative electronic basis in which the derivative couplings (Eq. (5.12)) vanish completely and which still allows a compact description with only a few electronic basis states contributing to the dynamics. This is the idea of a diabatic basis, see Refs. [193–195], which is usually constructed as a linear combination of adiabatic states and typically changes less abruptly in the nuclear position space than the adiabatic basis, see Refs. [194–197]. As pointed out by Ref. [198], however, in general no such diabatic basis exists, with the exception of the "trivial diabatic" basis that does not depend on the nuclear coordinates and for which the derivative couplings vanish by definition.

In the following, when we talk about the adiabatic or diabatic basis, we always refer to the Born-Oppenheimer or a nuclear-position-independent basis, respectively. For later reference the two possible expansions are:

$$|\Psi(t)\rangle = \sum_a \int \mathrm{d}R \, |R, \phi_a^{BO}(R)\rangle \, \Psi_a^{(a)}(R,t) \tag{5.17}$$

$$= \sum_a \int \mathrm{d}R \, |R, \chi_a\rangle \, \Psi_a^{(d)}(R,t) \tag{5.18}$$

where the superscripts (a) and (d) refer to the multicomponent nuclear wave function in the adiabatic and diabatic basis.

To summarize, the Born-Huang formalism is an exact reformulation of the dynamical electron-nuclear composite problem, which expands the total wave function in Born-Oppenheimer eigenstates. The corresponding nuclear wave function components evolve in a set of potential energy surfaces build from the Born-Oppenheimer eigenenergies under the influence of a vector potential called the derivative couplings.

5.2.3 The Born-Oppenheimer/adiabatic approximation

One of the best known approximations to electron-nuclear systems is the adiabatic, or Born-Oppenheimer, approximation. In the Born-Huang framework, with the Born-Oppenheimer electronic basis, this approximation simply corresponds to neglecting all derivative couplings $\vec{A}$ in the nuclear Schrödinger equation (5.15). With the couplings between the different surfaces removed, each component of the nuclear wave function evolves on a single Born-Oppenheimer surface, independent of the other components:

$$i\hbar\frac{\mathrm{d}}{\mathrm{d}t}\Psi_a^{(a)}(R,t) \approx \left[\sum_k \frac{-\hbar^2\nabla_k^2}{2m_k} + E_a^{BO}(R)\right]\Psi_a^{(a)}(R,t). \tag{5.19}$$

We note that some authors differentiate between the adiabatic and the Born-Oppenheimer approximation in that the latter only ignores the off-diagonal derivative couplings, see, e.g., Ref. [191]. In this thesis we will use both terms interchangeably to refer to the approximation which neglects all derivative couplings. A time-evolution obtained according to Eq. (5.19) will leave the electronic populations of the Born-Oppenheimer states $\int \mathrm{d}R|\Psi_a(R)|^2$ constant over time and the Born-Oppenheimer states are treated like (R-dependent) electronic eigenstates of the system.

This approximation forms the basis of the often used Born-Oppenheimer molecular dynamics (BO-MD) approach, discussed in the context of the manganite tight-binding model in Sec. 3.4.1, to which the Car-Parrinello molecular dynamics applied for the finite-temperature phase transitions presented in Sec. 4.2 can be seen as an approximation. BO-MD assumes that the electrons start in the lowest Born-Oppenheimer state. Furthermore, its energy surface is assumed to be sufficiently far separated from all other Born-Oppenheimer surfaces to justify that the Born-Oppenheimer approximation is valid and non-adiabatic transitions are negligible. In addition, quantum effects of the nuclei are neglected in the BO-MD approach and they are described as classical point particles (as in any molecular dynamics simulation). Instead of the Born-Oppenheimer Schrödinger equation (5.19), they follow the classical Newton's equation of motion for particles in a potential given by the lowest Born-Oppenheimer surface E_0^{BO}.

Once this energy surface has been constructed/calculated for a problem of interest, the electrons are not longer relevant for the dynamics of the system. In quantum chemistry this led for some time to a separation of tasks, with some groups working on determining the energy surfaces, and other groups using them, see Ref. [190]. For most realistic models describing materials, an exact (or suitably fitted) analytic expression for the lowest Born-Oppenheimer surface is not available and its energy and derivative (needed to calculate the forces acting on the nuclei) are obtained in on-the-fly electronic structure calculations, see Ref. [144, 199], denoted as *ab initio* molecular dynamics (see Sec. 3.4.1). We refer to Ref. [200] for a recent overview of methods relying on such an on-the-fly approach, several of which will be introduced later in Sec. 5.3.

One can certainly use the Born-Oppenheimer approximation and still con-

sider the nuclei as quantum mechanical particles, or utilize a mixed ansatz for the nuclear wave function, such as the truncated Wigner approach, see Ref. [201], where the initial quantum state is correctly sampled in phase space, but the subsequent dynamics follow approximated classical equations of motion. This ansatz will be described in more detail in Sec. 5.3.1. Alternatively, one can improve Born-Oppenheimer molecular dynamics in the other direction: keeping the classical nuclei, but allowing non-adiabatic transitions between electronic surfaces, i.e., going beyond the Born-Oppenheimer approximation. This is especially relevant for the non-equilibrium dynamics of excited electronic states, which will often involve more than one Born-Oppenheimer state. Such methods that combine a classical description of the nuclei with a quantum mechanical description of the electrons and allow for non-adiabatic transitions are one main focus for the remainder of this thesis and will be introduced in Sec. 5.3.

5.2.4 Born-Huang for the Holstein dimer and trimer

We can now apply the Born-Huang formalism to the Holstein dimer and trimer to better understand the shape of their Born-Oppenheimer surfaces. The Holstein dimer serves also as an example to visualize the effect of the non-adiabatic coupling and how to think in terms of the Born-Huang formalism.

Born-Huang for the Holstein dimer

The Born-Oppenheimer Hamiltonian of the Holstein dimer for a system with exactly one electron can be written as a 2×2-matrix in the basis of the two site-local electronic states $|\chi_i\rangle = c_i^\dagger |0\rangle$, $i = 1, 2$. Omitting the irrelevant center-of-mass phonon mode $\bar{Q}$ and keeping only the relative distortion mode $\bar{q} = (\bar{x}_1 - \bar{x}_2)/\sqrt{2}$ (see Eq. (5.4)), it becomes:

$$\hat{\bar{H}}^{BO}_{L=2}(\bar{q}) = \begin{pmatrix} \frac{\bar{q}^2}{2} - \bar{\gamma}\bar{q} & -\bar{t}_0 \\ -\bar{t}_0 & \frac{\bar{q}^2}{2} + \bar{\gamma}\bar{q} \end{pmatrix}. \tag{5.20}$$

This matrix can easily be diagonalized analytically, see Ref. [186], to obtain the Born-Oppenheimer energies:

$$\bar{E}^{BO}_{\pm}(\bar{q}) = \frac{\bar{q}^2}{2} \pm \sqrt{\bar{q}^2\bar{\gamma}^2 + \bar{t}_0^2}. \tag{5.21}$$

The two Born-Oppenheimer surfaces are shown in Fig. 5.2 for the case of $\bar{\gamma}^2/\bar{t}_0 > 1$, where the lower surface has two minima. The two minima merge for $\bar{\gamma}^2/\bar{t}_0 = 1$, and for $\bar{\gamma}^2/\bar{t}_0 < 1$ only a single minimum at $\bar{q} = 0$ is left.

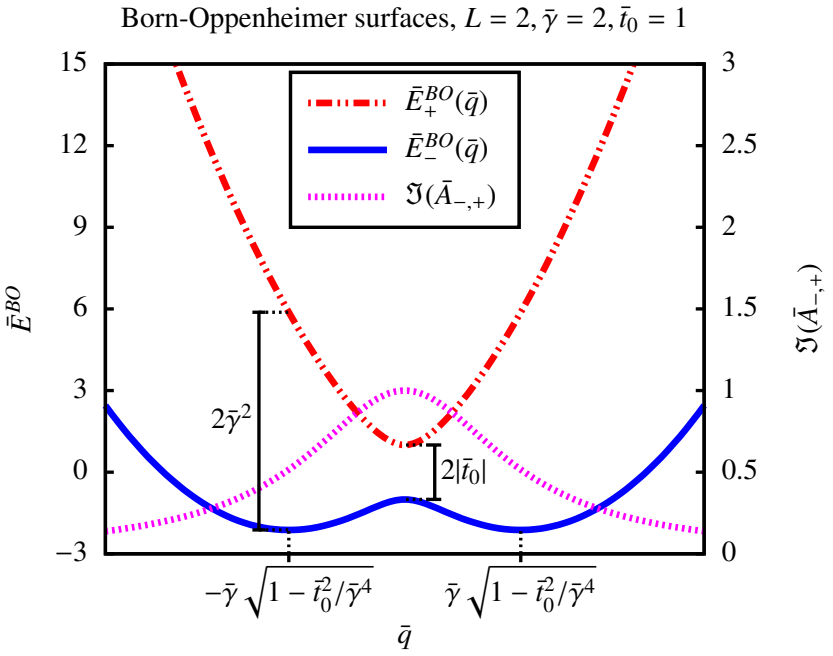

Figure 5.2: Lower and upper Born-Oppenheimer surfaces $\bar{E}^{BO}_{\pm}(\bar{q})$ for the Holstein dimer with $\bar{\gamma} = 2$ and $\bar{t}_0 = 1$, see Eq. (5.21). The imaginary part of the derivative coupling according to Eq. (5.23) is included as well. The separation of the two surfaces at the center and at one minimum of the lower surface are indicated. Reproduced from Ref. [37], with the permission of AIP Publishing. The position of the figure key has been adjusted.

The diagonalization also gives access to the Born-Oppenheimer states:

$$\begin{pmatrix} \phi^{BO}_{\pm,1}(\bar{q}) \\ \phi^{BO}_{\pm,2}(\bar{q}) \end{pmatrix} = \begin{pmatrix} \sqrt{1+\left(\frac{\bar{q}\bar{\gamma}}{\bar{t}_0} \pm \sqrt{\left(\frac{\bar{q}\bar{\gamma}}{\bar{t}_0}\right)^2+1}\right)^2}^{-1} \\ \mp\sqrt{1+\left(\frac{\bar{q}\bar{\gamma}}{\bar{t}_0} \mp \sqrt{\left(\frac{\bar{q}\bar{\gamma}}{\bar{t}_0}\right)^2+1}\right)^2}^{-1} \end{pmatrix}. \tag{5.22}$$

The energetically lower (−) state has the same sign on both dimer sites with the larger contribution on the site with the larger nuclear displacement (e.g., at site 1 for $\bar{q} > 0$, i.e., $\bar{x}_1 > \bar{x}_2$). The higher (+) state changes sign between both sites and has the larger contribution on the site with the lower nuclear displacement. In the language of chemical bonds we denote these states as a bonding (−) and an antibonding (+) state, respectively. A sketch of these Born-Oppenheimer wave functions at different $\bar{q}$ for both surfaces is shown in Fig. 5.3.

Ignoring the upper surface for a moment, i.e. in the spirit of the Born-Oppenheimer approximation, we can expect to observe different ground states, depending on the system parameters. In the small hopping/large coupling regime ($\bar{\gamma}^2/\bar{t}_0 > 1$), with the double-minimum shown before, the ground state

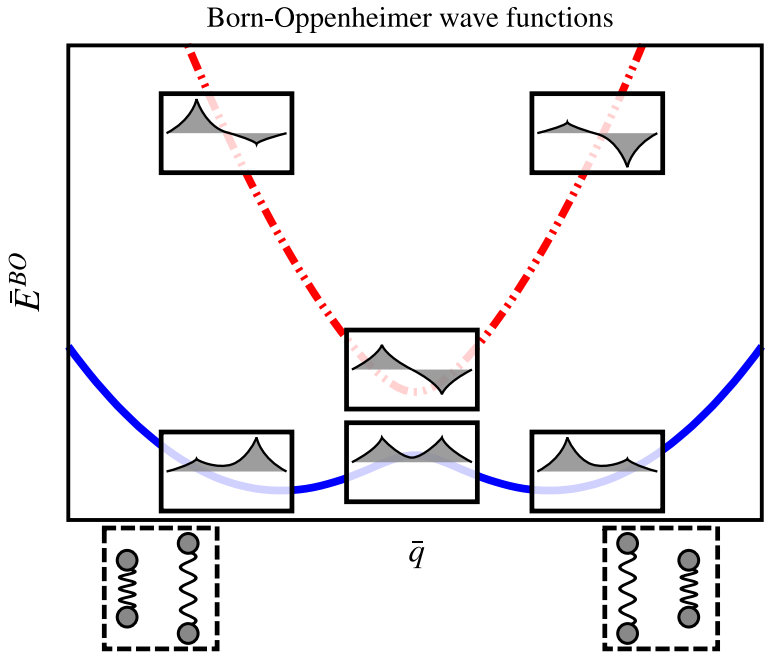

Figure 5.3: Sketch of the Born-Oppenheimer wave functions in the two states and at different nuclear positions in a Holstein dimer system similar as presented in Fig. 5.2. The lower (bonding) state has a large contribution on the site with the larger nuclear distortion (x_i, indicated with sketches of springs below the graph), while the higher (antibonding) state has the larger contribution on the opposite site and changes sign between the sites.

wave function will have dominant contributions at non-zero $\bar{q} = \pm\bar{\gamma}\sqrt{1 - \bar{t}_0^2/\bar{\gamma}^4}$ in the lower BO-state. Since this state has the electron density mostly localized on the site with the larger nuclear displacement, the ground state will be composed of localized electron-nuclear bound states. In the large hopping/small coupling regime ($\bar{\gamma}^2/\bar{t}_0 < 1$), with the single-minimum at $\bar{q} = 0$, the ground state wave function will have its largest contribution around $\bar{q} = 0$ and the electron density is delocalized between both sites.

From the Born-Oppenheimer states and energies we can calculate the derivative couplings according to Eq. (5.12) or Eq. (5.16) (the diagonal entries $A_{a,a}$ vanish for real Born-Oppenheimer wave functions), see, e.g., Refs. [202, 203]:

$$\bar{A}_{+,-} = \bar{A}^*_{-,+} = -i\frac{\bar{\gamma}}{2\bar{t}_0}\frac{1}{1 + (\bar{q}\bar{\gamma}/\bar{t}_0)^2}. \tag{5.23}$$

The imaginary part of these off-diagonal derivative couplings is included in Fig. 5.2. The functional form corresponds to a Lorentzian curve around the symmetric phonon distortion $\bar{q} = 0$, with its width proportional to $\bar{\gamma}/\bar{t}_0$. For a small hopping matrix element $\bar{t}_0$, the couplings become strongly peaked at the avoided crossing, see Refs. [204–206], allowing for transitions of the wave function between both Born-Oppenheimer surfaces, see Sec. 5.2.2.

An early estimate for the transition probability between the two electronic states is given by the Landau-Zener formula, see Refs. [207, 208]. This formula approximates the nuclei as classical point particles, which move along a fixed

path $\bar{q}(t)$ with a constant velocity $\dot{\bar{q}}$. With only the electrons described on a quantum mechanical level, their Schrödinger equation becomes much simpler than the full nuclear Schrödinger equation (5.10) given before. In the basis of the two site-local electronic states $|\Psi^{el}(t)\rangle = \sum_i |\chi_i\rangle \Psi_i^{el}$, it can be written as:

$$i\hbar \frac{\mathrm{d}}{\mathrm{d}t}\Psi_i^{el}(t) = \sum_j \langle \chi_i | \hat{H}^{BO}(q(t)) | \chi_j \rangle \Psi_j^{el}(t), \tag{5.24}$$

with the nuclear coordinate q entering as a time-dependent external potential. For a simple two-level system with a linear electron-phonon coupling and a constant hopping term, like in Eq. (5.20), one can integrate this differential equation to determine transition probabilities between electronic states. Starting on the lower Born-Oppenheimer surface at $\bar{q} \to -\infty$ (where $|\phi_-\rangle = |\chi_2\rangle$) one can ask for the transition probability $P^{LZ}_{-\to+}$ to the upper Born-Oppenheimer surface once the system reached $\bar{q} \to \infty$ (where $|\phi_+\rangle = |\chi_2\rangle$). This integration yields (see Ref. [208]):

$$P^{LZ}_{-\to+} = \exp\left(\frac{-\pi|\bar{t}_0|^2}{\dot{\bar{q}}\bar{\gamma}}\right). \tag{5.25}$$

Hence, in this approximation, the transition probability between both Born-Oppenheimer surfaces becomes large when the electron hopping $\bar{t}_0$ is small, or the nuclear velocity approaching the avoided crossing $\dot{\bar{q}}$ is large. This fits to our previous expectations that the adiabatic approximation (where $P_{-\to+}$ should be small) works best when the Born-Oppenheimer surfaces are far separated and the nuclei move adiabatically slow compared to the electrons.

Exact approach in the Born-Huang formalism for the Holstein dimer

If one seeks a correct quantum mechanical description of the composite electron-nuclear system, the time evolution and surface transitions become more complicated. Due to the quadratic restoring forces included in the Holstein dimer, a wave packet initially localized to, for example, the upper Born-Oppenheimer surface, can enter the avoided crossing region several times and different wave packets might interfere when they collide. To get a better impression of the dynamics and the role of non-adiabatic effects we will now present one example case for (numerically) exact dynamics in the Holstein dimer. The method used here will also serve as the benchmark method to evaluate several trajectory-based quantum-classical methods in Sec. 6.1 in the Holstein dimer.

The idea is to solve the complete nuclear Schrödinger equation in the Born-Oppenheimer basis (Eq. (5.15)). In this subsection we will always use the (adiabatic) Born-Oppenheimer basis and omit the superscript (a) of the wave function. For the Holstein dimer (Eq. (5.20)) the nuclear Schrödinger equation in the time-independent form becomes:

$$\bar{E}^n \Psi^n_\pm(\bar{q}) = \left[-\frac{1}{2}\nabla^2_{\bar{q}} + \frac{\tilde{A}^2}{2} + \bar{E}^{BO}_\pm\right] \Psi^n_\pm(\bar{q}) \mp \left[\frac{1}{2}\frac{\partial \tilde{A}}{\partial q} + \tilde{A}\nabla_{\bar{q}}\right] \Psi^n_\mp(\bar{q}), \tag{5.26}$$

with $\tilde{A} = \Im(\bar{A}_{-,+})$. In Eq. (5.26) the derivative coupling appears several times. First, it contributes to the diagonal elements of the Hamiltonian with a term $\tilde{A}^2/2$, thus modifying the shape of the effective potential acting on the wave function from the pure Born-Oppenheimer surfaces. If one differentiates between the adiabatic and the Born-Oppenheimer approximation, then in the latter this contribution would remain. Second, the derivative coupling and its derivative couple the two Born-Oppenheimer states, so that, in general, the eigenstates solving Eq. (5.26) will have contributions on both surfaces. The resulting eigenenergies $\bar{E}^n$ and eigenstates $|\Psi^n\rangle = \sum_{\pm} \int \mathrm{d}\bar{q}\, |\bar{q}, \phi^{BO}_{\pm}(\bar{q})\rangle\, \Psi^n_{\pm}(\bar{q})$ are the same as obtained from solving the complete Schrödinger equation of the system in any other, e.g., second quantized, basis, and should not be confused with the Born-Oppenheimer energies or states.

Of the many ways to solve Eq. (5.26), we follow here a Car-Parrinello (see Ref. [129]) motivated scheme, suggested by P. E. Blöchl (Ref. [209]). For this, we discretize the nuclear coordinate space on a grid to obtain a set of basis states $\langle \bar{q}, \phi^{BO}_{\pm}(\bar{q})|$. We then set up a fictitious Lagrangian for all components of the one-particle wave functions $\Psi^n_{\pm}(\bar{q})$:

$$\mathcal{L} = \sum_{\pm,\bar{q},n} M_{\Psi} |\dot{\Psi}^n_{\pm}(\bar{q})|^2 - \sum_n \langle \Psi^n | \hat{\bar{H}} | \Psi^n \rangle - \sum_{m,n} \Lambda_{m,n} (\langle \Psi^n | \Psi^m \rangle - \delta_{m,n}), \quad (5.27)$$

where $\hat{\bar{H}}$ refers to the complete dimer Hamiltonian (without $\bar{Q}$), not the Born-Oppenheimer Hamiltonian. This ansatz is similar to the already presented ground-state Car-Parrinello search described in Sec. 3.3.2, see there for details. A trial wave function $\Psi^n_{\pm}(\bar{q})$ evolves for each eigenstate n according to the forces determined from the full instantaneous energy expression $\frac{\partial \langle \Psi^n | \hat{\bar{H}} | \Psi^n \rangle}{\partial \Psi^{n,*}_{\pm,\bar{q}}} = \langle \bar{q}, \phi^{BO}_{\pm}(\bar{q}) | \hat{\bar{H}} | \Psi^n \rangle$, which here forms a one-dimensional energy surface for each component of the wave function.

A fictitious kinetic energy term is added for each such wave function component, which is damped over time. Of the additional orthonormalization included by the Lagrange-multiplier $\Lambda_{m,n}$, only the normalization of each state and the orthogonalization to lower lying eigenstates is included in the equations of motion (i.e., $\Lambda_{m,n}$ is replaced by a triangular matrix). This ensures that the $n = 0$ state relaxes to the one-particle ground state of the Hamiltonian, while higher states relax to their respective one-particle excited states. In practice, we obtained the eigenstates consecutively, and orthogonalized the forces acting on the wave functions to the previously obtained lower-lying eigenstates. This relaxation is again done with a Verlet-algorithm (see Ref. [139]). The final total energy of each state is the eigenenergy of the corresponding state.

The eigenenergies have been compared to an exact diagonalization in second quantization method, implemented by D. Jansen, see Ref. [37], which confirmed that both methods yield the same eigenenergies. We note that if one diagonalizes the full dimer Hamiltonian (Eq. (5.4)) with the center-of-mass coordinate $\bar{Q}$ included, one gets additional eigenstates separated in energy by multiples of $\hbar\omega_0$, due to the additional (independent) harmonic oscillator.

Six example eigenstates of the Holstein dimer are visualized in Fig. 5.4.

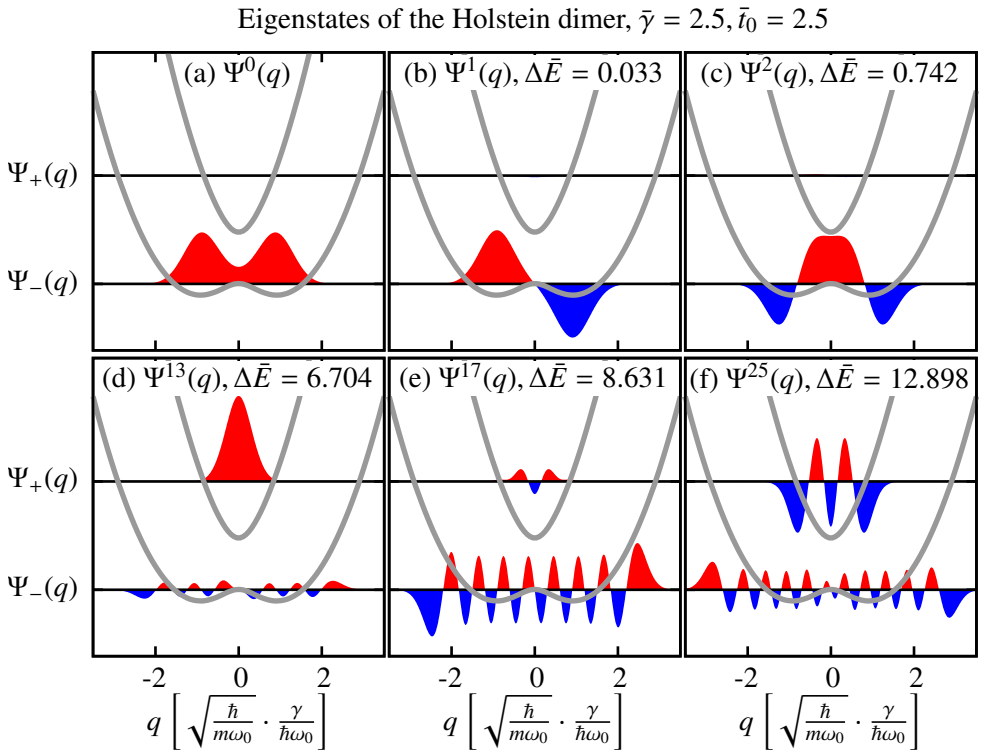

Figure 5.4: Six different eigenstates $|\Psi^n\rangle$ of the Holstein dimer for $\bar{\gamma} = \bar{t}_0 = 2.5$ obtained with the approach outlined in Sec. 5.2.4. The contributions of the (real) eigenfunctions in both the upper ($\Psi_+(q)$) and lower ($\Psi_-(q)$) Born-Oppenheimer state are shown, with the respective surfaces indicated by gray lines. Positive and negative values of the wave functions are drawn as red and blue filled curves.

Shown are the two components on the lower and upper Born-Oppenheimer surface over the q-phonon degree of freedom. Figs. 5.4(a)-(c) show the lowest three eigenstates, which all have only very little contribution on the upper Born-Oppenheimer surface. The ground state Ψ^0 is almost a linear combination of two Gaussians localized around the two minima of the lowest Born-Oppenheimer surface, while the first excited state Ψ^1 changes sign between the two minima. Linear combinations of these two states are a good approximation to Gaussians localized to one of the minima. The third eigenstate changes sign twice on the lower surface and has a larger contribution at the symmetric nuclear distortion $q = 0$. In Fig. 5.4(d) the first eigenstate with a large contribution on the upper Born-Oppenheimer surface (Ψ^{13}) is shown. Higher lying eigenstates have a varying contribution on the two surfaces, with the 17th (Ψ^{17}) and the 25th (Ψ^{25}) excited states being examples with a small and large contribution on the upper surface, respectively.

We note that with the knowledge of the eigenstates one can directly calculate, for example, an optical absorption spectrum. For this we need to obtain the transition dipole moment between two states from the dipole operator acting on the electron $\hat{\mu} = (\hat{n}_1 - \hat{n}_2)$ (we set the charge and the position of the electron to unity). In the basis of the Born-Oppenheimer states (see Eq. (5.22)) this

becomes:

$$\langle\Psi^m|\hat{\mu}|\Psi^n\rangle = \int \mathrm{d}\bar{q}\,\left(\Psi_-^{*m}(\bar{q})\Psi_-^n(\bar{q}) - \Psi_+^{*m}(\bar{q})\Psi_+^n(\bar{q})\right)\frac{\bar{q}\bar{\gamma}/\bar{t}_0}{\sqrt{(\bar{q}\bar{\gamma}/\bar{t}_0)^2+1}} + \int \mathrm{d}\bar{q}\,\left(\Psi_-^{*m}(\bar{q})\Psi_+^n(\bar{q}) + \Psi_+^{*m}(\bar{q})\Psi_-^n(\bar{q})\right)\frac{1}{\sqrt{(\bar{q}\bar{\gamma}/\bar{t}_0)^2+1}}. \quad (5.28)$$

The first term in Eq. (5.28) measures the overlap of the two states $|\Psi^m\rangle$ and $|\Psi^n\rangle$ on the same Born-Oppenheimer surfaces, with a different sign for the lower and upper surface. The scaling factor is odd in $\bar{q}$-space and thus the two states must have a different parity in the respective surface. The scaling factor, which is (up to the sign) just the diagonal entry of the dipole operator in the Born-Oppenheimer basis, is zero at $\bar{q} = 0$ and becomes finite and constant for larger $\pm\bar{q}$. It gives rise to tunneling transitions between states and leads to a large transition dipole moment between, for example, the ground state and the first excited state shown in Figs. 5.4(a),(b), corresponding to a small excitation energy of $\Delta E \ll \hbar\omega_0$.

The second term measures the off-diagonal overlap between two states, i.e. the wave function contributions on different Born-Oppenheimer surfaces. The scaling factor (the off-diagonal matrix element of the dipole operator) is even in $\bar{q}$-space, thus the relevant contributions of the states must have the same parity, and largest around $\bar{q} = 0$ (it is proportional to the imaginary part of the derivative couplings, see Fig. 5.2). This term leads to a large transition dipole moment between, for example, the states $|\Psi^2\rangle$ and $|\Psi^{13}\rangle$ (see Figs. 5.4(c),(d)), which have a strong off-diagonal overlap around $\bar{q} = 0$ (with $\Delta\bar{E} \approx 2|\bar{t}_0|$). Since this involves an excitation from a state that is not the ground state, it is thermally activated. Such a transition has been observed also in small one-dimensional Holstein chains, see Ref. [210]. In addition, the second term gives rise to a transition dipole moment between the ground-state $|\Psi^0\rangle$ and high-excited states (for example $|\Psi^{25}\rangle$, see Figs.5.4(a),(f)), which have a strong off-diagonal overlap around the minima of the lower Born-Oppenheimer surface (with $\Delta\bar{E} \approx 2\bar{\gamma}^2$). This corresponds to an optical excitation from the lower to the upper Born-Oppenheimer surface at roughly the same nuclear positions, i.e. a vertical, "Franck-Condon"-like excitation, see Refs. [211, 212].

More relevant for the rest of this thesis is the calculation of real-time dynamics of an initial non-equilibrium state $|\Psi_{ini}\rangle$. We can project this state onto the eigenstates $|\Psi^n\rangle$ of the system to obtain the expectation value of some observable $\hat{O}$ via:

$$\langle\Psi(t)|\hat{O}|\Psi(t)\rangle = \sum_{m,n}\langle\Psi_{ini}|\Psi^m\rangle\langle\Psi^n|\Psi_{ini}\rangle\exp\left(-\frac{i}{\hbar}(E_n - E_m)t\right)\langle\Psi^m|\hat{O}|\Psi^n\rangle\,. \quad (5.29)$$

One example is the Born-Oppenheimer probability density $|\Psi_\pm(\bar{q},t)|^2$ ($\hat{O} = |\bar{q},\phi_\pm^{BO}(\bar{q})\rangle\langle\bar{q},\phi_\pm^{BO}(\bar{q})|$). Let us start from an initial state with contributions only on the upper Born-Oppenheimer surface, i.e., an antibonding initial state,

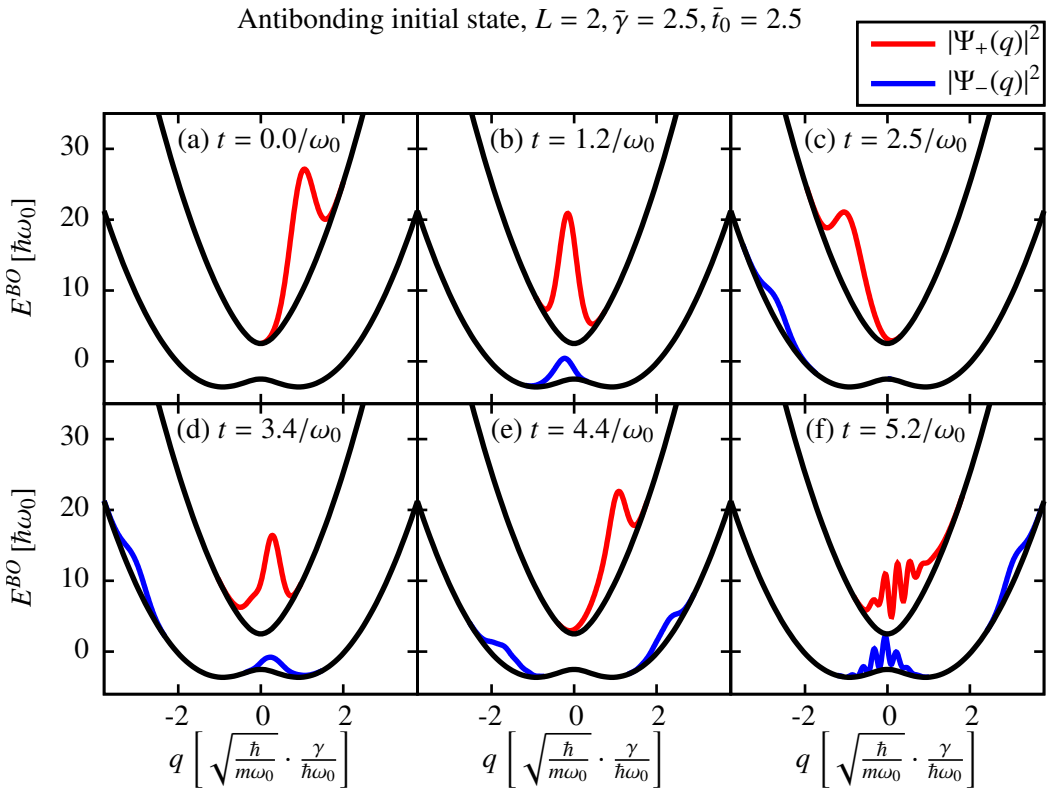

Figure 5.5: Born-Oppenheimer probability densities $|\Psi_\pm(\bar{q}, t)|^2$ calculated numerically exact via Eq. (5.29) for an antibonding initial state (Eq. (5.30)). Shown are six snapshots at different times, (a) $t = 0$, the initial state, (b) $t = 1.2/\omega_0$, (c) $t = 2.5/\omega_0$, (d) $t = 3.4/\omega_0$, (e) $t = 4.4/\omega_0$ and (f) $t = 5.2/\omega_0$. Each snapshot shows the probability density on the upper (lower) surface as red (blue) line drawn on top of the respective Born-Oppenheimer surface (black) with a constant, arbitrary scaling. Non-adiabatic transitions (b) and (d), separation of wave packets (c) and (e), and interference between wave packets (f) are visible.

with a Gaussian-shape around $\bar{q}_0 = \bar{\gamma}$:

$$|\Psi_{ini}\rangle = \int \mathrm{d}\bar{q}\, |\bar{q}, \phi_+^{BO}(\bar{q})\rangle\, \pi^{-1/4} \exp\left(-(\bar{q} - \bar{q}_0)^2/2\right). \tag{5.30}$$

We stay with the same system parameters as presented in Fig. 5.4 ($\bar{\gamma} = \bar{t}_0 = 2.5$), and obtain the first 250 eigenstates and eigenvalues to get an accurate representation of the initial state. We then calculate the Born-Oppenheimer probability densities $|\Psi_\pm(\bar{q}, t)|^2$, of which we show six time-snapshots in Fig. 5.5. The Gaussian probability density of the initial state is visible in Fig. 5.5(a). The wave packet propagates toward the avoided crossing at $\bar{q} = 0$, where a partial non-adiabatic transition to the lower surface takes place (Fig. 5.5(b)). After leaving the avoided crossing region, the derivative couplings become small again and the contributions on the two surfaces evolve mostly independently. Due to the different slopes of the surfaces, the two wave packets split in nuclear

coordinate space, with the wave packet on the upper surface being reflected at smaller $|\bar{q}|$ than the wave packet on the lower surface (Fig. 5.5(c)). This is called a wave packet splitting. The confining potential of the system returns both wave packets to the avoided crossing point. The upper wave packet splits again (Fig. 5.5(d)), which leads to three distinct wave packets at later times (Fig. 5.5(e)). When previously splitted parts of the wave packet meet again (Fig. 5.5(f)), they might interfere. This is especially relevant in a small system like in the Holstein dimer with no dissipation channels and no decoherence. We note that no complete relaxation to the lower Born-Oppenheimer surface is observed at later times, because the wave function cannot dissipate its energy. We see that these exemplary exact dynamics support the sketch of the non-adiabatic dynamics drawn when introducing the Born-Huang expansion (Fig. 5.1). The same initial state will be analyzed in more detail when comparing the exact dynamics to trajectory-based methods, see Sec. 6.1.2.

Holstein trimer

In the Holstein trimer we can still easily visualize the shape of the Born-Oppenheimer surfaces. We already introduced the symmetric ($\hat{\bar{x}}_s$) (Eq. (5.5)) and antisymmetric ($\hat{\bar{x}}_a$) (Eq. (5.6)) nuclear modes, which allowed us to remove the center-of-mass nuclear coordinate from the Hamiltonian. The Born-Oppenheimer Hamiltonian for the Holstein trimer with a single electron in the basis of the three site-local electronic states $|\chi_i\rangle = c_i^\dagger |0\rangle$, $i = 1, 2, 3$ becomes:

$$\hat{\bar{H}}^{BO}_{L=3}(\bar{x}_s, \bar{x}_a) = \frac{\bar{x}_s^2}{2} + \frac{\bar{x}_a^2}{2} + \begin{pmatrix} \bar{\gamma}\left(\bar{x}_a + \frac{1}{\sqrt{3}}\bar{x}_s\right) & -\bar{t}_0 & 0 \\ -\bar{t}_0 & -\bar{\gamma}\frac{2}{\sqrt{3}}\bar{x}_s & -\bar{t}_0 \\ 0 & -\bar{t}_0 & \bar{\gamma}\left(-\bar{x}_a + \frac{1}{\sqrt{3}}\bar{x}_s\right) \end{pmatrix}. \tag{5.31}$$

This 3×3 matrix can easily be diagonalized numerically for various $\bar{x}_s$ and $\bar{x}_a$ to obtain the Born-Oppenheimer states and energies. As example, the Born-Oppenheimer surfaces are shown for $\bar{\gamma} = \bar{t}_0 = 2.5$ in a contour-plot in Fig. 5.6 and as surface-plot in Fig. 5.7. The former allows to understand the form of the surfaces and their minima, while in the latter the energy separation between the surfaces is better visible, especially at the line $\bar{x}_a = 0$. Since the surfaces are symmetric under the operation $\bar{x}_a \rightarrow -\bar{x}_a$, see Ref. [37], only non-negative values for $\bar{x}_a$ are shown in the surface-plot.

The lowest surface $\bar{E}_0^{BO}$ (Fig. 5.6(c)) has three local minima. The lowest (global) minimum is at positive $\bar{\gamma}$ and $\bar{x}_a = 0$. This corresponds to a large nuclear distortion on the central site ($x_2 > x_1 = x_3$), compared to the edge sites. The other two minima have the large nuclear distortions on the left (x_1) and right (x_3) site, respectively. Similar as in the dimer we might use the language of chemical bonds to categorize the lowest Born-Oppenheimer state as a bonding state, which has the same sign on all three trimer sites. The Born-Oppenheimer states at the nuclear positions of the three minima are sketched in Fig. 5.6(c). The largest electronic contribution is in all cases on the site with

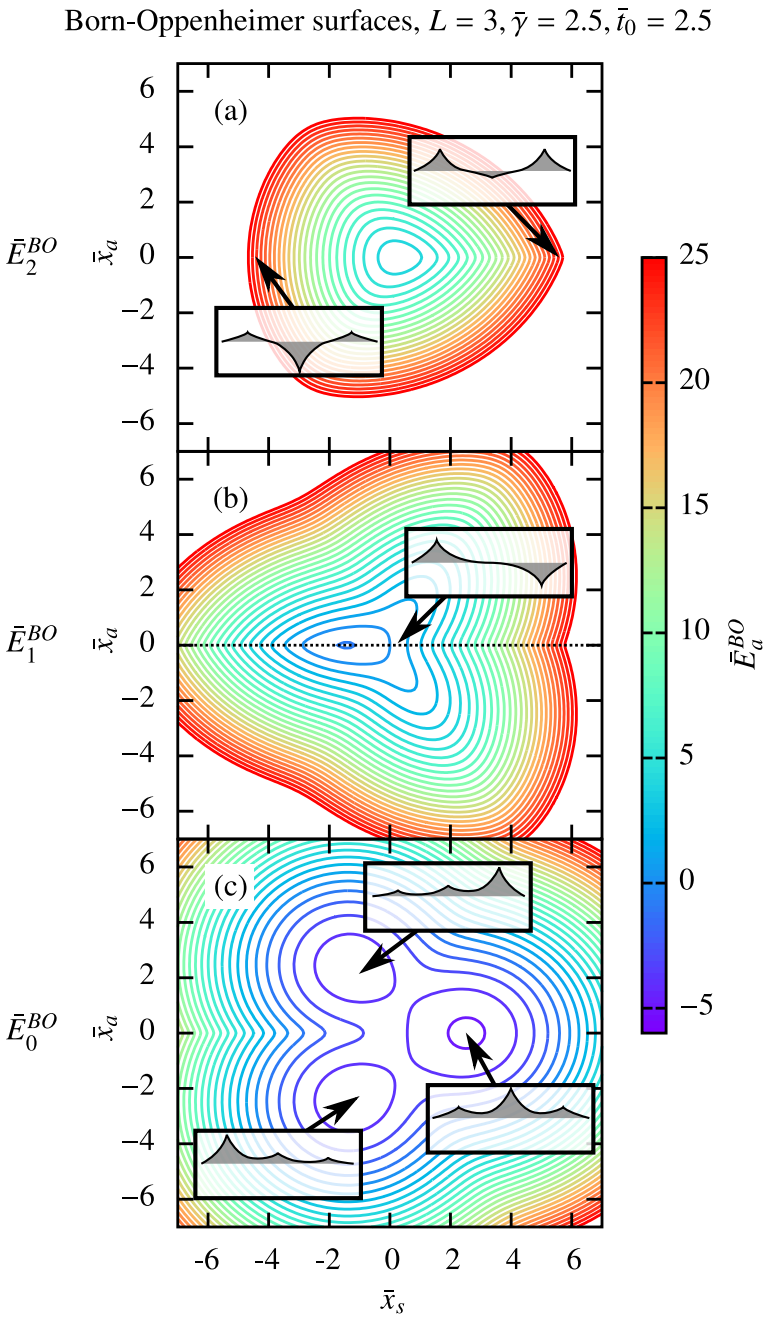

Figure 5.6: Contours of the Born-Oppenheimer surfaces $\bar{E}_a^{BO}$, drawn every $\Delta\bar{E}_a^{BO} = 1$, of the Holstein trimer with $\bar{\gamma} = \bar{t}_0 = 2.5$. Shown are the (a) highest, (b) middle and (c) lowest Born-Oppenheimer surfaces. Some sketches of the Born-Oppenheimer wave functions at the positions of the three minima in the lowest surface (c), along the indicated line in the middle surface (b), and at two selected points in the highest surface (a) are included. The contours are obtained from numerical diagonalization of $\hat{\bar{H}}_{L=3}^{BO}$ (see Eq. (5.31)) in the nuclear coordinate space of the symmetric and antisymmetric nuclear modes $\bar{x}_s$ and $\bar{x}_a$. Reproduced from Ref. [37], with the permission of AIP Publishing, the Born-Oppenheimer wave function sketches and the dotted line in the middle surface have been added.

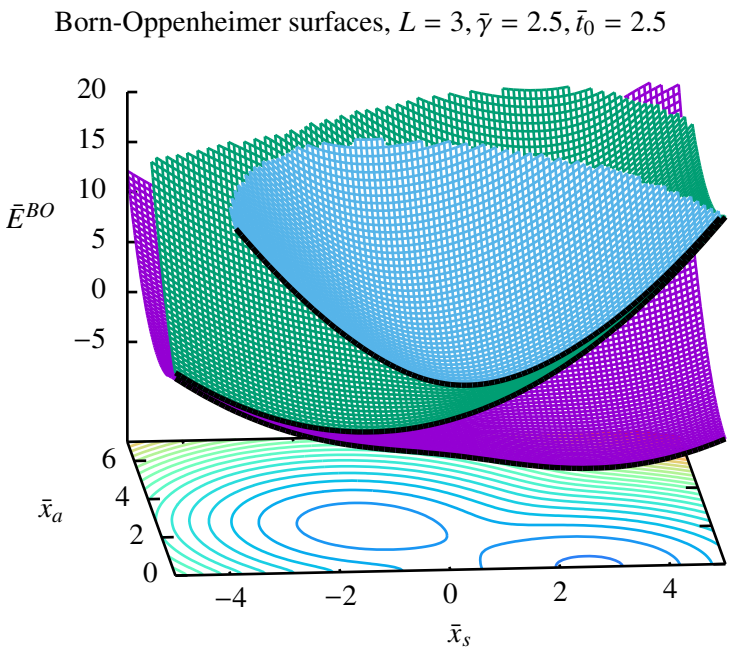

Figure 5.7: Born-Oppenheimer surfaces $\bar{E}_a^{BO}(\bar{x}_s, \bar{x}_a)$ of the Holstein trimer with $\bar{\gamma} = \bar{t}_0 = 2.5$, obtained from numerical diagonalization of $\hat{\bar{H}}_{L=3}^{BO}$ (see Eq. (5.31)) in the nuclear coordinate space of the symmetric and anti-symmetric nuclear modes $\bar{x}_s$ and $\bar{x}_a$. Only non-negative values of $\bar{x}_a$ are shown. The three surfaces in blue, green, and magenta correspond to the three contours shown in Fig. 5.6(a)-(c), with the contour of the lowest surface included on the x-y-plane. Reproduced from Ref. [37], with the permission of AIP Publishing, the color of the lines at $\bar{x}_a = 0$ has been changed to black.

the large nuclear distortion. The higher Born-Oppenheimer surfaces each have only one minimum for the parameters chosen here. Along the $\bar{x}_a = 0$ line the middle Born-Oppenheimer state has no contribution on the central site and thus corresponds to a true non-bonding state, indicated by the sketch and the dotted line in Fig. 5.6(b). As seen from Fig. 5.7, the lower two surfaces approach each other asymptotically for $\bar{x}_a = 0, \bar{x}_s \to -\infty$. With the nuclear distortions on the edge sites becoming large compared to the central site in this limit, the bonding state will have more and more electronic weight on these edge sites, thus becoming degenerate to the non-bonding state. Finally, the highest surface $\bar{E}_2^{BO}$ (Fig. 5.6(a)) has a single minimum and its Born-Oppenheimer states change sign twice between the sites and can be associated with an antibonding state. The two sketches of the Born-Oppenheimer states in Fig. 5.6(a) illustrate that the electronic density of the antibonding state is distributed complementary to the bonding state for $\bar{x}_s$ sufficiently away from zero. The antibonding surface approaches the non-bonding surface asymptotically for $\bar{x}_a = 0, \bar{x}_s \to \infty$ (see Fig. 5.7), where the distortion on the central site becomes large and the antibonding state has less and less contribution on this site.

While we will only investigate the parameter set presented here in our bench-

mark study in the Holstein trimer, see Sec. 6.2, we mention that for small $\bar{t}_0$, two additional local minima can appear on the middle surface and the whole system comes closer to a three-fold symmetry between the three sites. For large $\bar{t}_0$, all surfaces have each only one minimum, similar as in the Holstein dimer, which leads to delocalized states. The qualitative picture of the asymptotically approaching surfaces on the $\bar{x}_a = 0$ line stays the same for any positive parameter choice of $\bar{t}_0$ and $\bar{\gamma}$.

For larger systems both obtaining the Born-Oppenheimer surfaces for the whole nuclear configuration space, as well as interpreting the associated Born-Oppenheimer states becomes a difficult task. In practice one often relies on on-the-fly methods to calculate both surfaces and states locally, see Refs. [199, 200]. It is clear that this local approach is not well suited to obtain the quantum mechanical dynamics of an extended wave packet, and instead one often turns to trajectory-based descriptions. These trajectory-based methods will be discussed in detail in Sec. 5.3. We will see that in fact exact trajectory-based methods exist, which however retain some quantum mechanical character of the individual trajectories (often of a Gaussian type). Due to their inherently non-local formulation, implementations of these methods in a Born-Huang approach have to rely on some kind of local analytic estimate of the Born-Oppenheimer surfaces, or on costly integrals in nuclear configuration space. Hence, while it is definitely possible to obtain exact quantum mechanical dynamics in a Born-Huang framework also for large composite systems, the approach truly shines when turning to approximate methods, i.e., to local trajectory-based methods that only require a local evaluation of the Born-Oppenheimer surfaces. In the following we will describe two of the most common (independent) trajectory-based methods often applied in quantum chemistry: Ehrenfest and surface-hopping dynamics. While only the latter makes explicit use of the Born-Huang expansion, this formalism helps us to also assess the strengths and weaknesses of the former method.

5.3 Trajectory-based methods

We now turn to the trajectory-based methods Ehrenfest and surface-hopping dynamics. These methods are mixed quantum-classical descriptions, which combine (trajectory-based) classical Newtonian dynamics of the nuclei with a quantum mechanical description of the electronic degrees of freedom. Both methods do not employ the adiabatic approximation and thus go beyond standard Born-Oppenheimer molecular dynamics (see Sec. 5.2.3). In particular, the potential in which the classical nuclear trajectories evolve is (in general) not always the lowest Born-Oppenheimer surface. Instead, the potential is determined directly during the time evolution. We note that a mixture of a quantum mechanical and a phase-space description of the electron-nuclear composite system is not an approximation by itself and it can be rigorously derived in the context of the partial Wigner transform. This section is again closely oriented on the corresponding published article, see Ref. [37].

5.3.1 The Wigner function formalism

Without electrons

Let us start with a bosonic system which can be represented in a general (many-particle) real-space basis $\langle R|$ (or equivalently in its momentum basis). One can describe the quantum mechanical problem of this system in a phase space representation without making an approximation. This is typically done by using the Wigner transform to map an operator $\hat{O} = O(\hat{R}, \hat{P})$ to a function in phase space, denoted as $O_W(R, P)$, see Refs. [213–217]:

$$O_W(R, P) = \int \mathrm{d}Z \; e^{iP\cdot Z/\hbar} \, \langle R - \frac{Z}{2}|\hat{O}|R + \frac{Z}{2}\rangle \,, \tag{5.32}$$

with the integral extending over the whole position space Z. This transformation allows to calculate expectation values via a phase-space average, similarly as in classical mechanics:

$$\langle \hat{O} \rangle = \int \mathrm{d}R \int \mathrm{d}P \; O_W(R, P) \frac{\rho_W(R, P)}{(2\pi\hbar)^n}. \tag{5.33}$$

Here, n is the spatial dimension of the system and $\rho_W(R, P)$ is the Wigner transform of the density matrix $\hat{\rho}$. In the following we deal with pure states, for which $\hat{\rho} = |\Psi\rangle \langle\Psi|$. One calls $W(R, P) = \frac{\rho_W(R,P)}{(2\pi\hbar)^n}$ the Wigner function of this state $|\Psi\rangle$, which has many desirable characteristics for a phase-space description of a quantum mechanical state, for example (see Ref. [216] for a detailed list):

$$\int \mathrm{d}R \int \mathrm{d}P \; W(R, P) = \mathrm{Tr}\,[\hat{\rho}] = 1, \tag{5.34}$$

$$\int \mathrm{d}P \; W(R, P) = |\Psi(R)|^2, \tag{5.35}$$

$$\int \mathrm{d}R \; W(R, P) = |\phi(P)|^2, \tag{5.36}$$

with $\phi(P) = \langle P|\Psi\rangle$. The Wigner transform is linear and for an operator that is a function of only the position or only the momentum operators it amounts to replacing the operators $\hat{R}$ and $\hat{P}$ by their classical values R and P, respectively. Hence, one can easily calculate, for example, the energy of an harmonic oscillator with (in dimensionless units) $\hat{H} = \hat{P}^2/2 + \hat{R}^2/2$ via $\langle H \rangle = \int \mathrm{d}R \int \mathrm{d}P \; W(R, P)(P^2/2 + R^2/2)$. However, the Wigner function does not have to be positive everywhere, thus we cannot think of it as a proper probability distribution in phase space. Instead, it is often called a quasidistribution, see Ref. [217].

Using Eqs. (5.32) and (5.33), we can calculate the quasidistribution in phase space and determine expectation values of any operator by a phase-space average, as soon as we know the time evolved state $|\Psi(t)\rangle$ (in a Schrödinger picture). To completely stay within a phase-space description we need to obtain a dynamical equation for the Wigner function. From the von Neumann equation for

the density matrix, we obtain such an equation by taking the Wigner transform of both sides (see Refs. [201, 216]):

$$i\hbar\frac{\partial}{\partial t}\hat{\rho} = \left[\hat{H},\hat{\rho}\right] \quad \Rightarrow \quad i\hbar\frac{\partial}{\partial t}W = \left[\hat{H},\hat{\rho}\right]_W/(2\pi\hbar)^n. \tag{5.37}$$

Unfortunately, the Wigner transform of a product of two operators is a Moyal product (see Ref. [218]):

$$(\hat{A}\cdot\hat{B})_W = A_W(R,P)\exp\left(-\frac{i\hbar}{2}\Lambda\right)B_W(R,P), \tag{5.38}$$

with the symplectic operator (see Ref. [201]):

$$\Lambda = \sum_{i=1}^{n}\frac{\overleftarrow{\partial}}{\partial P_i}\frac{\overrightarrow{\partial}}{\partial X_i} - \frac{\overleftarrow{\partial}}{\partial X_i}\frac{\overrightarrow{\partial}}{\partial P_i}. \tag{5.39}$$

The arrows ← and → indicate whether the derivative acts on the function before or after the Λ-operator. The symplectic operator acting on two functions is similar to the Poisson bracket: $A\Lambda B = -\{A,B\} = -\sum_{i=1}^{n}\left(\frac{\partial A}{\partial P_i}\frac{\partial B}{\partial X_i} - \frac{\partial A}{\partial X_i}\frac{\partial B}{\partial P_i}\right)$, see Ref. [201]. Thus, the dynamical equation for the Wigner function becomes:

$$\frac{\partial}{\partial t}W = -\frac{2}{\hbar}H_W\sin\left(\frac{\hbar}{2}\Lambda\right)W. \tag{5.40}$$

To lowest order in $\hbar$ this is equivalent to the classical Liouville equation:

$$\frac{\partial}{\partial t}W = \{H_W,W\} + O(\hbar^2). \tag{5.41}$$

The classical Liouville equation can be solved with the method of characteristics by starting with a swarm of independent trajectories sampled from the initial condition $W(t=0)$ and time evolving them according to Hamilton's equations of motion, see, e.g., Ref. [201]. If the initial Wigner function is completely positive, the trajectories can be thought of as realizations of a classical ensemble. From Eq. (5.41) we see that the initial sampling of the trajectories from the correct Wigner function is already sufficient to include quantum corrections in first order in $\hbar$. For a system where the higher order terms vanish, such as a harmonic oscillator, the difference between a quantum mechanical and a classical treatment of a dynamical problem is thus only in the sampling of the initial conditions, see Ref. [216]. This ansatz is also called the truncated Wigner approximation (see, e.g., Ref. [201]).

With electrons

We now turn to a composite electron-nuclear system, which can be represented by basis states of the form $\langle R,\phi_a(R)|$, which can refer both to nuclear position dependent (e.g., adiabatic (a), $\phi_a(R) = \phi_a^{BO}(R)$) and position independent (trivially diabatic (d), $\phi_a(R) = \chi_a$) electronic states, see Eqs. (5.17) and (5.18).

Only the nuclear degrees of freedom should be described in phase space, which can be done with a partial Wigner transform, see Refs. [219–221]. Here, we use the definition following Ando et al. (Refs. [221, 222]):

$$O_{a,b:W}(R,P) = \int \mathrm{d}Z\, e^{iP\cdot Z/\hbar} \left\langle R - \frac{Z}{2}, \phi_a \left(R - \frac{Z}{2}\right) |\hat{O}| R + \frac{Z}{2}, \phi_b \left(R + \frac{Z}{2}\right) \right\rangle, \tag{5.42}$$

which corresponds to first representing the operator in the chosen electronic basis and afterward performing the Wigner transform of every component in the electronic basis. The resulting partially Wigner-transformed operator can be understood as an operator acting on the electrons only: $\hat{O}_W(R,P) \coloneqq \sum_{a,b} |\phi_a(R)\rangle\, O_{a,b:W}(R,P)\, \langle\phi_b(R)|$, which, however, now depends on the electronic basis chosen in its definition (Eq. 5.42). Taking the electronic trace $\mathrm{Tr}[\cdot]_e$, expectation values can be obtained via:

$$\langle \hat{O} \rangle = \int \mathrm{d}R \int \mathrm{d}P\, \mathrm{Tr}\left[\hat{O}_W(R,P)\hat{W}(R,P)\right]_e, \tag{5.43}$$

with $\hat{W}(R,P) = \frac{\hat{\rho}_W(R,P)}{(2\pi\hbar)^n}$, similar to before, which for simplicity we will also refer to as the Wigner function of the now composite electron-nuclear system. For a pure state the Wigner function can be expressed as:

$$W_{a,b:W}(R,P) = \int \mathrm{d}Z \frac{e^{iP\cdot Z/\hbar}}{(2\pi\hbar)^n} \Psi_a \left(R - \frac{Z}{2}\right) \Psi_b^* \left(R + \frac{Z}{2}\right). \tag{5.44}$$

Let us for simplicity turn for a moment completely to a diabatic electronic basis (d). By applying the corresponding partial Wigner transform to the von Neumann equation, one arrives at (see Ref. [219]):

$$\frac{\partial}{\partial t}\hat{W}^{(d)} = -\frac{i}{\hbar}\left(\hat{H}_W^{(d)} \exp\left(\frac{-i\hbar}{2}\Lambda\right) \hat{W}^{(d)} - \hat{W}^{(d)} \exp\left(\frac{-i\hbar}{2}\Lambda\right) \hat{H}_W^{(d)}\right). \tag{5.45}$$

Λ is still the symplectic operator (see Eq. (5.39)), but in comparison to the case without electrons, the operators $\hat{H}_W^{(d)}$ and $\hat{W}^{(d)}$ do not commute. One can now either expand the exponential in powers of $\hbar$, or equivalently (see Ref. [219]) in powers of m/M, where m and M are the masses of the electrons and nuclei, respectively. Keeping only the first term in either expansion leads to the same approximate equation:

$$\frac{\partial}{\partial t}\hat{W}^{(d)} \approx -\frac{i}{\hbar}\left[\hat{H}_W^{(d)}, \hat{W}^{(d)}\right] + \frac{1}{2}\left(\{\hat{H}_W^{(d)}, \hat{W}^{(d)}\} - \{\hat{W}^{(d)}, \hat{H}_W^{(d)}\}\right). \tag{5.46}$$

Eq. (5.46) is called the quantum-classical Liouville equation (QCLE, see Refs. [219, 223]). It is more involved than the classical Liouville equation (5.41), obtained in the truncated Wigner approximation for the pure bosonic system. The first term in this equation (5.46) is proportional to the commutator of the partially Wigner-transformed Hamiltonian $\hat{H}_W$ and density matrix $\hat{\rho}_W$, as in the von Neumann equation, while the second term includes the Poisson

brackets between both (non-commuting) operators. Most importantly, it cannot be solved with the method of characteristics (see Ref. [220]), i.e., one cannot directly simulate the dynamics of the quantum-classical Liouville equation with an ensemble of independent trajectories. However, it is a useful starting point for additional approximations, which can be used to arrive at one of the independent-trajectory based methods used later (Ehrenfest dynamics, see Ref. [220]), or at least to compare the resulting equations of motion with the other method (surface-hopping dynamics, see Ref. [224]).

Even without a proper trajectory-based solution to the dynamical equation, one can still use Eqs. (5.42) and (5.43) to calculate the correct expectation value of any operator as long as the partially Wigner-transformed operator and density matrix are available. Hence, if one samples an ensemble of trajectories (potentially with associated negative weights) from the initial partially Wigner-transformed density matrix, then at least all observables calculated from this initial state via Eq. (5.43) will be correctly recovered. Used in this way, the Wigner function formalism can be used to relate a trajectory ensemble uniquely to the given quantum mechanical electron-nuclear state, but it does not provide equations of motion that keep the trajectory ensemble close to the true Wigner function.

As an example, let us take an initial state that is restricted to a single adiabatic surface, such as the example shown for the Holstein dimer, see Fig. 5.5(a) corresponding to $|\Psi_{ini}\rangle$ defined in Eq. (5.30). The Wigner function obtained via Eq. (5.44) in the adiabatic basis (a) has just one non-zero component, which is then the normal Wigner transform of the nuclear wave packet. For this example initial state (Eq. (5.30)) the Wigner function (in dimensionless units) becomes:

$$W^{(a)}_{a,b:W}(\bar{q},\bar{p}) = \delta_{a,b}\cdot\delta_{a,+}\cdot\frac{1}{\pi}\exp\left(-\bar{p}^2-(\bar{q}-\bar{q}_0)^2\right). \tag{5.47}$$

We note that with the definition of the partial Wigner transform according to Eq. (5.42), the R-dependence of the electronic basis needs to be taken into account even for an operator acting on the nuclei only, as long as the operator is not diagonal in the position basis. For example, the partial Wigner transform of the operator whose expectation value is the momentum distribution $\hat{A} = |P'\rangle\langle P'|$ (with $\langle\hat{A}\rangle = |\Psi(P')|^2$ for a pure state) becomes in the adiabatic basis:

$$A^{(a)}_{a,b:W}(R,P) = \int \mathrm{d}Z \frac{1}{\pi\hbar} e^{-i(P-P')Z/\hbar}\,\langle\phi_a(R+\frac{Z}{2})|\phi_b(R-\frac{Z}{2})\rangle\,, \tag{5.48}$$

which is significantly more difficult to calculate compared to the partial Wigner transform in the diabatic basis: $A^{(d)}_{a,b:W}(R,P) = \delta(P-P')\delta_{a,b}$.

Alternatively, one could always perform the Wigner transform in the diabatic basis and only afterward represent the $\hat{W}^{(d)}$ in an adiabatic basis. This approach was actually suggested first (see Ref. [219]) and differs from Eq. (5.42) in that the electronic states do not depend on the integral variable Z: $|\phi(R-\frac{Z}{2})\rangle \to |\phi(R)\rangle$, i.e., the electronic states are evaluated at a different

nuclear position than the nuclear states in the integral. This form of the partial Wigner transform (which one might denote with a reversed order of the subscripts, $O^{(a)}_{W:a,b}$, see Ref. [222]) has the benefit that operators acting only on the nuclei can always be Wigner transformed without referring to the electronic basis. However, the partial Wigner transform of an adiabatic initial state, such as the example mentioned before (Eq. (5.30)), will be non-trivial and in general lead to some negative values in the resulting Wigner function. This also includes the important case of a system starting from the lowest Born-Oppenheimer surface, such as most systems starting close to the ground state (see the first eigenstate of the Holstein dimer for $\bar{\gamma}$=$\bar{t}_0$=2.5 shown in Fig. 5.4(a), which has no visible contribution on the upper surface). Hence, in this thesis, where the Wigner function is mainly used for sampling initial states, we will always use the definition Eq. (5.42).

5.3.2 Independent-trajectory approach

We now want to turn to a trajectory-based description of the electron-nuclear composite problem. Without the attached electrons we saw that to first order in $\hbar$ the dynamics in phase space can be described with the classical Liouville equation (5.41) (truncated Wigner approximation, see also Ref. [201]), which can be solved by a swarm of independent trajectories evolving according to the corresponding Hamilton's equations of motion, with initial conditions sampled from the Wigner function $W(t = 0)$. In the same spirit, the ansatz for the independent-trajectory methods is to approximate the Wigner function of the composite system (Eq. (5.44)) by an ensemble of classical nuclear trajectories $(R^\alpha(t), P^\alpha(t))$ (where α labels the trajectories) that each have an attached electronic density matrix $\hat{\rho}^{el,\alpha}(t)$ (see also Ref. [37]):

$$\hat{W}(R, P, t) \approx \frac{1}{N_{traj}} \sum_{\alpha}^{N_{traj}} w^\alpha \delta(R - R^\alpha(t))\delta(P - P^\alpha(t)) \cdot \hat{\rho}^{el,\alpha}(t). \tag{5.49}$$

The constant w^α is a weighting factor. For a Wigner function that in the chosen electronic basis is completely positive, it can be set to $w^\alpha = 1$, $\forall\alpha$. For each trajectory the nuclear degrees of freedom should be propagated according to Hamilton's equations of motion:

$$\frac{\partial R^\alpha_k}{\partial t} = \frac{\partial H^{nuc,\alpha}}{\partial P^\alpha_k}, \quad \frac{\partial P^\alpha_k}{\partial t} = -\frac{\partial H^{nuc,\alpha}}{\partial R^\alpha_k}, \tag{5.50}$$

where the effective nuclear Hamiltonian $H^{nuc,\alpha}$ will depend on the electronic configuration at that instant of time (and can be regarded as time-dependent). In both independent-trajectory methods discussed in the following, a classical-trajectory equation (see Refs. [225, 226]) is used to propagate an electronic density matrix $\hat{\tilde{\rho}}^\alpha$ (or wave function $\tilde{\Psi}^\alpha$, for a pure state) in time. The classical-trajectory ansatz replaces the position and momentum operators in the Hamiltonian with the time-dependent classical variables $(\hat{R}^\alpha, \hat{P}^\alpha) \rightarrow (R^\alpha(t), P^\alpha(t))$,

which leads to:

$$\frac{d}{dt}\hat{\tilde{\rho}}^{\alpha}(t) = -\frac{i}{\hbar}\left[\hat{H}^{BO}(R^{\alpha}(t)), \hat{\tilde{\rho}}^{\alpha}(t)\right]. \tag{5.51}$$

The connection of this time-dependent electronic density matrix $\hat{\tilde{\rho}}^{\alpha}$ to the one used in the ensemble average ansatz $\hat{\rho}^{el,\alpha}$, see Eq. (5.49), is different in the two independent-trajectory approaches discussed below.

We already mentioned that this independent-trajectory ensemble approach (Eqs. (5.49), (5.50) and (5.51)) is not an exact solution to the quantum-classical Liouville equation (5.46), see Ref. [220]. Hence, in addition to neglecting higher-order terms of $\hbar$ (or m/M), further approximations are needed to arrive at this independent-trajectory ansatz. Depending on the approximations involved, the form of the effective nuclear Hamiltonian $H^{nuc,\alpha}$ and the interpretation of the electronic density matrix $\hat{\tilde{\rho}}^{\alpha}$ will differ. In the following, we omit the trajectory-index α where it does not lead to confusion, as each trajectory is propagated completely independently from the others.

5.3.3 Multitrajectory Ehrenfest

One of the most common trajectory-based descriptions to include non-adiabatic effects is the Ehrenfest approach, in which the electron-nuclear couplings are described in a mean-field approximation, see Refs. [30, 227, 228]. It is also called the mixed quantum/classical time-dependent self-consistent-field method, see Refs. [229, 230].

Here, the nuclear Hamiltonian takes the form

$$H^{nuc} = T^{nuc} + \mathrm{Tr}\left[\hat{H}^{BO}\hat{\rho}^{el}(t)\right]_e, \tag{5.52}$$

where $T^{nuc} = \sum_k P_k^2/(2m_k)$ is the classical nuclear kinetic energy and the trace $\mathrm{Tr}[\cdot]_e$ is taken over the electronic subsystem only (see Ref. [37]). In the example of the Holstein model, taking the electronic trace of the Born-Oppenheimer Hamiltonian corresponds to the replacement $\hat{n}_i \to \langle \hat{n}_i \rangle$. By taking this electronic trace, the nuclei of each trajectory evolve according to the mean-field of the propagated electrons of that trajectory. Since multitrajectory Ehrenfest includes a whole ensemble of trajectories, see Eq. (5.49), each with their own electron density, it might be oversimplified to refer to the whole method as a mean-field ansatz (in the electron-phonon coupling). We will nonetheless follow this typical naming convention, see, e.g., Refs. [45, 228, 231]. The electronic degrees of freedom time-evolve under the classical-trajectory Hamiltonian (Eq. (5.51)), i.e., $\hat{\rho}^{el} = \hat{\tilde{\rho}}$.

The independent-trajectory equations of motion, Eqs. (5.51) and (5.50), with the nuclear Hamiltonian given by Eq. (5.52) define the Ehrenfest dynamics. The multitrajectory approach (Eq. (5.49)) allows to sample initial states described by a distribution in phase space, but afterward the different trajectories do not influence each other. Ehrenfest dynamics with multiple trajectories is also called multitrajectory Ehrenfest (MTE), see Refs. [45, 231], and we will follow this notation to differentiate it from the alternative multiconfigurational

Ehrenfest method mentioned later, see Sec. 5.3.6.

One can derive (see Ref. [30] for details) the Ehrenfest dynamics equations of motion (for a single trajectory) by assuming that the total wave function of the composite system is (for all times) a product of an electronic and a nuclear wave function. By integrating out one or the other part of the wave function in the Schrödinger equation, one arrives at two coupled time-dependent mean-field effective Schrödinger equations. Afterward, one takes the classical limit for the nuclear degrees of freedom in both equations. First, the nuclear wave function is factored into amplitude and phase terms, and in the equation for the phases one takes $\hbar \to 0$, which leads to a Hamilton-Jacobi equation that is equivalent to Hamilton's equations, Eq. (5.50), with the Ehrenfest nuclear Hamiltonian, Eq. (5.52). Second, the nuclear wave function appearing in the electronic effective Schrödinger equation is replaced with a delta function at the nuclear position, which leads to the electronic equation of motion used in Ehrenfest dynamics, Eq. (5.51). Hence, one can think of Ehrenfest dynamics as a combination of a classical approximation for the nuclei with an electron-nuclear product ansatz (leading to a mean-field coupling) for the total wave function.

One can also take these two approximations in the opposite order, which we will look at in slightly more detail. The classical approximation for the nuclei (or at least lowest order approximation in $\hbar$) leads to the quantum-classical Liouville equation (5.46). As stated earlier, the first term and second term on the r.h.s. of this equation are similar to the terms appearing in the quantum mechanical von Neumann and the classical Liouville equation, respectively. They can be separated by a product ansatz for the total density matrix of the system (where $\hat{W}$ takes the role of the quantum-classical density matrix), see Refs. [220, 232]: $\hat{\rho}(X) = \hat{\rho}^{el} \cdot \rho^{nuc}(X)$ (with $X = (R, P)$). The electronic and nuclear density matrices are the reduced density matrices of their respective subsystems, $\hat{\rho}^{el} = \int \hat{\rho}(X) \mathrm{d}X$ and $\rho^{nuc}(X) = \mathrm{Tr}\left[\hat{\rho}(X)\right]$ and both are normalized to have a trace of one (for the classical (nuclear) subsystem the integral over the phase-space is one). This ansatz neglects correlations between the electronic and nuclear subsystems.

Taking then either the trace over the electronic, or the phase-space integral over the nuclear degrees of freedom of the quantum-classical Liouville equation, one gets two coupled equations of motion:

$$\frac{\partial}{\partial t}\hat{\rho}^{el}(t) = -\frac{i}{\hbar}\left[\int \mathrm{d}X \hat{H}_W^{(d)}(X)\rho^{nuc}(X,t), \hat{\rho}^{el}(t)\right] \tag{5.53}$$

$$\frac{\partial}{\partial t}\rho^{nuc}(X,t) = \left\{\mathrm{Tr}\left[\hat{H}_W^{(d)}(X)\hat{\rho}^{el}(t)\right], \rho^{nuc}(X,t)\right\}. \tag{5.54}$$

The first equation is a von Neumann equation where the electronic density matrix evolves according to an effective (time-dependent) Hamiltonian given by $\int \mathrm{d}X \hat{H}_W^{(d)}(X)\rho^{nuc}(X,t)$. The second equation is a classical Liouville equation with an effective nuclear Hamiltonian given by $\mathrm{Tr}\left[\hat{H}_W^{(d)}(X)\hat{\rho}^{el}(t)\right]$, which corresponds exactly to the nuclear Hamiltonian used in Ehrenfest dynamics, Eq. (5.52). For pure states (see Ref. [232]) these coupled equations can be

solved by a classical nuclear trajectory $\rho^{nuc}(X') = \delta(X' - X(t))$, where $X(t)$ solves the Hamilton's equations of motion, which leads to the Ehrenfest dynamics equations of motion.

Ehrenfest dynamics is one of the simplest implementations of non-adiabatic dynamics. Its time-evolution is completely deterministic and if one starts from an initial condition in a pure classical nuclear state (R_0, P_0), then only a single trajectory is needed. It can be used to augment a molecular dynamics simulation with the possibility to go beyond the lowest Born-Oppenheimer surface, which was done in a recent implementation of photoinduced non-equilibrium dynamics for the manganite tight-binding model, see Refs. [32, 33]. In addition, neither Eqs. (5.51) nor (5.52) referred to a specific basis and Ehrenfest dynamics is thus independent of the electronic basis.

To see that Ehrenfest dynamics does capture at least some non-adiabatic effects, let us represent (for a pure state) the electronic wave function in the adiabatic (Born-Oppenheimer) basis $|\phi_a^{BO}(R(t))\rangle$ (see also Ref. [37]), which depends on the classical nuclear path $R(t)$: $|\Psi^{el}(t)\rangle = \sum_a \Psi_a^{el,(a)}(t)\,|\phi_a^{BO}(R(t))\rangle$. The time evolution for the electrons is then described by the following Schrödinger equation (see also Ref. [29]):

$$i\hbar\partial_t \Psi_a^{el,(a)}(t) = \sum_b \left(\delta_{a,b} E_b^{BO}(R(t)) + \sum_k \dot{R}_k(t) A_{a,b,(k)}(R(t)) \right) \Psi_b^{el,(a)}(t), \quad (5.55)$$

In contrast to the exact (multicomponent) nuclear Schrödinger equation (5.15), this equation (5.55) is a purely electronic time evolution and the nuclei enter only as time-dependent external variables. However, it has the similarity that the off-diagonal elements of the derivative couplings allow non-adiabatic transitions between different Born-Oppenheimer states, here appearing in a scalar product with the nuclear velocities $\dot{R}(t)$. As already in the Landau-Zener formula (see Refs. [207, 208]), Eq. (5.25), a wave packet approaching a region of strong derivative couplings with a higher velocity will lead to a higher transition probability between the surfaces. In fact, both equations ((5.25) and (5.55)) are the same Schrödinger equation in different representations, with the only difference that in Ehrenfest dynamics the nuclear path is not predetermined, but obtained by Hamilton's equations of the mean-field nuclear Hamiltonian.

One of the main problems of the mean-field approximation becomes apparent when comparing the nuclear Hamiltonian, Eq. (5.52) to the exact equation (5.15). In the exact Born-Huang framework, the dynamics on different surfaces are coupled only when the derivative couplings become significant. Otherwise wave packets on different surfaces evolve independently under the potential given by their Born-Oppenheimer surfaces. This is not the case for the Ehrenfest nuclear Hamiltonian, in which the potential is given by the trace of the electronic density matrix with the Born-Oppenheimer Hamiltonian. If the density matrix of any trajectory has contributions on several Born-Oppenheimer surfaces, then the trajectory will evolve according to a mixture of surfaces, even when the derivative couplings are negligible. This can be problematic for quenched systems, where the electron usually already starts in some superposition of several states, but also for a wave packet starting on one

Born-Oppenheimer surface moving through an avoided crossing, which should in the exact case lead to a wave packet splitting, as observed, for example, in Fig. 5.5. In addition, MTE violates detailed balance, which can lead to wrong long-time results and deviations from the quantum Boltzmann distribution of excited states in an equilibrium quantum-classical ensemble, see Ref. [233].

5.3.4 Fewest-switches surface hopping

Alternative independent-trajectory approaches are surface-hopping methods, see Refs. [234, 235], which try to solve the mean-field problem of Ehrenfest dynamics mentioned above. The idea is that the nuclear potential for a trajectory is given by a single energy surface $E_\lambda = \langle\phi_\lambda|\hat{H}^{BO}(R)|\phi_\lambda\rangle$ at a time, which is indicated by the currently active surface (AS) variable $\lambda(t)$ of that trajectory ($|\phi_\lambda\rangle$ is then also called the active state of the trajectory). This surface, and thus the whole algorithm, depends strongly on the chosen electronic basis $|\phi_a\rangle$. The standard choice (see Ref. [30]) is the Born-Oppenheimer (adiabatic) basis, which will also be used here. In this basis the surface hopping nuclear Hamiltonian for a certain trajectory has the form:

$$H^{nuc} = T^{nuc} + E^{BO}_{\lambda(t)}. \tag{5.56}$$

A stochastic hopping algorithm is applied to account for non-adiabatic transitions between surfaces. We use here the most common hopping algorithm, which is the fewest-switches surface hopping (FSSH) algorithm, see Ref. [29]. Here, the distribution of trajectories on the surfaces should approximately reproduce the weights of an electronic density matrix time evolved under the classical trajectory. This is the same time-evolution equation as for MTE, i.e., Eq. (5.51) for the density matrix, or Eq. (5.55) for the wave function in the adiabatic basis. Hence, the electronic populations obtained from $|\tilde{\Psi}_a(t)|^2 = \tilde{\rho}_{a,a}$ (we will deal here only with pure electronic states for each trajectory) represents the probability of a trajectory to be on surface a at a certain time t. The $\tilde{\Psi}_a$ are denoted as electronic wave functions or amplitudes here, to differentiate them from the active surfaces. In the literature on mean-field molecular dynamics with surface hopping, the active surfaces are denoted as "auxiliary electronic wave functions", which are used to determine the nuclear forces, in contrast to the "primary wave functions" $\tilde{\Psi}_a$ containing all quantum coherences, see Refs. [236, 237]. We will not follow this notation here, as we will see that the active surfaces are useful for more than just determining the nuclear forces and are also relevant for calculating observables.

The time derivative of the surface probabilities determined from the electronic populations $\tilde{\rho}_{a,a}$ can be expressed as (see Ref. [29]):

$$\frac{\partial}{\partial t}\tilde{\rho}_{a,a} = \sum_{b\neq a} -2\Re\left[\frac{i}{\hbar}(\tilde{\Psi}_a)^*\tilde{\Psi}_b \sum_k \dot{R}_k \cdot A_{a,b,(k)}(R)\right] =: \sum_{b\neq a} b_{a,b}, \tag{5.57}$$

where $\Re$ is the real part. FSSH identifies from this sum-decomposition (Eq. (5.57)) the probability flow from surface a to surface b per time step

Δt as $-b_{a,b}\Delta t$. Assuming that an ensemble of N trajectories following the same nuclear path $R(t)$ are distributed on the surfaces according to $\tilde{\rho}_{a,a}(t)$ $(\forall a)$ at time t, then (to lowest order in Δt) at the time $t + \Delta t$ in total $-Nb_{a,b}\Delta t$ trajectories must switch from surface a to surface b, see Ref. [29]. Of the many possibilities to design a hopping algorithm in which these changing probabilities are fulfilled, the fewest-switches surface hopping tries to do this, as the name implies, with the fewest number of surface hops possible. This is done by allowing surface hops to occur only in the direction where the probability flow $-b_{a,b}\Delta t$ is positive. The hopping probability of an individual trajectory from active surface λ to another surface λ' is then:

$$p_{\lambda\to\lambda'} = \max\left\{\frac{-\Delta t b_{\lambda,\lambda'}}{\tilde{\rho}_{\lambda,\lambda}}, 0\right\}. \tag{5.58}$$

We can directly see that the assumption of a swarm of trajectories following the same nuclear path although being distributed on different surfaces will not be satisfied in general for long times, since the different potentials formed by the surfaces will affect the nuclear trajectories, see Ref. [238]. Hence, the so called internal consistency condition of FSSH

$$\frac{1}{N_{traj}}\sum_{r}^{N_{traj}} \tilde{\rho}^{\alpha}_{a,a}(t) \stackrel{!}{=} \frac{1}{N_{traj}}\sum_{r}^{N_{traj}} \delta_{a,\lambda^{\alpha}(t)}, \tag{5.59}$$

comparing the adiabatic populations according to the electronic wave functions and the active surface distributions, will not be fulfilled in general. Decoherence corrections of FSSH can improve the internal consistency, see Sec. 5.3.5.

After a hop between surfaces $\lambda \to \lambda'$, which differ in energy by $\Delta E = E_{\lambda'} - E_{\lambda}$, the nuclear kinetic energy of the trajectory is adjusted to conserve the total energy of the system. In this velocity adjustment, the nuclear momentum changes, here explicitly written as vectors, $\vec{P} \to \vec{P}'$. Normally this is not done in a uniform way, but along a unit hopping vector, which is typically taken as the normalized derivative coupling vector $\hat{A} := \vec{A}_{\lambda,\lambda'}/|\vec{A}_{\lambda,\lambda'}|$, see, e.g., Ref. [206] for a discussion of this choice. With the nuclear kinetic energy along the hopping vector defined as $T_A^{nuc} = \sum_k (\vec{P}\cdot\hat{A})^2/(2m_k)$), the velocity adjustment takes the following form (see also Ref. [239]):

$$\vec{P}' = \vec{P} - \left(\vec{P}\cdot\hat{A}\right)\left(1 - \sqrt{1 - \Delta E/T_A^{nuc}}\right)\hat{A}. \tag{5.60}$$

If the hop is toward a higher energy surface, $\Delta E > 0$, and the nuclear kinetic energy along the hopping vector T_A^{nuc} is too small to provide the necessary energy, $T_A^{nuc} < \Delta E$, then the hop is *frustrated* and ignored. These frustrated hops can lead to a further violation of the internal consistency in FSSH (Eq. (5.59)), most pronounced at low nuclear kinetic energies.

With this, the dynamical equations of FSSH for each trajectory α are set: (1) the nuclear trajectory $(R^{\alpha}(t), P^{\alpha}(t))$ evolves under the influence of a single Born-Oppenheimer surface, given by the active surface of that trajectory at the given time, Eq. (5.56), (2) the electronic wave function/amplitude $\tilde{\Psi}^{\alpha}(t)$

evolves via the classical nuclear trajectory equation (5.51), and (3) the active surface $\lambda^\alpha(t)$ changes according to a hopping algorithm, which refers to the adiabatic populations $\tilde{\rho}^\alpha_{a,a} = \tilde{\Psi}^\alpha_a \tilde{\Psi}^{\alpha *}_a$ obtained from the time-evolved electronic amplitudes (Eq. (5.58)). For calculating observables, however, we still need to connect the attached electronic density matrix $\rho^{el,\alpha}$ used for sampling the Wigner function (Eq. (5.49)) to these quantities.

Electronic wave function vs. active surfaces

Apparently, there are two variables in each trajectory which could be used to calculate electronic expectation values: the density matrix/wave function obtained from solving the classical-trajectory equation ($\tilde{\rho}$, resp. $\tilde{\Psi}$), or the active surface λ, see Ref. [224]. Even if one is only interested in, for example, calculating the populations of adiabatic states $\langle \hat{n}^{BO}_a \rangle$, the results from these two variables can differ, as the internal consistency condition of FSSH (Eq. (5.59)) will not be fulfilled in general. The standard way is to use the distribution of active surfaces for calculating these adiabatic observables, i.e. $\langle \hat{n}^{BO}_a \rangle = \frac{1}{N_{traj}} \sum_\alpha^{N_{traj}} \delta_{a,\lambda^\alpha}$, since, in contrast to the propagated wave function, the active surface distribution approximately obeys detailed balance, see Refs. [233, 240]. For obtaining populations in another electronic basis, for example diabatic populations, there is no obvious best option, see Refs. [224, 241, 242]. The two possibilities (from the propagated wave functions (WF), or the active surfaces (AS)) for defining the complete electronic density matrix in the adiabatic basis correspond to (see Refs. [224, 241–243]):

$$\rho^{el,(\mathrm{AS})}_{a,b} = \delta_{\lambda(t),a}\delta_{a,b}, \tag{5.61}$$

$$\rho^{el,(\mathrm{WF})}_{a,b} = \tilde{\Psi}_a \tilde{\Psi}^*_b. \tag{5.62}$$

According to the internal consistency condition (Eq. (5.59)) the trajectory-average of the diagonal entries of these two density matrices should be the same. Both options have advantages and disadvantages.

The first (AS) option leads to the desired form for calculating adiabatic populations from the active surfaces only, which also approximately obey detailed balance, as mentioned above. However, it can only describe a diagonal density matrix in the adiabatic basis. If one starts in a superposition of different adiabatic states, or if this superposition develops during the time-evolution, then the coherences, i.e., the off-diagonal elements of the electronic density matrix, cannot be captured with the first definition.

One very extreme example in the Holstein dimer is a trajectory which after some time arrives at $q = 0$. Depending on the transition probability, the trajectory might be on the upper or the lower surface. If one has many trajectories close to $q = 0$, the total density matrix will therefore be of the form $\rho^{el,(\mathrm{AS})} = |\phi^{BO}_+\rangle\, p_+ \,\langle \phi^{BO}_+| + |\phi^{BO}_-\rangle\, p_- \,\langle \phi^{BO}_-|$, where p_+ and p_- are the fraction of trajectories on the respective surfaces. At $q = 0$, however, we have for the Born-Oppenheimer states $|\phi^{BO}_{\pm,1}|^2 = |\phi^{BO}_{\pm,2}|^2 = 0.5$, independent of the active surface. Hence, if one now wants to calculate, for example, the electron density on one of the dimer sites close to this $q = 0$, then the result will always be 1/2,

which is clearly wrong in general (one can imagine starting on one dimer site with a hopping close to zero, then the trajectory should move through $q = 0$ with the electron density on the initially occupied site staying close to 1).

The second (WF) definition has no problem with describing such superposition states, and diabatic populations can be readily calculated, also with coherences included. One might consider in this case the active surfaces as an auxiliary quantity, used only to determine the nuclear forces (similar as in the mean-field literature mentioned above). On the downside, the electronic wave function amplitudes are not guaranteed to obey detailed balance (which is also violated in MTE), and in general are unreliable for long times, see Refs. [233, 240–242]. Hence, both of the above definitions should be used with caution. The decoherence correction mentioned later, Sec. 5.3.5, solves this problem by relaxing the electronic amplitudes toward the active surfaces over time, so that one can use the (WF)-definition (Eq. (5.62)) to describe the correct short-time coherences without having the problem of the unreliable long-time description.

We are not aware of any well defined approximation, in the sense that one can quantify the error of a series expansion, or systematically improve the results by increasing a variational space, which leads to the fewest-switches surface hopping algorithm, see also Ref. [46]. Already in the first proposal for the quantum-classical Liouville equation (QCLE) (see Ref. [219]) an approximate surface-hopping trajectory approach was derived by using a so-called momentum-jump approximation, which however did not directly derive the FSSH-equations of motion. The closest connection between FSSH and the QCLE was given by Subotnik et al. (Ref. [224]). They showed that the dynamical equation for the diagonal and off-diagonal elements of the partially Wigner transformed density matrix in both approaches can become equivalent under a series of conditions and one extension for FSSH: the inclusion of a decoherence correction. More information on the decoherence correction are given in Sec. 5.3.5.

The most important (termed major in Ref. [224]) conditions are first that all trajectories at the same point in nuclear phase space and on the same active surface always have the same attached electronic density matrix $\tilde{\rho}$ and second that the nuclear momenta are large. The first condition will certainly be violated when previously separated wave packets meet again, which is a so-called recoherence. The second condition will be fulfilled if in the strong-coupling regions, e.g., avoided crossings, the energy splitting of the surfaces is small compared to the nuclear kinetic energy, which is the same requirement that is also needed if one wants to avoid frustrated hops. Even with these two assumptions fulfilled, the equations only become nearly equivalent when including a special form of decoherence correction (named major condition 3 in Ref. [224]), which requires the propagation of additional variables, going beyond standard FSSH. This is not done in this thesis. Hence, one should be careful in deriving the validity or accuracy of FSSH by checking whether the two conditions mentioned above are fulfilled, but they give a good first indication.

Based on this approximate derivation of FSSH, an alternative (mixed) def-

inition for the electronic density matrix was proposed, see Ref. [241], which uses the active surfaces on the diagonal in the adiabatic basis, and the electronic amplitudes to recover the coherences:

$$\rho_{a,b}^{el,(\text{mixed})} = \begin{cases} \delta_{\lambda(t),a}, & \text{for } a = b \\ \tilde{\Psi}_a \tilde{\Psi}_b^*, & \text{for } a \neq b. \end{cases} \tag{5.63}$$

With this mixed definition the short-time coherences are correctly recovered, while at long times the electronic density matrix is dominated by the active surfaces, at least under the assumption that different trajectories carry different phases, so that the coherences cancel out, see also Ref. [242]. With this mixed definition one does not have to rely on a decoherence correction to calculate accurate electronic populations in any basis. In addition, adiabatic populations are calculated from the active surfaces only, as desired. One disadvantage is that the electronic populations obtained by this definition might become negative, which we observed in large systems with initial states starting in a superposition of many adiabatic states. In these cases one needs to resort to a decoherence correction to obtain both reasonable short- and long-time dynamics, see the analysis in Sec. 6.3.1.

The same problem as for the calculation of observables also applies to the setup of the initial state. Let us assume the Wigner function of the composite initial system in some electronic basis is separable $W_{a,b:W}(R,P) = W(R,P) \cdot \rho_{a,b}^{el}(R)$, which will always be the case for the initial states studied in this thesis (the electronic basis needs to be chosen first for the definition of the partial Wigner transform used here, see the discussions in Sec. 5.3.1). The nuclear trajectory can then be sampled from the Wigner function of the nuclear subsystem $W(R,P)$. If the electronic density matrix at the sampled nuclear position is restricted to a single adiabatic state c, i.e., in the adiabatic basis $\rho_{a,b}^{el} = \delta_{a,b}\delta_{a,c}$, then one can trivially set $\tilde{\Psi}_a = \delta_{a,c}$ and $\lambda = c$, so that all definitions of the electronic density matrix (Eqs. (5.61), (5.62) and (5.63)) are equivalent at $t = 0$. In the same way a mixed state of different adiabatic states can be sampled by starting with an ensemble of trajectories for each nuclear position, each of which starts from a selected adiabatic state c with the probability given by $\rho_{c,c}^{(a)}$, leading again to equivalence of all definitions of the electronic density matrix.

However, a general initial state will not be of these forms, but in a superposition of several, or many, adiabatic states, e.g., for a pure state, $\rho_{a,b}^{el} = \Psi_a^{el}\Psi_b^{el}$. This can be a state obtained after an excitation with a photon field, see Ref. [242], or simply a diabatic initial state, such as an electron localized to a single site in a crystal. The adiabatic electronic density matrix will then contain coherences (off-diagonal terms). The best guess for the active surface λ is to randomly select them from the diagonal entries of the density matrix according to $\rho_{c,c}^{(a)}$ (in this way the active-surface electronic density matrix (Eq. (5.61)) will at least recover the diagonal entries of ρ^{el}). To achieve equivalence of the density matrix definitions at $t = 0$, one could now also project the electronic amplitudes $\tilde{\Psi}$ completely on the selected adiabatic state. This will discard all coherences and observables relying on them will not be recovered for the initial state (which

is the same problem as discussed for the definition of the active-surface electronic density matrix, Eq. (5.61)). If one is interested in long-time results, high-temperature thermal states or observables depending only on adiabatic populations, then this projection might be suitable, which has been used, for example, in Ref. [243]. The alternative is to set (for a pure state) $\tilde{\Psi} = \Psi^{el}(t{=}0)$. Using the wave-function or the mixed definition of the electronic density matrix (Eq. (5.62) and (5.63)), one can recover all observables of the initial state, but these definitions will deviate from the active-surface definition (Eq. (5.61)) from the beginning. This ansatz was also suggested based on the approximate derivation of FSSH from the QCLE, see Ref. [242], and will be used in this thesis. We note that the nuclear potential is always calculated from the active surfaces according to Eq. (5.56), i.e., for a such a superposition state, the forces acting on the nuclei will deviate from the correct quantum mechanical forces. Hence, in contrast to MTE, we cannot guarantee that the ultra-short time dynamics in FSSH are recovered correctly when starting from a superposition of adiabatic states.

5.3.5 FSSH improvements

The FSSH algorithm is more prone to numerical errors and can easier give wrong results if not used carefully, compared to MTE. Due to the general success of the surface-hopping technique, a large variety of improved algorithms have been proposed in recent years, see Refs. [244, 245]. Here, we are interested in variations that still stay close to the core formalism of FSSH, while solving some of the problems that especially appear in large systems, see Ref. [205]. The most important correction includes some form of decoherence, which helps to ensure internal consistency (Eq. (5.59)) and to converge the different definitions of the electronic density matrix. In addition, we have to consider corrections necessary for sharply peaked derivative couplings, where numerical convergence is difficult to achieve and very small time-steps are needed with the standard hopping algorithm of FSSH (Eq. (5.58)). When starting in a superposition of adiabatic states and in general in large systems, applying a decoherence correction can lead to the problem of spurious charge transfer, which we also need to address. The corrections are outlined in the following.

Decoherence correction

The first idea for a correction to the standard FSSH algorithm was proposed already in the original paper by Tully, Ref. [29], which was to add damping terms for the off-diagonal elements of the propagated density matrix $\tilde{\rho}$, to approach, over time, a diagonal electronic ensemble in the adiabatic basis. This damping of the coherences, hence called decoherence correction, does not only improve the internal consistency condition (Eq. (5.59)) mentioned above, it also solves the problem of over-coherence inherent to the standard FSSH algorithm (and in general all independent-trajectory methods): Since the trajectories do not influence each other at all, a trajectory will coherently propagate any phase

relation between surfaces for arbitrary long times. Hence, even if a trajectory stays on a certain Born-Oppenheimer surface for a very long time and then re-enters a region of strong non-adiabatic coupling, it will still "remember" if it had electronic contributions on the other surfaces, while one would expect in typical large systems that these have decayed in the meantime by interactions with the environment. Adding any type of artificial decoherence correction which is implemented on the independent-trajectory level will always be a heuristic approach and many variations have been proposed in literature, see, for example, Refs. [200, 205, 242, 244].

In this thesis, a force-based decoherence correction is used, which is based on a frozen Gaussian method, see Refs. [246, 247], and was proposed in Refs. [248, 249]. The decoherence time is estimated from considering the influence of the overlap of two Gaussian wave packets located on different electronic energy surfaces but centered around the same nuclear phase space point on the transition probability between the two surfaces. The overlap decays in second order in time with the difference of the nuclear forces on the different surfaces, see Refs. [242, 248, 249]. Using this force-based decoherence rate in the FSSH algorithm, all electronic amplitudes of the non-active states are damped in each time step Δt: $\tilde{\Psi}'_a = \tilde{\Psi}_a \cdot \exp(-\Delta t/\tau_a)$, $\forall a \neq \lambda$ with the surface-specific decoherence rate:

$$\frac{1}{\tau_a} = \sqrt{\sum_k \left(F_k^\lambda - F_k^a\right)^2 / (4 a_k \hbar^2)}, \tag{5.64}$$

while the electronic amplitude of the active state is rescaled to conserve the norm. Here, the forces are defined by $F_k^a = \nabla_k E_a^{BO}$ and a_k is the so-called "width of the frozen Gaussians" (see, e.g., Ref. [248]), which has units of inverse length squared. Applied to the harmonic oscillators of the Holstein model it is straightforward to take it as the inverse squared natural length scale $a_k = \frac{m\omega_0}{\hbar}$.

As mentioned earlier, the approximate connection of FSSH to the QCLE by Subotnik et al. (Ref. [224]) led to a more involved expression for the decoherence rates that require the propagation of additional variables in the algorithm and is not done here. Using a frozen Gaussian ansatz for this more involved expression also leads to a decoherence rate proportional to the difference in forces, equivalent to a previously proposed so-called augmented FSSH (A-FSSH) algorithm (see Refs. [203, 250]). This supports the force-based choice for the decoherence rate taken here, see also Ref. [242], although the expression presented in Ref. [224] leads to prefactors for the decay-rate of on- and off-diagonal elements of the electronic density matrix that cannot be recovered completely by using a wave-function based decoherence rate, see Ref. [224].

Dealing with strongly peaked derivative couplings

The derivative couplings between two surfaces can become strongly peaked when these surfaces come close together. One can see this in the example

of the Holstein dimer, where the derivative couplings diverge for $t_0 \to 0$, see Eq. (5.23). This can lead to numerical problems in the FSSH algorithm, as the derivative couplings are needed for the time evolution of the density matrix if an adiabatic basis is used (Eq. (5.55)), for calculating the hopping probabilities (Eq. (5.57)) and for determining the direction of the velocity correction after a surface hop (Eq. (5.60)). Very small time steps are then needed to still reliably sample the derivative couplings, as otherwise the trajectory might completely transition through an avoided crossing region between two time-steps, see Refs. [204, 206, 251, 252]. While for a two-level system as in the Holstein dimer this requires quite unphysical parameters (e.g., a very small electronic hopping term), in large systems energy surfaces can regularly come very close or cross completely, see Ref. [205], for example when two adiabatic states are localized to different regions of the system and are only very weakly coupled. Hence, in large systems, it is advisable to avoid referring to the derivative couplings in the dynamical equations, when possible.

Since the time-evolution of the electronic amplitudes can be performed in any basis, one can easily switch, for example, to the diabatic basis, which will not depend on the derivative couplings. If the adiabatic electronic amplitudes are needed to determine the hopping probabilities, then one can still obtain them by performing the corresponding basis transformation after the wave function propagation step, see Ref. [251]. This is also referred to as the representation transformation technique in Ref. [205].

Avoiding the derivative couplings is not as simple for the hopping probabilities, which explicitly refer to the probability flow between adiabatic states (at least with the standard basis choice, see Ref. [30]) and several corrections to obtain numerically stable variants have been proposed, see Ref. [205]. With the electronic amplitudes propagated with the representation transformation technique, the adiabatic probabilities at subsequent time steps, $|\tilde{\Psi}_a(t)|^2$ and $|\tilde{\Psi}_a(t+\Delta t)|^2$, are obtained without numerical difficulties. This can be used to enforce the FSSH sum rule for the hopping probabilities (Eq. (5.57)) to linear order in Δt exactly:

$$\frac{|\tilde{\Psi}_\lambda(t)|^2 - |\tilde{\Psi}_\lambda(t+\Delta t)|^2}{|\tilde{\Psi}_\lambda(t)|^2} = \sum_{a\neq\lambda} g_a^{(\lambda)}, \tag{5.65}$$

where λ is the active surface and the $g_a^{(\lambda)}$ are used to determine the hopping probabilities in a time step Δt: $p_{\lambda\to a} = \max\{g_a^{(\lambda)}, 0\}$, which was $g_a^{(\lambda)} = \frac{-\Delta t b_{\lambda,a}}{\tilde{\rho}_{\lambda,a}}$ in the standard FSSH implementation (see Eq. (5.58)). This sum rule is fulfilled approximately if sufficiently small time steps are used, but can be violated around a surface crossing or near-crossing when the derivative couplings are sharply peaked, especially when the electronic amplitudes are propagated in the diabatic basis, while the $g_a^{(\lambda)}$ are obtained from the (numerically challenging) adiabatic expression (Eq. (5.57)).

One option is to use a self-consistent correction, first proposed in Ref. [252], in which the sum rule is enforced by adjusting the hopping probability from the active state to one other state if a "trivial" surface crossing between the two

states is detected, where the character of the two surfaces interchanges within one time step. This is typically the case when two surfaces (nearly) cross. In this self-consistent corrected algorithm, the overlap of the Born-Oppenheimer eigenstates is used to identify these situations. Slightly more advanced is the crossing-corrected algorithm, where both surfaces involved in a surface hop are checked for trivial crossings with all other surfaces, and the final state after both a successful and a frustrated hop is adjusted accordingly, see Ref. [253]. In addition, the energy conservation step via nuclear velocity adjustment is omitted in the crossing-corrected algorithm if a trivial crossing is detected between the two surfaces involved in the surface hop, see Ref. [253]. The disadvantage of these corrections is that they rely on the identification of the trivial crossing situations. For Born-Oppenheimer surfaces that approach each other asymptotically, as in the Holstein trimer, see Fig. 5.7, this might not suffice.

Hence, in this thesis, we follow a different approach to obtain corrected hopping probabilities in large systems. If the unitary time evolution operator connecting the adiabatic wave functions between two time steps, $\tilde{\Psi}_a(t+\Delta t) = \sum_b P_{a,b}(t, t+\Delta t)\tilde{\Psi}_b(t)$, is known from the representation transformation technique, then one can fulfill the sum rule (Eq. (5.65)) exactly by choosing an alternative expression for the $g_a^{(\lambda)}$:

$$g_a^{(\lambda)} = \frac{|\tilde{\Psi}_\lambda(t)|^2 - |\tilde{\Psi}_\lambda(t+\Delta t)|^2}{|\tilde{\Psi}_\lambda(t)|^2} \times \frac{\Re\left[P^*_{a,\lambda}(t, t+\Delta t)\tilde{\Psi}_a(t+\Delta t)\tilde{\Psi}^*_\lambda(t)\right]}{|\tilde{\Psi}_\lambda(t)|^2 - \Re\left[P^*_{\lambda,\lambda}(t, t+\Delta t)\tilde{\Psi}_\lambda(t+\Delta t)\tilde{\Psi}^*_\lambda(t)\right]}. \tag{5.66}$$

This expression for the hopping probabilities was suggested in Ref. [254] as an improvement of a similar variant presented first in Ref. [251].

For the velocity adjustment after a surface hop we still have to rely on the derivative couplings. In the crossing corrected algorithm (see Ref. [253]) the velocity adjustment would be simply omitted when a trivial surface crossing is encountered. Since in these cases the energy difference between surfaces is very small anyway, we continue to use the numerically challenging derivative couplings in this step, which will likely not influence the dynamics significantly.

Spurious charge transfer

One problem of introducing a decoherence correction might occur in large systems, which is called spurious charge transfer (Refs. [243, 255]) or decoherence correction enhanced trivial crossing problem (Refs [205, 256]), see also Ref. [37]. If one starts with an initial state in a superposition of many adiabatic states, then the decoherence correction quickly removes the coherences necessary to correctly describe this initial state. One example is a state where an electron is initially localized to a single site of the Holstein chain, while all phonon harmonic oscillators are in the ground state (this will be one of the example systems studied later, called *bare local* initial state, see Fig. 6.1(d)).

For a trajectory where now most nuclei are around $x_i = 0$, the adiabatic states will be standing wave modes and delocalized in the whole system. The decoherence correction can then lead to an artificial fast charge transfer throughout the system, independent of which form of the density matrix is used (which become mostly equivalent when using the decoherence correction).

This problem occurs as well if one starts in a single adiabatic state, but then encounters an erroneous surface hop (for example close to a trivial crossing without using corrected hopping probabilities as discussed previously in Sec. 5.3.5). In the worst case, a hop could happen between two surfaces located to distant regions of the system. Without a decoherence correction, the electronic amplitudes are still propagated via Eq. (5.51) and one can obtain a reasonable electronic density from them (via Eq. (5.62)). With the decoherence correction included, the electronic amplitudes are relaxed toward the new adiabatic state, potentially leading to a system-size dependent spurious charge transfer that is not related to a physical propagation. This was the main problem identified in the original publications (Refs. [205, 243, 255, 256]), and using corrected hopping probabilities or small time-steps can already alleviate a large part of the problem (see Ref. [205] and also Ref. [257], where almost system-size independent dynamics were achieved when using a crossing-corrected algorithm). To further reduce the problem, and for dealing with initial states in a superposition of many adiabatic states, where improving the hopping algorithm is not sufficient, one can implement restrictions on the decoherence correction.

Two variants of such restrictions have been proposed, which either allow for decoherence only when the adiabatic population of the active state is sufficiently large (Ref. [256], also used in [257] to obtain even better system-size independence), or only within a certain active region of diabatic states (Ref. [255]). For the case of the bare local initial state mentioned before, most adiabatic states will have a significant contribution at the beginning and the first approach cannot be used to prevent the unphysical charge spreading. Hence, in this thesis, the second approach is used. This ansatz was already applied to organic semiconductor systems to study mobilities (see Refs. [243, 255]).

The active region of each trajectory is chosen to include a fraction R of the electronic charge density, which in the original paper was set as $R = 0.999$ (Ref. [255]). This region is determined in each time step after the propagation of electrons and nuclei, but before the decoherence correction. In our implementation (see Ref. [37]) the active region is constructed by adding diabatic states with decreasing population (for the one-electron case studied here these are the site-local orbitals in the Holstein chain) to a subset until the threshold R is exceeded. The higher the threshold, the more sites are included, while a small R leads to a stronger restriction. Afterward, the decoherence correction is applied, but all changes to the diabatic electronic amplitudes (which are obtained by a representation transformation) outside of the active region are ignored and the amplitudes inside the region are scaled to conserve the total norm. This restriction is only applied to the decoherence correction, not the normal electronic time evolution. It works especially well when the electronic amplitudes $\tilde{\Psi}$ are localized to certain regions of the system, while

the adiabatic states are delocalized, or localized to a different region. Hence, it can counteract the spurious charge transfer both after an erroneous surface hop, or for local initial states that are in a superposition of delocalized adiabatic states.

The threshold value R gives some freedom in the degree of the restriction. In the large systems where we apply this restriction later ($L \geq 11$ in the Holstein chain), we find that a value of $R = 0.99$ works even slightly better, see Sec. 6.3.1. As a new approach we also tested to completely turn off the decoherence correction for a fixed time at the beginning of the simulation. This can help for the short-time dynamics of initial states that clearly depend on the correct description of coherences, such as local initial states. Here (and in Ref. [37]), when studying the Holstein chain, we use a simple ansatz of delaying the use of a decoherence correction until a quarter phonon oscillation period $\pi/(2\omega_0)$ has passed, see Sec. 6.3.1.

An ever stronger restriction to surface hopping is the subsystem surface hopping (see Ref. [258]), in which the surface hopping description is used only for a dynamic part of the system, while the other sites are simulated with molecular dynamics. With less adiabatic states included in the algorithm, trivial crossings are less likely to be encountered, and adiabatic states localized to distant regions of the system cannot influence the dynamics. Even a three-level description combining surface hopping, molecular dynamics and a statistical description for different regions of the system has been proposed, see Ref. [259]. Such approaches might be useful if one wants to treat large systems where the important adiabatic states and surface transitions are still localized. These combined descriptions are, however, beyond the scope of this thesis.

5.3.6 Coupled-trajectory approaches

As apparent from the discussions above, both MTE and FSSH introduce strong approximations for the dynamics of a composite electron-nuclear system. A trajectory-based approach can, however, be used to solve the system (in principle) exactly if one allows for a coupling between the individual trajectories. A typical ansatz is to regard the trajectories as a moving basis used to represent the time-evolving wave function, in most cases taken as frozen Gaussian states (with fixed width), see Refs. [168, 246, 260]. If the Gaussian basis states follow the true dynamics of the nuclear wave packet tightly, then (ideally) a small number of such basis states for each electronic state is sufficient to represent the wave function at any time. This can be taken as a fully variational ansatz, leading to the variational multiconfiguration Gaussian (vMCG) method, see Ref. [261], which gives an equation of motion both for the coefficients of the wave function expansion and for the Gaussian parameters (the center points in phase space and a phase term). We note that one can choose to use a different set of Gaussian nuclear states for each electronic state (multi-set formalism), or to expand the total wave function in a single set of electron-nuclear product states (single-set formalism), see Ref. [262]. In any case, the basis states used in the wave function expansion are also called configurations.

The resulting complicated equations of motion can be simplified if the center

points of the Gaussians $X(t) = (R(t), P(t))$ of a configuration instead evolve according to Ehrenfest dynamics (Eqs. (5.50)) with H^{nuc} given by the average of the Hamiltonian over this configuration. This leads to multiconfigurational Ehrenfest (MCE), see Refs. [40, 41]. While MCE is simpler than vMCG, the non-variational ansatz conserves the total energy of the system only approximately, see Ref. [263].

There are two variants of MCE: in MCEv1, see Ref. [40], the wave function is expanded in a set of configurations α given by electron-nuclear product states $|\Psi(t)\rangle = \sum_\alpha \sum_i a_i^\alpha(t)\,|\chi_i\rangle\,|z^\alpha(t)\rangle$, where the $|z^\alpha(t)\rangle$ are the Gaussian nuclear states and the electronic basis $|\chi_i\rangle$ stays fixed over time. Hence, the coupled expansion coefficients $a_i^\alpha(t)$ take the role of electronic amplitudes. In contrast, the alternative version, MCEv2, see Ref. [41], uses a time-dependent electronic state $|\phi_i^\alpha(t)\rangle$ for each configuration, which is propagated independently from all other configurations as in the standard MTE algorithm via Eq. (5.51). These electronic states are normalized (in contrast to the expansion coefficients interpreted as electronic amplitudes in MCEv1), and additional expansion coefficients $A^\alpha(t)$ are introduced to represent the total wave function in these configurations: $|\Psi(t)\rangle = \sum_\alpha \sum_i A^\alpha(t)\,|\phi_i^\alpha(t)\rangle\,|z^\alpha(t)\rangle$. The equations of motion for both the nuclear Gaussians and the electronic amplitudes in MCEv2 depend only on the configuration itself, while the expansion coefficients $A^\alpha(t)$ couple the different configurations. Hence, if one identifies the center point of the Gaussian nuclear state as a classical nuclear particle in phase space $X(t)$, then the time-evolution of a configuration in MCEv2 is nearly equivalent to the one of an MTE trajectory. The difference is that the nuclear forces in MTE are determined solely from the classical nuclear position, while in MCEv2 one has to take the average forces over the configuration $H^{nuc} = \sum_i \langle \phi_i^\alpha, z^\alpha | \hat{H} | \phi_i^\alpha, z^\alpha \rangle$. For a nuclear Hamiltonian that is quadratic in the nuclear position, such as for the Holstein Hamiltonian (Eq. (5.2)) in a diabatic basis, both forces are equivalent. In this case one could take a finished MTE simulation (with the nuclear trajectory and electronic density matrix known for all simulated time) and only *a posteriori* time-evolve the coupled expansion coefficients $A^\alpha(t)$ to obtain the MCEv2 wave function at any time.

The MCE algorithm has been carefully implemented and tested by Stefan Gräber, see Ref. [264]. Besides exact diagonalization and a density matrix renormalization group method, it will be used as a benchmark method to evaluate MTE and FSSH in the Holstein model, see Ch. 6, which presents the results of a comparative study published in Ref. [37]. For more numerical details and convergence studies we thus refer to Refs. [37, 264], because these tests have not been carried out by the author of this thesis. Here we note only that while the method can become exact in principle (for a large number of configurations), this convergence is difficult to reach in large systems, not to the least because the total energy is not conserved when using too few configurations. This will become evident in Ch. 6, where MCE turns out to be a useful benchmark tool mainly for small systems, or specific observables in large systems. Nonetheless, whenever the method can be converged, it will correspond to the exact quantum mechanical time-evolution, which is a significant difference to the independent-trajectory methods MTE and FSSH

introduced above.

Other coupled-trajectory methods include the full multiple spawning, see Ref. [265], in which the number of nuclear basis states increases dynamically by spawning new trajectories when needed, and the Davydov D2 ansatz, see Refs. [42, 43, 266–268]. In addition, ab initio MCE, see Ref. [269], and ab initio multiple spawning, see Ref. [270], introduce further approximations to deal with systems where the potential energy surfaces are only known locally and in an adiabatic basis, as is often the case in electronic structure methods. Lastly, the multiconfiguration time-dependent Hartree (MCTDH) method, see Refs. [271, 272], is also based on an expansion of the wave function in time-dependent single-particle functions, which, however, are themselves expressed in a constant (often grid-based) basis set. The single-particle functions can be expanded recursively using the MCTDH scheme, leading to the multilayer MCTDH, see Refs. [273–275], suitable to describe large systems. When generalized to include non-orthogonal basis states and by replacing some single-particle functions with Gaussian functions, one arrives at the Gaussian MCTDH method, see Refs. [31, 276–278], which is the basis of the variational multi-configuration Gaussian (vMCG) method mentioned above.

It is evident that a large pool of methods exist that rely on the idea of a dynamically moving basis set, often described by a set of coupled trajectories, and that in principle converge to the exact dynamics for a sufficiently large basis set. In this thesis, the focus is on evaluating the performance of the independent-trajectory methods MTE and FSSH, and only the MCE results obtained by Stefan Gräber will be used to serve both as an additional benchmark and as an outlook on the improved performance to be gained by coupling the trajectories.

5.3.7 Implementation and convergence of the independent-trajectory methods

Initial states in the Holstein chain

Both the MTE and FSSH algorithm will be used to investigate the non-equilibrium dynamics of different initial states in the Holstein chain (Eq. (5.2)), which have been investigated in detail in Ref. [37]. The partially Wigner transformed density matrices of these initial states can always be separated into a purely nuclear Wigner function and an electronic density matrix corresponding to a pure state in some electronic basis: $W^{ini}_{a,b:W}(R,P) = W^{ini}(R,P) \cdot \Psi^{ini}_a(R)\Psi^{ini}_b(R)$, where the nuclear Wigner function corresponds to a product of Gaussians in the positions and momenta ($R = \vec{x} = (x_1, \ldots, x_L)$ and $P = \vec{p} = (p_1, \ldots, p_L)$), which in dimensionless units gives (see Ref. [37]):

$$W^{ini}\left(\vec{\bar{x}}, \vec{\bar{p}}\right) = \frac{1}{(\pi)^L} \prod_{i=1}^{L} \exp\left(-\left(\bar{x}_i - \bar{x}_i^{ini}\right)^2\right) \exp\left(-\bar{p}_i^2\right). \tag{5.67}$$

The center positions of the Gaussians, $\vec{\bar{x}}_i^{ini}$, are given by the initial state and will typically be on any site either zero or $\sqrt{2}\bar{\gamma}$. For these initial states, it is not necessary to include any negative weights for the trajectories to approximate the Wigner function of the composite system (see Eq. (5.49)) and all weights are set to one: $w^\alpha = 1$, $\forall\alpha$. Only single-electron states are considered in the following and the diabatic basis will always be the site-local basis $|\chi_i\rangle = \hat{c}_i^\dagger |0\rangle$, where the diabatic populations correspond to the local electron densities $n_i = |\Psi_i^{(d)}|^2$. The initial sampling and the implementation of the time evolution in both algorithms is presented in the following.

Implementation of MTE

The MTE algorithm is composed of the following steps:

1. An ensemble of N_{traj} trajectories is sampled from the initial state. For this, the nuclear configuration $\vec{x}^\alpha, \vec{p}^\alpha$ of each trajectory α is selected randomly according to the probability distribution given by the Wigner function Eq. (5.67) (which here is completely positive). The whole set of nuclear configurations is uniformly shifted and scaled in phase space so that the mean and variance of the nuclear positions and momenta matches the corresponding values from the nuclear Wigner function W^{ini}. Afterward, the electronic wave function of each trajectory is set to the initial state $\Psi^{el,\alpha} = \Psi^{ini}(\vec{x}^\alpha)$. If the initial state is given in the adiabatic electronic basis, the wave function is transformed to the diabatic basis.

2. In each time step $t \to t + \Delta t$, for every trajectory α (omitting the superscript α for clarity), first the nuclei are propagated according to the nuclear Hamiltonian Eq. (5.52) for fixed electron densities $n_i = |\Psi_i^{el}(t)|^2$:

$$\bar{H}^{nuc} = \sum_{i=1}^{L} \left[\frac{1}{2}\bar{p}_i^2 + \frac{1}{2}\bar{x}_i^2 - \sqrt{2}\bar{\gamma} n_i \bar{x}_i \right] . \tag{5.68}$$

   When assuming constant n_i, the Hamilton's equations of motion (see Eq. (5.50)) can be solved exactly for each site i:

$$\bar{x}_i(t + \Delta t) = \bar{x}_i(t)\cos(\omega_0 \Delta t) + \bar{p}_i(t)\sin(\omega_0 \Delta t) + \sqrt{2}\bar{\gamma} n_i \left[1 - \cos(\omega_0 \Delta t)\right], \tag{5.69}$$

   and similarly for the momenta.

3. Thereafter, in the same time step, the electronic state of every trajectory is propagated by assuming fixed nuclear positions $\vec{x}(t + \Delta t)$, for which the electronic eigenstates are just the Born-Oppenheimer states at that nuclear position $|\phi^{BO}(\vec{x}(t + \Delta t))\rangle$ with the eigenenergies $E^{BO}(\vec{x}(t + \Delta t))$, both obtained by diagonalizing the Born-Oppenheimer Hamiltonian at that nuclear position. Under this assumption, the electronic state can be

propagated exactly via:

$$|\Psi^{el}(t+\Delta t)\rangle = \sum_a |\phi_a^{BO}(\vec{x}(t+\Delta t))\rangle \exp\left(-\frac{i}{\hbar}\Delta t E_a^{BO}(\vec{x}(t+\Delta t))\right) \times \langle \phi_a^{BO}(\vec{x}(t+\Delta t))|\Psi^{el}(t)\rangle \,. \tag{5.70}$$

The time step Δt needs to be chosen small enough to control the error of this electron-nuclear propagation separation, i.e. convergence of observables with the time step needs to be ensured.

4. For calculating observables, the Wigner function of the composite system is constructed via Eq. (5.44) and expectation values are calculated with Eq. (5.33), where the partial Wigner transform is carried out in the electronic basis used in the representation of the initial state Ψ^{ini} to ensure that all expectation values of the initial state are recovered correctly for a sufficiently large number of trajectories.

5. Using the new electron density $n_i(t+\Delta t)$, the algorithm repeats the last steps starting with step 2 until the desired time t_{max} is reached.

Implementation of FSSH

The FSSH algorithm differs in various aspects from MTE and the exact form of the algorithm depends on which improvements and changes are utilized (see Sec. 5.3.5). The algorithm will be used in the adiabatic basis, i.e. the Born-Oppenheimer surfaces are used to calculate the nuclear forces, which is the typical choice for FSSH (see Ref. [30]). The integration of the electronic state $|\tilde{\Psi}\rangle$ will, however, always be carried out with the representation transformation technique in the diabatic basis (see Sec. 5.3.5), making use of the fact that the electronic time evolution (Eq. (5.51)) is independent of the chosen basis. The algorithm for FSSH can then be written in the following way:

1. The sampling of the nuclear configuration $\vec{x}^\alpha, \vec{p}^\alpha$ is equivalent to the sampling in MTE (step 1) taken from the nuclear Wigner function of the initial state. The electronic amplitudes are set to the initial state $\tilde{\Psi}^\alpha = \Psi^{ini}(\vec{x}^\alpha)$ and, if necessary, represented in the adiabatic electronic basis (determined at that position $\vec{x}^\alpha$). Afterward, the active state λ^α is selected randomly with the probabilities of the states a given by their electronic populations $|\tilde{\Psi}_a^\alpha|^2$.

2. Similar as for MTE, for every time step $t \to t+\Delta t$ and every trajectory α (we again omit the superscript α), first the nuclei and afterward the electrons (and active states) are propagated. In FSSH, the nuclear potential is given by the active Born-Oppenheimer surface $E_\lambda^{BO}(\vec{x})$, which explicitly depends on the nuclear position. Hence, in general, we cannot exactly integrate the nuclei as done in MTE. Instead we resort to a velocity Verlet integration (see Refs. [279, 280]), which is mathematically equivalent to the normal Verlet integration (see Ref. [139]) used also in the manganite

tight-binding model (see Sec. 3.3.2), with the difference that the new nuclear momenta $\vec{p}(t + \Delta t)$ are obtained explicitly after each integration step, which is necessary in FSSH to determine the hopping probabilities (at least in the original formulation) and for the velocity adjustment after a surface hop. Under the assumption of a constant active surface λ, the propagation of the nuclei is then done in three steps:

a) A half-step in the momenta: $p_i(t + \Delta t/2) = p_i(t) - \left.\frac{\partial E_\lambda^{BO}(\vec{x})}{\partial x_i}\right|_{\vec{x}(t)}$.

b) A full-step in the positions: $x_i(t + \Delta t) = x_i(t) + \frac{1}{m_i} p_i(t + \Delta t/2)$.

c) A second half-step in the momenta with the forces obtained at the new nuclear position: $p_i(t + \Delta t) = p_i(t + \Delta t/2) - \left.\frac{\partial E_\lambda^{BO}(\vec{x})}{\partial x_i}\right|_{\vec{x}(t+\Delta t)}$.

The derivatives of the Born-Oppenheimer surfaces of the Holstein model can be calculated (using dimensionless units) via:

$$\left.\frac{\partial \bar{E}_\lambda^{BO}(\vec{\bar{x}})}{\partial \bar{x}_i}\right|_{\vec{\bar{x}}(t)} = \bar{x}_i(t) - \sqrt{2}\bar{\gamma} \left\langle \phi_\lambda^{BO}\left(\vec{\bar{x}}(t)\right) \middle| \hat{n}_i \middle| \phi_\lambda^{BO}\left(\vec{\bar{x}}(t)\right) \right\rangle . \tag{5.71}$$

3. After the nuclear propagation, the electronic amplitudes $\tilde{\Psi}$ are evolved in the same way as in MTE (step 3), i.e., for fixed nuclei $x(t + \Delta t)$. When representing the states at the times t and $t + \Delta t$ in their respective adiabatic bases, this amounts to:

$$\tilde{\Psi}_a^{(a)}(t + \Delta t) = \sum_b P_{a,b}(t, t + \Delta t)\tilde{\Psi}_b^{(a)}(t) \coloneqq$$
$$\sum_b \exp\left(-\frac{i}{\hbar}\Delta t E_a^{BO}(\vec{x}(t + \Delta t))\right) \left\langle \phi_a^{BO}\left(\vec{x}(t + \Delta t)\right) \middle| \phi_b^{BO}\left(\vec{x}(t)\right) \right\rangle \tilde{\Psi}_b^{(a)}(t). \tag{5.72}$$

Note that the derivative couplings do not appear in this expression, which is different than if one would naively integrate the Schrödinger equation in the adiabatic basis via Eq. (5.55) as proposed originally (see Ref. [29]). Eq. (5.72) can be thought of as a propagation in the diabatic basis, nestled between basis transformations from and into the adiabatic basis. $P_{a,b}(t, t + \Delta t)$ defines the unitary adiabatic propagator needed in the alternative hopping expression (Eq. (5.66)). The overlap of Born-Oppenheimer states at different nuclear positions is evaluated in the diabatic basis:

$$\left\langle \phi_a^{BO}(\vec{x}(t + \Delta t)) \middle| \phi_b^{BO}(\vec{x}(t)) \right\rangle = \sum_i \left\langle \phi_a^{BO}(\vec{x}(t + \Delta t)) \middle| \chi_i \right\rangle \left\langle \chi_i \middle| \phi_b^{BO}(\vec{x}(t)) \right\rangle . \tag{5.73}$$

The representation of the Born-Oppenheimer states in the diabatic basis $\langle \chi_i | \phi_b^{BO}(\vec{x}(t)) \rangle$ is in principle defined only up to a phase and obtained from numerical diagonalization of the Born-Oppenheimer Hamiltonian.

Since the Born-Oppenheimer Hamiltonian is real and symmetric, the phase ambivalence is reduced to a sign flip. Hence, we ensure that between subsequent time steps this sign does not change. In addition, the off-diagonal derivative couplings $\vec{A}_{a,b}(\vec{x}(t+\Delta t))$ are calculated from the expression Eq. (5.16).

4. From the electronic amplitudes $\tilde{\Psi}(t)$, the nuclear momenta $p(t+\Delta t)$, and the derivative couplings $\vec{A}_{a,b}(\vec{x}(t+\Delta t))$, the hopping probabilities from the active to all other surfaces are calculated (a) via the original expression (Eqs. (5.57) and (5.58)) for the Holstein dimer (L=2); or (b) with the alternative expression Eq. (5.66), relying on the adiabatic propagator $P_{a,b}(t, t+\Delta t)$, for all larger systems $L \geq 3$. In both cases a random number is generated and compared to the hopping probabilities to check for a surface hop.

5. After a successful surface hop $\lambda(t) \rightarrow \lambda'$ the velocity adjustment of the nuclei is carried out according to Eq. (5.60). In case of a too small velocity in the direction of the derivative coupling (a frustrated hop), the surface hop is discarded. Otherwise the new active surface is set to $\lambda(t+\Delta t) = \lambda'$.

6. Only in case a decoherence correction is used:
   a) Without restriction (FSSH+D, used here in the Holstein chain for $L \leq 3$): The force-based decoherence rate according to Eq. (5.64) is applied to all non-active states $\tilde{\Psi}_a$, $\forall a \neq \lambda(t+\Delta t)$ and the active state is rescaled to conserve the norm.
   b) With restricted decoherence (FSSH+RD, used here for $L \geq 11$): The restrictions mentioned in Sec. 5.3.5 are applied, i.e., the decoherence correction is only used after a quarter phonon oscillation period has passed and the active region restriction is used with an electronic charge density threshold R that for the results presented in Ch. 6 is set to $R = 0.99$, see the test of the influence of this threshold in Fig. 6.12.

7. Observables are calculated via the partial Wigner transform formalism, i.e. the approximated Wigner function Eq. (5.44) is used to obtain expectation values via Eq. (5.33). The electronic density matrix in this approximation to the partial Wigner transformed density matrix $\hat{\rho}^{el}$ is obtained from the mixed definition (Eq. (5.63)) for most simulations presented in Ch. 6, the exception being the large system results $L \geq 11$, for which the mixed definition can lead to numerical problems, especially far outside of the initially occupied sites (see Sec. 6.3.1). Here, the wave-function definition (Eq. (5.62)) is used for FSSH+RD. Without decoherence correction the wave-function definition is even less reliable than the mixed definition, and we thus stay with the latter (see Sec. 6.3.1).

8. Using the new active state $\lambda(t+\Delta t)$, the algorithm repeats the last steps starting with step 2 until the desired time t_{max} is reached.

Numerical details of the FSSH algorithm

While the implementation of the MTE algorithm is relatively straightforward, we made a few choices for the implementation of the FSSH algorithm above, in particular which of the surface-hopping improvements presented in Sec. 5.3.5 to be used. The most drastic variation of the original FSSH algorithm is the introduction of a decoherence correction. Testing this correction is left as one of the goals of the next chapter (Ch. 6) when comparing MTE and FSSH to numerically exact approaches and a coupled-trajectory method. The additional variations/choices include: (a) The starting electronic amplitudes are set to the amplitudes of the initial state $\tilde{\Psi}_a^\alpha(t=0) = \Psi_a^{ini}(\vec{x}^\alpha(t=0))$, rather than projecting them onto the chosen active state $\tilde{\Psi}_a^\alpha(t=0) = \delta_{a,\lambda^\alpha(t=0)}$ (see the discussion at the end of Sec. 5.3.4). (b) The propagation of the electronic amplitudes is essentially carried out in the diabatic basis via Eq. (5.72) instead of relying on the derivative couplings used in Eq. (5.55), originally proposed in Ref. [29]. (c) The mixed definition of the density matrix (Eq. (5.63)) is used to calculate observables, with the exception of the large systems $L \geq 11$ when using a decoherence correction, where the wave-function definition is used (Eq. (5.62)). (d) An alternative hopping expression is used in large systems $L \geq 11$ (Eq. (5.66)), which does not rely on derivative couplings. (e) Restrictions to the decoherence correction are implemented in large systems $L \geq 11$ to avoid a spurious charge transfer (see Sec. 5.3.5). Most of these choices have been justified already when they were introduced (see Secs. 5.3.4 and 5.3.5) and we will see and discuss their influence on the results in the next chapter (Ch. 6).

Two of these are, however, of a purely numerical importance and affect the convergence properties of FSSH. These are the approaches to avoid using derivative couplings in the electronic propagation and for calculating the hopping probabilities, relevant for the trivial crossing problem, i.e., when two surfaces come very close or cross. This problem can be visualized already in the Holstein dimer when a very small electron hopping term t_0 is used, serving as a prototype for large systems, where such trivial crossings are expected to occur frequently even for larger values of the electron hopping (see the analysis in Ref. [205]). While not analyzed here, such a surface crossing can also appear in small systems, like the Jahn-Teller model of a single manganite octahedron, see the energy surfaces in Fig. 3.1.

To understand the trivial crossing problem, we start with an initial state restricted to the upper Born-Oppenheimer surface, with a Gaussian nuclear wave packet around $\bar{q} = \bar{\gamma}$, just like the example case studied before with an exact method (see Fig. 5.5). However, as parameters we choose now $\bar{\gamma} = 2.5$ and $\bar{t}_0 = 0.01$. For a t_0 this small, the adiabatic and diabatic electronic states are almost identical, but change character around $\bar{q} = 0$: for $\bar{q} > 0$ the antibonding state is very close to $|\chi_2\rangle$, while for $\bar{q} < 0$ it is very close to $|\chi_1\rangle$, i.e., it corresponds to the electronic state on the site with the smaller nuclear displacement x_i. The bonding state corresponds to the other state in both cases. Since for this very small electron hopping we can expect the electron to stay on the initially (mostly) occupied Holstein site $|\chi_2\rangle$ for an extended period, a

trajectory passing $\bar{q} = 0$ *should* undergo a surface transition between the two adiabatic states. With a very localized derivative coupling, the trajectory can easily miss the large hopping amplitude around $\bar{q} = 0$ between two time steps. The same problem also applies to the propagation of the electronic amplitudes if the adiabatic formulation according to Eq. (5.55) is used.

Fig. 5.8 visualizes this trivial crossing problem. The time evolution of the population of the upper (initially occupied) Born-Oppenheimer surface is shown in Figs. 5.8(a)-(c) for different time steps Δt in three variations of FSSH. In all cases the population is calculated both from the electronic amplitudes (solid lines) and from the distribution of active surfaces (dashed lines). In the first variant, Fig. 5.8(a), the electronic amplitudes are propagated by integrating the Schrödinger equation in the adiabatic basis (Eq. (5.55) (by inserting the derivative couplings, nuclear momenta and Born-Oppenheimer energies obtained at the time $t + \Delta t$ in each time step, and then diagonalizing the resulting matrix) and the hopping probabilities are calculated in the original way via Eq. (5.57). Both depend on the derivative couplings, which leads to erroneous results for too large time steps, as seen from that Fig. 5.8(a). For $\Delta t = 0.1/\omega_0$ and $\Delta t = 0.01/\omega_0$, the electronic amplitudes $\tilde{\Psi}$ (solid lines) do not capture the wave packet transitions between the surfaces and the distribution of trajectories (dashed lines) follows this trend. Only for $\Delta t = 0.001/\omega_0$ the surface transitions are captured correctly.

In the second variant, Fig. 5.8(b), the electronic amplitudes are propagated in the diabatic basis, Eq. (5.72), and correctly capture the wave packet transition. However, the surface hops still depend on the derivative couplings and, in particular, for $\Delta t = 0.1/\omega_0$ many trajectories stay on the upper Born-Oppenheimer surface (dashed line). For later times with we see that also the average population of the upper Born-Oppenheimer surface calculated from the electronic amplitudes (solid line) deviates from the converged results. Each individual trajectory still correctly predicts an electron density localized to the second Holstein site $|\chi_2\rangle$, but due to the (erroneous) incomplete surface switching, the wave packet splits into several parts. Therefore, at later times, some of the trajectories are at $\bar{q} < 0$ and some at $\bar{q} > 0$ which on average leads to the deviation in the shown observable. Reducing the time step to $\Delta t = 0.01/\omega_0$ already improves the results significantly and at $\Delta t = 0.001/\omega_0$ the converged time evolution is obtained. Finally, both the electronic amplitudes propagation and the hopping probabilities are obtained without relying on derivative couplings by using the corresponding Eqs. (5.72) and (5.66) in Fig. 5.8(c). Here, even for a large time step of $\Delta t = 0.1/\omega_0$, ten times larger than t_0, the surface transitions are captured correctly.

In addition, we show in Figs. 5.8(d)-(f) the time evolution of $\langle \hat{q} \rangle (t)$ for the same three FSSH variants. Since the nuclear forces are given by the active surfaces, only the combination of the diabatic electronic amplitude propagation and the alternative hopping expression used in Fig. 5.8(f) provides a dynamical evolution that is almost independent of the used time step. However, already using the diabatic electronic propagation alone, in Fig. 5.8(e), improves the results if time steps in the order of the electronic hopping term t_0 are used. This motivates our choice to always use the diabatic electronic time evolution

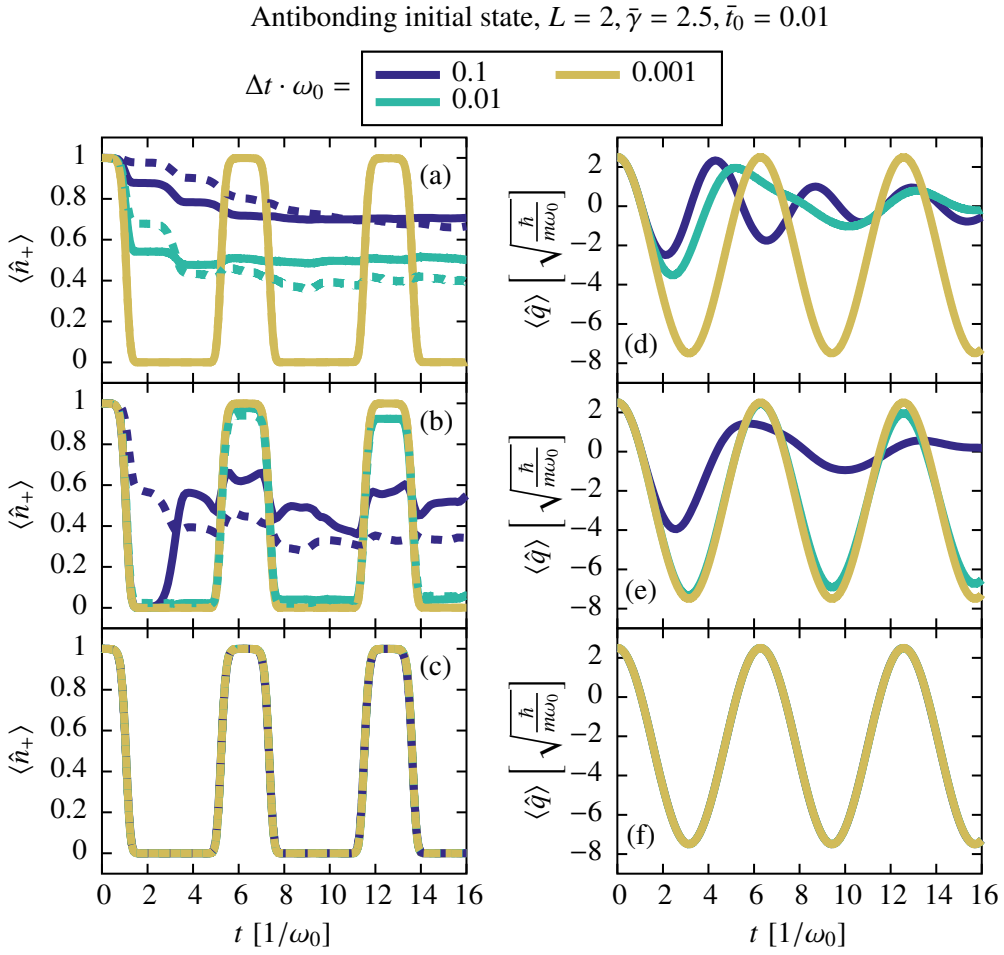

Figure 5.8: Visualization of the trivial crossing problem in different variations of FSSH in the Holstein dimer with $\bar{\gamma} = 2.5$ and $\bar{t}_0 = 0.01$. Starting from a Gaussian nuclear wave packet in the antibonding state around $\bar{q}_0 = \bar{\gamma}$, the time evolution of the (a)-(c) population of the antibonding state $\langle \hat{n}_+ \rangle$ and (d)-(f) average relative nuclear position $\langle \hat{q} \rangle$ are shown using different time steps Δt. The three rows correspond to three variations of FSSH: (a) and (d) the propagation of electronic amplitudes and the calculation of hopping probabilities are performed in the original way (see Ref. [29]) in the adiabatic basis and depend on the derivative couplings. (b) and (e) the electronic amplitudes are instead propagated according to Eq. (5.72) without referring to the derivative couplings. (c) and (f) the electronic amplitudes are propagated according to Eq. (5.72) and the alternative hopping expression, Eq. (5.66), is used (both do not rely on the derivative couplings). To show the difference of the time evolution of the electronic amplitudes and the distribution of the trajectories, the electron densities in (a)-(c) are calculated both from the electronic amplitudes $\left(\frac{1}{N_{traj}} \sum_{\alpha}^{N_{traj}} \tilde{\rho}^{\alpha}_{a,a}(t)\right)$ as solid lines and from the distribution of active surfaces $\left(\frac{1}{N_{traj}} \sum_{\alpha}^{N_{traj}} \delta_{a,\lambda^{\alpha}(t)}\right)$ as dashed lines, corresponding to using the wave-function or active-surface definition of the electronic density matrix (see Eqs. (5.62) and (5.61)).

of Eq. (5.72) in all following calculations. For calculating the hopping probabilities, we stay with the original version (Eq. (5.57)) for the Holstein dimer, where we will not investigate such extremely small values for the electronic hopping term t_0, but use the alternative expression (Eq. (5.66)) for all larger systems. We saw already from the Born-Oppenheimer surfaces of the Holstein trimer (see Fig. 5.7) that the energy separation of the surfaces can become very small, even for a large t_0. As mentioned in Ref. [205], this tendency is found in general in large systems and an algorithm which is fit to deal with trivial crossings is thus needed. We note that the same accuracy as presented in Figs. 5.8(c),(f) can also be achieved by using the self-consistent correction of the hopping probability, as mentioned in Sec. 5.3.5. This correction is actually implemented in our simulations of the Holstein dimer, but has no influence due to the sufficiently small time steps used in the following in comparison to t_0.

Convergence of the independent-trajectory methods

We now turn to a general convergence study of both independent-trajectory methods. It is important to keep in mind that the methods will not converge to the exact results, independent of the number of used trajectories or the time step (as opposed to most coupled-trajectory methods introduced in Sec. 5.3.6). Nonetheless, it is important to use a sufficient number of trajectories and a small enough time step so that the results become, up to the desired accuracy, independent of these parameters. This is also called internal convergence of the algorithms.

In MTE, the number of trajectories N_{traj} is only relevant to sample the initial state and all following dynamics are completely deterministic. In FSSH, the trajectories also perform random hops, so that one could sample many trajectories from every previously sampled nuclear phase space point. In practice, both samplings are done together by just using a large enough number of trajectories randomly sampled from the Wigner function. We can thus expect that FSSH needs a higher N_{traj} to achieve internal convergence compared to MTE. The convergence needs to be checked for every system, initial state and even observable to be shown and here we will only present two example cases.

To evaluate the convergence with the number of used trajectories, we repeat the simulation N_{run} times for different random samplings of the Wigner function (and different seeds for the random hops in FSSH). Since the trajectories are time evolved completely independent from each other, the run-average of an observable $\langle\langle \hat{O} \rangle\rangle \coloneqq \frac{1}{N_{run}} \sum_{l=1}^{N_{run}} \langle \hat{O} \rangle_l$ over a large number of runs should correspond to the normal expectation value $\langle \hat{O} \rangle_l$ of a single run l averaged over a large number of trajectories (with one caveat: the shifting and scaling of the trajectory-ensemble to reproduce the mean and variance of the initial state is one collective modification breaking this equivalence, which, however, has very little influence at large N_{traj}).

The sample standard deviation $\sigma_O = \sqrt{\frac{1}{N_{run}-1} \sum_{l=1}^{N_{run}} \left(\langle \hat{O} \rangle_l - \langle\langle \hat{O} \rangle\rangle \right)^2}$ across different runs indicates how far the different runs spread around their average value, which depends on N_{traj}. In a converged simulation we would expect the

result to become (almost) independent of the sampling and thus the standard deviation across runs should become small. We show two examples of the standard deviation over the number of used trajectories in Fig. 5.9.

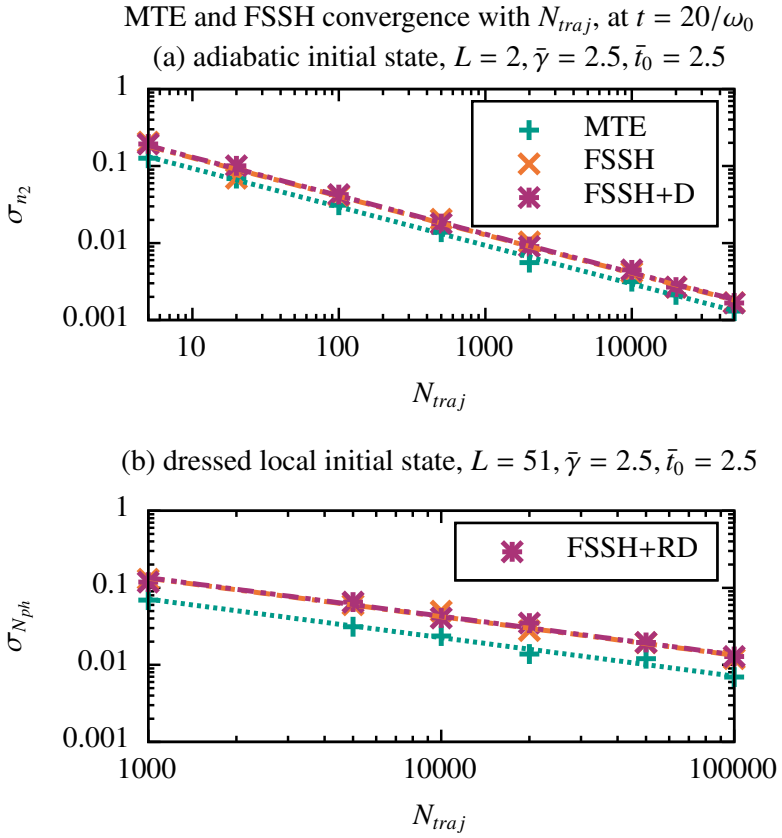

Figure 5.9: Convergence of MTE, FSSH and FSSH+D/RD with the number of used trajectories N_{traj}. Shown are the run-averaged standard deviation of (a) the electron density on the second Holstein site n_2 in the Holstein dimer with $\bar{\gamma} = \bar{t}_0 = 2.5$ at time $t = 20/\omega_0$ after starting from the antibonding (adiabatic) initial state, and (b) the total phonon number N_{ph} in the Holstein chain with $L = 51$ sites, for the same parameters and time, after starting from a dressed local state at the center of the chain (see the text for details). In both cases, a time step of $\Delta t = 0.001/\omega_0$ is used and linear fits of the log-log data with a fixed slope of -0.5 (corresponding to an inverse square root decay) are included as dashed lines. We used $N_{run} = 50$ runs for averaging data points with $N_{traj} \leq 20\,000$ and $N_{run} = 25$ runs for data points with $N_{traj} \geq 50\,000$. Reproduced from Ref. [37], with the permission of AIP Publishing.

In Fig. 5.9(a) we take the antibonding (adiabatic) initial state in the Holstein dimer, already used as example in Fig. 5.5, and select as observable the electronic occupation on the second dimer site $\langle \hat{n}_2 \rangle$ at time $t = 20/\omega_0$. Fig. 5.9(b) shows a result in a large system ($L = 51$), in an initial state of a single electron localized at the center of the chain, with all harmonic oscillators starting in their ground state, except the one at the position of the electron, which starts around $\sqrt{2}\bar{\gamma}$ (the ground state of an isolated Holstein site with one electron). This will

later be called the dressed local initial state. Here, we take as observable the total phonon number in the system $\langle \hat{N}_{ph} \rangle = \langle \sum \hat{b}_i^\dagger \hat{b}_i \rangle$ at $t = 20/\omega_0$.

In both examples, the standard deviation approximately follows an inverse square-root decay as one would expect for a large number of random samples, indicated as dashed/dotted lines in Fig. 5.9 and fitted to the data. For FSSH both a variant without and with decoherence (restricted for $L = 51$) are shown, which, however, do not differ significantly. MTE seems to need less trajectories to obtain the same accuracy. The distance of the fitted lines indicates that FSSH and FSSH+D need ≈ 1.88 and ≈ 1.96 times more trajectories than MTE in the dimer example and ≈ 3.5 and ≈ 3.6 times more in the extended system. We note, however, that we show the absolute standard deviation here. Since the methods converge to different values, the relative standard deviation might give different results. In general, our observations are close to the examples shown here, with FSSH needing more trajectories than MTE, but still in a similar order of magnitude. In our results in Ch. 6 we use 20 000 trajectories for most calculations, while in some exceptions ($L \geq 11$ with a dressed local initial state and $L = 25$ with the small electron hopping term $t_0 = 1$) we use 50 000 trajectories.

Next, the convergence with the used integration time step Δt needs to be ensured. An example is presented in Fig. 5.10 for the same system and initial state as the second case in the N_{traj}-convergence study before (Fig. 5.9(b)). 100 000 trajectories are used to keep the statistical error of the trajectory sampling small and the expectation value of the total phonon number (of a single run) at $t = 20/\omega_0$ is shown over the used time step. We see that MTE and FSSH converge to vastly different values, while the difference of using a decoherence correction in FSSH seems to have a smaller effect. For $\Delta t \leq 0.01/\omega_0$ there remain small variations of the observable in the order of the standard variation of the respective methods shown in Fig. 5.9(b) for $N_{traj} = 100\,000$, which we consider as sufficiently converged. For the Holstein dimer ($L = 2$) we use in the following $\Delta t = 0.01/\omega_0$ and for all larger systems we use the even more accurate $\Delta t = 0.001/\omega_0$.

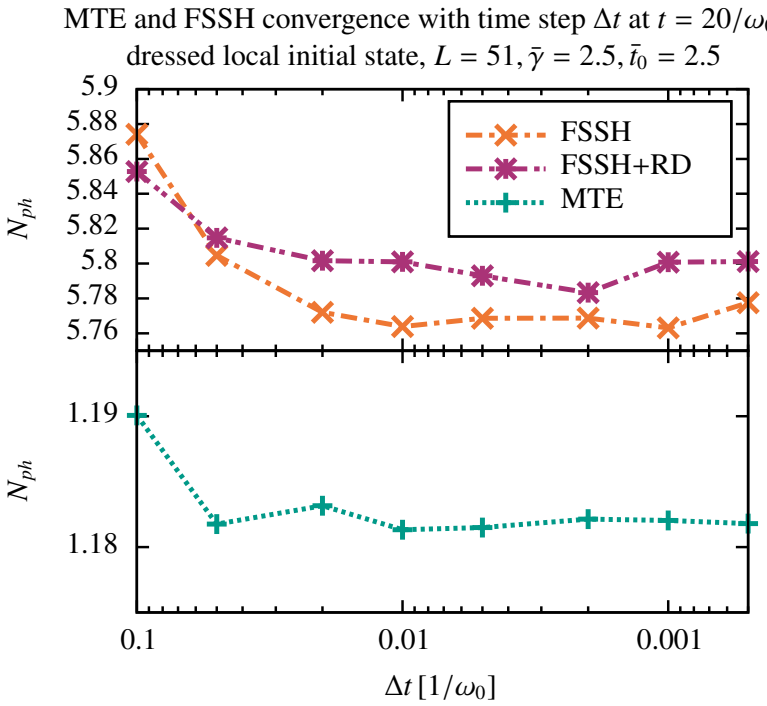

Figure 5.10: Convergence of MTE, FSSH and FSSH+RD with the integration time step Δt in the Holstein chain with $L = 51$, $\bar{\gamma} = \bar{t}_0 = 2.5$ and $N_{traj} = 100\,000$. We show the convergence of the total phonon number N_{ph} at time $t = 20/\omega_0$ after starting from a dressed local state at the center of the chain. Lines are included as guides for the eye. Reproduced from Ref. [37], with the permission of AIP Publishing.

6 Real-time non-adiabatic dynamics of exact and quantum-classical methods in the Holstein model

In the previous chapter, we discussed the concept of non-adiabatic effects in electron-phonon coupled systems and described in detail two quantum-classical independent-trajectory methods capable of dealing with these effects: multi-trajectory Ehrenfest (MTE) and fewest-switches surface hopping (FSSH and its decoherence corrected variants FSSH+D/FSSH+RD), see Secs. 5.3.3, 5.3.4 and 5.3.5. In this chapter, we put both methods to test, using the prototypical one-dimensional Holstein model, see Eq. (5.2), to carry out a benchmark study for the real-time dynamics of mostly quenched systems. The results of this study have been published in Ref. [37] and this chapter will closely follow the results of that article. The aim is to evaluate the strengths and limitations of MTE and FSSH, among other things in view of their potential application to describe the real-time dynamics in the more complicated tight-binding model for manganites (see Ch. 3). One example would be the relaxation after an optical excitation, as carried out, e.g., in Ref. [32], using an Ehrenfest description. We will not model the photo-excitation explicitly here, but instead start from various (non-equilibrium) initial states and analyze the subsequent time evolution. Since we cannot guarantee that the system after a photoexcitation is restricted to a single adiabatic state, we put a special focus on initial states starting in a superposition of several adiabatic states, which forms a particular challenge for the FSSH method.

Besides the independent-trajectory methods, several other methods contribute results in this benchmark study. Firstly, the coupled-trajectory method multiconfigurational Ehrenfest (MCEv1, in the following denoted as MCE), see Sec. 5.3.6. S. Gräber implemented this method and carried out the calculations. As mentioned previously, the method can, in principle, converge to exact dynamics if a large number of configurations is used. In practice, we find that convergence can be reached best in small systems and for specific observables and that in large systems further methods are needed to provide exact reference data. The benchmark study thus serves also as a test for this coupled-trajectory method. MCE is not the focus of this thesis and for details in the implementation and numerical tests we refer to the Master's thesis of S. Gräber (see Ref. [264]) and to our article (Ref. [37]). Here, we mention only that an insufficient convergence of the method leads, among other things, to a violation of the total energy conservation. For small systems this total energy drift, which increases over time, was identified as a helpful indicator for the methods convergence in Ref. [37], and we will follow the proposal of that reference to indicate the time at which the energy drift exceeds the threshold

of $0.2\,\hbar\omega_0$ as $t^{MCE}_{0.2\,\hbar\omega_0}$. While the threshold value is chosen rather arbitrary, it allows a comparison of the relative convergence of MCE in different systems.

For numerically exact benchmark data we instead rely on different methods. In the Holstein dimer we already presented one algorithm to obtain a numerically exact solution to the eigenvalue problem in the Born-Huang basis on a grid (see Sec. 5.2.4), to which we will also refer to as exact diagonalization (ED) in the Born-Huang basis. This is complemented by two additional wavefunction based methods carried out in a second quantized basis. Both methods rely on a finite Hilbert space and introduce a cutoff of the number of harmonic oscillator eigenstates M to be included on every Holstein site. The first is exact diagonalization in second quantization, which is just a diagonalization of the full matrix build from the truncated number of electron-phonon basis states. D. Jansen implemented this method and carried out the calculations, see Ref. [37] for details. ED in second quantization is used to obtain numerically exact results in the Holstein trimer, but it also confirmed the results from ED in the Born-Huang basis for the Holstein dimer (not shown here).

For larger systems obtaining numerically exact results becomes increasingly difficult, as the Hilbert space increases exponentially. Here, we rely on the density matrix renormalization group (DMRG) method, see Refs. [48–50]. The following short discussion follows Ref. [37]. The method is especially well suited for one-dimensional (1D) systems, but generalizations can also be applied to two-dimensional systems, see Refs. [281–285]. DMRG is still actively developed, see Refs. [54, 286–291] and in this benchmark study a combination of DMRG with a local basis optimization (LBO) (see Refs. [51–53]) is used. The basic idea of DMRG is to represent the wave function in a matrix-product state (MPS) form, which can be efficiently truncated with a controlled error. The LBO aims at reducing the number of local basis states by diagonalizing local reduced density matrices and truncating the number of used eigenstates by their eigenvalues, which increases the efficiency of the algorithm (see Refs. [51–53, 286, 288, 292–295]). DMRG has been successfully applied to simulate time evolution, see Refs. [296–300] and is a state-of-the-art method of theoretical solid-state physics to obtain numerically exact results mostly in 1D systems, see also the reviews [49, 50, 301].

Implementation, tests and calculations of DMRG-LBO in our benchmark study were performed by D. Jansen and J. Stolpp, see Ref. [37] and their PhD theses [302, 303] for further analysis of the method. In this thesis, the DMRG results are taken as numerically exact reference data to benchmark MTE and FSSH. It is important to note that the accuracy of the DMRG-LBO results are quantified by two errors, introduced from the truncation of the bond-dimension in the matrix-product state representation (ϵ_{bond}) and from the LBO truncation (ϵ_{LBO}), which can be chosen and fixed during a DMRG-LBO simulation. Convergence with these errors and with the used truncation of the local phonon modes M needs to be ensured in all simulations. In contrast to the MCEv1 method, this was always possible in all following systems and initial states. Rather than obtaining inaccurate results, the reached maximum time t_{max} is limited in DMRG.

MTE, FSSH and MCE are typical quantum chemistry methods, which have

been subject to several benchmark studies in the past, see Refs. [39, 43–47] and their discussion in Ch. 1. The DMRG-LBO simulations of our study provide systematic, unbiased and new reference data to evaluate these methods in an extended Holstein model. In addition, our study puts a special focus on the influence of the initial state and its coherences and carefully evaluates the different variations and improvements of FSSH necessary to describe these states. The results are interpreted in the Born-Huang framework, which can be explicitly applied in the small systems studied and helps to understand the methods' performance in large systems.

We start with an analysis of the Holstein dimer (with one electron), which is not only the smallest non-trivial Holstein chain, but also a fundamental model system in quantum-chemistry, see Refs. [176–185]. We study both initial states restricted to one of the adiabatic states (adiabatic initial state), as we did already in the previous chapter, e.g., in Figs. 5.5 and 5.8, as well as initial states where the electron is restricted to a single Holstein site (local initial states), which sometimes are also called diabatic initial states, as the electronic configuration does not depend on the nuclear positions and can be represented by a diagonal density matrix in the diabatic basis.

Two types of local initial states will be analyzed: First, the bare local state, in which all nuclear harmonic oscillators are prepared in their lowest vibrational state. This corresponds to a quantum quench, where before time zero the electron-phonon coupling γ is set to zero, a single electron is inserted at one Holstein site, and then at $t \geq 0$ the coupling is turned on, leading to non-equilibrium dynamics. One can also think of this as a local excitation of an electron into a previously unoccupied chain of electronic orbitals that couple to some phonon bath. Second, the dressed local state. Here, the harmonic oscillator on the site initially occupied by the electron has already adjusted to its electron density, which leads to a shift of the center of its Gaussian wave function from zero to $\sqrt{2}\bar{\gamma}$, while all other harmonic oscillators start again in their lowest vibrational state. This initial state corresponds to a quantum quench were the electron hopping term t_0 is suddenly turned on at time $t = 0$. All three initial states are schematically shown in Figs. 6.1(a)-(c), which also includes their nuclear wave function density on the two Born-Oppenheimer surfaces as sketch.

Adiabatic and local states are investigated in the Holstein trimer as well, where the Born-Oppenheimer surfaces are still easy to visualize, see Figs. 5.6 and 5.7. This serves as the transition to large Holstein chains, where mainly the bare and dressed local state of a single electron are investigated, see Figs. 6.1(d)-(e). These states, in which the formation and dynamics of a polaron can be investigated, have been studied recently with MCE for up to 16 sites in a periodic Holstein chain (Holstein ring), see Ref. [43], which has been compared to a previous study with the hierachical equations of motion method (see Ref. [304]) with a good agreement between both methods. In addition, the bare and dressed local states in the Holstein chain were studied with a numerically exact tensor network state method in Ref. [54], where the states are referred to as "Franck-Condon" and "relaxed" initial states. The parameters used in that study will also be used later, see Sec. 6.3.4, which allows us to confirm their

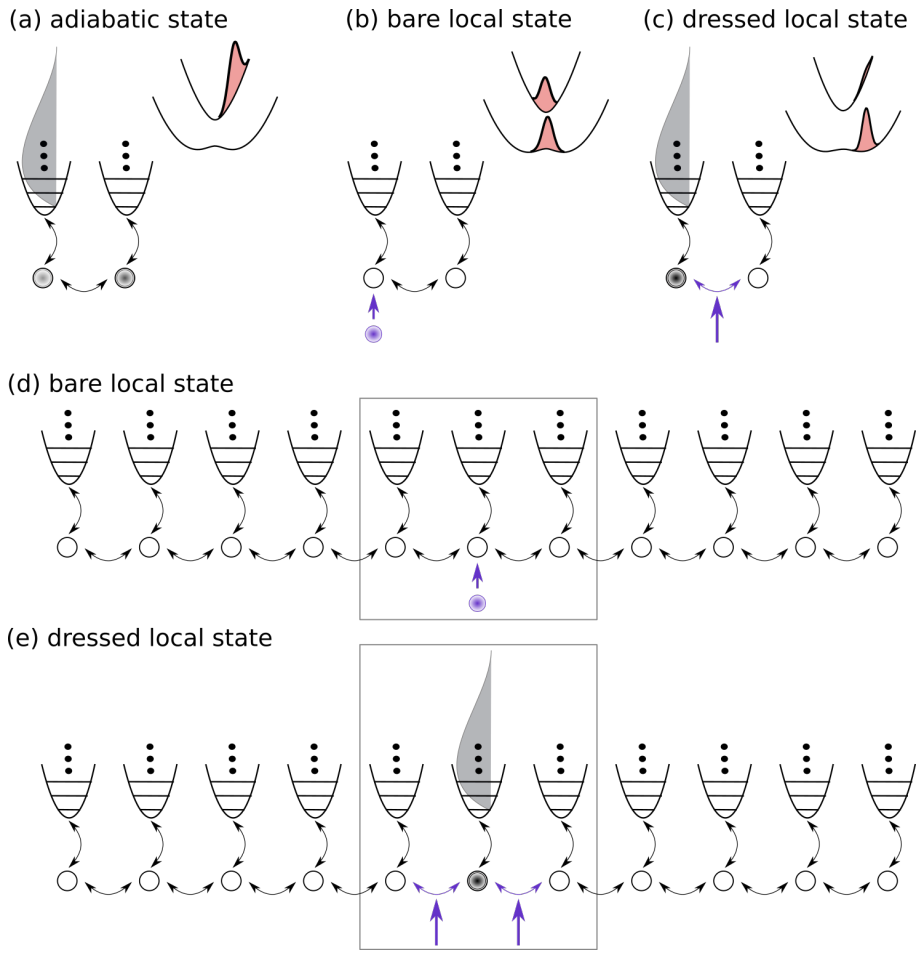

Figure 6.1: Sketches of the different one-electron initial states studied in this chapter and in the published article, Ref. [37]. (a)-(c) Initial states in the Holstein dimer: (a) An adiabatic initial state, with the electron starting on the upper Born-Oppenheimer surface, (b) the bare local state, where an electron is locally added into an empty Holstein dimer which was previously in its ground state, (c) the dressed local state, where the electron hopping is turned on at time $t = 0$ between one occupied (polaronic) and one empty site. (d)-(e) The same states are also investigated for the Holstein trimer (marked as rectangles) and in large Holstein chains, in particular the bare and dressed local states. Reproduced from Ref. [37], with the permission of AIP Publishing, the positions of the two sites in the Holstein dimer (a)-(c) have been adjusted to the definitions used in the rest of this thesis.

results and evaluate our trajectory-based methods against numerically exact literature results. Similarly, such local states have been investigated with FSSH to extract mobilities (see Refs. [243, 256]), where, however, the phonons were prepared to initially mimic a thermal ensemble and the study was focused on steady-state results. Our results for the Holstein dimer, trimer and the Holstein chain are presented in Secs. 6.1, 6.2 and 6.3. The analysis in these sections closely follows the corresponding published article, Ref. [37], although with a larger focus on investigating the independent-trajectory methods. Most, but not all, presented figures have also been published there, as indicated in the

respective figure captions. We note that in the following FSSH refers to the surface hopping method without decoherence correction, and otherwise we explicitly mention FSSH+D or FSSH+RD.

6.1 Holstein dimer

Before coming to the more difficult and interesting cases of the Holstein trimer and the large Holstein chains, we first analyze the performance of MTE and FSSH in the Holstein dimer. As mentioned above, this is a prototypical system in quantum chemistry and has been used for comparative studies before, see, e.g., Ref. [47]. It allows us to quantify the strengths and weaknesses of both independent-trajectory methods, which can later be transferred to the larger systems. The importance of the initial state for the performance of FSSH has been pointed out in Ref. [241] and we will investigate this in more detail here.

6.1.1 The Born-Oppenheimer case

Let us start with a system and initial state where non-adiabatic transitions are mostly prohibited. For this we choose the system parameters as $\bar{\gamma} = 4$, $\bar{t}_0 = 10$ and for the initial state we start with the electron on the upper Born-Oppenheimer surface (antibonding adiabatic state) with the nuclear wave function Gauss-distributed around $\bar{q}^{ini} = \bar{\gamma}$ (see Eq. (5.67) for the form of the initial Wigner function), depicted in Fig. 6.1(a). With the wave function initially restricted to the upper surface and non-adiabatic transitions being unlikely due to the large electron hopping t_0, the wave function will stay on the upper Born-Oppenheimer surface for a long time. Hence, only a single energy surface determines the whole dynamics, which is exactly the case where the Born-Oppenheimer approximation is justified. In this case, both MTE and FSSH become equivalent and are reduced to the truncated Wigner approach (see Sec. 5.3.1) for a wave function evolving in the potential $E_+^{BO}(q)$. The time evolution of the relative nuclear distortion $\langle \hat{q} \rangle$, the electron density on the first Holstein site $\langle \hat{n}_1 \rangle$ and the electronic population on the upper (initially occupied) Born-Oppenheimer surface $\langle \hat{n}_+ \rangle$, obtained with MTE, FSSH, FSSH+D and with exact diagonalization in the Born-Huang basis (ED) are shown in Fig. 6.2.

We observe an excellent agreement of all methods both for the average nuclear distortion and the electron density (Figs. 6.2(a),(b)), with a slight frequency shift appearing only after many phonon oscillation periods. The overall damping of both observables toward the symmetric configuration is very similar in all methods. We note that the potential given by the upper Born-Oppenheimer surface $E_+^{BO}(q)$ is not harmonic, see Eq. (5.21). In the population on the upper Born-Oppenheimer surface, both MTE and FSSH stay close to a value of one, while FSSH+D predicts a small decay of the population, stronger than the decay obtained in the other methods. This case is an example where the decoherence correction has a detrimental effect. While the probability is small, some trajectories in both FSSH and FSSH+D hop from the upper to the lower

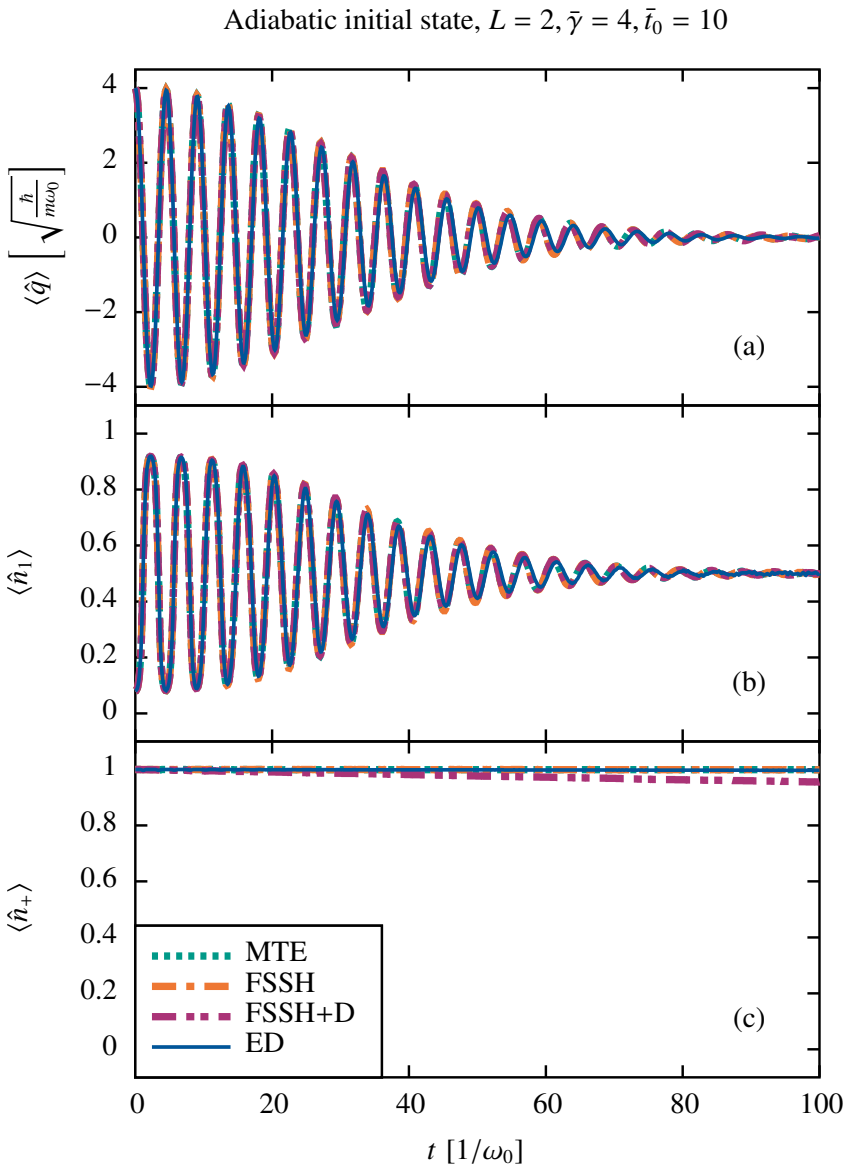

Figure 6.2: Time evolution of the (a) relative nuclear distortion $\langle \hat{q} \rangle$, (b) electron density on site 1 $\langle \hat{n}_1 \rangle$ and (c) population on the upper Born-Oppenheimer state $\langle \hat{n}_+ \rangle$, obtained in the Holstein dimer with $\bar{\gamma} = 4$ and $\bar{t}_0 = 10$ for the antibonding adiabatic initial state centered around $\bar{q}^{ini} = \bar{\gamma}$. Results are shown for the methods MTE (dotted green line), FSSH and FSSH+D (dashed-dotted orange and magenta lines) and ED (in the Born-Huang basis, solid blue line). We use the following method parameters: $N_{traj} = 20\,000$ and $\Delta t = 0.01/\omega_0$ for the independent-trajectory methods MTE, FSSH and FSSH+D, and calculated the first 250 eigenstates with ED using 1000 equidistant grid points in the range $\bar{q} \in [-6, 6]$. The lines connect datapoints at every $0.1/\omega_0$.

surface over time (because $\bar{t}_0$ is large, but not infinite). With the electronic amplitudes on the lower surface being very small, the probability to hop back to the upper surface becomes large for these trajectories (see the hopping probability Eq. (5.58)), which leads to the correct distribution of trajectories in normal FSSH. In contrast, the decoherence correction in FSSH+D quickly relaxes the electronic amplitudes of the switched trajectories toward the lower surface, leading to the slow decay of trajectories toward the lower surface. We see, however, that this effect takes a long time and that the other observables, at least in this case, are well recovered. One can avoid this draining of trajectories from the upper surface by applying an active surface decoherence restriction, see Ref. [256], in which a decoherence correction is only applied if the active surface has a large enough electronic population. In this thesis, where in most cases the dynamics are not restricted to a subset of the adiabatic states, we will not apply this kind of restriction.

In the case presented here, where (i) the parameters are in the adiabatic regime (the surfaces are far separated) and (ii) the initial state is restricted to a single adiabatic state, one could resort to a normal adiabatic molecular dynamics simulation for the given potential $E_+^{BO}(q)$. With FSSH and MTE being mostly equivalent, the latter would be the method of choice, because it is (even for the same number of trajectories and the same time step) slightly faster (see Sec. 5.3.7 for the presentation of the algorithm and the necessary steps in both methods).

6.1.2 Non-adiabatic transitions

Let us now switch to a parameter regime with frequent non-adiabatic transitions, where one is forced to go beyond Born-Oppenheimer molecular dynamics if one seeks to correctly capture the time evolution. As parameters we use $\bar{\gamma} = \bar{t}_0 = 2.5$, which was already used in a few example cases before (see Figs. 5.5 and 5.9(a)). This parameter set appears several times in this thesis (and in Ref. [37]) and serves as the standard set to combine a strong electron-phonon coupling with (relatively) fast electrons that are still slow enough to allow for non-adiabatic transitions. We stay with the same initial state as before (the antibonding adiabatic state centered around $\bar{q}^{ini} = \bar{\gamma}$), see Fig. 6.1(a). The dynamics of the Born-Oppenheimer probability densities obtained with ED (in the Born-Huang basis) were already presented in Fig. 5.5, where we observed several transitions in the avoided crossing region leading to wave function splittings, and the interference of these splitted wave packets at a later time. This is compared to the Born-Oppenheimer probability densities obtained with MTE and FSSH (without decoherence) in Fig. 6.3 for four selected snapshots.

With the used number of 20 000 trajectories, both independent-trajectory methods are able to recover the Gauss-distribution of the initial state to a good extent (see Figs. 6.3(a)-(c)). In the next snapshot (Figs. 6.3(d)-(f)) the wave packet should split into two parts on the two surfaces, centered around different q. It is evident that this spatial separation of the wave packets is only reproduced in the FSSH method, while in MTE the whole nuclear density is located around a single value of q, which is located somewhere in between the centers of the

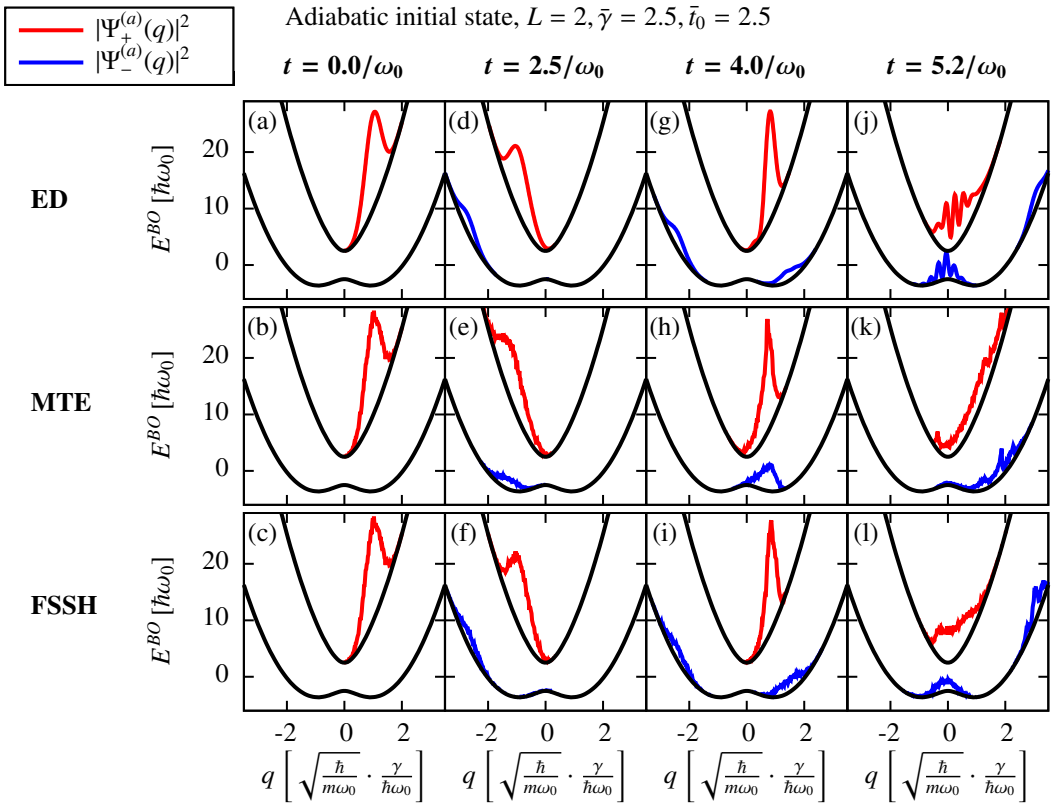

Figure 6.3: Born-Oppenheimer probability densities $|\Psi_\pm^{(a)}(q,t)|^2$ at four time-snapshots in the four columns and for the three methods ED, MTE and FSSH in the three rows, obtained in the Holstein dimer with $\bar{\gamma} = \bar{t}_0 = 2.5$ for the antibonding adiabatic initial state centered around $\bar{q}^{ini} = \bar{\gamma}$. The selected snapshots are (a)-(c) $t = 0/\omega_0$, (d)-(f) $t = 2.5/\omega_0$, (g)-(i) $t = 4/\omega_0$ and (j)-(l) $t = 5.2/\omega_0$, each for all three methods. Each snapshot shows the probability density on the upper and lower surface as red and blue lines drawn on top of their Born-Oppenheimer surfaces with a constant (arbitrary) scaling. The same method parameters as in Fig. 6.2 are used. Reproduced from Ref. [37], with the permission of AIP Publishing, line widths and graph positions have been adapted to the format of this thesis.

two wave packets obtained with the exact (and FSSH) method. This visualizes that MTE already fails to describe a single wave packet splitting during a non-adiabatic transition. The third column (Figs. 6.3(g)-(i)) shows a snapshot after the second non-adiabatic transition and wave packet splitting. While FSSH shows a qualitative agreement with the exact results, the probability density in MTE is still localized to a narrow region. Finally, at $t = 5.2/\omega_0$ (Figs. 6.3(j)-(l)), the interference between the previously split parts of the wave function occurs. Here, we observe the first significant deviation in the FSSH method from the exact results, as the interference pattern is not recovered. This is not surprising, as already in the approximate derivation of FSSH from the QCLE (see Sec. 5.3.4) one of the assumptions breaks down when such a recoherence (collision of previously split wave packets) occurs, see Ref. [224] and the discussion in Ref. [242]. Meanwhile, the time evolved probability density of MTE has lost any resemblance to the exact results.

To quantify the performance of the methods and to also compare to FSSH+D and MCE, we show the time evolution of $\langle \hat{n}_+ \rangle$, $\langle \hat{n}_1 \rangle$ and $\langle \hat{q} \rangle$ obtained with MTE, FSSH, FSSH+D, MCE and ED (in the Born-Huang basis) in Fig. 6.4. In the exact dynamics, we observe several partial non-adiabatic transitions, where the population on the upper Born-Oppenheimer surface decreases (see Fig. 6.4(a)). At later times, the wave packets on the lower surface can also partly move back to the upper surface, and we do not observe equilibration (at least in the time interval shown). The electron density initially oscillates between the two Holstein sites (see Fig. 6.4(b)), but settles around $\langle \hat{n}_1 \rangle \approx 0.5$ for later times when the nuclear density is far spread. The average nuclear distortion (Fig. 6.4(c)) also starts with a single strong oscillation, which later turns into the average of the oscillations of the various wave packets.

In all observables we see an excellent agreement of the coupled-trajectory method MCE with the exact results, with significant deviations occurring only at late times, beyond the time of the energy-drift indicator $t^{MCE}_{0.2\,\hbar\omega_0}$. None of the independent-trajectory methods is able to follow the exact results at late times, but their performance differs for the first few phonon oscillation periods. In MTE all observables start to deviate strongly from the exact results already after a single oscillation period. Too little relaxation to the lower Born-Oppenheimer surface is predicted during the non-adiabatic transitions, and the time evolution of the nuclear observable $\langle \hat{q} \rangle$ reflects that the nuclear density in MTE is not able to split into several parts, with a strong coherent oscillation prevailing for long times. In contrast, both FSSH and FSSH+D qualitatively follow the exact dynamics, even for some time after the first recoherence event at around $t \approx 5.2/\omega_0$. We see that the decoherence correction improves the agreement with the exact results, with barely any noticeable deviation until $t \approx 7/\omega_0$.

In this example case, using a coupled-trajectory method like MCE seems to be the method of choice, at least out of the tested trajectory-based methods. The closest competition is FSSH+D, which can recover the shown observables quantitatively for several phonon oscillation periods. In contrast, MTE seems to be unable to describe partial non-adiabatic transitions correctly. We note that the wave packet in this system is periodically forced back to the same avoided crossing region, which is significantly more difficult to treat compared to the

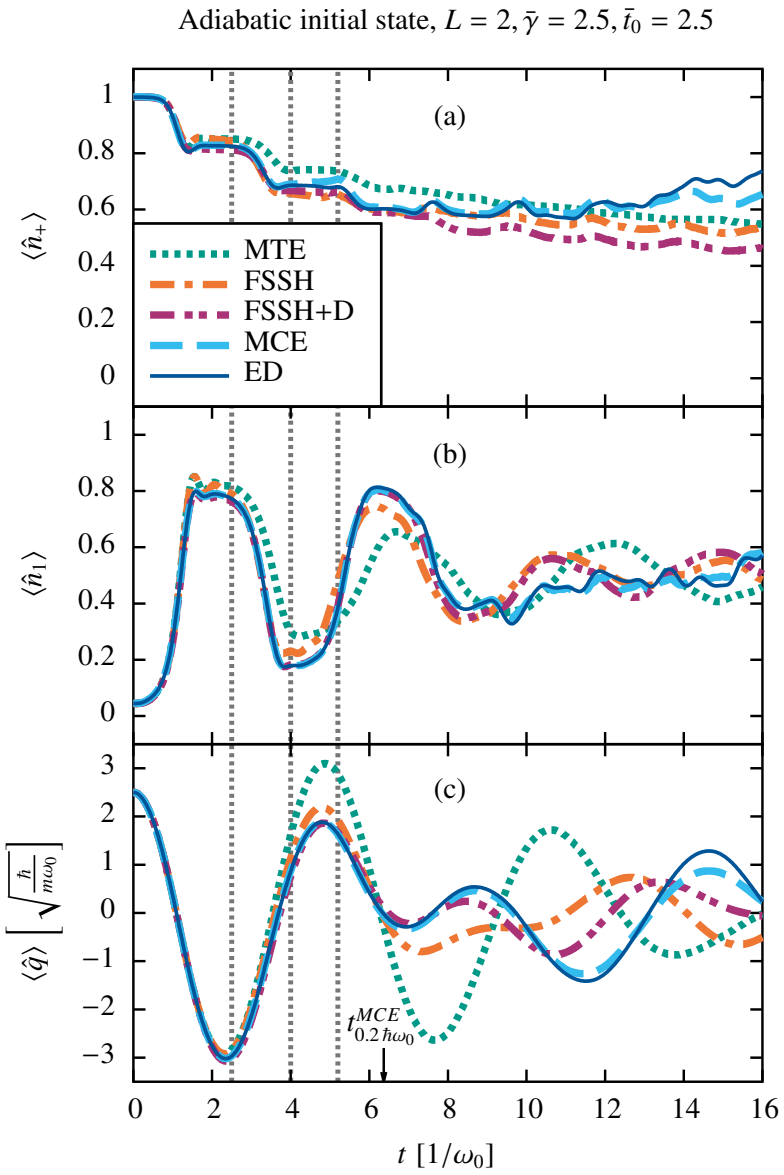

Figure 6.4: Time evolution of the (a) population on the upper Born-Oppenheimer state $\langle \hat{n}_+ \rangle$, (b) electron density on site 1 $\langle \hat{n}_1 \rangle$ and (c) relative nuclear distortion $\langle \hat{q} \rangle$, obtained in the Holstein dimer with $\bar{\gamma} = \bar{t}_0 = 2.5$ for the antibonding adiabatic initial state centered around $\bar{q}^{ini} = \bar{\gamma}$. Results are shown for the methods MTE (dotted green line), FSSH and FSSH+D (dashed-dotted orange and magenta lines), MCE (dashed light blue line) and ED (solid blue line). The independent-trajectory methods and ED use the same method parameters as in Fig. 6.2. MCE is performed with 300 configurations and reaches an energy drift of $0.2\,\hbar\omega_0$ at $t^{MCE}_{0.2\,\hbar\omega_0} = 6.37/\omega_0$. The snapshot-times shown in Fig. 6.3 are marked with vertical gray dashed lines. Reproduced from Ref. [37], with the permission of AIP Publishing.

typical avoided crossing problems of quantum chemistry, see, e.g., the original FSSH article, Ref. [29].

6.1.3 Coherences in the initial state

The last example was the ideal situation for the surface hopping methods, with the wave packet starting from a single adiabatic state and then approaching an avoided crossing region, and FSSH+D seems like a suitable independent-trajectory improvement of Born-Oppenheimer molecular dynamics in this case (if more advanced methods are computationally too expensive). Instead of having contributions on different Born-Oppenheimer states to build up over time, one could also directly start in a coherent superposition of several of these states. In such an initial state, the correct nuclear forces at every position are not given by the derivatives of the Born-Oppenheimer surfaces, as assumed in the surface hopping methods. One example is the bare local initial state (see Fig. 6.1(b)), where the electron starts on one Holstein site and thus the nuclei should initially move according to an electron density of zero on the unoccupied and one on the occupied site. For a method to be able to deal with such coherences widens its scope of applicability, for example to describe the relaxation after a photoexcitation when one cannot guarantee to be initially restricted to a single adiabatic state, see Ref. [242].

To discriminate the effects of non-adiabatic transitions occurring during the time evolution and initial coherences between adiabatic states, we return to the adiabatic parameter regime $\bar{\gamma} = 4$, $\bar{t}_0 = 10$ used before (see Fig. 6.2). With the derivative couplings being very delocalized and non-adiabatic transitions prohibited, the dynamics of the two components of the adiabatic wave function ($\Psi_+^{(a)}$ and $\Psi_-^{(a)}$) should depend on their respective Born-Oppenheimer surfaces only, see Eq. (5.15), and one could utilize the Born-Oppenheimer approximation, see Eq. (5.19). This separation of the dynamics on the different surfaces holds for the wave function amplitudes only. When using a classical approximation for the nuclei instead and propagating them as trajectories, as in MTE and FSSH, the local phase relation of both electronic wave function components is important to correctly determine the nuclear forces, at least in the short-time regime.

To better visualize the exact dynamics, we present two snapshots showing the time-evolved probability densities of the bare local initial state in this adiabatic parameter regime obtained with ED (in the Born-Huang basis) in Fig. 6.5. The densities are shown both in the Born-Oppenheimer basis (Figs. 6.5(a),(c)) and in the diabatic (site-local) basis (Figs. 6.5(b),(d)), and the diagonal entries of the Born-Oppenheimer Hamiltonian in the respective bases are included in the figure. With the electron of the initial state being restricted to site one in the Holstein dimer, the correct potential determining the forces at time $t = 0$ corresponds to the shifted right harmonic oscillator $V(\bar{q}) = \bar{q}^2/2 - \bar{\gamma}\bar{q}$, see Fig. 6.5(b). This is also the force which is used in MTE to propagate the nuclear trajectory. In FSSH, however, the forces are calculated from the active surfaces, which for this initial state are either the upper or lower Born-Oppenheimer surface. If we take a trajectory sampled close to $q = 0$, the

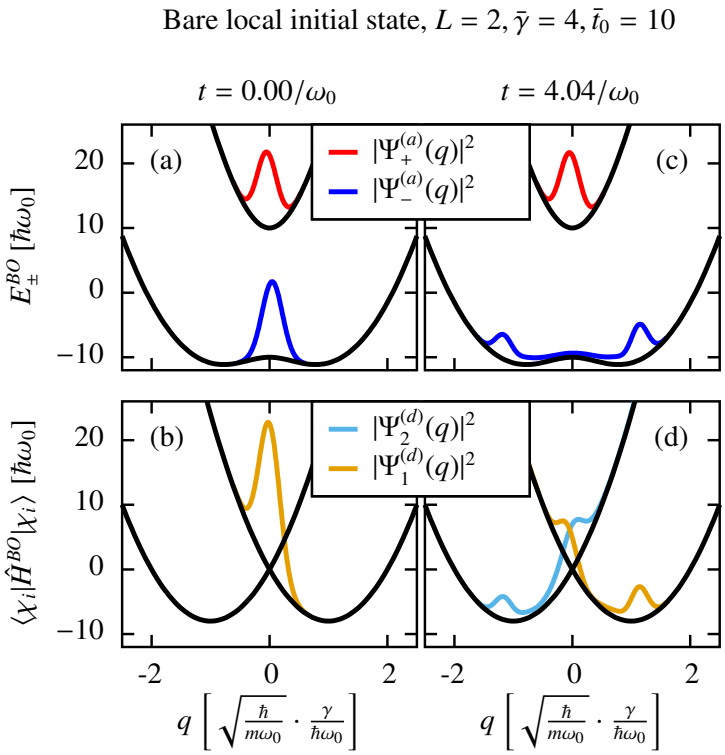

Figure 6.5: Adiabatic ((a) and (c)) probability densities $|\Psi_\pm^{(a)}(q,t)|^2$ and diabatic ((b) and (d)) probability densities $|\Psi_i^{(d)}(q,t)|^2$, each for the two times $t = 0/\omega_0$ and $t = 4.04/\omega_0$, obtained with ED in the Holstein dimer with $\bar{\gamma} = 4$ and $\bar{t}_0 = 10$ for the bare local initial state. The probability densities in each snapshot are drawn with a constant (arbitrary) scaling on top of the diagonal entries of the Born-Oppenheimer Hamiltonian in the used basis, i.e., $E_\pm^{BO}(q)$ for the adiabatic and $\langle\chi_i|\hat{H}^{BO}(q)|\chi_i\rangle$ for the diabatic probability densities. The ED method uses the same method parameters as in Fig. 6.2. Reproduced from Ref. [37], with the permission of AIP Publishing.

slope of either surface is close to zero, leading to a completely different nuclear force. Conversely, the dynamics of the total wave function amplitudes take place on the two surfaces separately. At later times (Figs. 6.5(c)-(d)), the contribution of the wave function on the upper (antibonding) surface remains close to $q = 0$, while the contribution on the lower surface is splitted into the two bound states at the minima of the potential. This spatial separation limits the influence of the initial coherences on the late-time dynamics. The exception is the diabatic probability density close to the symmetric configuration ($q \approx 0$), which oscillates very fast between the two sites, due to the choice of the initial state, and is delocalized in the snapshot selected in Fig. 6.5(d).

To see how the trajectory-based methods deal with this combination of having coherences in the initial state and a wave packet splitting at later times, we compare MTE, FSSH, FSSH+D, MCE and ED for two observables in Fig. 6.6. First, we start with the population on the upper Born-Oppenheimer state, which starts at $\langle\hat{n}_+^{BO}\rangle = 0.5$. We observe that MTE and MCE correctly

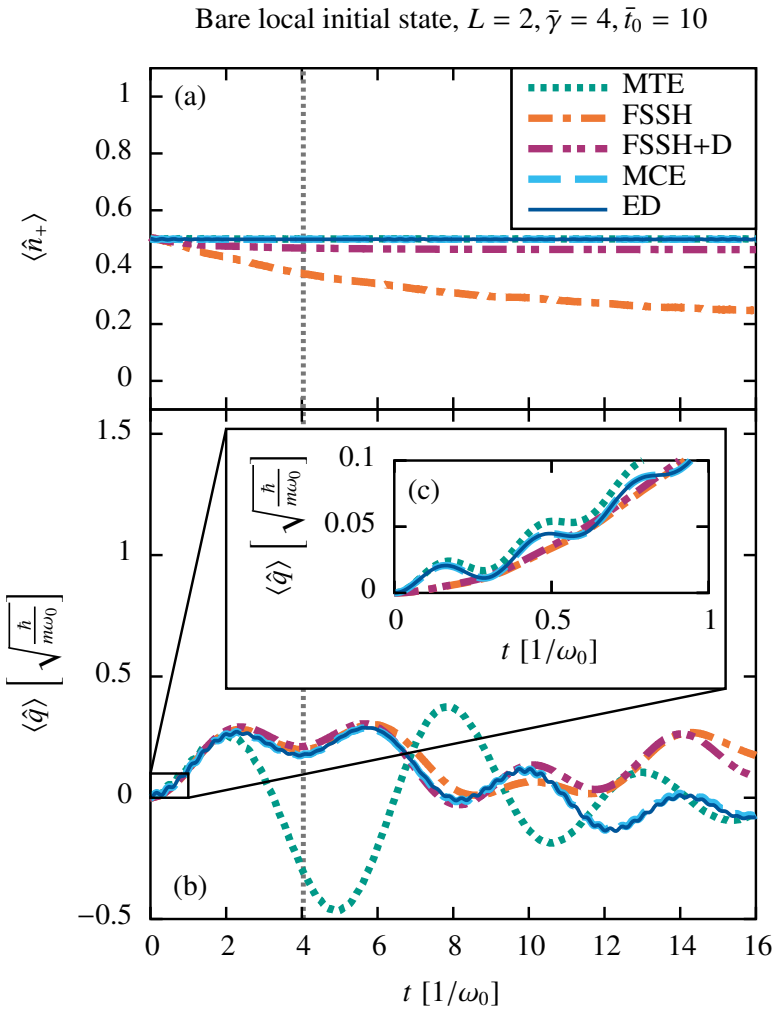

Figure 6.6: Time evolution of the (a) population on the upper Born-Oppenheimer state $\langle \hat{n}_+ \rangle$ and (b) relative nuclear distortion $\langle \hat{q} \rangle$, obtained in the Holstein dimer with $\bar{\gamma} = 4$ and $\bar{t}_0 = 10$ for the bare local initial state. The inset (c) shows the short-time evolution of $\langle \hat{q} \rangle$. Results are obtained with the methods MTE (dotted green line), FSSH and FSSH+D (dashed-dotted orange and magenta lines), MCE (dashed light blue line) and ED (solid blue line). The independent-trajectory methods and ED use the same method parameters as in Fig. 6.2. MCE is performed with 60 configurations and does not reach an energy drift of $0.2\,\hbar\omega_0$ in the shown time interval. The snapshot time of Figs. 6.5(c)-(d) is marked with a vertical gray dashed line. Reproduced from Ref. [37], with the permission of AIP Publishing.

reproduce that this observable hardly changes over time. In contrast, FSSH shows a large relaxation toward the lower Born-Oppenheimer state. This is caused by one of the caveats of the surface hopping methods, mentioned in Sec. 5.3.4: the frustrated hops. With the energy separation between the two surfaces being large compared to the nuclear momenta, trajectories starting on the lower surface are not able to hop toward the upper surface. In contrast the trajectories starting on the upper surface can switch to the lower surface (and potentially later back up to the upper surface). This leads to an asymmetry of the populations and the observed decay. The approximate derivation of FSSH from the QCLE also mentions large nuclear momenta as one of its assumptions, see Ref. [224]. The decoherence correction removes the coherences between the adiabatic states, leading to a much reduced hopping rate between the surfaces and to a better prediction of the adiabatic populations (non-adiabatic transitions at late times are very unlikely with the very small nuclear kinetic energy and we could not observe the slow decoherence-correction induced decay observed previously in Fig. 6.2).

Second, the time evolution of the average nuclear distortion is shown in Fig. 6.6(b), and magnified in the short-time regime in Fig. 6.6(c). For the whole time MCE coincides with ED, and there is no conceivable deviation even for late times, which fits to the fact that the energy drift threshold of $0.2\,\hbar\omega_0$ is not reached in that time interval. For short times the exact and MCE dynamics predict a fast small oscillation of $\langle\hat{q}\rangle$, which is at least partially reproduced by the MTE method. This oscillation is caused by the fast electronic transitions between the two Holstein sites and persists even for late times. Both FSSH and FSSH+D do not capture these small oscillations, which is exactly because the nuclear forces are calculated from the Born-Oppenheimer surfaces alone, as explained before. In contrast, the large scale oscillations of the observable, caused by the movement of the nuclei and the wave packet separation, is surprisingly well reproduced with both surface hopping methods. In particular FSSH+D shows a qualitative agreement with the exact results up to $t \approx 10/\omega_0$. With the electron switching rapidly between both sites, the average nuclear forces are very close to adiabatic forces used in the surface hopping methods. The opposite is true for MTE, which completely fails to describe this large scale time evolution. With the nuclear forces calculated by the trace over both surfaces in MTE, the wave packet separation seen in Fig. 6.5(c) cannot be reproduced and not even a single phonon oscillation period is recovered correctly.

While we used the same parameter regime as before in the Born-Oppenheimer case (see Fig. 6.2), the performance of the independent-trajectory methods is completely different. The coherences present in the initial state lead to wrong short-time dynamics in the surface hopping methods, while the independent dynamics on the two far separated surfaces for later times are well captured. MTE can reproduce the ultra-short time dynamics, but the mean-field description leads to completely wrong long-time results. This underlines the influence of the initial state on the performance of the independent-trajectory methods.

6.1.4 The bare local state with small electron hopping

In both previous cases, (i) the non-adiabatic transitions of an adiabatic initial state and (ii) the initial state with coherences but in an adiabatic parameter regime, FSSH+D seems like the best of the studied independent-trajectory methods, at least beyond ultra-short times. We now turn to an example which is far away from the adiabatic initial state or parameter regime: the bare local state with a much reduced electron hopping of $\bar{t}_0 = 0.5$ and a strong coupling $\bar{\gamma} = 2$. This was also labeled the resonant regime, see Ref. [188], since the oscillation period of a localized electron charge in the undistorted Holstein dimer equals the classical harmonic oscillator period for these parameters. This case of a relatively slow electron (or fast phonon) might seem unphysical for realistic materials, but it is excellent to test how the trajectory-based methods deal with coherences in the initial state in a truly non-adiabatic regime. With the nuclei and electrons moving at a similar speed, temporal polaronic trapping effects were observed in large charge-density wave systems, visible in a plateau-formation in the electronic densities, see Ref. [288]. In the Born-Oppenheimer surfaces of the dimer (see Fig. 5.2) this corresponds to moments in time when the wave packet is away from the symmetric point $q = 0$, where transitions both between the surfaces and the Holstein sites are unlikely (for small t_0, the adiabatic and diabatic states are similar and change character around $q = 0$, see the discussion in Sec. 5.3.7). This trapping alternates with time periods in which the wave packet is close to $q = 0$, allowing for rapid transitions. In the large systems the situation is similar, with the trapping occurring when a large phonon number builds up temporarily on the occupied sites.

To see how the methods deal with such an initial state, the time evolution of the electron density on one Holstein site is shown for the bare local initial state in Fig. 6.7. A plateau in the electron density is clearly visible in both ED and MCE, whose time evolutions coincide for the whole time-interval shown. We see that MTE is able to somehow recover the plateau formation, although at a slightly reduced value. The deviation is significantly stronger in the surface hopping methods, where a plateau-like constant electron density is not visible. All independent-trajectory methods predict a too strong localization of the electron density on the initially occupied site after the first nuclear oscillation period, with FSSH following the decline of the density slightly better than MTE and FSSH+D for a short time interval.

It seems that neither of the independent-trajectory methods is able to properly deal with this combination of initial state and parameter regime, with MTE at least giving a proper time evolution within the first nuclear oscillation period. As before, the coherences of the initial state prevent an accurate short-time description of the surface hopping method, but in contrast to the adiabatic regime this is not compensated by better long time dynamics in this case, making FSSH/FSSH+D unsuitable to describe this case. We note that if one would use the active surface definition of the density matrix, see Eq. (5.61), or project the wave function amplitudes of the initial state toward the active surfaces, then the electron density of both FSSH and FSSH+D would start at $\langle \hat{n}_1 \rangle = 0.5$, far away from the true result. In our results for the larger

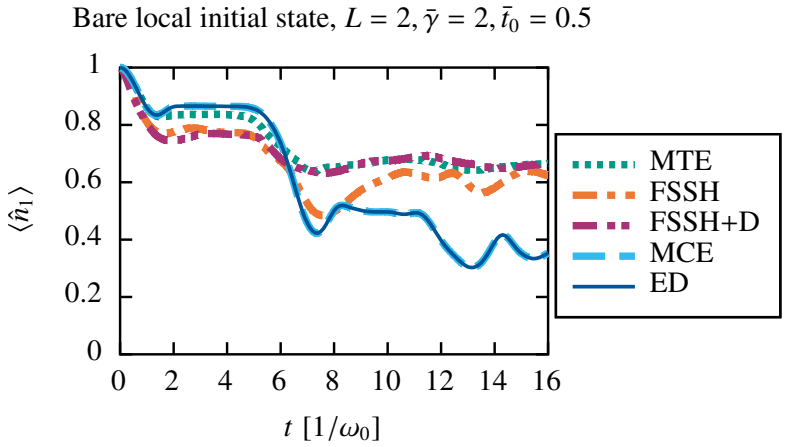

Figure 6.7: Time evolution of the electron density on the initially occupied site $\langle \hat{n}_1 \rangle$, obtained in the Holstein dimer with $\bar{\gamma} = 2$ and $\bar{t}_0 = 0.5$ for the bare local initial state. Results are shown for the methods MTE (dotted green line), FSSH and FSSH+D (dashed-dotted orange and magenta lines), MCE (dashed light blue line) and ED (solid blue line). The independent-trajectory methods and ED use the same method parameters as in Fig. 6.2. MCE is performed with 150 configurations and does not reach an energy drift of $0.2\,\hbar\omega_0$ in the shown time interval. Reproduced from Ref. [37], with the permission of AIP Publishing.

systems, we will focus on an intermediate electron hopping parameter regime of $\bar{t}_0 = 2.5$, where non-adiabatic transitions happen frequently (see Fig. 6.3), but the electrons are still faster than the phonons.

6.1.5 Tunneling

Another example where the independent-trajectories fail is the description of tunneling. With the nuclei described as classical particles, the trajectories are not able to overcome an energy barrier if their kinetic energy is insufficient. Extensions of the methods to include tunneling exist, see Refs. [305, 306], but are not included for the calculations carried out in this thesis (or in the corresponding article, Ref. [37]). The inability to describe tunneling is especially relevant at longer times and relatively low nuclear kinetic energies.

To visualize the problem, we selected the dressed local initial state, see Fig. 6.1(c), in which much of the nuclear density is located close to the minimum of the lower Born-Oppenheimer surface. For the parameters we stay with the ones from the previous example, i.e., $\bar{\gamma} = 2$, $\bar{t}_0 = 0.5$, making non-adiabatic transitions around $q = 0$ in principle possible. The resulting time evolution of the electron density on the initially occupied site is shown in Fig. 6.8.

We see that ED indeed predicts a very slow tunneling transition between the two Holstein sites with a period of approximately $T \approx 100\pi/\omega_0$. From the shape of the eigenstates of the Holstein dimer (see Fig. 5.3), we can speculate that the initial state is in a superposition of the lowest two eigenstates. Their energy splitting for the parameters used here is $\Delta E \approx 0.02\,\hbar\omega_0$, which fits very well to the observed tunneling period, see also Ref. [37]. All independent-

trajectory methods are unable to describe the tunneling, as expected. The coupled-trajectory method MCE shows the long-time tunneling effect to some degree, but even for the used 200 configurations and the larger standard deviation used in the initial sampling (see Ref. [37]) it could not be converged sufficiently to capture the complete recovery of the electron density after one period. Extensions of coupled-trajectory methods to improve the description of tunneling have also been proposed, see Refs. [307, 308].

6.1.6 Summary for the Holstein dimer

In this section, we presented a few example cases to illustrate the performance of the independent-trajectory methods MTE, FSSH and FSSH+D in dealing with non-adiabatic effects, either due to non-adiabatic transitions, or by starting from an initial state with coherences between adiabatic states, or both. The methods have been compared to ED and to the coupled-trajectory method MCE. The latter significantly improved upon the MTE method and coincided well with ED where converged. We saw that the surface hopping methods are well prepared to deal with non-adiabatic transitions and can describe a wave packet splitting. Coherences of the initial state impede their ability to describe the short-time dynamics, but in an adiabatic parameter regime they still provide a decent long-time description. In most examples, applying a decoherence correction improved the results, in particular for nuclear observables. MTE could always recover the ultra-short time dynamics, independent of the initial

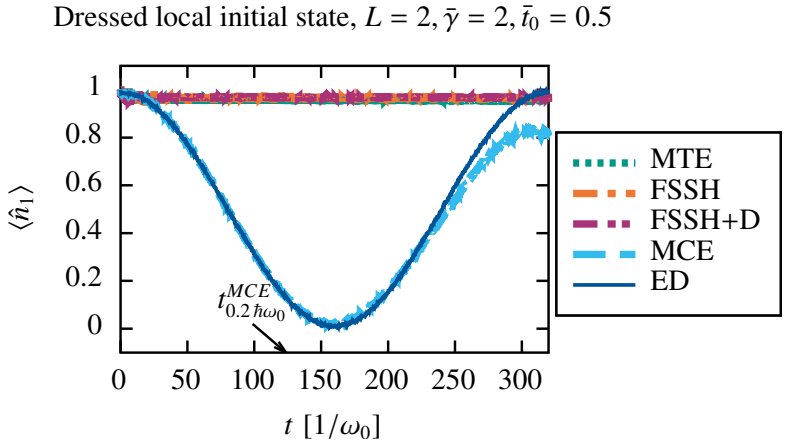

Figure 6.8: Time evolution of the electron density on the initially occupied site $\langle \hat{n}_1 \rangle$, obtained in the Holstein dimer with $\bar{\gamma} = 2$ and $\bar{t}_0 = 0.5$ for the dressed local initial state. Results are shown for the methods MTE (dotted green line), FSSH and FSSH+D (dashed-dotted orange and magenta lines), MCE (dashed light blue line) and ED (solid blue line). The independent-trajectory methods and ED use the same method parameters as in Fig. 6.2. MCE is performed with 200 configurations and reaches an energy drift of $0.2\,\hbar\omega_0$ at $t^{MCE}_{0.2\,\hbar\omega_0} = 123.7/\omega_0$. The quantum superposition sampling of MCE was carried out with a larger standard deviation than normally, see Ref. [37] for details. Reproduced from Ref. [37], with the permission of AIP Publishing.

state and parameters, but both non-adiabatic transitions and initial coherences can lead to strong deviations from the exact results already after a single phonon oscillation period. In larger systems, the separation of Born-Oppenheimer surfaces can become smaller and also the shape of these surfaces changes significantly. This is analyzed in the following.

6.2 Holstein trimer

We now turn to the Holstein trimer, which serves as an intermediate step before continuing with the extended Holstein chain. The Born-Oppenheimer surfaces of the trimer can still be visualized easily and are shown in Figs. 5.6 and 5.7. The shape of the surfaces differs drastically from the dimer, with the middle (non-bonding) Born-Oppenheimer surface approaching either of the other two surfaces for a large positive or negative symmetric nuclear distortion $\bar{x}_s$ (for $\bar{x}_a = 0$). We stay with a fixed parameter set of $\bar{\gamma} = \bar{t}_0 = 2.5$, i.e., a strong electron-phonon coupling, with electrons that are faster than the nuclei, but still allow for non-adiabatic transitions also outside of the asymptotically approaching surfaces. As before, we investigate both adiabatic and local initial states. For the comparison we have again the coupled-trajectory method MCE and a version of exact diagonalization (ED), now carried out in a second quantized basis, implemented and tested by D. Jansen, see Ref. [37] for details.

6.2.1 Non-bonding adiabatic initial state

We start with an adiabatic initial state, for which, unfortunately, no ED data are available. As the starting surface we choose the middle, non-bonding, Born-Oppenheimer surface with an initial Gaussian wave packet centered around $\bar{x}_a = 0$ and $\bar{x}_s = \frac{2}{\sqrt{3}}\bar{\gamma}$ (corresponding to the nuclear distortions of the dressed local state, but with the electron promoted to the non-bonding state). This non-bonding state has no contribution on the central trimer site for $\bar{x}_a = 0$, see Fig. 5.6(b). Even with the Gaussian wave packet having a finite width in $\bar{x}_a$, the electron density on the central site is still very small. The time evolution of the electron density on this central site $\langle \hat{n}_2 \rangle$ and of the symmetric phonon distortion $\langle \hat{x}_s \rangle$ is shown in Fig. 6.9.

While no ED data are available, we consider the MCE simulation as a good reference method, at least until the energy convergence criterion $t^{MCE}_{0.2\,\hbar\omega_0}$ is reached. The time evolution of $\langle \hat{x}_s \rangle$ shows several large oscillations, slightly damped for later times. During the first quarter nuclear oscillation, when the wave packet approaches $\bar{x}_s = 0$, we see that the electron density on the central site $\langle \hat{n}_2 \rangle$ increases sharply. Here, already a large part of the wave packet switched from the non-bonding to the bonding state, which has a significant contribution on the central site for $\bar{x}_s \approx 0$. Continuing to negative $\bar{x}_s$, however, the bonding state has less contribution on the central site, visible in a decline of the electron density on that site. With most of the electronic population staying in the bonding state (Born-Oppenheimer ground state) for later times, the density on the central site continues to oscillate together with the symmetric

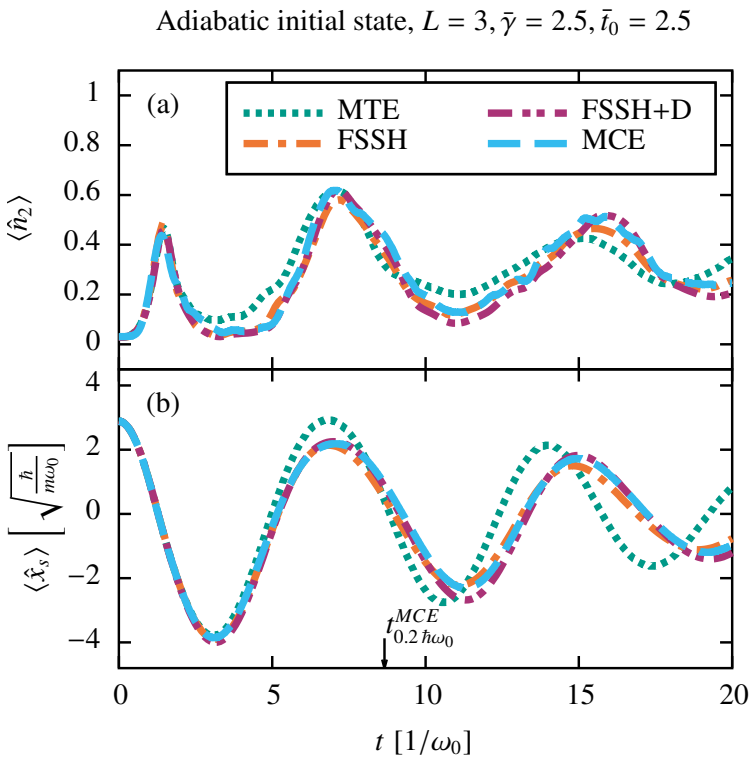

Figure 6.9: Time evolution of the (a) electron density on the central site $\langle \hat{n}_2 \rangle$ and (b) symmetric nuclear distortion $\langle \hat{x}_s \rangle$, obtained in the Holstein trimer with $\bar{\gamma} = \bar{t}_0 = 2.5$ for the non-bonding adiabatic initial state ($\langle \hat{n}_1^{BO}(t{=}0) \rangle = 1$) centered around $\bar{x}_s^{ini} = 2\bar{\gamma}/\sqrt{3}, \bar{x}_a^{ini} = 0$. Results are shown for the methods MTE (dotted green line), FSSH and FSSH+D (dashed-dotted orange and magenta lines) and MCE (dashed light blue line). We use the following method parameters: For the independent-trajectory methods $N_{traj} = 20\,000$ and $\Delta t = 0.001/\omega_0$, while MCE uses 1200 configurations and reaches an energy drift of $0.2\,\hbar\omega_0$ at $t^{MCE}_{0.2\,\hbar\omega_0} = 8.66/\omega_0$. Reproduced from Ref. [37], with the permission of AIP Publishing.

nuclear distortion. The dynamics obtained with all methods are relatively similar, with the surface hopping methods reproducing the MCE results better than MTE. MTE also underestimates the nuclear oscillation period of $\langle \hat{x}_s \rangle$ for later times. We attribute the relatively good agreement of all methods to the beneficial form of the Born-Oppenheimer surfaces: In the asymptotic regions with strong non-adiabatic coupling, the slope of the approaching surfaces is similar, resulting in roughly the same nuclear forces, independent of whether a mean-field or a surface hopping approach is used. The performance of the surface hopping methods is, as far as we can judge with the lack of ED data, even better than in the Holstein dimer for the same parameters (see Fig. 6.4).

6.2.2 Bare local initial state

Next, we continue with the difficult case of a bare local initial state on the central site (i.e., $\langle \hat{n}_2(t=0) \rangle = 1$), with strong coherences mainly between the

lowest (bonding) and highest (antibonding) Born-Oppenheimer surfaces, using the same parameters as before. The electronic population on the bonding state ($\langle \hat{n}_0^{BO} \rangle$), the electron density on the central site, and the average symmetric nuclear distortion are shown in Fig. 6.10.

From a similar initial state in the Holstein dimer (see Fig. 6.6), we expect rapid electronic transitions between the Holstein sites. This is visible in the electron density in Fig. 6.10(b). The effect of these transitions on the nuclear distortions seems to be less pronounced here compared to the dimer case, with Fig. 6.10(c) showing only small oscillations caused by these electronic transitions. Nonetheless, we can observe that the ultra-short time description of $\langle \hat{x}_s \rangle$ in the surface hopping methods deviates slightly from the results obtained with the other methods. In addition, the fast electronic transitions between the sites, which persist in ED and MCE until late times, are quickly damped in all independent-trajectory methods, with this damping being the fastest in FSSH+D and slowest in MTE.

For the long-time behavior, we see that both FSSH and FSSH+D are closer to the exact results for $\langle \hat{x}_s \rangle$ than MTE, and show a similar oscillation period, although the agreement is more of a qualitative than quantitative nature. The electron density on the central site obtained in the surface hopping methods also seems to be slightly closer to the time-average of the exact and MCE dynamics, but the small-scale oscillations are completely lost. Furthermore, we show the relaxation of the initial state toward the lowest Born-Oppenheimer surface with $\langle \hat{n}_0^{BO} \rangle$ in Fig. 6.10(a). This observable reveals that there is nearly no relaxation in the MTE method toward the lowest surface and that the dynamics are thus strongly influenced by the higher surfaces at later times. FSSH, FSSH+D and MCE show a much stronger relaxation, with a better agreement of MCE and FSSH+D at late times. With no ED reference data available for this observable, this agreement should be taken with caution and further studies are needed.

6.2.3 Dressed local initial state

We now turn to the dressed local initial state, previously only used to investigate the tunneling transition. The electron is initially placed on the central trimer site and the nuclear distortion on that site is already adjusted to the electron, which results in a Gaussian wave packet around $\bar{x}_a = 0$ and $\bar{x}_s = \frac{2}{\sqrt{3}}\bar{\gamma}$, as before in the non-bonding case. The dressed local state starts with a large population on the lowest Born-Oppenheimer surface, with $\langle \hat{n}_0^{BO}(t=0) \rangle \approx 0.92225$, see also Ref. [37]. This state still has coherences between the adiabatic states, but these are much smaller compared to the bare local state, because the lowest Born-Oppenheimer surface is further separated from the excited ones at this point, see Fig. 5.7. With the far separation of the lowest and the excited Born-Oppenheimer surfaces, we expect the contribution on the lowest surface to be rather stationary, while the non-bonding and antibonding contributions should undergo large nuclear oscillations, which might be a challenge for the mean-field method MTE.

The dynamics of $\langle \hat{n}_2 \rangle$ and $\langle \hat{x}_s \rangle$ are shown in Fig. 6.11. The MCE and ED results show a better agreement compared to the bare local case, which fits to

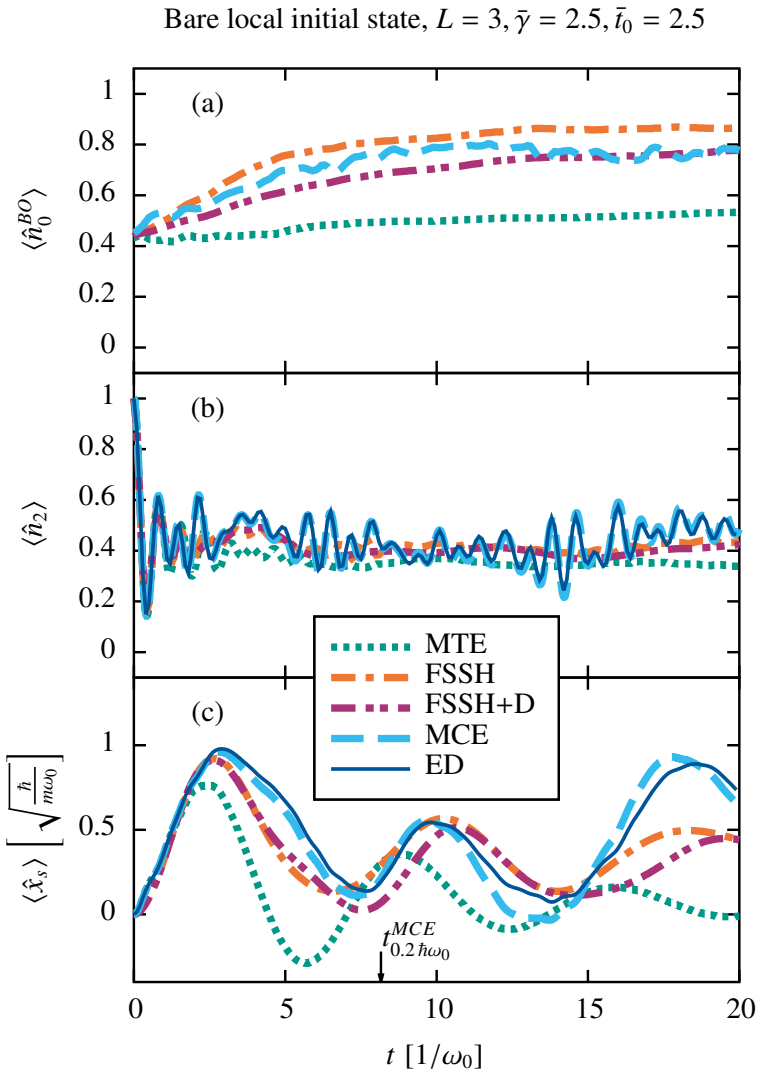

Figure 6.10: Time evolution of the (a) population on the lowest Born-Oppenheimer state $\langle \hat{n}_0 \rangle$, (b) electron density on the central site $\langle \hat{n}_2 \rangle$ and (c) symmetric nuclear distortion $\langle \hat{x}_s \rangle$, obtained in the Holstein trimer with $\bar{\gamma} = \bar{t}_0 = 2.5$ for the bare local initial state at the central site. Results are shown for the methods MTE (dotted green line), FSSH and FSSH+D (dashed-dotted orange and magenta lines), MCE (dashed light blue line) and ED (in second quantization, solid blue line). The independent-trajectory methods use the same method parameters as in Fig. 6.9. ED in second quantization is performed with $M = 26$ local phonon states, while MCE uses 1000 configurations and reaches an energy drift of $0.2\,\hbar\omega_0$ at $t^{MCE}_{0.2\,\hbar\omega_0} = 8.16/\omega_0$. Reproduced from Ref. [37], with the permission of AIP Publishing.

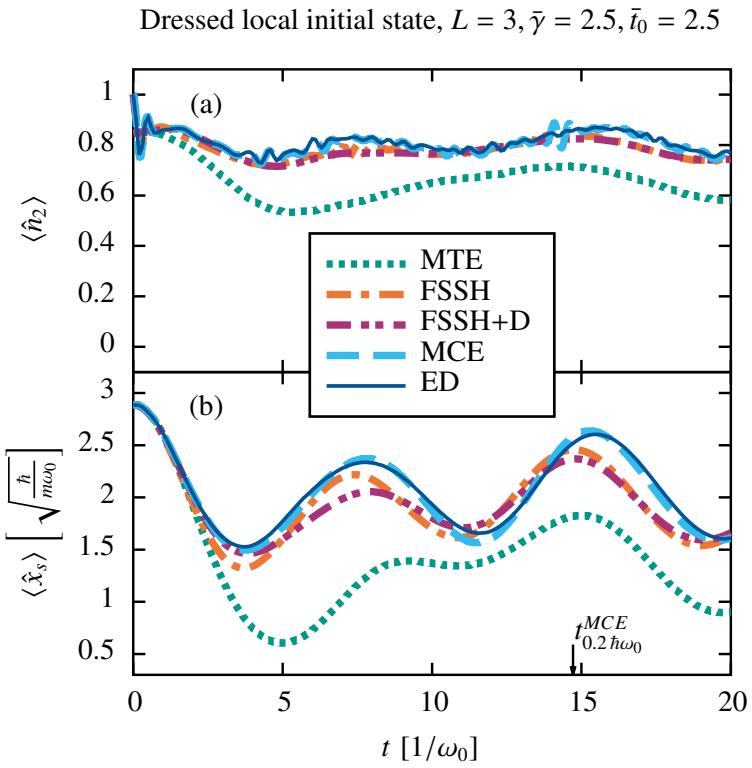

Figure 6.11: Time evolution of the (a) electron density on the central site $\langle \hat{n}_2 \rangle$ and (b) symmetric nuclear distortion $\langle \hat{x}_s \rangle$, obtained in the Holstein trimer with $\bar{\gamma} = \bar{t}_0 = 2.5$ for the dressed local initial state at the central site. Results are shown for the methods MTE (dotted green line), FSSH and FSSH+D (dashed-dotted orange and magenta lines), MCE (dashed light blue line) and ED (in second quantization, solid blue line). The independent-trajectory methods use the same method parameters as in Fig. 6.9. ED in second quantization is performed with $M = 21$ local phonon states, while MCE uses 1000 configurations and reaches an energy drift of $0.2\,\hbar\omega_0$ at $t^{MCE}_{0.2\,\hbar\omega_0} = 14.72/\omega_0$. Reproduced from Ref. [37], with the permission of AIP Publishing.

the better convergence of MCE visible from the energy convergence criterion $t^{MCE}_{0.2\,\hbar\omega_0}$, which is reached at a later time. The same holds for FSSH and FSSH+D, which deviate less from the exact results compared to the bare local case, as can be seen in the time evolution of $\langle \hat{x}_s \rangle$. The average electron density on the central site $\langle \hat{n}_2 \rangle$ stays close to the exact results, while its small-scale oscillations are again lost at late times.

The improvement of the other methods does not carry over to MTE. Here, the electron density on the central site decays too much and $\langle \hat{x}_s \rangle$ oscillates around too low values. As shown in the Holstein dimer, the mean-field averaging in MTE prevents an accurate separation of the contributions on the different surfaces. We find it surprising that even though the initial state has a very large population on a single adiabatic state, the remaining coherent contributions on the other states still influence and impair the dynamics to this extent.

6.2.4 Summary for the Holstein trimer

Similar as in the Holstein dimer, the coupled-trajectory method MCE shows a very good agreement with the exact results, where these are available. In these small systems, where the MCE method is computationally still cheap (in some cases even cheaper than the independent-trajectory methods), it is definitely the method of choice out of the tested trajectory-based algorithms.

Of the independent-trajectory methods, MTE seems to perform worst, both for an adiabatic and a local initial state. Even rough estimates for nuclear oscillation periods or average nuclear distortions are unreliable after a single oscillation period. The dressed local initial state shows that a small contribution in another adiabatic state can already significantly alter the resulting dynamics. In such a case it might be better to start independent dynamics of wave packets restricted on the different Born-Oppenheimer surfaces. This would, however, remove the short-time agreement of MTE with the exact methods that is one of the strong suits of this method.

The surface hopping methods, which were specifically designed to describe the independent dynamics on various surfaces, show a better agreement with the exact results. The methods still work best when starting from a single adiabatic state, as otherwise initial coherences prevent an accurate calculation of the nuclear forces in the short-time regime. For such coherent initial states, diabatic populations, such as local electron densities in the single-particle case, can still be reproduced for some time by avoiding an initial projection onto the Born-Oppenheimer surfaces (see the discussion at the end of Sec. 5.3.4) and by using the mixed definition of the density matrix in the calculation of observables (see Eq. (5.63)), although the short-time regime could also be described with the wave-function definition. We observe a better agreement of FSSH/FSSH+D with the exact results in the dressed local case, where the coherences are less pronounced and the initial state is "almost" restricted to a single adiabatic state. We could not observe a clear indication whether to use or omit a decoherence correction is the better choice in the Holstein trimer.

6.3 Holstein chain

In the small systems of the Holstein dimer and trimer, the coupled-trajectory method MCE clearly outperformed both MTE and the surface hopping methods. We now continue with the extended Holstein chain, for which we carried out benchmark calculations for sizes up to $L = 51$. These system sizes are comparable to the systems studied with the manganite tight-binding model (see Ch. 4), although still one-dimensional. The computational cost of MCE scales with the third power of the number of used configurations, while both MTE and FSSH do not only scale linearly with the number of trajectories, but can also be perfectly parallelized. While MCE in principle converges to the exact results, this convergence might not be reached in practice, see Ref. [263]. In the results presented here and in the corresponding article, Ref. [37], a strict convergence of MCE could not be achieved in general for long times and different methods are needed to serve for benchmark purposes. With the systems being much

too large for exact diagonalization, we will use the DMRG data provided by D. Jansen and J. Stolpp for the Holstein chain, see the introduction of this chapter.

In this thesis, we will stay with the single-electron case and analyze both bare and dressed local initial states located at the center of the Holstein chain, see Figs. 6.1(d),(e). As stated in Ref. [169], the time-evolution in such a small polaron setup already constitutes a challenging many-body problem, as the phonon-dressing of the electron and the formation of a quasi-particle needs to be captured. Here, we will analyze the spreading of the initially localized electron density in this polaronic model and the energy transfer between the electronic and nuclear subsystems. Additional results for charge-density wave states in the Holstein chain are presented in Ref. [37], where the MTE results were obtained by S. Gräber.

As mentioned already in Ref. [37], it is difficult to predict the transport behavior of, for example, an initially localized charge density in correlated 1D lattice models, see Ref. [309], and hence the new DMRG reference data provided in Ref. [37] are needed for the benchmark studies of the trajectory-based methods. A recent tensor network state method study of the same initial states has been presented in Ref. [54], whose results have been reproduced for the same parameters with the DMRG method used here and in Ref. [37], presented in Sec. 6.3.4. A benchmark test for MCE has been carried out in the periodic dispersive Holstein chain against the hierarchical equations of motion method for 10 sites and the multiple Davydov D2 ansatz for 16 sites (see Refs. [43, 304]), which found a good performance of MCE for the parameters chosen there. The Davydov D2 ansatz has also been applied to the same model including off-diagonal electron-phonon coupling for 32 sites, see Ref. [268].

Similar initial states, although starting with the phonons prepared in a thermal state, have been investigated with surface-hopping methods, see Refs. [243, 256] and references therein, from which we also adopted some of the FSSH correction algorithms for large systems, see Sec. 5.3.5. In these studies, the focus was on the long-time behavior and on estimating mobilities, but they provided no comparison against numerically exact reference data to confirm the accuracy of the methods. Bringing together the independent-trajectory methods with the coupled-trajectory method MCE and the numerically exact DMRG data, our benchmark study, published in Ref. [37], thus provides new insight into the performance of these methods in large electron-phonon coupled systems and serves as a starting point for testing future improvements and variants of trajectory-based methods. In view of the possible application to the manganite tight-binding model (see Ch. 3), we are mainly interested in the performance of MTE in comparison to FSSH or FSSH+D in this thesis.

6.3.1 FSSH in large systems

Before continuing with the benchmark tests in the Holstein chain, we have to evaluate our implementation of the FSSH method in these large systems. As mentioned in Sec. 5.3.5, we decided to include a restriction to the decoherence correction in this case. In addition, choosing an appropriate definition of the electronic density matrix becomes more difficult for certain initial states in

large systems. For the Holstein dimer and trimer, the mixed definition of the density matrix (see Eq. (5.63)), could reproduce both adiabatic and diabatic populations for all initial states in the short-time regime, and in many cases also for longer times (see Ref. [241] for a discussion of the advantages of this definition). As already mentioned in Sec. 5.3.4, this definition can lead to negative electronic populations in the diabatic basis. We observed this only for initial states starting with strong coherences between the adiabatic states, such as the bare local case. In the small systems this was rarely a problem, and also for the local states in large systems this leads only to very small negative and positive electron densities far away from the initially occupied sites at the edges of the Holstein chain.

However, one of the most interesting quantities for analyzing the spreading of an initially localized charge is the reduced mean-squared displacement (RMSD), defined as:

$$\mathrm{RMSD}(t) = \sqrt{\sum_{i=1}^{L} \langle \hat{n}_i(t) \rangle \left(a \cdot i - x_0^{el} \right)^2}, \tag{6.1}$$

where a is the distance between Holstein sites, here set to one, and $x_0^{el} = \left[\sum_{i=1}^{L} \langle \hat{n}_i(t=0) \rangle \, ai \right]$ is the (average) initial electron position, here always the center of the chain. The RMSD measures the spreading of the electron density and its square, the mean-square displacement (MSD), is often taken as the diffusion constant to determine the mobility via Einsteins relation when studying charge transport, see, e.g., Refs. [243, 310, 311]. Hence, a square-root growth of the RMSD is an indication for a diffusive transport behavior.

While important to quantify the transport behavior, it is a quantity highly sensitive to the electron densities on the edges of the Holstein chain, due to the quadratic prefactor scaling with the distance from the center of the chain in its expression, Eq. (6.1). Hence, the small negative densities obtained with the mixed definition of the density matrix on these sites can obscure the RMSD, which is shown in Fig. 6.12(a). Here, the RMSD of the bare local initial state for a very large system of $L = 101$ sites with $\bar{\gamma} = \bar{t}_0 = 2.5$ obtained with FSSH with the three introduced definitions of the electronic density matrix (see Sec. 5.3.4) is compared to the numerically exact results obtained with DMRG.

The DMRG results are only available for short times, which makes it difficult to judge the long-time accuracy of FSSH. Nonetheless, we can observe three vastly different results predicted from the three definitions for $\hat{\rho}^{el}$: Using the electronic wave function (WF) definition (see Eq. (5.62)), the RMSD continues to grow almost square-root like and seems to deviate from the DMRG curve, which, for the times available, flattens off faster. The active surface (AS) definition (see Eq. (5.61)) starts from a completely wrong value. Since the bare local initial state starts with all nuclear harmonic oscillators in their ground state, the adiabatic states of many trajectories are far spread throughout the system and the local electron will have significant contributions in most of them. This also visualizes again why we do not project the initial wave function amplitudes onto the selected active adiabatic surface: In this case the three definitions of the

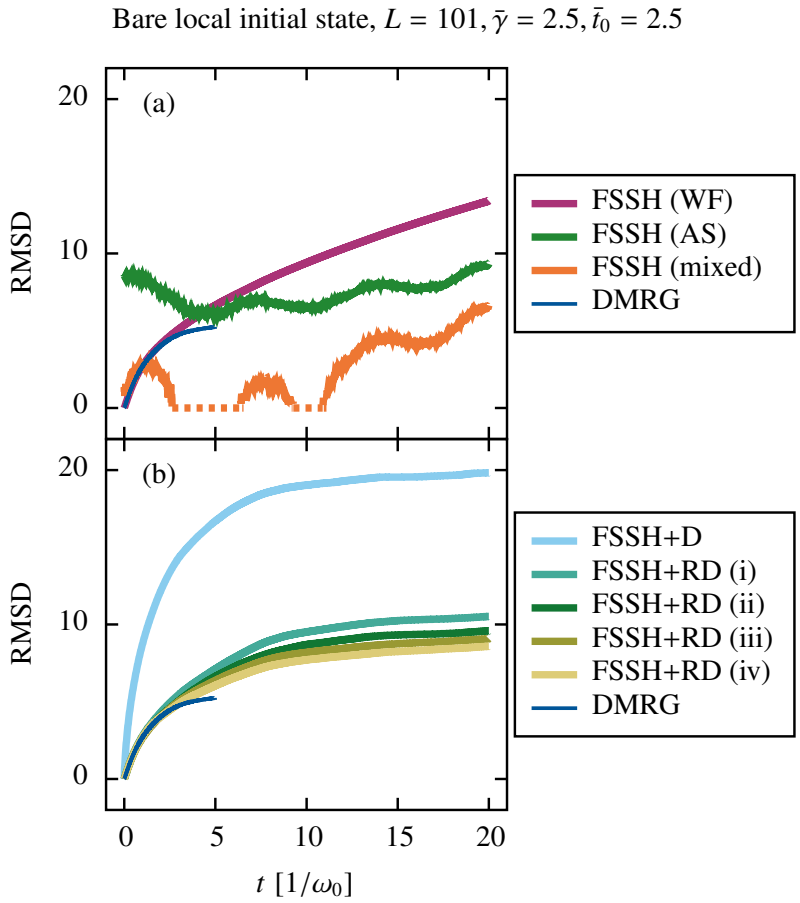

Figure 6.12: Time evolution of the reduced mean-squared displacement obtained in the Holstein chain with $L = 101$ and $\bar{\gamma} = \bar{t}_0 = 2.5$ for the bare local initial state on the central site. (a) The RMSD calculated with different definitions of the electronic density matrix in FSSH, $\hat{\rho}^{\mathrm{WF}}$, $\hat{\rho}^{\mathrm{AS}}$ and $\hat{\rho}^{\mathrm{mixed}}$ (see Eqs. (5.62), (5.61) and (5.63))) are compared to results obtained with DMRG. The dashed part of the *FSSH (mixed)*-line reveals a negative MSD. (b) FSSH with decoherence correction (FSSH+D) is compared to DMRG and various types of FSSH with restricted decoherence (FSSH+RD, see Sec. 5.3.5): (i) direct application of the decoherence correction (DC) with an active space threshold of $R = 0.999$, (ii) delayed application of the DC with $R = 0.999$, (iii) direct application of the DC with $R = 0.99$, and (iv) delayed application of the DC with $R = 0.99$. The independent-trajectory methods use the same method parameters as in Fig. 6.9. The DMRG simulations are performed with $\epsilon_{\mathrm{LBO}} = 10^{-9}$, $\epsilon_{\mathrm{bond}} = 10^{-9}$, $\Delta t = 0.004/\omega_0$ and $M = 40$. Reproduced from Ref. [37], with the permission of AIP Publishing.

density matrix (Eqs. (5.61), (5.62) and (5.63)) would be equal initially, but all lead to the wrong initial RMSD. For longer times, the (AS)-definition seems to level off more than the (WF)-definition. With the active surfaces approximately obeying detailed balance, we normally expect the long-time results according to the (AS)-definition to be more accurate, which we cannot check with the short-time DMRG results available here. The mixed definition of the density matrix (see Eq. (5.63)), which normally combines the strengths of the other two definitions and interpolates between the two, completely fails in the prediction of this very sensitive quantity. The MSD even becomes negative for some times, indicated by dashed lines in Fig. 6.12(a). From the results presented here, it seems that all three definitions of the electronic density matrix in FSSH are unable to provide reliable results for the RMSD in such large systems.

The ambiguity between the definitions is reduced (with their differences damped over time), when using a decoherence correction. Since the wave function amplitudes relax toward the active surfaces, we can stay with the (WF)-definition when using a decoherence correction, which will approach the (AS)-definition for later times. This is shown in Fig. 6.12(b). We see immediately that the FSSH+D results for the RMSD indeed level off to an almost constant value for late times, but show an unphysical super-fast spreading at short times. The problem lies again in the initial state, which, as mentioned previously, is in a superposition of many delocalized adiabatic states in most trajectories. With the decoherence correction removing the coherences between the adiabatic states, the electron density spreads artificially through the system, with the velocity given by the decoherence rate and not by the electron hopping. This is the reason why we have to apply the restrictions to the decoherence correction (FSSH+RD), mentioned in Sec. 5.3.5, designed to prevent such a "spurious charge transport" in large systems. We note that the restrictions were suggested for dealing with surface hops between spatially distant adiabatic states, but work just as well for the initial states with coherences studied here.

In Fig. 6.12(b) four variants of the decoherence-restriction are shown, with two different values for the active space threshold R combined both with and without the quarter-phonon oscillation period delay in the decoherence correction (see Sec. 5.3.5). In most observables the variant (iv) for the FSSH+RD results, using a value of $R = 0.99$ with the delayed decoherence correction, was the closest to the available DMRG results, which is therefore used in all following results in the Holstein chain.

We note that using normal FSSH one can still obtain reasonable results for most observables computed in the following. Despite its failure in describing the RMSD, we use the mixed definition of the electronic density matrix $\hat{\rho}^{\mathrm{mixed}}$ when computing diabatic electronic properties in FSSH, which for most other observables is sufficient. When using the restricted decoherence correction, we will instead use the wave function definition $\hat{\rho}^{\mathrm{WF}}$ for calculating diabatic electronic properties (like electron densities on the various Holstein sites) and the usual active surface distribution to determine the population on the Born-Oppenheimer states.

6.3.2 Bare local initial state

We now start with the bare local initial state on the central site in the Holstein chain, which we investigate for $L = 11$ and $L = 51$ for the same parameters as in the Holstein trimer: $\bar{\gamma} = \bar{t}_0 = 2.5$. We compare the independent-trajectory methods MTE, FSSH and FSSH+RD with the coupled-trajectory methods MCE and the (for our purposes) numerically exact DMRG results. The results and analysis are equivalent to the corresponding article, see Ref. [37], although in this thesis with a slightly higher focus on the independent-trajectory methods.

The first observable which allows to discern the spreading behavior of the local initial state in the studied methods is the electron density $\langle \hat{n}_i \rangle$ on the different sites i. The results for all methods, both for $L = 11$ and $L = 51$, are shown in Fig. 6.13. All methods show a ballistic (linear) spreading of the electron density for short times ($t < 2/\omega_0$), which reflects off the chain boundaries in the $L = 11$ system. The DMRG simulation reached a time of only about one nuclear oscillation period. In the $L = 11$ system, the electron densities of MCE, FSSH and FSSH+RD retain a large contribution close to the initially occupied site, which fits to the DMRG results for the times available. In contrast, the electron density obtained with MTE is much more delocalized throughout the system. In the $L = 51$ system, the DMRG results show that the whole electron density stays rather localized in the central region of the Holstein chain after the initial ballistic expansion. This is qualitatively reproduced with FSSH and FSSH+RD, and we mention that the small erroneous electron densities at the chain boundaries in FSSH caused by the mixed definition of the electron density are barely visible in this color-plot (they are in the range of a few $\pm 10^{-4}$). In MCE, the electron densities close to the central site seem to be close to the DMRG results, but a fraction of the density escapes toward the chain boundaries, with a (difficult to see) periodic modulation concomitant with the nuclear oscillation. MTE shows a large spreading of the electron density, which clearly deviates from the DMRG results.

A better quantitative analysis can be carried out with the RMSD, shown in Fig. 6.14. For $L = 11$, we indeed observe a good agreement of all methods except MTE. Also the results for FSSH, obtained with the mixed definition of the density matrix, are still reasonable and close to the results of FSSH+RD (obtained with the wave-function definition of the density matrix). For $L = 51$, the FSSH results are left out, since no definition of the density matrix can reproduce the RMSD, see Fig. 6.12. With the DMRG results obtained only for short times, it is difficult to judge the long-time performance of the other methods, which all show a qualitatively different time evolution. FSSH+RD converges to an almost constant value after the initial expansion, MTE continues with an almost diffusive spreading at late times, with a linear fit of the log-log curve in the times $t\omega_0 \in [1, 20]$ revealing a slope of approximately 0.48, and MCE shows a second large increase of the RMSD, not seen in any other method, and the method is clearly not converged (see also Ref. [37], where the convergence behavior of MCE in the Holstein chain is analyzed in more detail). As before with FSSH, most of the electron density seems to be well described with MCE, but the part of the density that escapes the trapping in the chain

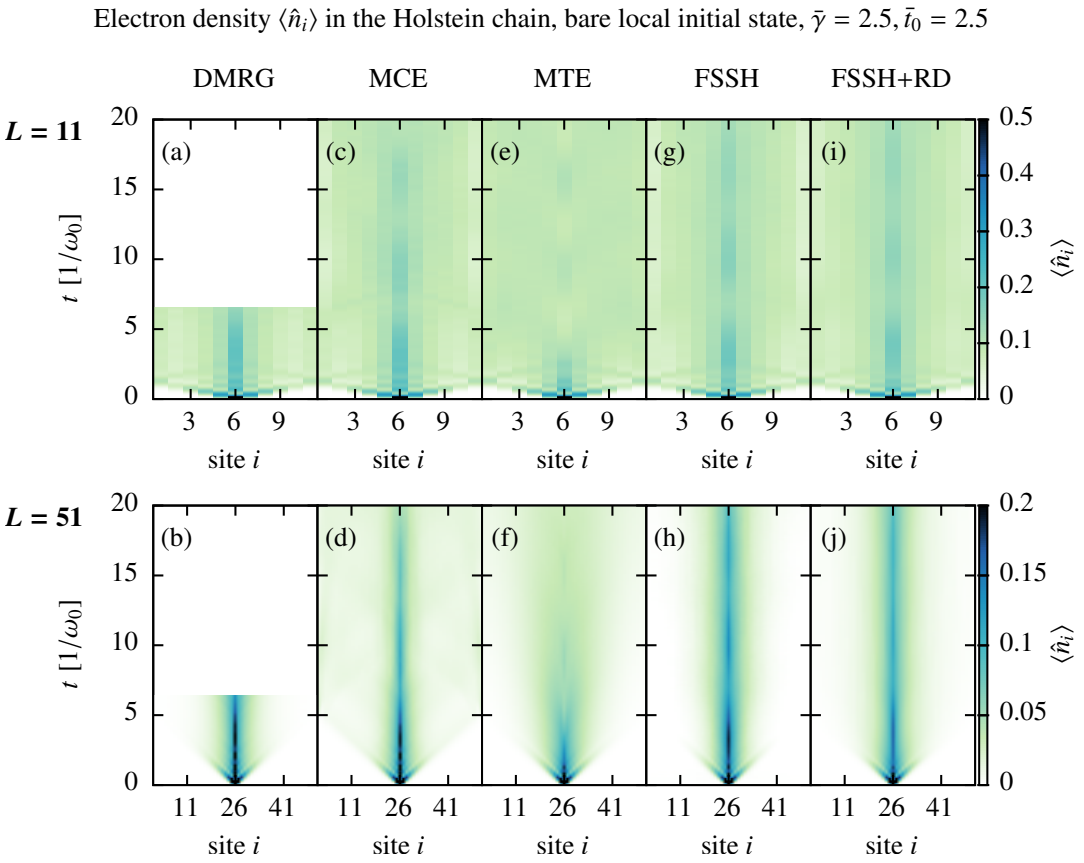

Figure 6.13: Time evolution of the electron densities $\langle \hat{n}_i \rangle$ in the Holstein chain of lengths $L = 11$ and $L = 51$, with $\bar{\gamma} = \bar{t}_0 = 2.5$ and starting from the bare local initial state at the central site. Results are shown for the methods (a) and (b) DMRG, (c) and (d) MCE, (e) and (f) MTE, (g) and (h) FSSH and (i) and (j) FSSH+RD, each both for $L = 11$ and $L = 51$. The independent-trajectory methods use the same method parameters as in Fig. 6.9: $N_{traj} = 20\,000$ and $\Delta t = 0.001/\omega_0$. The DMRG simulations are performed with $\epsilon_{\text{LBO}} = 10^{-8}$, $\epsilon_{\text{bond}} = 10^{-8}$, $\Delta t = 0.004/\omega_0$ and $M = 40$. MCE uses 5000 configurations, initialized with the pancake-like variant for sampling the initial state (see Ref. [37] for details). Reproduced from Ref. [37], with the permission of AIP Publishing, the figure layout has been adapted to the format of this thesis.

center and moves toward the boundaries dominates the RMSD expression. A longer time-evolution of the DMRG results is necessary to conclusively judge the other methods in a future study, but for the times available, the FSSH+RD method is the closest to DMRG.

The different behavior of at least MTE and the FSSH methods can be best understood if we investigate the populations of the Born-Oppenheimer states. This observable was computed neither with MCE nor DMRG, but it is still instructive to look at. The populations are shown in Fig. 6.15. All methods show very similar values for $t = 0$, with the distribution of active surfaces in the surface hopping methods being very close to the electronic populations of

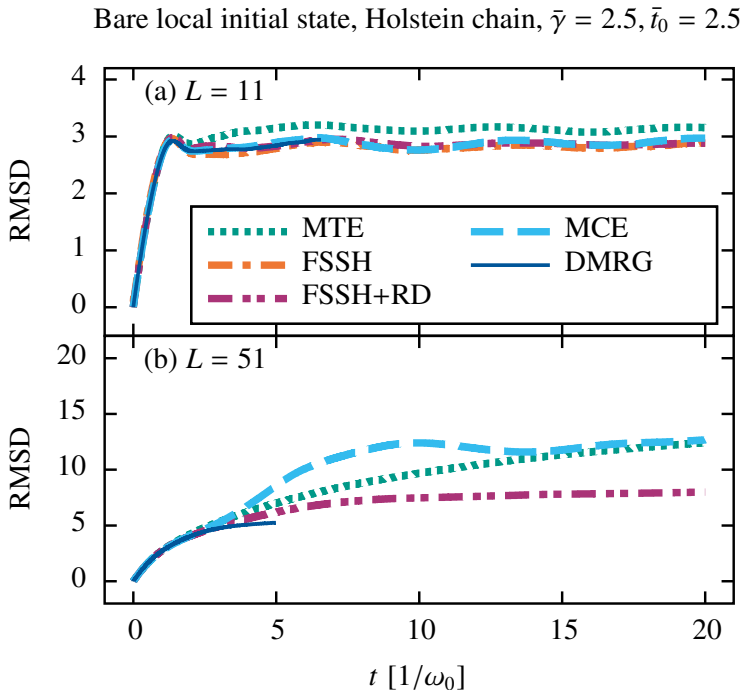

Figure 6.14: Time evolution of the reduced mean-squared displacement (RMSD), obtained in the Holstein chain with $\bar{\gamma} = \bar{t}_0 = 2.5$ and (a) $L = 11$ and (b) $L = 51$ for the bare local initial state at the central site. Results are shown for the methods MTE (dotted green line), FSSH and FSSH+RD (dashed-dotted orange and magenta lines), MCE (dashed light blue line) and DMRG (solid blue line). For $L = 51$, the results of FSSH are ambiguous and omitted, see the discussion in Sec. 6.3.1. The methods use the same method parameters as in Fig. 6.13, with the exception of DMRG, where the cutoffs are decreased to $\epsilon_{\text{LBO}} = 10^{-9}$ and $\epsilon_{\text{bond}} = 10^{-9}$ for $L = 51$. Reproduced from Ref. [37], with the permission of AIP Publishing.

MTE for the 20 000 trajectories used. As mentioned before, the bare local state has significant contributions in every adiabatic state, with the $L = 11$ system showing a slight alternation between even and odd states, and the $L = 51$ system having a population of close to 0.02 on every state.

The time evolution of the Born-Oppenheimer populations is, however, very different in these methods. A weak relaxation toward the lowest state is seen in MTE, with its population at time $t = 20/\omega_0$ increasing to $\langle \hat{n}_a^{BO} \rangle \approx 0.21$ for $L = 11$ and to $\langle \hat{n}_a^{BO} \rangle \approx 0.04$ for $L = 51$. Most of the electronic weight is still distributed among all of the adiabatic states. In contrast, the surface hopping methods show a strong relaxation toward the lowest state, whose population (determined from the active surface distributions) at time $t = 20/\omega_0$ increases to 0.86 and 0.83 for FSSH and FSSH+RD in the $L = 11$ system, and to 0.80 and 0.81 for $L = 51$. A weak modulation with the nuclear oscillation period is also visible. Hence, the long-time dynamics of both surface hopping methods are strongly dominated by the lowest Born-Oppenheimer state, while the dynamics of MTE are still influenced by most Born-Oppenheimer states,

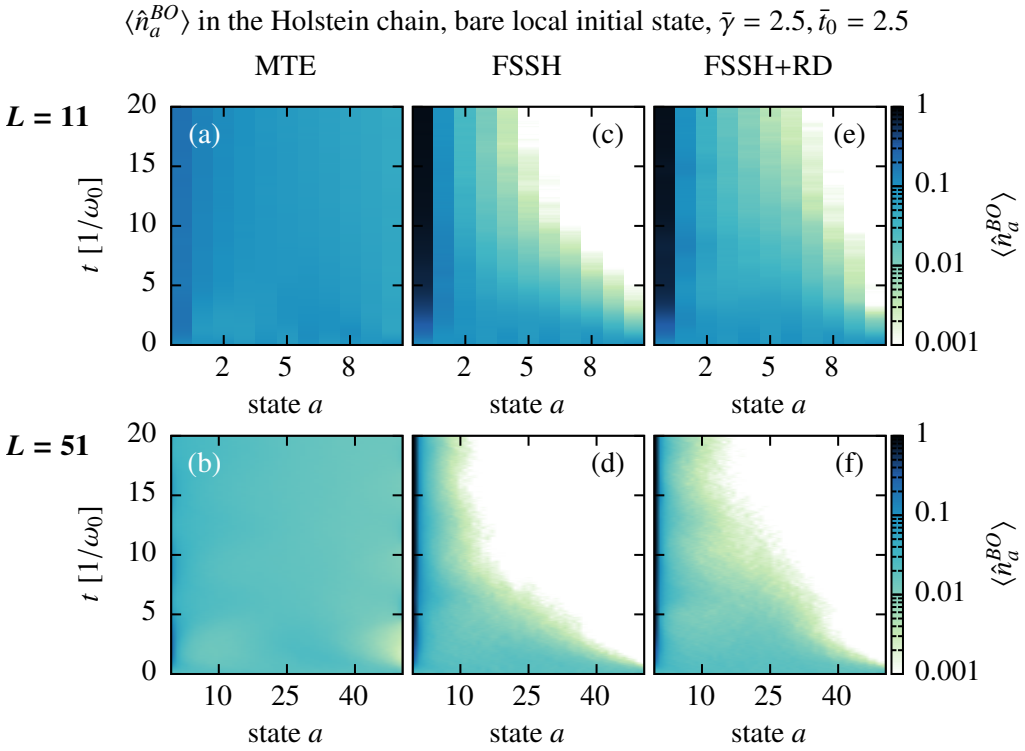

Figure 6.15: Time evolution of the Born-Oppenheimer states populations $\langle \hat{n}_a^{BO} \rangle$ in the Holstein chain of lengths $L = 11$ and $L = 51$, with $\bar{\gamma} = \bar{t}_0 = 2.5$, and starting from the bare local initial state at the central site. Results are shown for the methods (a) and (b) MTE, (c) and (d) FSSH, and (e) and (f) FSSH+RD, each both for $L = 11$ and $L = 51$. The methods use the same method parameters as in Fig. 6.13.

even at late times. Similar as in the Holstein dimer and trimer, the lowest Born-Oppenheimer state for each nuclear configuration places the electrons where their energy is lowest, which is typically a bonding state with the electron localized at sites with a large nuclear displacement. The relaxation of the surface hopping methods toward this lowest state thus indicates the formation of electron-nuclear bound states and the saturation of the RMSD shown in Fig. 6.14 might be attributed to a polaronic trapping of the electron density. With the electron in MTE having persistently large populations in all the high-excited Born-Oppenheimer states, the formation of such bound states is strongly suppressed, which might be the reason why the electron density shows the diffusive behavior in the RMSD.

Another indicator for the polaronic trapping of the electron density would be the build-up of large nuclear distortions on the occupied sites. We show the total number of phonons in the system, given by $N_{ph} = \sum_i \langle \hat{b}_i^\dagger \hat{b}_i \rangle$, for all studied methods in Fig. 6.16. The total phonon number determines the energy stored in the phonon subsystem, as it corresponds (up to the additive zero-point energies) to the harmonic oscillator terms of the Holstein-chain energy expression (see Eq. (5.1)). With this system starting with all oscillators in their ground state, it is thus an indicator for the energy transfer from the electron to

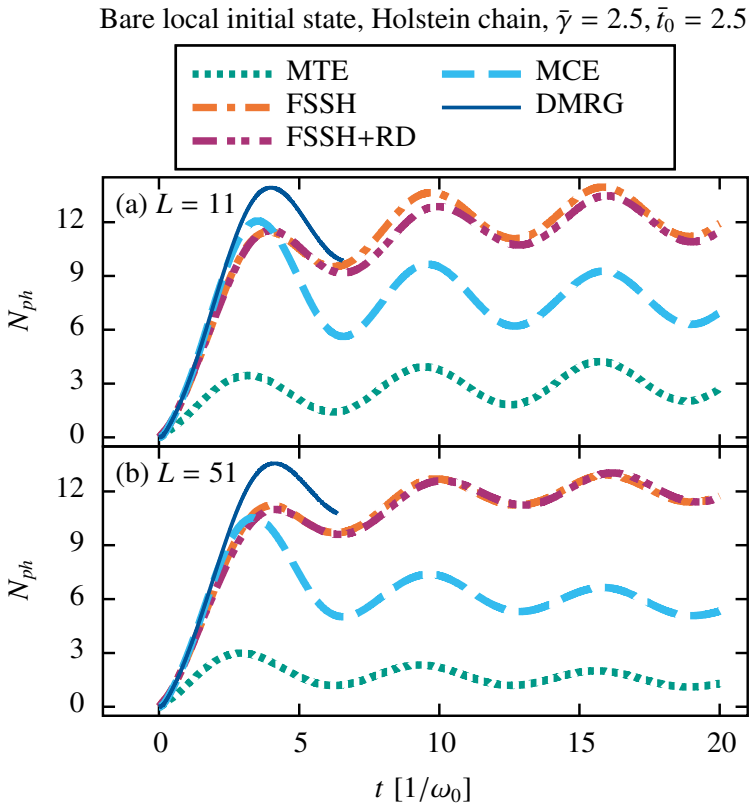

Figure 6.16: Time evolution of the total phonon number $N_{ph} = \langle \sum_i \hat{b}_i^\dagger \hat{b}_i \rangle$, obtained in the Holstein chain with $\bar{\gamma} = \bar{t}_0 = 2.5$ and (a) $L = 11$ and (b) $L = 51$ for the bare local initial state at the central site. Results are shown for the methods MTE (dotted green line), FSSH and FSSH+RD (dashed-dotted orange and magenta lines), MCE (dashed light blue line) and DMRG (solid blue line). All methods use the same method parameters as in Fig. 6.13. Reproduced from Ref. [37], with the permission of AIP Publishing.

the phonon subsystem. The curves for $L = 11$ and $L = 51$ are very similar, as the total energy in both systems is equivalent if one discards the zero-point energies. In both system sizes we observe a qualitatively different behavior in MTE and the surface hopping methods, with the total phonon number in MTE staying at very low values throughout the entire time evolution, while the surface hopping methods stay at high phonon numbers after an initial rapid build-up phase. This fits to the populations on the Born-Oppenheimer surfaces depicted in Fig. 6.15 and the presence and absence of polaronic trapping in FSSH/FSSH+RD and MTE, respectively. Both MCE and DMRG also show the creation of a large phonon number in the first nuclear oscillation period, with no other method reaching values as high as DMRG. For later times the total phonon number of MCE returns to a value between the surface hopping and MTE results. Unfortunately, the DMRG results are still only available for roughly one nuclear oscillation period, and we cannot unambiguously deduce the correct long-time behavior. The curve for $L = 11$ seems to suggest that the N_{ph} will stay at higher values, close to FSSH/FSSH+RD, but further studies

are needed in the future for an accurate evaluation.

The convergence of MCE in these large systems is much better for local observables close to the initially occupied site, see also Ref. [37], and also the electron densities close to the center of the chain in Fig. 6.13 are closer to the DMRG results, even for $L = 51$. We investigate this further by considering the nuclear displacement on the central site $\langle \hat{x}_{central} \rangle$ for $L = 51$ in Fig. 6.17.

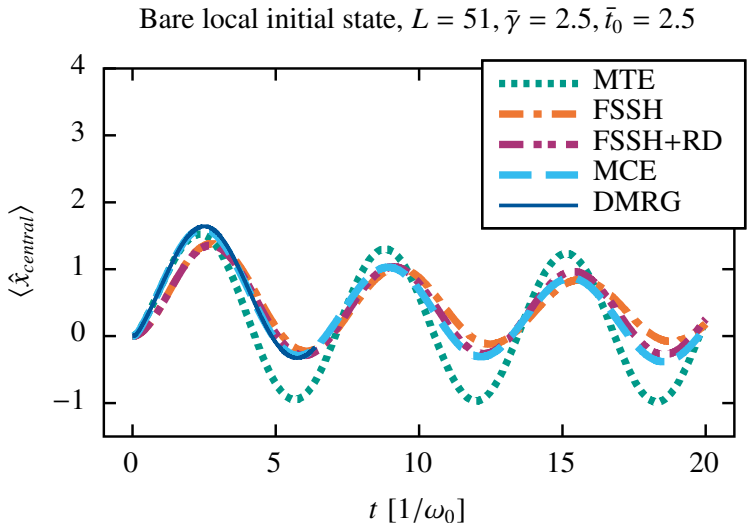

Figure 6.17: Time evolution of the nuclear position on the central site $\langle \hat{x}_{central} \rangle$, obtained in the Holstein chain with $L = 51$ and $\bar{\gamma} = \bar{t}_0 = 2.5$ for the bare local initial state at the central site. Results are shown for the methods MTE (dotted green line), FSSH and FSSH+RD (dashed-dotted orange and magenta lines), MCE (dashed light blue line) and DMRG (solid blue line). All methods use the same method parameters as in Fig. 6.13. Reproduced from Ref. [37], with the permission of AIP Publishing.

Here, the agreement of MCE and DMRG (for the times available) is nearly perfect, suggesting also a better performance of MCE at later times. We see that MTE reproduces at least the first half nuclear oscillation in this observable, but starts to oscillate around too low values later, indicative of the loss of electron density on the central site observed in the other observables. The surface hopping methods show again the surprising behavior that although the first half nuclear oscillation is not reproduced perfectly, the later results agree closely with the DMRG and MCE results (see also the example in the dimer discussing how FSSH calculates the wrong nuclear forces for an initial state with coherences, Sec. 6.1.3).

6.3.3 Dressed local initial state

We now turn to the dressed local initial state, which already starts with large nuclear distortions on the central site in the beginning and a large contribution on the lowest Born-Oppenheimer state. It is interesting to see how the performance of the methods, especially MTE, FSSH and FSSH+RD, changes for

this new initial state. We use the same parameters as before and show results for $L = 11$ and $L = 51$. We start with the electron densities on the different Holstein sites presented in Fig. 6.18.

All methods show a stronger localization around the central site compared to the bare local case and the DMRG results are, at least for some observables, available for longer times. During this time, for $L = 11$, there is almost no discernible difference between DMRG, MCE, FSSH and FSSH+RD. Only at late times the electron density of MCE delocalizes slightly, in contrast to the surface hopping methods, and no DMRG results are obtained that could decide the correct physical behavior. MTE, similar as in the bare local case, loses the large electron density on the central site already after about half a nuclear oscillation period, although here we observe a partial recurrence of that density at later times. For $L = 51$, the spreading of the electron density in all methods is similar to the bare local case, although on a smaller scale and we switched to a logarithmic scale for the electron density. All methods show again a ballistic spreading for very short times. Afterward, the DMRG and FSSH+RD electron densities stay with an almost constant and similar width. FSSH predicts a too small spreading for short times and extends to the DMRG/FSSH+RD width for later times. MCE is very close to DMRG around the center of the chain, but shows again the continued ballistic spreading for a portion of the electron density. Finally, MTE shows a strong delocalization of the electron density throughout the system, with only a small part of the density staying close to the central site.

For a quantitative analysis we switch again to the RMSD, presented in Fig. 6.19. For $L = 11$, in this observable, the difference of the independent-trajectory methods to DMRG is larger than before in the bare local case, with all methods deviating slightly after $t \approx 1/\omega_0$ already. For later times, the RMSD of MTE increases much higher than in any other method, while the FSSH and FSSH+RD results stay close to the DMRG values. The MCE results show an excellent agreement with DMRG. For $L = 51$, MTE shows a superdiffusive behavior with the linear fit of the log-log data in the time $t\omega_0 \in [1, 20]$ having a slope of approximately 0.61. MCE follows a similar curve for some time, but flattens off to a mostly constant value after about one nuclear oscillation period. The RMSD of FSSH+RD also shows a slight increment over time, but stays closest to the DMRG results while they are available. Unfortunately, smaller cutoffs in DMRG were needed to obtain converged results for this observable and thus we cannot verify the long-time agreement.

Switching from an electronic to a phonon global observable, we now turn to the total phonon number in Fig. 6.20. As before in the bare local case, this observable is very similar for both system sizes. The total phonon number in MTE rapidly decreases to a low value during the first oscillation period, while all other methods predict a total phonon number staying close to the initial value. Both the surface hopping methods and MCE show a qualitative agreement with the DMRG results, although the curves are not overlapping after half an oscillation period. It is difficult to judge which of these methods is the closest to DMRG. However, the high values predicted by DMRG, MCE, FSSH and FSSH+RD are compatible with the rather localized electron density

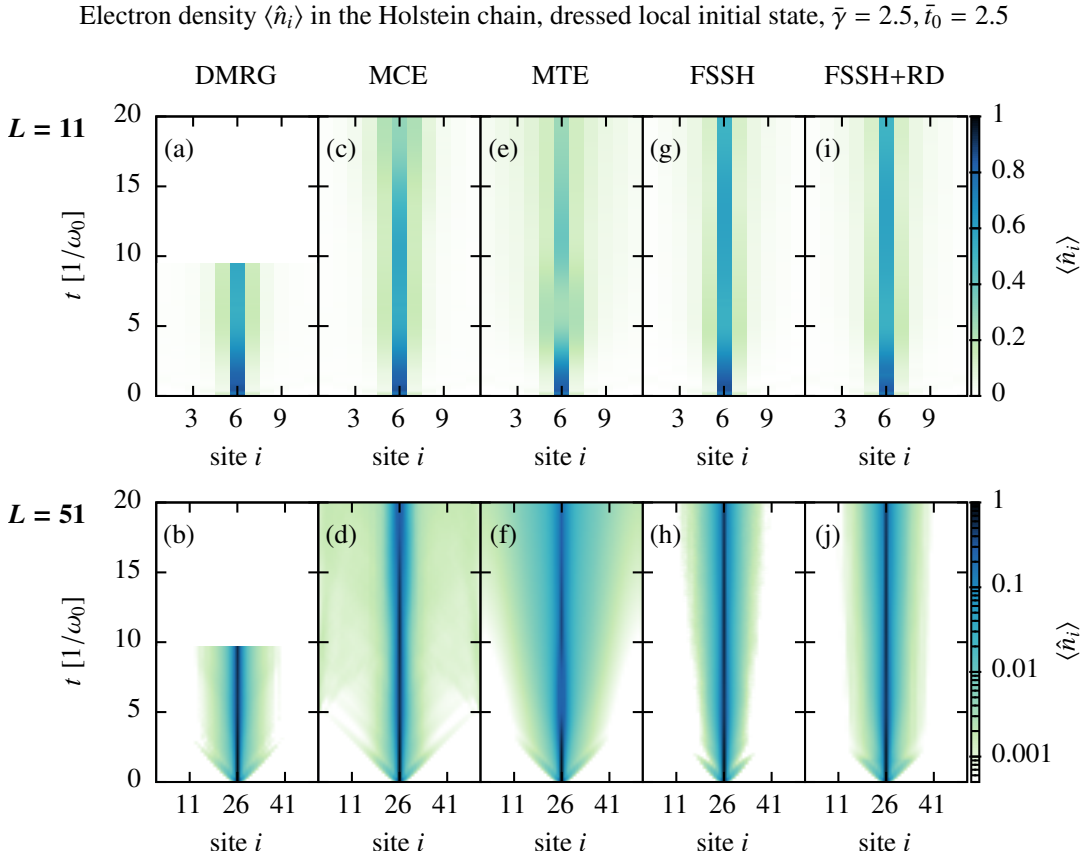

Figure 6.18: Time evolution of the electron densities $\langle \hat{n}_i \rangle$ in the Holstein chain of lengths $L = 11$ and $L = 51$, with $\bar{\gamma} = \bar{t}_0 = 2.5$, and starting from the dressed local initial state at the central site. Results are shown for the methods (a) and (b) DMRG, (c) and (d) MCE, (e) and (f) MTE, (g) and (h) FSSH and (i) and (j) FSSH+RD, each both for $L = 11$ and $L = 51$. The independent-trajectory methods use as parameters $N_{traj} = 50\,000$ and $\Delta t = 0.001/\omega_0$. The DMRG simulations are performed with $\epsilon_{\text{LBO}} = 10^{-8}$, $\epsilon_{\text{bond}} = 10^{-8}$, $\Delta t = 0.004/\omega_0$ and $M = 40$. MCE uses 5000 configurations, initialized with the pancake-like variant for sampling the initial state (see Ref. [37] for details). Reproduced from Ref. [37], with the permission of AIP Publishing, the figure layout has been adapted to the format of this thesis.

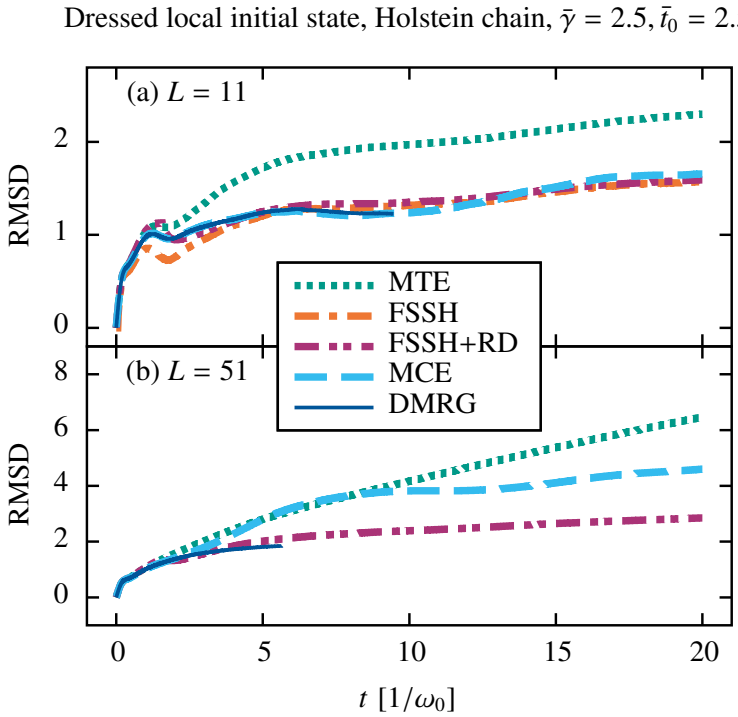

Figure 6.19: Time evolution of the reduced mean-squared displacement (RMSD), obtained in the Holstein chain with $\bar{\gamma} = \bar{t}_0 = 2.5$ and (a) $L = 11$ and (b) $L = 51$ for the dressed local initial state at the central site. Results are shown for the methods MTE (dotted green line), FSSH and FSSH+RD (dashed-dotted orange and magenta lines), MCE (dashed light blue line) and DMRG (solid blue line). For $L = 51$, the results of FSSH are ambiguous and omitted, see the discussion in Sec. 6.3.1. The methods use the same method parameters as in Fig. 6.18, with the exception of DMRG, where the cutoffs are decreased to $\epsilon_{\text{LBO}} = 10^{-9}$ and $\epsilon_{\text{bond}} = 10^{-9}$ for $L = 51$. Reproduced from Ref. [37], with the permission of AIP Publishing.

obtained by these methods in Fig. 6.18 (note the logarithmic scale for $L = 51$ which might hide that most of the electron density in MCE stays close to the center).

The very different behavior of MTE compared to the surface hopping methods can again be understood by considering the populations on the Born-Oppenheimer states, shown in Fig. 6.21. All start again at very similar populations, with the 50 000 trajectories giving an even closer agreement of the active surface distributions of FSSH/FSSH+RD and the adiabatic electronic amplitudes of MTE. The population of the lowest Born-Oppenheimer state $\langle \hat{n}_0^{BO} \rangle$ in all methods starts at 0.91 and 0.90 in the $L = 11$ and $L = 51$ system, respectively. The remaining population distributed among the higher Born-Oppenheimer states quickly decays in the surface hopping methods, similar as in the bare local case. In contrast, the electronic population in MTE transitions to the higher states and the system thus partly looses the electron-nuclear bound state. This was already observed in the dressed local initial state in the

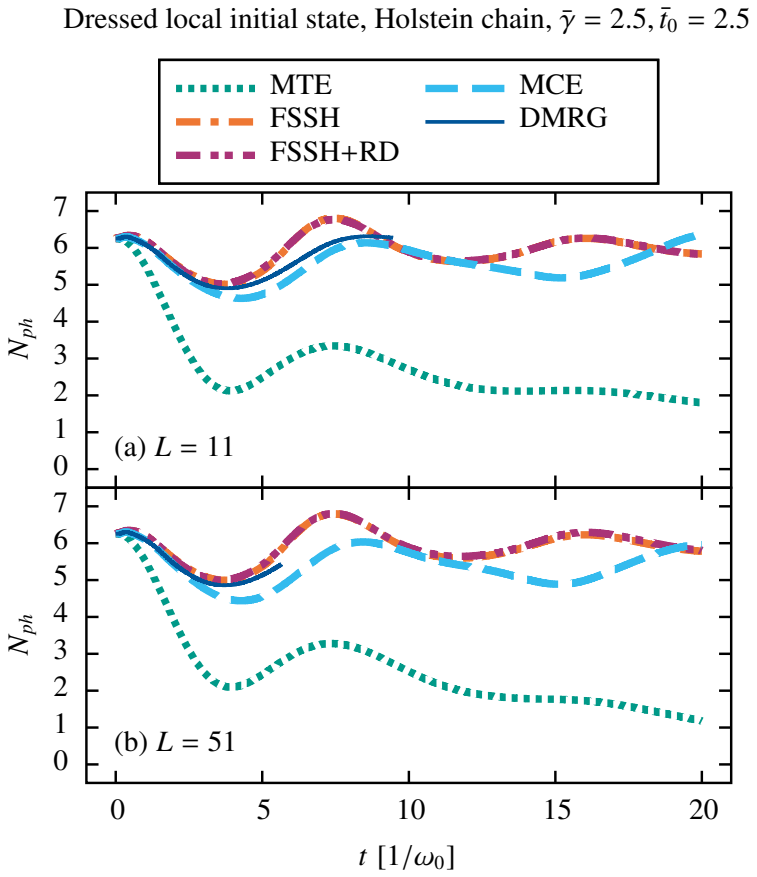

Figure 6.20: Time evolution of the total phonon number $N_{ph} = \langle \sum_i \hat{b}_i^\dagger \hat{b}_i \rangle$, obtained in the Holstein chain with $\bar{\gamma} = \bar{t}_0 = 2.5$ and (a) $L = 11$ and (b) $L = 51$ for the dressed local initial state at the central site. Results are shown for the methods MTE (dotted green line), FSSH and FSSH+RD (dashed-dotted orange and magenta lines), MCE (dashed light blue line) and DMRG (solid blue line). The methods use the same method parameters as in Fig. 6.18, with the exception of DMRG, where the cutoffs are decreased to $\epsilon_{\text{LBO}} = 10^{-9}$ and $\epsilon_{\text{bond}} = 10^{-9}$ for $L = 51$. Reproduced from Ref. [37], with the permission of AIP Publishing.

Holstein trimer, where the electron density on the (initially occupied) central site decayed too much compared to the other methods and the dynamics were influenced too much by the higher Born-Oppenheimer surfaces.

Qualitatively independent of the bare or dressed local initial state, the electron in the surface hopping methods tends to relax toward the lowest Born-Oppenheimer state, while the electron in MTE tends toward a population of a broad spectrum of adiabatic states. In the other studied observables, the dynamics of the surface hopping methods, in particular FSSH+RD, was always closer to the DMRG results compared to MTE. The short time duration for which these results could be obtained, does not allow a definitive statement about the performance of the methods for longer times. Hence, we now turn to another parameter set that allows for a longer time evolution in the DMRG method.

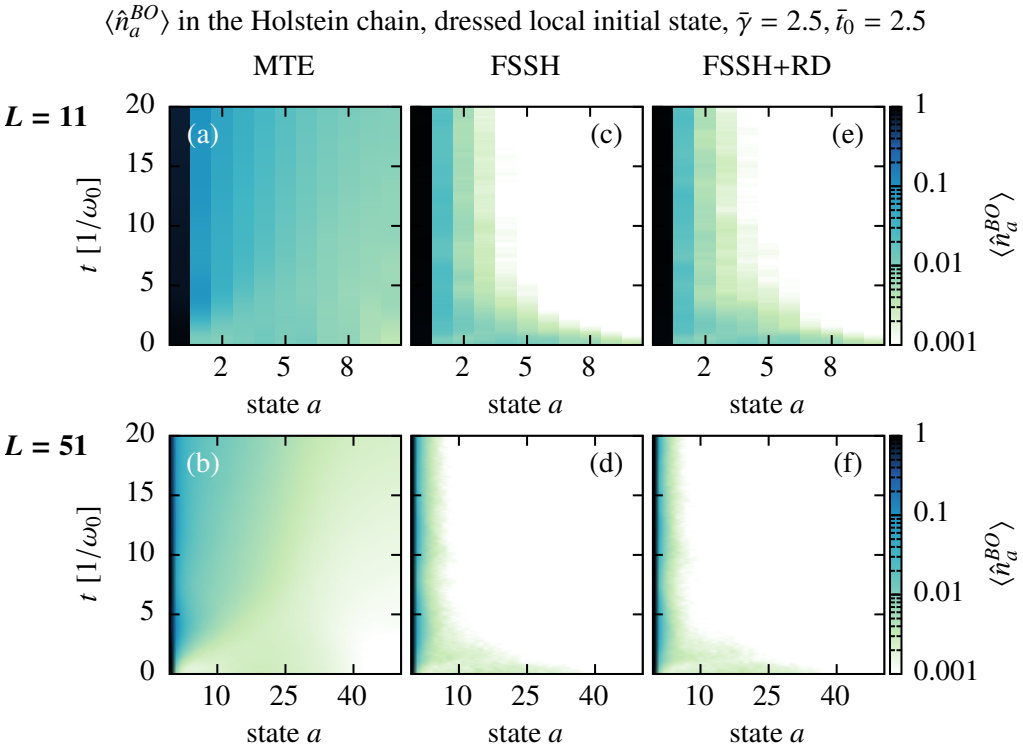

Figure 6.21: Time evolution of the Born-Oppenheimer states populations $\langle \hat{n}_a^{BO} \rangle$ in the Holstein chain of lengths $L = 11$ and $L = 51$, with $\bar{\gamma} = \bar{t}_0 = 2.5$, and starting from the dressed local initial state at the central site. Results are shown for the methods (a) and (b) MTE, (c) and (d) FSSH, and (e) and (f) FSSH+RD, each both for $L = 11$ and $L = 51$. The methods use the same method parameters as in Fig. 6.18.

6.3.4 Reduced electron hopping

As a final system we study the bare local initial state in the Holstein chain with a reduced electron hopping of $\bar{t}_0 = 1$ and with $L = 25$, which was also studied in Ref. [54]. The DMRG results could provide converged results for much longer times in this system and the calculated RMSD coincides with the values presented in Ref. [54], see Ref. [37]. Such a small electron hopping might be physically less interesting if we have an application to the manganite tight-binding model (see Ch. 3) in mind, but it is helpful to check the agreement of especially FSSH+RD and DMRG, which in the previous Holstein chain results were often close, but could only be analyzed for 1-2 nuclear oscillation periods. In addition, the RMSD of the bare local state for $\bar{t}_0 = 1$ computed in Ref. [54] showed a periodic increment with the nuclear oscillation period, similar to the transient trapping that we observed for a small electron hopping in the Holstein dimer (see Sec. 6.1.4). This leads to a more complicated form of the RMSD compared to the results at larger $\bar{t}_0$ shown before, where the RMSD leveled off to a constant value in DMRG for the times available (although we cannot exclude an increase of the RMSD happening at later times). The RMSD computed with MTE, FSSH+RD, MCE and DMRG is shown for two different values of the electron-phonon coupling $\bar{\gamma} = 4$ and $\bar{\gamma} = 2.5$ in Figs. 6.22 and 6.23. The

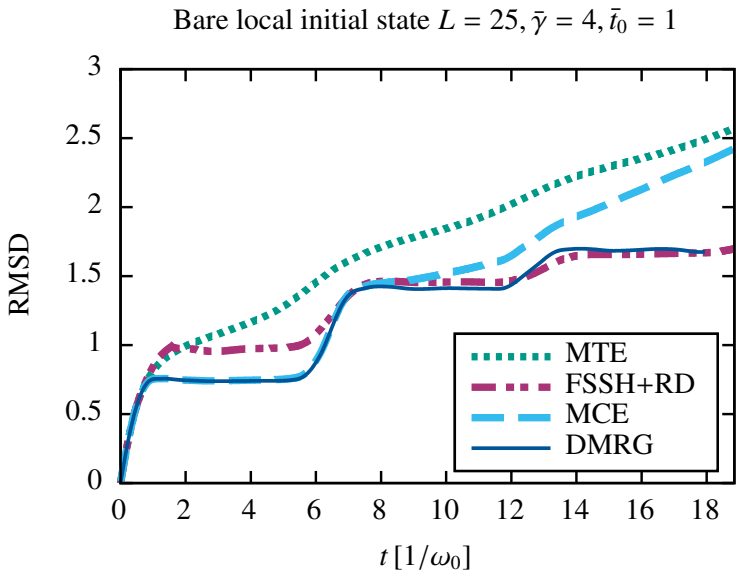

Figure 6.22: Time evolution of the reduced mean-squared displacement (RMSD), obtained in the Holstein chain with $L = 25$, $\bar{\gamma} = 4$ and $\bar{t}_0 = 1$ for the bare local initial state at the central site. Results are shown for the methods MTE (dotted green line), FSSH+RD (dashed-dotted magenta line), MCE (dashed light blue line) and DMRG (solid blue line). The independent-trajectory methods use the same method parameters as in Fig. 6.18. The DMRG simulation is performed with $\epsilon_{\mathrm{LBO}} = 10^{-8}$, $\epsilon_{\mathrm{bond}} = 10^{-8}$, $\Delta t = 0.01/\omega_0$ and $M = 90$. MCE uses 4500 configurations, initialized with the pancake-like variant for sampling the initial state (see Ref. [37] for details). The DMRG data agree with the results published in Ref. [54], see Ref. [37]. Reproduced from Ref. [37], with the permission of AIP Publishing, the data of Ref. [54] are omitted here.

DMRG data presented here agree with the results published in Ref. [54], see Ref. [37].

We see that DMRG reproduces the step-like increment of the RMSD after each nuclear oscillation period found in Ref. [54]. Starting with the $\bar{\gamma} = 4$ case (Fig. 6.22), the MCE data perfectly reproduce the height of the first plateau and the time and shape of the second increment of the RMSD. Afterward, the curve starts to deviate from the DMRG results and looses its step-like form. It then becomes closer to the MTE curve, which does not reproduce the plateaus at all and instead steeply rises with the nuclear oscillation period visible as a weak periodic modulation. The FSSH+RD method shows a step-like structure for the RMSD, but severely overestimates the height of the first plateau. Interestingly, it comes very close to the DMRG results for later times, as was observed before in some observables (see, e.g., Fig. 6.17), when the influence of the initial coherences weakens. All these observations also carry over to the $\bar{\gamma} = 2.5$ case, although the agreement of FSSH+RD and DMRG is slightly worse at later times.

The results for both of these systems are reassuring in the interpretation of the performance of FSSH+RD. In general, the surface hopping method is

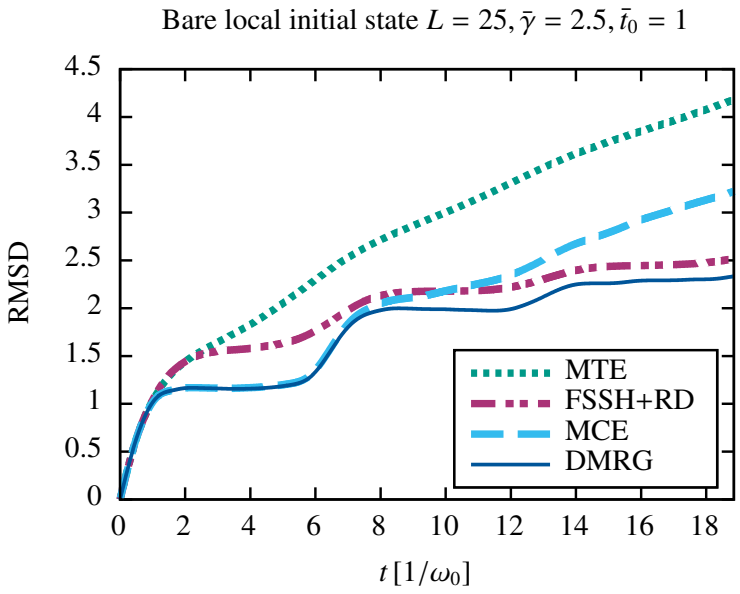

Figure 6.23: Time evolution of the reduced mean-squared displacement (RMSD), obtained in the Holstein chain with $L = 25$, $\bar{\gamma} = 2.5$ and $\bar{t}_0 = 1$ for the bare local initial state at the central site. Results are shown for the methods MTE (dotted green line), FSSH+RD (dashed-dotted magenta line), MCE (dashed light blue line) and DMRG (solid blue line). The methods use the same method parameters as in Fig. 6.22, with the exception of the number of local phonon states used in DMRG, which is reduced to $M = 35$. The DMRG data agree with the results published in Ref. [54], see Ref. [37]. Reproduced from Ref. [37], with the permission of AIP Publishing, the data of Ref. [54] are omitted here.

expected to work better for large values of $\bar{t}_0$ (the adiabatic regime, this is also clearly seen in our analysis of the Holstein dimer, see Sec. 6.1). The long-time agreement of a sensitive diabatic observable, such as the RMSD, for such a small value of $\bar{t}_0$ might imply that the qualitative agreement with DMRG observed in most observables for the previous parameter set of $\bar{\gamma} = \bar{t}_0 = 2.5$ could also hold in the long-time regime. However, this is only a speculation at this point and long-time numerically exact results for larger $\bar{t}_0$ are needed to confirm any statements.

Finally, we show the populations of the Born-Oppenheimer states for both cases of reduced electron hopping in Fig. 6.24, here only for MTE and FSSH+RD. For both values of the coupling $\bar{\gamma}$, the initial state has similar populations on all adiabatic states, as before in the bare local case (see Fig. 6.15). In both methods and for both parameters, we see a clear periodic modulation with the nuclear oscillation period. In FSSH+RD, the electron quickly relaxes toward the lower Born-Oppenheimer states at the beginning and after each oscillation period. This is interrupted by strong non-adiabatic transitions to a large range of adiabatic states at times when the polaronic trapping is weakened. In the MTE method, we also observe some relaxation toward the lower states, which is, however, much weaker compared to FSSH+RD and the dynamics

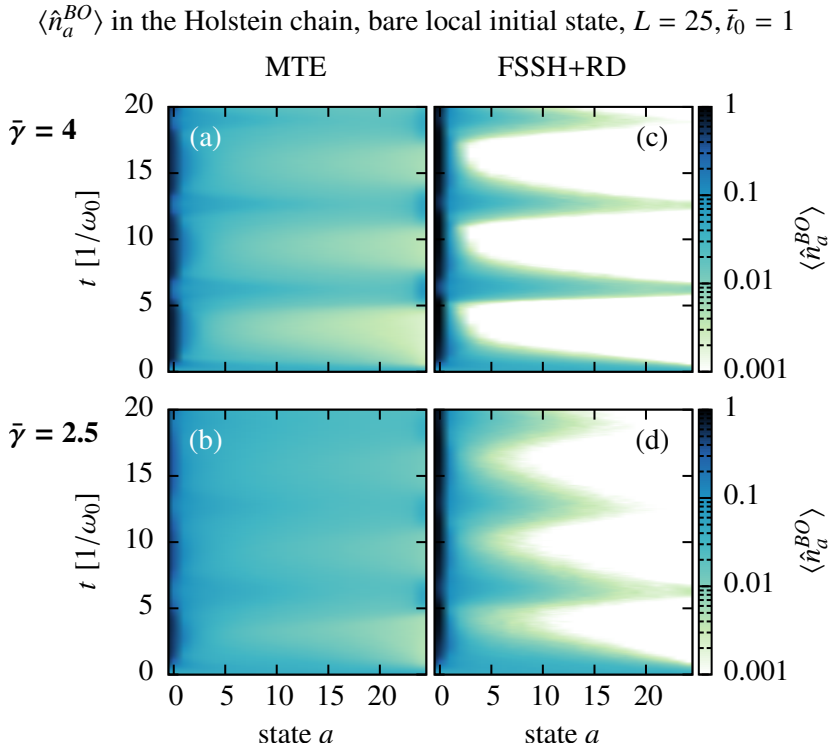

Figure 6.24: Time evolution of the Born-Oppenheimer states populations $\langle \hat{n}_a^{BO} \rangle$ in the Holstein chain of length $L = 25$ with $\bar{t}_0 = 1$, for both $\bar{\gamma} = 4$ and $\bar{\gamma} = 2.5$, and starting from the bare local initial state at the central site. Results are shown for the methods (a) and (b) MTE, (c) and (d) FSSH+RD, each for both values of $\bar{\gamma}$. The methods use the same time step and number of trajectories as in Fig. 6.18.

are again influenced significantly by the higher Born-Oppenheimer states. The periodic trapping is thus reproduced to a much smaller extend. For $\bar{\gamma} = 2.5$, the periodic modulation is barely visible at later times.

6.3.5 Summary for the Holstein chain

Analyzing the results in the Holstein chain is more difficult than for the smaller systems. In the $\bar{t}_0 = 2.5$ systems, the numerically exact method DMRG is available only for short times, and the other methods deviate strongly in their prediction for the long-time dynamics, at least in some observables (see Fig. 6.16 for a rather extreme example). Nonetheless, already the dynamics in this short-time region allow some statements about the performance of the different methods, which is supported by the longer reaching results for the reduced electron hopping $\bar{t}_0 = 1$.

We observed in several examples in the smaller systems that MTE is always able to describe the ultra-short dynamics, which holds to some degree also for the Holstein chain. For example, the initial ballistic expansion of the localized electron density was always recovered. However, in all studied cases, MTE was not able to establish (bare local), or stabilize (dressed local) a localization of the electron density supported by large nuclear distortions, a “polaronic trapping”,

for later times. The dynamics in MTE are always strongly influenced by most of the Born-Oppenheimer states, either because there is no relaxation (bare local), or because populations on the higher states are developed over time (dressed local). In its mean-field approach, this results in a particularly bad description of the total phonon numbers (see Fig. 6.16 and 6.20), even in the short-time regime. Hence, for the parameters chosen here, two of the more fundamental questions of (i) the transport behavior in a polaronic system, and (ii) the energy transfer between the electronic and nuclear subsystems, can both not be answered accurately with MTE, not even on a qualitative level. We note that the local initial states studied for the Holstein chain are all quenched systems which are not restricted to a single adiabatic state at the beginning, though the dressed local state is not too far away from an adiabatic state (with about 90 % of the electronic population in the lowest adiabatic state). The performance of MTE might be better if starting from an adiabatic initial state, for which, however, no benchmark data of either MCE or DMRG are available. Judging from our results in the Holstein dimer, it is unlikely that the MTE method will perform better once it encounters non-adiabatic transitions (see Fig. 6.3). In total, MTE seems unsuited to describe non-adiabatic dynamics in such large chains for the initial states and system parameters investigated here.

The coupled-trajectory method MCE, which performed remarkably in the smaller systems, could not be converged in the Holstein chain. In contrast to the independent-trajectory methods, which reached internal convergence up to our criteria and could only be improved by making algorithmic changes, one could thus achieve better MCE results by increasing the number of used configurations. Hence, one cannot claim that the method is inaccurate, but it is difficult to converge, which might have similar consequences in practical applications. The underlying nuclear dynamics of MCE are given by the Ehrenfest equations of motion (and for far separated configurations their dynamics become equivalent to MTE, see Ref. [264]). With MTE failing to describe the dynamics in large systems correctly, we can thus speculate that the poor convergence of MCE is partially caused by the misguided underlying basis set dynamics. Nonetheless, local observables close to the centers of the chain were recovered excellently (partially seen in the color-plots of the electronic density, Figs. 6.13 and 6.18, and even better for the nuclear distortion on the central site, shown in Fig. 6.17). Coupled-trajectory methods that do not rely on Ehrenfest dynamics (see Sec. 5.3.6) might be an alternative.

Lastly, we have the surface hopping methods. In contrast to MTE, we encountered several difficulties when applying FSSH to large systems, some of which were already known in literature, see Ref. [205]. These difficulties included: (i) the integration scheme and the calculation of hopping probabilities, for which alternative equations were used (see Sec. 5.3.7), (ii) the different definitions possible for calculating diabatic electronic properties, such as the electron densities and the RMSD, none of which were perfectly accurate in large systems (see Fig. 6.12(a)), and (iii) the problems of applying a decoherence correction in large systems, which solves the ambiguity of the electron density definitions, but leads to a spurious charge transfer when describing initial states with strong coherences, thus requiring a restricted decoherence correction, of

which again several options are possible, see Fig. 6.12(b). The benefit was that FSSH+RD showed a good qualitative agreement with the DMRG results for most observables. These include the spreading of the electron density and the RMSD, but also the build-up of a large total phonon number and thus the electron-nuclear energy transfer. We note that with the exception of the RMSD for $L > 11$, the results of normal FSSH were also acceptable when the mixed definition of the electronic density matrix was used, and closer to the DMRG results than MTE.

In order to generalize our statements for the performance of the methods, further studies are needed in the future, not only for more parameter regimes (in particular the large electron-hopping regime), but also for higher dimensional systems (which is challenging for DMRG), for many-electron states (which were to some degree studied in the article corresponding to this chapter, Ref. [37], although only with MTE and DMRG), and, maybe most importantly, for more complicated systems that include, e.g., a phonon dispersion or an electron-electron interaction.

6.4 Evaluation of the methods

In this chapter and the corresponding article, see Ref. [37], we presented a benchmark study of non-adiabatic dynamics described with the independent-trajectory methods MTE, FSSH and FSSH+D/RD introduced in the last chapter, the coupled-trajectory method MCE and the numerically exact ED and DMRG methods. The results for ED in second quantization, MCE and DMRG were obtained by S. Gräber, D. Jansen and J. Stolpp, see the beginning of Ch. 6 for details. By providing reference data for the extended Holstein chain for various quenched initial states, our results complement previous benchmark studies of the trajectory-based methods, see, e.g., Refs. [39, 43–47] and their description in Ch. 1. The comparison to the unbiased exact methods allows to accurately judge the quality of the independent-trajectory methods, beyond just relying on internal consistency criteria, such as size-independence of the mean-squared displacement in large systems, which has been used in the literature on the surface hopping methods (see Refs. [243, 256]).

As a specialty, at least for surface hopping simulations, we put a special focus on the influence of the initial state and its coherences. The local states can be regarded as quenched systems, not restricted to a single adiabatic state. Interestingly, we found this initial states to be not just a challenge for the surface hopping methods, but also for MTE, as we will describe in the following. Our results were always interpreted in the Born-Huang framework and in terms of adiabatic energy surfaces. While such a point of view is necessary to understand the FSSH algorithm, one could stay in a completely diabatic picture when dealing with the Ehrenfest method. However, as we presented both for small and extended systems, the Born-Huang analysis allows to easily understand the failure of MTE in many scenarios, and in our opinion this point of view is helpful for assessing its range of validity. The different methods are evaluated in the following, with a focus on the independent-trajectory methods.

MTE is easy to implement and has no numerical caveats. Its independent-trajectory nature allows for easy parallelization and it can be applied in large systems and for many-electron states without any problems. It improves upon the typical ground state Born-Oppenheimer or Car-Parrinello molecular dynamics (which were used for the thermal phase transition in Sec. 4.2) in that dynamics on several surfaces can be described, including excited state dynamics and non-adiabatic transitions. If the dynamics take place solely on a single Born-Oppenheimer surface (which might be an excited state), then the method is equivalent to the surface hopping methods, or the truncated Wigner approach with a potential given from the occupied surface. In this case, we find a good performance of the method (see Fig. 6.2). In addition, MTE is able to recover the ultra-short time dynamics for both local (diabatic) and adiabatic initial states, and in many cases the first quarter nuclear oscillation period ($t \approx \pi/(2\omega_0)$) is well described, with the exception of the total phonon number in the extended systems, see Figs. 6.16 and 6.20.

On the downside, the MTE method cannot capture independent dynamics of wave packets on different Born-Oppenheimer surfaces (at similar nuclear positions), which is a known problem of the method, see Refs. [29, 228], and was one of the reasons leading to the development of the surface hopping methods. We saw two cases where this is relevant: (i) when encountering a non-adiabatic transition, for example at an avoided crossing, which in the exact dynamics leads to a splitting of the wave packet (see Fig. 6.3), and (ii) for initial states with coherences between the adiabatic states, such as the bare and dressed local states. An extreme example for the latter is the bare local state in the adiabatic parameter regime in the Holstein dimer (see Fig. 6.6), in which the (coherent) upper and lower contribution of the wave function starts to separate in the exact dynamics (see Fig. 6.5), which is not reproduced by MTE. This is in strong contrast to the very good performance of MTE when starting in an adiabatic initial state for the same parameters (see Fig. 6.2).

In the Holstein trimer and chain, MTE shows much less relaxation toward the lower Born-Oppenheimer states compared to the surface hopping methods, and in the dressed local state even a leakage of electronic population to the higher states (see, e.g., Fig. 6.21). As presented in the Holstein trimer, even a very small population on different surfaces can lead to wrong nuclear forces in the mean-field description (see Sec. 6.2.3). The polaronic trapping and energy transfer between subsystems in the Holstein chain could not be recovered even qualitatively, see Sec. 6.3.5. As far as we can generalize from such a simple model system, MTE seems to be a questionable choice for describing the non-adiabatic dynamics in a strongly coupled polaronic material, at least when several Born-Oppenheimer surfaces are involved, and one should be careful in using the method to study energy transfer in solids, see also Ref. [312]. We note that we did not study the anti-adiabatic parameter regime (with $\bar{t}_0 \ll 1$), except in the numerical test for FSSH (see Fig. 5.8), as it is far away from any physical parameter choice relevant for a potential application to our manganite tight-binding model. Decoherence corrections of MTE exist, termed "decay-of-mixing" methods, see Refs. [313, 314], which can improve the performance of the method drastically, but make the algorithm basis dependent and closer

to a surface hopping approach, and are not studied in this thesis.

Another extension of MTE, which in principle can even converge to exact dynamics, was tested in this benchmark study: the coupled-trajectory method MCE. Its performance in the Holstein dimer and trimer was excellent and close to the results obtained with ED, and it could, in contrast to the independent-trajectory methods, even describe a tunneling transition to some degree. It works for both diabatic and adiabatic initial states, although for the implementation used in this study (see Refs. [37, 264]), calculating adiabatic observables and initial states requires to solve integrals over the Gaussian configurations for the projection onto the adiabatic basis, which is costly in large systems and was only done for the dimer and trimer.

MCE converges much slower in large systems. For $L = 11$, with the number of configurations used here, it still agreed with DMRG (for the times available) in the RMSD, but already showed deviations in the total phonon number. For $L = 25$, in the reduced electron hopping case, and for $L = 51$, it could not capture the global dynamics of the initially localized charge carrier and cannot be considered as a converged or exact method in this case. Local observables around the initially occupied sites were still well described, see Fig. 6.17, but in particular the RMSD increased to too high values, caused by the partial escape of electron density from the polaronic trapping. The convergence with an increasing number of configurations seems to be slow (see Refs. [37, 264]) and in the worst case could scale exponentially with the system size (when the MTE-guided basis gives no accurate representation needed for the dynamics, then a close to full basis might be needed). The computational cost scales with the third power of the number of configurations. The potential application of MCE to describe non-adiabatic dynamics in a complicated large system, such as the ones studied with the tight-binding model for manganites, might thus be limited. A plethora of alternative coupled-trajectory methods is available, see the overview in Sec. 5.3.6, and their either fully variational ansatz or their adiabatic spawning algorithms could make some of them more useful for describing non-adiabatic dynamics. The benchmark study presented here and in Ref. [37] might serve as a testbed for these methods.

Fewest-switches surface hopping, with its potential corrections, is the alternative independent-trajectory method studied here. Its formulation is basis dependent and was carried out in the adiabatic basis (i.e., the adiabatic energy surfaces were used for the nuclear dynamics). It is numerically much more involved than MTE and the algorithm is more ambiguous, as a systematic derivation from exact methods is missing (see Ref. [46]). From the definition of the electronic density matrix to be used when calculating diabatic populations (and setting up diabatic initial states), over the numerical problems when dealing with trivial crossings, up to the decoherence correction enhanced spurious charge transfer to look out for in large systems, one has to carefully evaluate and analyze the method if one wants to extract physically reasonable quantities (see Secs. 5.3.5, 5.3.7 and 6.3.1). Even with all these corrections, the method still performs best when starting from an adiabatic initial state. It can describe a wave packet splitting at an avoided crossing and the following independent dynamics on the energy surfaces. Only at later times when the different parts

of the wave function meet again, a recoherence, significant deviations from the exact results are visible (see Fig. 6.3). Like MTE, FSSH does not provide an accurate description of tunneling in its standard formulation, see Sec. 6.1.5, which is well known, see Ref. [315]. Many of the corrections included here were of special importance to allow a good description of initial states not restricted to a single adiabatic state, as the local initial states. With coherences between the adiabatic states being present from the beginning, the short-time nuclear dynamics of FSSH are not equivalent to the exact results anymore, see Fig. 6.6(c). As suggested in the discussion of highly coherent initial states created by an attosecond light-pulse, one might assume that a mean-field description would be the better choice for such states, see Ref. [228].

Surprisingly, with the corrections included, we observed in nearly all studied systems a better long-time dynamics description with the surface hopping methods compared to MTE. When the electron hopping is large enough, the initial coherences, neglected in the calculation of the nuclear forces, average out to allow for a reasonable description in terms of adiabatic surfaces, see Fig. 6.6(b). The same good long-time description was observed for the intermediate electron hopping in the Holstein trimer afterward, and for the reduced electron-hopping regime $\bar{t}_0 = 1$ in the Holstein chain, see Sec. 6.3.4. For the $\bar{t}_0 = 2.5$ results in the Holstein chain, longer exact reference data are needed for a final evaluation of the surface hopping performance, but in the covered time interval FSSH+RD showed the closest agreement to DMRG in the RMSD and the global trend of the electron densities. The general behavior of the non-adiabatic dynamics seem to qualitatively agree with the DMRG results as well, describing a polaronic trapping of the electron. Judging from this benchmark study, FSSH+RD seems to be a promising method to describe non-adiabatic dynamics, also in large systems and for initial states not restricted to a single adiabatic state, making it a valuable candidate for describing, for example, relaxation processes in our manganite tight-binding model.

We want to mention that an application of FSSH without any corrections and in particular for diabatic initial states can lead to wrong results and one should carefully evaluate the system and its parameters. We refer to Ref. [45] for a benchmark study in a cavity model, in which a diabatic initial state is used (although this is never mentioned in that article), and the (uncorrected) FSSH shows the worst performance of all investigated methods.

The ability of FSSH to approximately capture detailed balance (see Refs. [233, 242]) and its often surprisingly accurate long-time description of non-adiabatic dynamics leads to a constant development in the area of surface hopping methods and new variants or improvements are introduced frequently, see the excellent reviews, Refs. [244, 316] for an overview over the last years. This thesis covers the basic form of FSSH and all corrections necessary to obtain a good description of the chosen initial states in small and large systems, but we hope that the benchmark study presented here and in Ref. [37] can be used in the future to test other variants of surface hopping methods.

For the application of FSSH to the manganite tight-binding model, it needs to be able to describe many-particle electron states. Since the algorithm is formulated in terms of such states, see Ref. [29], one can directly apply the

method there. However, calculating the hopping probability between all possible many-particle states can become exponentially difficult in large systems. For a system without direct electron-electron interactions, where the electronic state is described by one Slater determinant, the independent-electron surface hopping was proposed, see Ref. [317]. It is an exact reformulation of the hopping probabilities (and the derivative couplings) in terms of the single-particle orbitals used to construct the Slater determinant, which can be used to reduce the computational cost of the method. Hence, an efficient implementation of FSSH for many-electron states in the Holstein chain, such as the charge-density wave states analyzed with MTE and DMRG in Ref. [37], is straightforward, but not done here.

In interacting many-particle systems, a variety of electronic-structure methods has been combined with surface hopping approaches, see the overview in Ref. [200]. Obtaining the true adiabatic many-particle states, energies and derivative couplings can be demanding or impossible in practical applications. Mentioning two well known single-reference methods, excited states can be calculated from linear-response time-dependent Hartree-Fock or density-functional theory (LR-TDHF or LR-TDDFT), see Refs. [152, 153, 318, 319]. Alternatively, the excited states can be estimated from Slater determinants build from the adiabatic single-particle states of the effective single-particle formulation of Hartree-Fock or density-functional theory, see Refs. [200, 320–323]. Excitation energies estimated from this effective single-particle picture can differ from the exact results (see Ref. [324]), but have been benchmarked with a good agreement to the linear-response results (see Ref. [322]) and allow a very efficient numerical implementation of FSSH, as surface transitions take place only between Slater determinants differing by one single-particle state, see Refs. [321, 323]. This ansatz can also directly be applied to the manganite tight-binding model.

Finally, the used reference method for large systems, DMRG (with LBO), could always be converged for all system sizes, although the reached maximum time is limited, which in the method is related to the growing entanglement, see Ref. [50]. While most often used in one-dimensional systems, there are approaches to deal with two dimensions, see Refs. [49, 50, 281–285]. Systematic efficient algorithms in 2D that include phonons are not yet available, but would be interesting for future benchmark studies toward more realistic model systems. The method is not suited to describe the complicated three-dimensional manganite tight-binding model, but is an excellent choice to benchmark the trajectory-based methods in one-dimensional model systems, and is just as well suited to describe many-electron states.

7 Conclusion and Outlook

In this thesis we analyzed systems with strong electron-phonon coupling. The two focus points of the thesis were: (a) A theoretical investigation of the breakdown of the long-range orbital/Jahn-Teller order in low-doped $Pr_{1-x}Ca_xMnO_3$ (PCMO) at finite temperature using a tight-binding model for manganites. Here, our results support new experimental evidence indicating that the spontaneous orbital order breaks down at much lower temperatures than previously believed, and correlates with the onset of a photovoltaic effect, see Ref. [24] and Sec. 4.2. (b) The second focus point was a detailed benchmark study of two quantum-classical trajectory-based methods, multitrajectory Ehrenfest (MTE) and fewest-switches surface hopping (FSSH). We carefully tested and evaluated their capability of describing non-adiabatic real-time dynamics in a prototypical polaronic system, the Holstein model. In most studied cases, the FSSH method yielded a better description of both the mobility/spreading of the excited charge carrier and the electron-nuclear energy transfer, see Ref. [37] and Ch. 6. A good description of these quantities is necessary for an accurate simulation of the relaxation after a photo-excitation in a system with strong electron-phonon coupling.

One intriguing prospect for a future study is the combination of both obtained insights: An application of FSSH to the manganite tight-binding model for a direct simulation of the photoexcitation in both the orbital ordered and disordered phases. This could provide a deeper understanding of the fundamental requirements for a photovoltaic effect in such strongly coupled electron-phonon systems and the general field of hot carrier solar cells. Let us now discuss our theoretical results in more detail.

In the first part, we investigated the material class of manganites, specifically $Pr_{1-x}Ca_xMnO_3$ (PCMO). This material shows a strong coupling of mobile electrons, cooperative lattice distortions, and localized spins. An adequate theoretical description that allows a direct comparison to experimental results requires the use of an intricate tight-binding model including the dominant interactions between all degrees of freedom, see Ch. 3. Such a model was applied to predict the ordered ground states of PCMO in the low-doping region $0 \leq x \leq 0.25$, see Sec. 4.1. The obtained spin and orbital order fits well to experimental measurements, with one deviation being the lattice constant c/a ratio around $x = 0$. For the intermediate region $0 < x < 0.25$ various nanoscale mixed structures were obtained that are nearly degenerate with the phase separation energy of the neighboring pure phases. Such nanoscale phase separation phenomena have been suggested in Ref. [26] and agree with more recent experimental studies around that doping, see Refs. [85, 86]. The good agreement of the model with experimental results is encouraging, see also the general study including higher dopings in Ref. [126]. Nonetheless, several improvements of the tight-binding model are conceivable to cure the remaining

problems. The inclusion of a site-dependent hopping that reacts to the local octahedral distortions and spin background could remove the necessity to artificially increase the antiferromagnetic superexchange coupling, see Sec. 3.2.5. In addition, anharmonic terms of the Jahn-Teller restoring forces could stabilize prolate orbitals over the oblate ones and stabilize the correct c/a ratio, as discussed in Secs. 3.2.3 and 4.1.2, see also Ref. [132].

Starting from the obtained ground and metastable mixed states at $x = 0$ and $x = 0.1$, we investigated the breakdown of the long-range orbital/Jahn-Teller order with increasing temperature. For this, we used a Car-Parrinello molecular dynamics approach, in which we heated the nuclei with a Nosé-Hoover thermostat to a finite temperature, while the electrons and spins were kept close to their adiabatic ground state. We obtained transition temperatures of $\sim 270\,\mathrm{K}$ for $x = 0.1$ and $\sim 400\,\mathrm{K}$ at $x = 0$ that are in line with new photovoltaic measurements observing the onset of the open circuit voltage around $\sim 220\,\mathrm{K}$ in thin film PCMO, see Ref. [24]. Anomalies in magnetization, electron transport and optical properties around 220-250 K in $x = 0.1$ thin films and in X-ray diffraction experiments around 300 K ($x = 0.1$) and 350 K ($x = 0$) in bulk PCMO, see Ref. [24], are further evidence for a phase transition in this temperature range. The continuous change of the lattice constants measured in the X-ray diffraction experiments indicates a second-order transition. All these results are in sharp contrast to the established phase diagram of PCMO, which predicts the melting of the orbital order only around $\sim 675\,\mathrm{K}$ at $x = 0.1$ and 945 K at $x = 0$, see Refs. [57, 58, 118, 119]. Motivated by resonant X-ray diffraction experiments at $x = 0.25$ (see Ref. [88]) and for the similar material $LaMnO_3$ (see Ref. [120]), which in both cases observe a two-step decay of the orbital order, the new results were interpreted as a spontaneous orbital-order phase transition around room temperature for $x = 0.1$. Above that transition, a remaining tilting-induced order remains until the high temperature tilting-transition, see Ref. [24] and Sec. 4.2. A revised phase diagram following this proposal was presented in Ref. [24] and shown in Fig. 4.15.

The adiabatic description of the electrons and spins prevented us from obtaining the independent magnetic phase transition at low temperatures that is indicated by experimental measurements (see Refs. [58, 83–86]). As the spin transition might affect the orbital-order phase transition as well, we consider augmenting the thermostat calculations with a thermal description for the spins as one of the most important future extensions to our simulations. One straightforward approach would be to apply the Nosé-Hoover thermostat to the spin degrees of freedom, as presented in Refs. [147, 154, 155].

The complexity of the model limits the size of the simulation cells and we could not provide a proper finite size scaling of the phase transition. One future path is thus to extend the model to larger systems. To reach these larger systems, one could reduce sampling times or the complexity of the model (e.g., by removing the electron-electron interaction), or increase the fictitious masses for the spins and electrons together with the integration time step. All of these approaches should then be carefully tested against the small systems analyzed here, before approaching larger systems.

In the second part of this thesis, we analyzed the importance of non-adiabatic

effects on electron-phonon coupled systems, see Ch. 5. We outlined how the coupled electron-nuclear dynamics can be described in the Born-Huang formalism, see Ref. [34], where a multicomponent nuclear wave function evolves in a set of adiabatic Born-Oppenheimer surfaces. A contribution called the derivative couplings acts as a vector potential that couples these surfaces and is responsible for non-adiabatic effects. The examples of the Holstein dimer and trimer were used to showcase how this formalism can be used to understand the fully quantum mechanical coupled dynamics. We discussed the two trajectory-based methods MTE and FSSH, see Refs. [29–31], which retain a non-adiabatic description, while relying on the propagation of classical nuclei. In MTE, each nuclear trajectory evolves according to a potential determined from the trace of the mixed quantum-classical Hamiltonian over the electronic degrees of freedom, which one might regard as a mean-field ansatz. In contrast, FSSH is designed around the concept of adiabatic states, with the nuclear dynamics evolving step-wise along single Born-Oppenheimer surfaces, interrupted by stochastic switching.

Both quantum-classical methods have been benchmarked in the one-dimensional Holstein model against the coupled trajectory method MCE, as well as ED in the Born-Huang basis and in second quantization, and DMRG-LBO, see Ch. 6 and the article [37]. Our results complement previous benchmark studies (see Ch. 1 and Refs. [39, 43–47]) with a comparison to numerically exact reference data in large condensed matter systems and a detailed investigation of the role of the initial state. The calculations, implementations and tests of MCE, ED in second quantization and DMRG-LBO were carried out by S. Gräber, D. Jansen and J. Stolpp, see the beginning of Ch. 6. A detailed evaluation covering the small and large system results of all methods was already given in Sec. 6.4, including an outlook on potential method improvements.

The main results for the quantum-classical methods were: MTE provided a good description of the ultra-short time dynamics in almost all studied cases, while its long-time results deviated drastically from the exact reference data, as soon as more than a single Born-Oppenheimer surface contributed to the dynamics. This was observed after a non-adiabatic transition and for initial configurations with coherences between the adiabatic states. In large systems, the MTE-predictions for the energy stored in the nuclear subsystem (measured from the total phonon number) and for the long-time localization of the electron density (measured from the reduced mean-squared displacement) deviated drastically from all other methods.

FSSH showed in most cases a better intermediate- to long-time agreement with the exact data, where they were available. As far as we could judge from these exact reference data, it provided a better order of magnitude estimate for the nuclear energy and the electron density localization. The only long-time large-system results available, shown in Figs. 6.22 and 6.23, supported this interpretation. Surprisingly, the FSSH method provided a reasonable long-time description even for initial states in a superposition of adiabatic states in most studied cases. This is outside of the typical use-case of this method, but broadens its scope of applicability, for example, in view of a potential application for the direct simulation of a photoexcitation and relaxation in

the manganite tight-binding model. As mentioned in Sec. 6.4, the method's performance in large systems relied heavily on the introduced corrections for the propagation, calculation of hopping probabilities, decoherence and avoidance of spurious charge transfer, see Secs. 5.3.4, 5.3.5 and 6.3.1.

We note that MCE outperformed both quantum-classical methods in the small systems, while it could not be converged in large systems beyond short times. A direct application of MCE to the manganite tight-binding model is an interesting alternative to FSSH or MTE. We cannot judge at this point whether the convergence of MCE in a three-dimensional model might be improved compared to a one-dimensional model when both have the same total number of sites.

Besides possible algorithmic improvements or method variants for MTE and FSSH, see Sec. 6.4, several extensions of this benchmark study are conceivable. First and foremost, longer exact reference data could confirm our current interpretation of the methods' performance. Second, our study is based on a selection of example systems and parameters. A possible improvement is to extend this study to a systematic parameter scan in the electron hopping and electron-phonon coupling $\bar{t}_0$ and $\bar{\gamma}$, ideally for a variety of initial states. Third, adiabatic initial conditions could not be tested in large systems, due to the lack of exact reference data for such initial states. The performance of both MTE and FSSH was better for adiabatic initial states in the smaller systems, and it would be insightful to confirm the same for the extended Holstein chain. Lastly, our initial conditions all started with most harmonic oscillators sampled from their ground state. Extending the study to phonons prepared in a thermal state might be the next step toward an application to the finite-temperature phases in the manganite tight-binding model.

Bibliography

[1] T. Jenkins, *Phys. Educ.* **40**, 430 (2005).

[2] S. Sharma, K. K. Jain, and A. Sharma, *Mater. Sci. Appl.* **06**, 1145 (2015).

[3] J. Cho, J. H. Park, J. K. Kim, and E. F. Schubert, *Laser Photon. Rev.* **11**, 1600147 (2017).

[4] G. Fisher, M. R. Seacrist, and R. W. Standley, *Proceedings of the IEEE* **100**, 1454 (2012).

[5] W. Shockley and H. J. Queisser, *J. Appl. Phys.* **32**, 510 (1961).

[6] G. Conibeer, *Mater. Today* **10**, 42 (2007).

[7] B. G. Akinoglu, B. Tuncel, and V. Badescu, *Sustain. Energy Technol. Assess.* **46**, 101287 (2021).

[8] G. Conibeer, S. Shrestha, S. Huang, R. Patterson, H. Xia, Y. Feng, P. Zhang, N. Gupta, M. Tayebjee, S. Smyth, Y. Liao, S. Lin, P. Wang, X. Dai, and S. Chung, *Sol. Energ. Mater. Sol. C.* **135**, 124 (2015).

[9] D. Raiser, S. Mildner, B. Ifland, M. Sotoudeh, P. Blöchl, S. Techert, and C. Jooss, *Adv. Energy Mater.* **7**, 1602174 (2017).

[10] B. Ifland, J. Hoffmann, B. Kressdorf, V. Roddatis, M. Seibt, and C. Jooss, *New J. Phys.* **19**, 063046 (2017).

[11] B. Kressdorf, T. Meyer, A. Belenchuk, O. Shapoval, M. ten Brink, S. Melles, U. Ross, J. Hoffmann, V. Moshnyaga, M. Seibt, P. Blöchl, and C. Jooss, *Phys. Rev. Applied* **14**, 054006 (2020).

[12] L. D. Landau, *Sow. Phys.* **3**, 664 (1933).

[13] S. I. Pekar, *Untersuchungen über die Elektronentheorie der Kristalle*, Akademie-Verlag Berlin, 1954.

[14] C. Franchini, M. Reticcioli, M. Setvin, and U. Diebold, *Nat. Rev. Mater.* **6**, 560 (2021).

[15] E. O. Wollan and W. C. Koehler, *Phys. Rev.* **100**, 545 (1955).

[16] J. B. Goodenough, *Phys. Rev.* **100**, 564 (1955).

[17] Y. Tokura and Y. Tomioka, *J. Magn. Magn. Mater.* **200**, 1 (1999).

[18] S. Katano, J. A. Fernandez-Baca, and Y. Yamada, *Physica B* **276**, 786 (2000).

[19] V. Kiryukhin, D. Casa, J. P. Hill, B. Keimer, A. Vigliante, Y. Tomioka, and Y. Tokura, *Nature* **386**, 813 (1997).

[20] D. E. Cox, P. G. Radaelli, M. Marezio, and S.-W. Cheong, *Phys. Rev. B* **57**, 3305 (1998).

[21] M. C. Langner, S. Zhou, G. Coslovich, Y.-D. Chuang, Y. Zhu, J. S. Robinson, W. F. Schlotter, J. J. Turner, M. P. Minitti, R. G. Moore, W. S. Lee, D. H. Lu, D. Doering, P. Denes, Y. Tomioka, Y. Tokura, R. A. Kaindl, and R. W. Schoenlein, *Phys. Rev. B* **92**, 155148 (2015).

[22] H. Yoshizawa, R. Kajimoto, H. Kawano, Y. Tomioka, and Y. Tokura, *Phys. Rev. B* **55**, 2729 (1997).

[23] M. Hervieu, A. Barnabé, C. Martin, A. Maignan, and B. Raveau, *Phys. Rev. B* **60**, R726 (1999).

[24] B. Kressdorf, T. Meyer, M. ten Brink, C. Seick, S. Melles, N. Ottinger, T. Titze, H. Meer, A. Weisser, J. Hoffmann, S. Mathias, H. Ulrichs, D. Steil, M. Seibt, P. E. Blöchl, and C. Jooss, *Phys. Rev. B* **103**, 235122 (2021).

[25] E. Dagotto, T. Hotta, and A. Moreo, *Phys. Rep.* **344**, 1 (2001).

[26] E. Dagotto, *Nanoscale phase separation and colossal magnetoresistance*, Springer-Verlag Berlin Heidelberg, 2003.

[27] T. Hotta, *Rep. Prog. Phys.* **69**, 2061 (2006).

[28] M. Sotoudeh, S. Rajpurohit, P. Blöchl, D. Mierwaldt, J. Norpoth, V. Roddatis, S. Mildner, B. Kressdorf, B. Ifland, and C. Jooss, *Phys. Rev. B* **95**, 235150 (2017).

[29] J. C. Tully, *J. Chem. Phys.* **93**, 1061 (1990).

[30] J. C. Tully, *Faraday Discuss.* **110**, 407 (1998).

[31] L. González and R. Lindh, *Quantum Chemistry and Dynamics of Excited States: Methods and Applications*, John Wiley & Sons, Ltd, 2020.

[32] S. Rajpurohit, C. Jooss, and P. E. Blöchl, *Phys. Rev. B* **102**, 014302 (2020).

[33] S. Rajpurohit, L. Z. Tan, C. Jooss, and P. E. Blöchl, *Phys. Rev. B* **102**, 174430 (2020).

[34] M. Born and K. Huang, *Dynamical Theory of Crystal Lattices*, Clarendon Press, 1954.

[35] T. Holstein, *Ann. Phys.* **8**, 325 (1959).

[36] S. Mildner, J. Hoffmann, P. E. Blöchl, S. Techert, and C. Jooss, *Phys. Rev. B* **92**, 035145 (2015).

[37] M. ten Brink, S. Gräber, M. Hopjan, D. Jansen, J. Stolpp, F. Heidrich-Meisner, and P. E. Blöchl, *J. Chem. Phys.* **156**, 234109 (2022).

[38] Y. Tanimura and R. Kubo, *J. Phys. Soc. Jpn.* **58**, 101 (1989).

[39] A. Krotz and R. Tempelaar, *J. Chem. Phys.* **156**, 024105 (2022).

[40] D. V. Shalashilin, *J. Chem. Phys.* **130**, 244101 (2009).

[41] D. V. Shalashilin, *J. Chem. Phys.* **132**, 244111 (2010).

[42] N. Zhou, Z. Huang, J. Zhu, V. Chernyak, and Y. Zhao, *J. Chem. Phys.* **143**, 014113 (2015).

[43] L. Chen, M. F. Gelin, and D. V. Shalashilin, *J. Chem. Phys.* **151**, 244116 (2019).

[44] V. M. Freixas, A. J. White, T. Nelson, H. Song, D. V. Makhov, D. Shalashilin, S. Fernandez-Alberti, and S. Tretiak, *J. Phys. Chem. Lett.* **12**, 2970 (2021).

[45] N. M. Hoffmann, C. Schäfer, N. Säkkinen, A. Rubio, H. Appel, and A. Kelly, *J. Chem. Phys.* **151**, 244113 (2019).

[46] H.-T. Chen and D. R. Reichman, *J. Chem. Phys.* **144**, 094104 (2016).

[47] G. Stock and M. Thoss, *Adv. Chem. Phys.* **131**, 243 (2005).

[48] S. R. White, *Phys. Rev. Lett.* **69**, 2863 (1992).

[49] U. Schollwöck, *Rev. Mod. Phys.* **77**, 259 (2005).

[50] U. Schollwöck, *Ann. Phys.* **326**, 96 (2011).

[51] C. Zhang, E. Jeckelmann, and S. R. White, *Phys. Rev. Lett.* **80**, 2661 (1998).

[52] C. Zhang, E. Jeckelmann, and S. R. White, *Phys. Rev. B* **60**, 14092 (1999).

[53] C. Guo, A. Weichselbaum, J. von Delft, and M. Vojta, *Phys. Rev. Lett.* **108**, 160401 (2012).

[54] B. Kloss, D. R. Reichman, and R. Tempelaar, *Phys. Rev. Lett.* **123**, 126601 (2019).

[55] G. H. Jonker and J. H. Van Santen, *Physica* **16**, 337 (1950).

[56] M. ten Brink, *Analysis of a tight-binding model and its predictions about the ground state properties of manganites*, Master's thesis, Georg-August-Universität Göttingen, Institute for Theoretical Physics, 2017.

[57] E. Pollert, S. Krupička, and E. Kuzmičová, *J. Phys. Chem. Solids* **43**, 1137 (1982).

[58] Z. Jirák, S. Krupička, Z. Šimša, M. Dlouhá, and S. Vratislav, *J. Magn. Magn. Mater.* **53**, 153 (1985).

[59] V. M. Goldschmidt, *Naturwissenschaften* **14**, 477 (1926).

[60] H. Y. Hwang, S.-W. Cheong, P. G. Radaelli, M. Marezio, and B. Batlogg, *Phys. Rev. Lett.* **75**, 914 (1995).

[61] J. B. A. A. Elemans, B. Van Laar, K. R. Van Der Veen, and B. O. Loopstra, *J. Solid State Chem.* **3**, 238 (1971).

[62] C. Ederer, C. Lin, and A. J. Millis, *Phys. Rev. B* **76**, 155105 (2007).

[63] R. Kováčik and C. Ederer, *Phys. Rev. B* **81**, 245108 (2010).

[64] E. Pavarini and E. Koch, *Phys. Rev. Lett.* **104**, 086402 (2010).

[65] M. T. Hutchings, Point-Charge Calculations of Energy Levels of Magnetic Ions in Crystalline Electric Fields, in *Solid State Phys.*, edited by F. Seitz and D. Turnbull, volume 16, pp. 227–273, Academic Press, 1964.

[66] H. A. Jahn and E. Teller, *Proc. R. Soc. Lond. A* **161**, 220 (1937).

[67] J. H. Van Vleck, *J. Chem. Phys.* **7**, 72 (1939).

[68] J. Kanamori, *J. Appl. Phys.* **31**, S14 (1960).

[69] J. Rodríguez-Carvajal, M. Hennion, F. Moussa, A. H. Moudden, L. Pinsard, and A. Revcolevschi, *Phys. Rev. B* **57**, R3189 (1998).

[70] H. C. Longuet-Higgins, *Adv. Spectrosc.* **2**, 429 (1961).

[71] G. Herzberg and H. C. Longuet-Higgins, *Discuss. Faraday Soc.* **35**, 77 (1963).

[72] C. A. Mead and D. G. Truhlar, *J. Chem. Phys.* **70**, 2284 (1979).

[73] M. V. Berry, *Proc. R. Soc. Lond. A* **392**, 45 (1984).

[74] D. R. Yarkony, *Rev. Mod. Phys.* **68**, 985 (1996).

[75] P. W. Anderson, *Phys. Rev.* **79**, 350 (1950).

[76] H. A. Kramers, *Physica* **1**, 182 (1934).

[77] J. Kanamori, *J. Phys. Chem. Solids* **10**, 87 (1959).

[78] J. B. Goodenough and A. L. Loeb, *Phys. Rev.* **98**, 391 (1955).

[79] E. Koch, Exchange Mechanisms, in *The Physics of Correlated Insulators, Metals, and Superconductors*, edited by E. Pavarini, E. Koch, R. Scalettar, and R. Martin, number 7 in Schriften des Forschungszentrums Jülich. Reihe Modeling and Simulation, Forschungszentrum, Zentralbibliothek, Jülich, 2017.

[80] C. Zener, *Phys. Rev.* **82**, 403 (1951).

[81] P. W. Anderson and H. Hasegawa, *Phys. Rev.* **100**, 675 (1955).

[82] T. Hotta and E. Dagotto, *Phys. Rev. B* **61**, R11879 (2000).

[83] Z. Jirák, S. Krupička, V. Nekvasil, E. Pollert, G. Villeneuve, and F. Zounová, *J. Magn. Magn. Mater.* **15-18**, 519 (1980).

[84] S. Majumdar, T. Elovaara, H. Huhtinen, S. Granroth, and P. Paturi, *J. Appl. Phys.* **113**, 063906 (2013).

[85] T. Elovaara, H. Huhtinen, S. Majumdar, and P. Paturi, *J. Phys.: Condens. Matter* **26**, 266005 (2014).

[86] J. Tikkanen, M. Geilhufe, M. Frontzek, W. Hergert, A. Ernst, P. Paturi, and L. Udby, *J. Phys.: Condens. Matter* **28**, 036001 (2016).

[87] R. Kajimoto, H. Mochizuki, H. Yoshizawa, S. Okamoto, and S. Ishihara, *Phys. Rev. B* **69**, 054433 (2004).

[88] M. v. Zimmermann, C. S. Nelson, J. P. Hill, D. Gibbs, M. Blume, D. Casa, B. Keimer, Y. Murakami, C.-C. Kao, C. Venkataraman, T. Gog, Y. Tomioka, and Y. Tokura, *Phys. Rev. B* **64**, 195133 (2001).

[89] Y. Tomioka, A. Asamitsu, H. Kuwahara, Y. Moritomo, and Y. Tokura, *Phys. Rev. B* **53**, R1689 (1996).

[90] A. Daoud-Aladine, J. Rodríguez-Carvajal, L. Pinsard-Gaudart, M. T. Fernández-Díaz, and A. Revcolevschi, *Phys. Rev. Lett.* **89**, 097205 (2002).

[91] L. Wu, R. F. Klie, Y. Zhu, and C. Jooss, *Phys. Rev. B* **76**, 174210 (2007).

[92] S. Grenier, J. P. Hill, D. Gibbs, K. J. Thomas, M. v. Zimmermann, C. S. Nelson, V. Kiryukhin, Y. Tokura, Y. Tomioka, D. Casa, T. Gog, and C. Venkataraman, *Phys. Rev. B* **69**, 134419 (2004).

[93] H. Yoshizawa, H. Kawano, Y. Tomioka, and Y. Tokura, *Phys. Rev. B* **52**, R13145 (1995).

[94] T. Asaka, S. Yamada, S. Tsutsumi, C. Tsuruta, K. Kimoto, T. Arima, and Y. Matsui, *Phys. Rev. Lett.* **88**, 097201 (2002).

[95] S. Cox, J. C. Lashley, E. Rosten, J. Singleton, A. J. Williams, and P. B. Littlewood, *J. Phys.: Condens. Matter* **19**, 192201 (2007).

[96] S. Y. Zhou, Y. Zhu, M. C. Langner, Y.-D. Chuang, P. Yu, W. L. Yang, A. G. Cruz Gonzalez, N. Tahir, M. Rini, Y.-H. Chu, R. Ramesh, D.-H. Lee, Y. Tomioka, Y. Tokura, Z. Hussain, and R. W. Schoenlein, *Phys. Rev. Lett.* **106**, 186404 (2011).

[97] P. G. Radaelli, R. M. Ibberson, D. N. Argyriou, H. Casalta, K. H. Andersen, S.-W. Cheong, and J. F. Mitchell, *Phys. Rev. B* **63**, 172419 (2001).

[98] M. S. Reis, V. S. Amaral, J. P. Araújo, P. B. Tavares, A. M. Gomes, and I. S. Oliveira, *Phys. Rev. B* **71**, 144413 (2005).

[99] K. Tobe, T. Kimura, and Y. Tokura, *Phys. Rev. B* **69**, 014407 (2004).

[100] V. I. Anisimov, I. S. Elfimov, M. A. Korotin, and K. Terakura, *Phys. Rev. B* **55**, 15494 (1997).

[101] Z. Jirák, S. Vratislav, and J. Zajíček, *Phys. Status Solidi A* **52**, K39 (1979).

[102] P. G. de Gennes, *Phys. Rev.* **118**, 141 (1960).

[103] T. Mizokawa, D. I. Khomskii, and G. A. Sawatzky, *Phys. Rev. B* **63**, 024403 (2000).

[104] Y. Tokura, *Rep. Prog. Phys.* **69**, 797 (2006).

[105] T. Hotta, Y. Takada, and H. Koizumi, *Int. J. Mod. Phys. B* **12**, 3437 (1998).

[106] C. Jooss, L. Wu, T. Beetz, R. F. Klie, M. Beleggia, M. A. Schofield, S. Schramm, J. Hoffmann, and Y. Zhu, *Proc. Natl. Acad. Sci. USA* **104**, 13597 (2007).

[107] C. H. Chen, S.-W. Cheong, and H. Y. Hwang, *J. Appl. Phys.* **81**, 4326 (1997).

[108] Mori S., Chen C. H., and Cheong S.-W., *Nature* **392**, 473 (1998).

[109] P. G. Radaelli, D. E. Cox, L. Capogna, S.-W. Cheong, and M. Marezio, *Phys. Rev. B* **59**, 14440 (1999).

[110] M. T. Fernández-Díaz, J. L. Martínez, J. M. Alonso, and E. Herrero, *Phys. Rev. B* **59**, 1277 (1999).

[111] Z. Jirák, C. Martin, M. Hervieu, and J. Hejtmánek, *Appl. Phys. A* **74**, s1755 (2002).

[112] M. M. Savosta, P. Novák, M. Maryško, Z. Jirák, J. Hejtmánek, J. Englich, J. Kohout, C. Martin, and B. Raveau, *Phys. Rev. B* **62**, 9532 (2000).

[113] C. D. Ling, E. Granado, J. J. Neumeier, J. W. Lynn, and D. N. Argyriou, *Phys. Rev. B* **68**, 134439 (2003).

[114] E. Granado, C. D. Ling, J. J. Neumeier, J. W. Lynn, and D. N. Argyriou, *Phys. Rev. B* **68**, 134440 (2003).

[115] P. G. Radaelli, D. E. Cox, M. Marezio, and S.-W. Cheong, *Phys. Rev. B* **55**, 3015 (1997).

[116] C. H. Chen, S. Mori, and S.-W. Cheong, *Phys. Rev. Lett.* **83**, 4792 (1999).

[117] R. K. Zheng, G. Li, Y. Yang, A. N. Tang, W. Wang, T. Qian, and X. G. Li, *Phys. Rev. B* **70**, 014408 (2004).

[118] D. Sánchez, J. A. Alonso, and M. J. Martínez-Lope, *J. Chem. Soc., Dalton Trans.* **23**, 4422 (2002).

[119] J.-S. Zhou and J. B. Goodenough, *Phys. Rev. B* **68**, 144406 (2003).

[120] Y. Murakami, J. P. Hill, D. Gibbs, M. Blume, I. Koyama, M. Tanaka, H. Kawata, T. Arima, Y. Tokura, K. Hirota, and Y. Endoh, *Phys. Rev. Lett.* **81**, 582 (1998).

[121] S. B. Wilkins, T. A. W. Beale, P. D. Hatton, J. A. Purton, P. Bencok, D. Prabhakaran, and A. T. Boothroyd, *New J. Phys.* **7**, 80 (2005).

[122] A. J. Millis, B. I. Shraiman, and R. Mueller, *Phys. Rev. Lett.* **77**, 175 (1996).

[123] A. Szabo and N. S. Ostlund, *Modern Quantum Chemistry: Introduction to Advanced Electronic Structure Theory*, Courier Corporation, 2012.

[124] P. Hohenberg and W. Kohn, *Phys. Rev.* **136**, B864 (1964).

[125] W. Kohn and L. J. Sham, *Phys. Rev.* **140**, A1133 (1965).

[126] S. Rajpurohit, *The study of magnetic and polaronic microstructure in $Pr_{1-x}Ca_xMnO_3$ manganite series*, PhD thesis, Georg-August-Universität Göttingen, http://dx.doi.org/10.53846/goediss-7058, 2018.

[127] T. Hotta, S. Yunoki, M. Mayr, and E. Dagotto, *Phys. Rev. B* **60**, R15009 (1999).

[128] P. B. Allen and V. Perebeinos, *Phys. Rev. B* **60**, 10747 (1999).

[129] R. Car and M. Parrinello, *Phys. Rev. Lett.* **55**, 2471 (1985).

[130] J. C. Slater and G. F. Koster, *Phys. Rev.* **94**, 1498 (1954).

[131] J. Kanamori, *Prog. Theor. Phys.* **30**, 275 (1963).

[132] K. I. Kugel' and D. I. Khomskiĭ, *Sov. Phys.-JETP.* **37**, 725 (1973).

[133] W. Domcke, D. R. Yarkony, and H. Köppel, *Conical Intersections: Theory, Computation and Experiment*, volume 17 of *Advanced Series in Physical Chemistry*, World Scientific, 2011.

[134] M. A. Robb, F. Bernardi, and M. Olivucci, *Pure Appl. Chem.* **67**, 783 (1995).

[135] S. Quezel-Ambrunaz, *Bull. Soc. Franc. Miner. Crist.* **91**, 339 (1968).

[136] N. Metropolis and S. Ulam, *J. Am. Stat. Assoc.* **44**, 335 (1949).

[137] M. P. Allen and D. J. Tildesley, *Computer simulation of liquids*, Oxford Univ. Press, 1996.

[138] W. M. C. Foulkes, L. Mitas, R. J. Needs, and G. Rajagopal, *Rev. Mod. Phys.* **73**, 33 (2001).

[139] L. Verlet, *Phys. Rev.* **159**, 98 (1967).

[140] P. E. Blöchl, CP-PAW Hands-On Course on First-Principles Calculations: Theory of first-principles calculations, `http://www2.pt.tu-clausthal.de/atp/downloads/scripts/firstprinciples.pdf`, 2021, [Online; accessed 12-October-2022].

[141] J.-P. Ryckaert, G. Ciccotti, and H. J. C. Berendsen, *J. Comput. Phys.* **23**, 327 (1977).

[142] K. Laasonen, A. Pasquarello, R. Car, C. Lee, and D. Vanderbilt, *Phys. Rev. B* **47**, 10142 (1993).

[143] P. E. Blöchl, *Phys. Rev. B* **50**, 17953 (1994).

[144] D. Marx and J. Hutter, Ab initio molecular dynamics: Theory and implementation, in *Modern methods and algorithms of quantum chemistry*, edited by J. Grotendorst, volume 1, pp. 301–449, NIC Series Forschungszentrum, Germany, 2000.

[145] S. Nosé, *J. Chem. Phys.* **81**, 511 (1984).

[146] W. G. Hoover, *Phys. Rev. A* **31**, 1695 (1985).

[147] S. Nosé, *Prog. Theor. Phys. Suppl.* **103**, 1 (1991).

[148] G. J. Martyna, M. L. Klein, and M. Tuckerman, *J. Chem. Phys.* **97**, 2635 (1992).

[149] H. Flyvbjerg and H. G. Petersen, *J. Chem. Phys.* **91**, 461 (1989).

[150] Frenkel, D. and Smit, B., *Understanding molecular simulation : from algorithms to applications*, Elsevier (formely published by Academic Press), 1996.

[151] J. L. Alonso, C. Bouthelier-Madre, A. Castro, J. Clemente-Gallardo, and J. A. Jover-Galtier, *New J. Phys.* **23**, 063011 (2021).

[152] A. Dreuw and M. Head-Gordon, *Chem. Rev.* **105**, 4009 (2005).

[153] M. Casida and M. Huix-Rotllant, *Annu. Rev. Phys. Chem.* **63**, 287 (2012).

[154] A. Bulgac and D. Kusnezov, *Phys. Rev. A* **42**, 5045 (1990).

[155] D. Kusnezov, A. Bulgac, and W. Bauer, *Ann. of Phys.* **204**, 155 (1990).

[156] H. Taguchi, M. Nagao, T. Sato, and M. Shimada, *J. Solid State Chem.* **78**, 312 (1989).

[157] K. Binder, Finite size effects at phase transitions, in *Computational Methods in Field Theory*, edited by H. Gausterer and C. B. Lang, Lecture Notes in Physics, pp. 59–125, Berlin, Heidelberg, 1992, Springer.

[158] H. E. Stanley, *Introduction to Phase transitions and critical phenomena*, volume 7, Oxford University Press, New York, 1971.

[159] K. Levenberg, *Quart. Appl. Math.* **2**, 164 (1944).

[160] D. W. Marquardt, *J. Soc. Indust. Appl. Math.* **11**, 431 (1963).

[161] T. Williams, C. Kelley, R. Lang, D. Kotz, J. Campbell, G. Elber, A. Woo, and many others, Gnuplot 5.2, `http://gnuplot.sourceforge.net/`, 2017, [Online; accessed 12-October-2022].

[162] M. E. Fisher and M. N. Barber, *Phys. Rev. Lett.* **28**, 1516 (1972).

[163] M. S. S. Challa, D. P. Landau, and K. Binder, *Phys. Rev. B* **34**, 1841 (1986).

[164] K. Binder and D. P. Landau, *Phys. Rev. B* **30**, 1477 (1984).

[165] R. Cowley, *Adv. Phys.* **29**, 1 (1980).

[166] M. A. Carpenter, R. E. A. McKnight, C. J. Howard, and K. S. Knight, *Phys. Rev. B* **82**, 094101 (2010).

[167] B. F. E. Curchod and T. J. Martínez, *Chem. Rev.* **118**, 3305 (2018).

[168] F. Agostini and B. F. E. Curchod, *Wiley Interdiscip. Rev.: Comput. Mol. Sci.* **9**, e1417 (2019).

[169] S. Ciuchi, F. de Pasquale, S. Fratini, and D. Feinberg, *Phys. Rev. B* **56**, 4494 (1997).

[170] O. S. Barišić, *Phys. Rev. B* **65**, 144301 (2002).

[171] S. Fratini and S. Ciuchi, *Phys. Rev. Lett.* **91**, 256403 (2003).

[172] O. S. Barišić and S. Barišić, *Eur. Phys. J. B* **64**, 1 (2008).

[173] F. Dorfner, L. Vidmar, C. Brockt, E. Jeckelmann, and F. Heidrich-Meisner, *Phys. Rev. B* **91**, 104302 (2015).

[174] J. Bonča, S. A. Trugman, and M. Berciu, *Phys. Rev. B* **100**, 094307 (2019).

[175] V. Janković and N. Vukmirović, *Phys. Rev. B* **105**, 054311 (2022).

[176] J. Ranninger and U. Thibblin, *Phys. Rev. B* **45**, 7730 (1992).

[177] E. V. L. de Mello and J. Ranninger, *Phys. Rev. B* **55**, 14872 (1997).

[178] Y. A. Firsov and E. K. Kudinov, *Phys. Solid State* **39**, 1930 (1997).

[179] J. Chatterjee and A. N. Das, *Phys. Rev. B* **61**, 4592 (2000).

[180] T. Hakioğlu, V. A. Ivanov, and M. Y. Zhuravlev, *Physica A* **284**, 172 (2000).

[181] H. Rongsheng, L. Zijing, and W. Kelin, *Phys. Rev. B* **65**, 174303 (2002).

[182] R. Qing-Bao and C. Qing-Hu, *Commun. Theor. Phys.* **43**, 357 (2005).

[183] S. Paganelli and S. Ciuchi, *Eur. Phys. J. Spec. Top.* **160**, 343 (2008).

[184] S. Paganelli and S. Ciuchi, *J. Phys. Condens. Matter* **20**, 235203 (2008).

[185] Y. Y. Zhang, X. G. Wang, and Q. H. Chen, *Solid State Commun.* **149**, 2106 (2009).

[186] L. K. McKemmish, R. H. McKenzie, N. S. Hush, and J. R. Reimers, *Phys. Chem. Chem. Phys.* **17**, 24666 (2015).

[187] J. R. Reimers, L. K. McKemmish, R. H. McKenzie, and N. S. Hush, *Phys. Chem. Chem. Phys.* **17**, 24641 (2015).

[188] S. A. Sato, A. Kelly, and A. Rubio, *Phys. Rev. B* **97**, 134308 (2018).

[189] M. Born and R. Oppenheimer, *Ann. Phys.* **389**, 457 (1927).

[190] J. C. Tully, Perspective on „Zur Quantentheorie der Molekeln“, in *Theoretical Chemistry Accounts: New Century Issue*, edited by C. J. Cramer and D. G. Truhlar, pp. 173–176, Springer, Berlin, Heidelberg, 2000.

[191] G. A. Worth and L. S. Cederbaum, *Annu. Rev. Phys. Chem.* **55**, 127 (2004).

[192] J. C. Tully, *J. Chem. Phys.* **137**, 22A301 (2012).

[193] W. Lichten, *Phys. Rev.* **131**, 229 (1963).

[194] F. T. Smith, *Phys. Rev.* **179**, 111 (1969).

[195] M. Baer, *Chem. Phys. Lett.* **35**, 112 (1975).

[196] T. Van Voorhis, T. Kowalczyk, B. Kaduk, L.-P. Wang, C.-L. Cheng, and Q. Wu, *Annu. Rev. Phys. Chem.* **61**, 149 (2010).

[197] H. Köppel, W. Domcke, and L. S. Cederbaum, *Adv. Chem. Phys.* **57**, 59 (1984).

[198] C. A. Mead and D. G. Truhlar, *J. Chem. Phys.* **77**, 6090 (1982).

[199] G. Worth, M. Robb, and B. Lasorne, *Mol. Phys.* **106**, 2077 (2008).

[200] R. Crespo-Otero and M. Barbatti, *Chem. Rev.* **118**, 7026 (2018).

[201] A. Polkovnikov, *Ann. Phys.* **325**, 1790 (2010).

[202] B. R. Landry and J. E. Subotnik, *J. Chem. Phys.* **135**, 191101 (2011).

[203] B. R. Landry and J. E. Subotnik, *J. Chem. Phys.* **137**, 22A513 (2012).

[204] S. Fernandez-Alberti, A. E. Roitberg, T. Nelson, and S. Tretiak, *J. Chem. Phys.* **137**, 014512 (2012).

[205] L. Wang, J. Qiu, X. Bai, and J. Xu, *WIREs Comput. Mol. Sci.* **10**, e1435 (2020).

[206] S. Mai, P. Marquetand, and L. González, Surface Hopping Molecular Dynamics, in *Quantum Chemistry and Dynamics of Excited States*, edited by L. González and R. Lindh, pp. 499–530, John Wiley & Sons, Ltd, 2020.

[207] L. D. Landau, *Z. Sowjetunion* **2**, 46 (1932).

[208] C. Zener, *Proc. R. Soc. Lond. A* **137**, 696 (1932).

[209] P. E. Blöchl, Personal communication, 2016.

[210] G. Schubert, G. Wellein, A. Weisse, A. Alvermann, and H. Fehske, *Phys. Rev. B* **72**, 104304 (2005).

[211] J. Franck and E. G. Dymond, *Trans. Faraday Soc.* **21**, 536 (1926).

[212] E. Condon, *Phys. Rev.* **28**, 1182 (1926).

[213] E. Wigner, *Phys. Rev.* **40**, 749 (1932).

[214] H. Weyl, *Z. Physik* **46**, 1 (1927).

[215] J. E. Moyal, *Math. Proc. Cambridge Philos. Soc.* **45**, 99 (1949).

[216] M. Hillery, R. F. O'Connell, M. O. Scully, and E. P. Wigner, *Phys. Rep.* **106**, 121 (1984).

[217] W. B. Case, *Am. J. Phys.* **76**, 937 (2008).

[218] H. J. Groenewold, *Physica* **12**, 405 (1946).

[219] R. Kapral and G. Ciccotti, *J. Chem. Phys.* **110**, 8919 (1999).

[220] R. Grunwald, A. Kelly, and R. Kapral, Quantum Dynamics in Almost Classical Environments, in *Energy Transfer Dynamics in Biomaterial Systems*, edited by I. Burghardt, V. May, D. A. Micha, and E. R. Bittner, Springer Series in Chemical Physics, pp. 383–413, Springer, Berlin, Heidelberg, 2009.

[221] K. Ando, *Chem. Phys. Lett.* **360**, 240 (2002).

[222] K. Ando and M. Santer, *J. Chem. Phys.* **118**, 10399 (2003).

[223] S. Nielsen, R. Kapral, and G. Ciccotti, *J. Chem. Phys.* **112**, 6543 (2000).

[224] J. E. Subotnik, W. Ouyang, and B. R. Landry, *J. Chem. Phys.* **139**, 214107 (2013).

[225] N. F. Mott, *Proc. Cambridge Phil. Soc.* **27**, 553–560 (1931).

[226] J. B. Delos, W. R. Thorson, and S. K. Knudson, *Phys. Rev. A* **6**, 709 (1972).

[227] P. Ehrenfest, *Z. Physik* **45**, 455 (1927).

[228] A. Kirrander and M. Vacher, Ehrenfest Methods for Electron and Nuclear Dynamics, in *Quantum Chemistry and Dynamics of Excited States*, edited by L. González and R. Lindh, pp. 469–497, John Wiley & Sons, Ltd, 2020.

[229] A. García-Vela, R. B. Gerber, and D. G. Imre, *J. Chem. Phys.* **97**, 7242 (1992).

[230] M. S. Topaler, T. C. Allison, D. W. Schwenke, and D. G. Truhlar, *J. Chem. Phys.* **109**, 3321 (1998).

[231] N. M. Hoffmann, C. Schäfer, A. Rubio, A. Kelly, and H. Appel, *Phys. Rev. A* **99**, 063819 (2019).

[232] V. I. Gerasimenko, *Theor. Math. Phys.* **50**, 49 (1982).

[233] P. V. Parandekar and J. C. Tully, *J. Chem. Phys.* **122**, 094102 (2005).

[234] A. Bjerre and E. E. Nikitin, *Chem. Phys. Lett.* **1**, 179 (1967).

[235] J. C. Tully and R. K. Preston, *J. Chem. Phys.* **55**, 562 (1971).

[236] O. V. Prezhdo and P. J. Rossky, *J. Chem. Phys.* **107**, 825 (1997).

[237] K. F. Wong and P. J. Rossky, *J. Chem. Phys.* **105**, 2546 (2001).

[238] G. Granucci and M. Persico, *J. Chem. Phys.* **126**, 134114 (2007).

[239] A. W. Jasper and D. G. Truhlar, Non-Born Oppenheimer Molecular Dynamics for Conical Intersections, Avoided Crossings, and Weak Interactions, in *Conical Intersections*, edited by W. Domcke, D. R. Yarkony, and H. Köppel, volume 17 of *Advanced Series in Physical Chemistry*, pp. 375–414, World Scientific, 2011.

[240] J. R. Schmidt, P. V. Parandekar, and J. C. Tully, *J. Chem. Phys.* **129**, 044104 (2008).

[241] B. R. Landry, M. J. Falk, and J. E. Subotnik, *J. Chem. Phys.* **139**, 211101 (2013).

[242] J. E. Subotnik, A. Jain, B. Landry, A. Petit, W. Ouyang, and N. Bellonzi, *Annu. Rev. Phys. Chem.* **67**, 387 (2016).

[243] A. Carof, S. Giannini, and J. Blumberger, *Phys. Chem. Chem. Phys.* **21**, 26368 (2019).

[244] L. Wang, A. Akimov, and O. V. Prezhdo, *J. Phys. Chem. Lett.* **7**, 2100 (2016).

[245] B. Smith and A. V. Akimov, *J. Phys.: Condens. Matter* **32**, 073001 (2019).

[246] E. J. Heller, *J. Chem. Phys.* **62**, 1544 (1975).

[247] E. Neria and A. Nitzan, *J. Chem. Phys.* **99**, 1109 (1993).

[248] B. J. Schwartz, E. R. Bittner, O. V. Prezhdo, and P. J. Rossky, *J. Chem. Phys.* **104**, 5942 (1996).

[249] E. R. Bittner and P. J. Rossky, *J. Chem. Phys.* **103**, 8130 (1995).

[250] J. E. Subotnik and N. Shenvi, *J. Chem. Phys.* **134**, 024105 (2011).

[251] G. Granucci, M. Persico, and A. Toniolo, *J. Chem. Phys.* **114**, 10608 (2001).

[252] L. Wang and O. V. Prezhdo, *J. Phys. Chem. Lett.* **5**, 713 (2014).

[253] J. Qiu, X. Bai, and L. Wang, *J. Phys. Chem. Lett.* **9**, 4319 (2018).

[254] S. Mai, P. Marquetand, and L. González, *Int. J. Quantum Chem.* **115**, 1215 (2015).

[255] S. Giannini, A. Carof, and J. Blumberger, *J. Phys. Chem. Lett.* **9**, 3116 (2018).

[256] X. Bai, J. Qiu, and L. Wang, *J. Chem. Phys.* **148**, 104106 (2018).

[257] J. Qiu, X. Bai, and L. Wang, *J. Phys. Chem. Lett.* **10**, 637 (2019).

[258] L. Wang and D. Beljonne, *J. Phys. Chem. Lett.* **4**, 1888 (2013).

[259] J. Qiu, Y. Lu, and L. Wang, *J. Chem. Theory Comput.* **18**, 2803 (2022).

[260] E. J. Heller, *J. Chem. Phys.* **75**, 2923 (1981).

[261] G. A. Worth, M. A. Robb, and I. Burghardt, *Faraday Discuss.* **127**, 307 (2004).

[262] G. W. Richings, I. Polyak, K. E. Spinlove, G. A. Worth, I. Burghardt, and B. Lasorne, *Int. Rev. Phys. Chem.* **34**, 269 (2015).

[263] T. Ma, M. Bonfanti, P. Eisenbrandt, R. Martinazzo, and I. Burghardt, *J. Chem. Phys.* **149**, 244107 (2018).

[264] S. A. Gräber, *Simulating real-time dynamics in the Holstein model with Ehrenfest methods*, Master's thesis, Georg-August-Universität Göttingen, Institute for Theoretical Physics, 2021.

[265] T. J. Martinez, M. Ben-Nun, and R. D. Levine, *J. Phys. Chem.* **100**, 7884 (1996).

[266] A. S. Davydov, *Sov. Phys. Usp.* **25**, 898 (1982).

[267] L. Cruzeiro-Hansson, *Phys. Rev. Lett.* **73**, 2927 (1994).

[268] Y. Zhao, B. Luo, Y. Zhang, and J. Ye, *J. Chem. Phys.* **137**, 084113 (2012).

[269] K. Saita and D. V. Shalashilin, *J. Chem. Phys.* **137**, 22A506 (2012).

[270] M. Ben-Nun, J. Quenneville, and T. J. Martínez, *J. Phys. Chem. A* **104**, 5161 (2000).

[271] H. D. Meyer, U. Manthe, and L. S. Cederbaum, *Chem. Phys. Lett.* **165**, 73 (1990).

[272] M. H. Beck, A. Jäckle, G. A. Worth, and H. D. Meyer, *Phys. Rep.* **324**, 1 (2000).

[273] H. Wang and M. Thoss, *J. Chem. Phys.* **119**, 1289 (2003).

[274] H. Wang and M. Thoss, Multilayer Formulation of the Multiconfiguration Time-Dependent Hartree Theory, in *Multidimensional Quantum Dynamics*, edited by H.-D. Meyer, F. Gatti, and G. A. Worth, chapter 14, pp. 131–147, Wiley, 2009.

[275] H. Wang, *J. Phys. Chem. A* **119**, 7951 (2015).

[276] I. Burghardt, H.-D. Meyer, and L. S. Cederbaum, *J. Chem. Phys.* **111**, 2927 (1999).

[277] I. Burghardt, M. Nest, and G. A. Worth, *J. Chem. Phys.* **119**, 5364 (2003).

[278] I. Burghardt, K. Giri, and G. A. Worth, *J. Chem. Phys.* **129**, 174104 (2008).

[279] W. C. Swope, H. C. Andersen, P. H. Berens, and K. R. Wilson, *J. Chem. Phys.* **76**, 637 (1982).

[280] G. Dahlquist and A. Björck, *Numerical methods*, Prentice-Hall, Englewood Cliffs, N.J, 1974.

[281] F. Verstraete and J. I. Cirac, *arXiv:cond-mat/0407066* (2004).

[282] E. M. Stoudenmire and S. R. White, *Annu. Rev. Condens. Matter Phys.* **3**, 111 (2012).

[283] R. Orús, *Ann. Phys.* **349**, 117 (2014).

[284] B.-X. Zheng, C.-M. Chung, P. Corboz, G. Ehlers, M.-P. Qin, R. M. Noack, H. Shi, S. R. White, S. Zhang, and G. K.-L. Chan, *Science* **358**, 1155 (2017).

[285] B. Bruognolo, J.-W. Li, J. von Delft, and A. Weichselbaum, *SciPost Phys. Lect. Notes* , 25 (2021).

[286] C. Brockt, F. Dorfner, L. Vidmar, F. Heidrich-Meisner, and E. Jeckelmann, *Phys. Rev. B* **92**, 241106 (2015).

[287] M. L. Wall, A. Safavi-Naini, and A. M. Rey, *Phys. Rev. A* **94**, 053637 (2016).

[288] J. Stolpp, J. Herbrych, F. Dorfner, E. Dagotto, and F. Heidrich-Meisner, *Phys. Rev. B* **101**, 035134 (2020).

[289] T. Köhler, J. Stolpp, and S. Paeckel, *SciPost Phys.* **10**, 058 (2021).

[290] J. Stolpp, T. Köhler, S. R. Manmana, E. Jeckelmann, F. Heidrich-Meisner, and S. Paeckel, *Comput. Phys. Commun.* **269**, 108106 (2021).

[291] E. Jeckelmann and S. R. White, *Phys. Rev. B* **57**, 6376 (1998).

[292] B. Friedman, *Phys. Rev. B* **61**, 6701 (2000).

[293] H. Wong and Z.-D. Chen, *Phys. Rev. B* **77**, 174305 (2008).

[294] D. Jansen, J. Bonča, and F. Heidrich-Meisner, *Phys. Rev. B* **102**, 165155 (2020).

[295] D. Jansen, C. Jooss, and F. Heidrich-Meisner, *Phys. Rev. B* **104**, 195116 (2021).

[296] G. Vidal, *Phys. Rev. Lett.* **93**, 040502 (2004).

[297] A. J. Daley, C. Kollath, U. Schollwöck, and G. Vidal, *J. Stat. Mech.* **2004**, P04005 (2004).

[298] S. R. White and A. E. Feiguin, *Phys. Rev. Lett.* **93**, 076401 (2004).

[299] J. Haegeman, J. I. Cirac, T. J. Osborne, I. Pižorn, H. Verschelde, and F. Verstraete, *Phys. Rev. Lett.* **107**, 070601 (2011).

[300] J. Haegeman, C. Lubich, I. Oseledets, B. Vandereycken, and F. Verstraete, *Phys. Rev. B* **94**, 165116 (2016).

[301] S. Paeckel, T. Köhler, A. Swoboda, S. R. Manmana, U. Schollwöck, and C. Hubig, *Ann. Phys.* **411**, 167998 (2019).

[302] J. F. Stolpp, *Transport and nonequilibrium dynamics in 1d many-body systems with bosonic degrees of freedom*, PhD thesis, Georg-August-Universität Göttingen, http://dx.doi.org/10.53846/goediss-8867, 2021.

[303] D. Jansen, *Transport and dynamical properties of electron-phonon coupled systems*, PhD thesis, Georg-August-Universität Göttingen, http://dx.doi.org/10.53846/goediss-9675, 2023.

[304] L. Chen, Y. Zhao, and Y. Tanimura, *J. Phys. Chem. Lett.* **6**, 3110 (2015).

[305] J. Zheng, X. Xu, R. Meana-Pañeda, and D. G. Truhlar, *Chem. Sci.* **5**, 2091 (2014).

[306] J. Zheng, R. Meana-Pañeda, and D. G. Truhlar, *J. Phys. Chem. Lett.* **5**, 2039 (2014).

[307] D. V. Makhov, W. J. Glover, T. J. Martinez, and D. V. Shalashilin, *J. Chem. Phys.* **141**, 054110 (2014).

[308] D. V. Makhov, T. J. Martinez, and D. V. Shalashilin, *Faraday Discuss.* **194**, 81 (2016).

[309] B. Bertini, F. Heidrich-Meisner, C. Karrasch, T. Prosen, R. Steinigeweg, and M. Žnidarič, *Rev. Mod. Phys.* **93**, 025003 (2021).

[310] A. Heck, J. J. Kranz, T. Kubař, and M. Elstner, *J. Chem. Theory Comput.* **11**, 5068 (2015).

[311] A. Heck, J. J. Kranz, and M. Elstner, *J. Chem. Theory Comput.* **12**, 3087 (2016).

[312] A. P. Horsfield, D. R. Bowler, H. Ness, C. G. Sánchez, T. N. Todorov, and A. J. Fisher, *Rep. Prog. Phys.* **69**, 1195 (2006).

[313] C. Zhu, A. W. Jasper, and D. G. Truhlar, *J. Chem. Phys.* **120**, 5543 (2004).

[314] C. Zhu, S. Nangia, A. W. Jasper, and D. G. Truhlar, *J. Chem. Phys.* **121**, 7658 (2004).

[315] K. Drukker, *J. Comp. Phys.* **153**, 225 (1999).

[316] B. Smith and A. V. Akimov, *J. Phys.: Condens. Matter* **32**, 073001 (2019).

[317] N. Shenvi, S. Roy, and J. C. Tully, *J. Chem. Phys.* **130**, 174107 (2009).

[318] E. Tapavicza, I. Tavernelli, and U. Rothlisberger, *Phys. Rev. Lett.* **98**, 023001 (2007).

[319] B. F. E. Curchod, U. Rothlisberger, and I. Tavernelli, *ChemPhysChem* **14**, 1314 (2013).

[320] A. Görling, *Phys. Rev. A* **54**, 3912 (1996).

[321] C. F. Craig, W. R. Duncan, and O. V. Prezhdo, *Phys. Rev. Lett.* **95**, 163001 (2005).

[322] S. A. Fischer, B. F. Habenicht, A. B. Madrid, W. R. Duncan, and O. V. Prezhdo, *J. Chem. Phys.* **134**, 024102 (2011).

[323] M. Fischer, J. Handt, and R. Schmidt, *Phys. Rev. A* **90**, 012525 (2014).

[324] N. T. Maitra, *J. Chem. Phys.* **125**, 014110 (2006).

Acknowledgment

First of all, I would like to express my gratitude to Peter E. Blöchl for his excellent supervision during the years of my doctoral studies. His invaluable feedback, constant support and our many scientific discussions made this project possible and broadened my understanding of physics. I am grateful to Fabian Heidrich-Meisner for becoming the second reviewer of this work and for his general feedback and scientific advise during the last years. I would like to extend my sincere thanks to Christian Jooß and Stefan Kehrein for being part of my thesis advisory committee. Furthermore, I thank all members of my examination board.

Special thanks go to all my collaborators in our joined projects. I particularly enjoyed the many fruitful discussions with Fabian Heidrich-Meisner, Christian Jooß, Sangeeta Rajpurohit, Birte Kressdorf, Tobias Meyer, Miroslav Hopjan, David Jansen, and Stefan Gräber. I am grateful to the DFG and the SFB 1073 for their financial support and for enabling such collaborative projects.

I thank my former and present colleagues in the institutes in both Göttingen and Clausthal for their scientific and moral support during my doctoral studies and the great atmosphere in the research groups. In particular, but not limited to: Nils Abeling, Florian Sohn, Thomas Köhler, Sebastian Paeckel, Kristof Harms, Constantin Meyer, Robert Schade, Lukas Rump, Simon Luca Villani, Kai Stroh, Jan Stolpp, and Laura Endter. I also thank Lukas Rump and David Jansen for proofreading parts of the manuscript, and the administrative and technical staff of Göttingen and Clausthal for all their help.

I would like to express my personal thanks to my family for their ongoing support for as long as I can remember. Finally, I want to thank Christin, for her continuous help, motivation and inspiration since more than 11 years and for going with me through all ups and downs of the last years.